Maria Pszona

Single molecule surface-enhanced Raman spectroscopy of porphycene and its derivatives

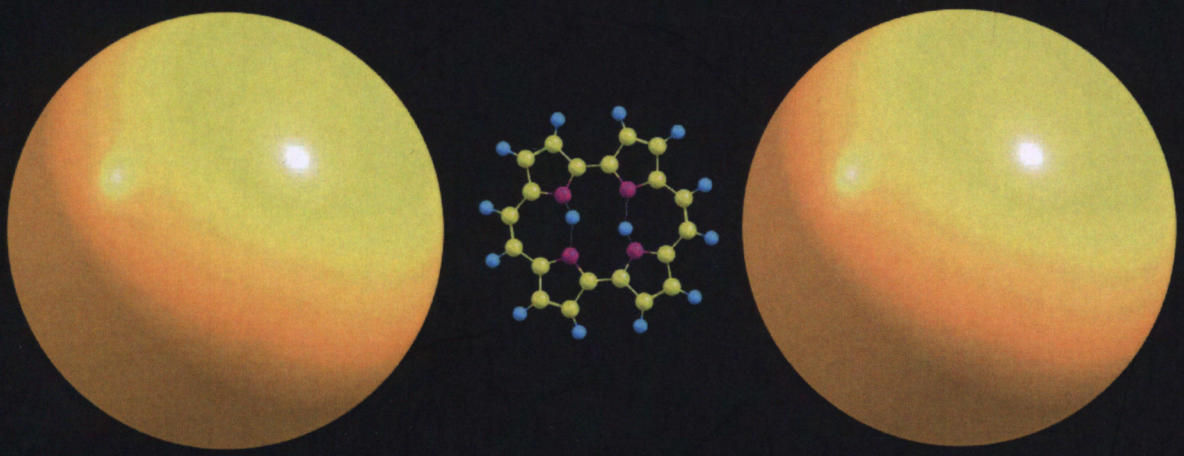

Institute of Physical Chemistry
Polish Academy of Sciences
Kasprzaka 44/52
01-224 Warsaw, Poland

Single molecule surface-enhanced Raman spectroscopy of porphycene and its derivatives

Maria Pszona

PhD dissertation written under the supervision of
Prof. Jacek Waluk

This dissertation has been completed in the framework of the International PhD Studies at the Institute of Physical Chemistry of the Polish Academy of Sciences in Warsaw

Project operated within the Foundation for Polish Science International PhD Projects Programme co-financed by the European Regional Development Fund, Operational Program Innovative Economy 2007-2013.
This work was partially supported by the Polish National Science Centre (NCN) through Grant 2014/15/N/ST4/02757.

INNOVATIVE ECONOMY
NATIONAL COHESION STRATEGY

FNP
Foundation for Polish Science

EUROPEAN UNION
EUROPEAN REGIONAL
DEVELOPMENT FUND

Warsaw, 2019

Cała nasza nauka,
w porównaniu z rzeczywistością,
jest prymitywna i dziecinna
– ale nadal jest to najcenniejsza rzecz,
jaką posiadamy.

Albert Einstein (1879-1955)

Rodzicom

Acknowledgements

First and foremost, I would like to thank my supervisor prof. Jacek Waluk for his enthusiasm, patience, and guidance. For providing me a lot of interesting topics, stimulating discussions, and leaving me a great deal of freedom in choosing the direction of research.

I am also deeply indebted to dr. Sylwester Gawinkowski, who introduced me into the exciting field of surface-enhanced Raman spectroscopy and spent with me long hours in the laboratory: planning, measuring, and discussing both scientific and non-scientific topics. I was really lucky to have such a good companion during my PhD studies, from whom I could learn a lot. Thank you for all that time.

I would also like to thank dr. Izabela Kamińska and dr. Joanna Niedziółka-Jönsson for the preparation of efficient SERS substrates, which I used in some experiments.

I am also very grateful to the excellent professors who allowed me to visit their labs, learn new techniques, and perform experiments: prof. Johan Hofkens and prof. Hiroshi Uji-i from KU Leuven, prof. Alfred Meixner form University of Tübingen, and Takashi Kumagai from Fritz Haber Institute of the Max Planck Socienty in Berlin. I really appreciate this stimulating time.

I would like to thank all my colleagues from the Photochemistry and Spectroscopy Department who were there during the course of my PhD studies for the nice atmosphere, interesting discussions, and support in the not-so good days. Especially thanks to Natalia Masiera, Basia Golec, Anna Kelm, Michał Kijak, Aleksander Gorski, and Hubert Piwoński.

I would like to thank Jędrzej Solarski, with whom I share not only scientific interest, but also personal life. With his sense of humor, he has always been a great support for me in the moments of doubt.

Finally, I would like to thank my parents, who were always very supportive and from the very beginning of my life aroused the curiosity of the world. But, most importantly, they raised me to be an honest person. Therefore, in my scientific work, I always tried to be objective and described what I really measured, not what I hoped to measure. Big thanks to my brother Paweł, for his unlimited patience, support, and being a perfect older brother.

Contents

Abbreviations

AFM	atomic force microscopy
DMPc	9,20-dimethylporphycene
DFT	density functional theory
EF	enhancement factor
EM	electromagnetic
FWHM	full width at half maximum
HOMO	highest occupied molecular orbital
LSPRs	localized surface plasmon resonances
LUMO	lowest unoccupied molecular orbital
MCD	magnetic circular dichroism
MGTIC	malachite green isothiocyanate
NP	nanopartcile
NR	nanorod
Pc	porphycene
PCA	principal component analysis
PL	photoluminescence
PSSE	plasmonic spectral shaping effect
SERS	surface-enhanced Raman scattering
SEM	scanning electron microscopy
SM	single molecule
SM SERS	single molecule surface-enhanced Raman spectroscopy
STM	scanning tunnelling microscopy
TERS	tip-enhanced Raman scattering
TDDFT	time-dependent density functional theory
TMPc	9,10,19,20-tetramethylporphycene

Chapter 1

Introduction

Every molecule may interact with electromagnetic radiation in a variety of ways, including absorption, emission, and scattering. These phenomena may be exploited to probe the molecular vibrational states, which contain specific information on the studied molecule, thus allowing for unambiguous identification. Typically, the energies required to excite a molecule to higher vibrational states lie in the infrared region. One of the methods that offer an access to these energies is infrared spectroscopy, which is based on the absorption process. Another very commonly used technique is based on Raman scattering (inelastic scattering of photons). The energy differences between incident and scattered photons directly correspond to the frequencies of molecular vibrations or rotations, and give rise to the Raman spectrum: the unique fingerprint of a molecule. Such high specificity of Raman spectroscopy made it an attractive and powerful analytical tool. This technique, however, suffers from a serious limitation: low sensitivity. Since statistically only one out of a million photons is inelastically scattered,[1] the Raman spectra are usually obtainable for gases, crystals, and concentrated solutions, where millions of molecules of the same type coexist. Nevertheless, the problem of low sensitivity can be overcome by placing molecules close to plasmonic nanostructures, which was reported for the first time in 1974,[2] and correctly interpreted only three years later.[3,4] Attempts to understand the phenomena underlying the enhancement observed in this new technique called surface-enhanced Raman spectroscopy (SERS) have attracted many researchers to this field. But the most serious stimulus for further development in this research area was provided by the demonstration of

its ultra-high sensitivity, reaching a single molecules level.[5,6] Since then, much effort was put into designing new efficient SERS-active substrates and optimising instrumental setups. Nowadays, the SERS technique, due to its great analytical potential is the technique of choice in a wide range of disciplines: from chemistry and physics through materials to life sciences.

Despite the fact that the first single-molecule SERS spectra were registered already 20 years ago, only about 40 different species have been observed on a single molecule level by the SERS technique so far. That is not many. Moreover, the vast majority of them were dyes excited with resonant laser lines, including rhodamine 6G,[5,7,8,9,10,11,12,13,14,15] crystal violet,[6,16,17,18] brilliant green,[19] and Nile blue.[20,21,14,11] A few orders of magnitude higher resonance Raman cross section compared to Raman cross section greatly facilitates reaching a single molecule regime.

A constantly small number of species for which single molecules were observed proves that, even after a rapid development in nanofabrication, achieving single molecule sensitivity still remains a challenge. Nevertheless, the wealth of information which can be obtained from single molecule studies shows that it is worth the effort. First of all, measurements of individual molecules provide distributions of the investigated properties instead of the averaged values which are delivered by bulk measurements. Moreover, some 'exotic' species or behaviours typically 'disappear' upon averaging, whereas, due to single molecule studies, such rare events may be observed. Furthermore, observation of individual molecules may provide a deeper insight into their dynamics: changes of the orientation and chemical reactions. At this point, it is worth noting that in SERS spectroscopy only very specific molecules can be observed: the ones located in so-called hot spots, i.e., places exhibiting enormous enhancement of electromagnetic field. When we refer to single molecule spectra, it does not mean that within the laser spot, which size is limited by diffraction, only one molecule is present. Indeed, most probably there are many molecules, but the registered signal is dominated by one molecule. The one situated in a hot spot.

It is worth mentioning that the research in the field of single molecule spectroscopy

was awarded in 2014 the Nobel Prize in chemistry for the development of super-resolution techniques based on fluorescence microscopy, which would not be possible without single molecule sensitivity. This thesis, however, is primarily focused on single molecule SERS spectroscopy. Contrary to fluorescence, which is typically a few orders of magnitude stronger, observation of Raman signal from single molecules requires the vicinity of a metallic nanostructure that supports plasmon resonances. The observed enhancement may originate from different mechanisms, which cannot be easily disentangled. Moreover, the measured SERS spectra contain not only information on the studied molecule, but also on its environment. Therefore, modelling of the phenomena behind surface-enhanced Raman scattering is rather complicated and some of the aspects of this process are still not well understood.

Thus far, a great deal of single molecule research has been focused on the fundamental issues: a reliable proof of observing single molecules,[22,23,24] analysis of spectral and intensity fluctuations,[8,18,25] and the impact of competition between adsorption and diffusion.[26] It turned out that single molecule studies, except providing a deeper insight into the properties of the studied species, may also contribute to better understanding of the phenomena related to the SERS process, particularly in relation to hot spots. First, single molecule studies provided experimental confirmation of theoretical predictions that large enhancement factors (EF) occur only at very localized positions, called hot spots.[27] According to the theoretical studies, the electromagnetic enhancement at points distant by only a few nanometers may differ by orders of magnitude.[28] For comparison, typical size of relatively small organic molecules, such as rhodamine or porphycene is about one nanometer. The highest values of the enhancement factor on the substrate are probed just by single molecules.[29] Second, single molecule studies revealed that the enhancement factor shows a so-called long-tail distribution, and "2% of the (randomly adsorbed) molecules contribute to 98% of the SERS signal".[30] Furthermore, the correlation between Raman spectra and topography showed which kind of structures create efficient hot spots.[17] On the other hand, Stranahan and Willets, utilizing single molecule sensitivity combined with on-off blinking behaviour of SERS signal obtained super-resolution optical images of hot spots.[31] These

achievements demonstrate that studies on a single molecule level are of key importance from a fundamental knowledge point of view.

Despite the fact that nowadays SERS exists as a well established analytical technique, there are still some unresolved fundamental questions regarding the SERS phenomenon. For instance, blinking, which is often attributed to thermal diffusion in and out of hot spots,[31] is not a fully addressed issue. Even small modification of a nanostructure leading to a change of a gap size between nanoparticles might also be manifested as blinking. Not to mention other possible photoinduced effects like desorption, molecule dissociation, the charge or electron-transfer processes, or chemical reactions.[27] Another problem that remains open is the determination of molecular orientation in a hot spot. Theoretically, this should be achievable, but it is hampered by (i) dispersion of the localized surface plamon resonance influencing the Raman peaks intensities and (ii) the need of the exact knowledge of Raman tensor, which can be modified upon adsorption to metal and by resonance conditions.[28] Another fundamental question to deal with is why molecules reach hot spots. Basically, the area of hot spots accounts for only a tiny fraction of the total surface. If the interaction energies between a molecule and a surface were equally distributed, statistically the occupation of hot spots would not be probable. Therefore, most likely, molecules experience some binding interactions, but complete understanding of this phenomenon requires further research. Additionally, the role of laser illumination in trapping molecules into hot spots has not yet been determined. As Raman measurements require laser illumination, evaluation of its impact is complicated due to photoeffects, which cannot be eliminated.[28] As can be seen, there are still numerous fundamental issues that need to be addressed and deserve careful investigation. In this thesis single molecule studies were employed not only to broaden the knowledge of the studied species, but also to gain a better insight into an impact of molecular features on SERS dectactability. So far the molecular parameters such as steric hindrance or charge distribution have not been considered in terms of factors affecting the possibility of reaching hot spots. But they should, which is proved by the results presented in this thesis.

This thesis is organised as follows: Chapter 1 gives an overview of single molecule spectroscopy and introduces issues raised in this work. Chapter 2 outlines the

theoretical background and the current status of surface-enhanced Raman spectroscopy, with particular emphasis put on single molecule studies. Moreover, a short description of the studied molecules is given. Chapter 3 formulates the main objectives of this dissertation. Chapter 4 addresses experimental issues, including the procedures of SERS substrate preparation and deuteration of porphycene, materials and instrumentation used in the research. Chapter 5 is entirely devoted to unsubstituted porphycene and contains experimental results, which aim at proving single molecule sensitivity. Furthermore, it discusses the presence of different tautomers, mobility of porphycene molecules on the surface of a SERS substrate and estimates the enhancement factor experienced by single molecules. Chapter 6 analyses the obtained time traces of porphycene in terms of positive and negative correlations between Raman bands intensities. Chapter 7 focuses on the impact of spatial structure of chromophores on the detectability on a single molecule level by SERS on the basis of *tert*-butyl derivatives of porphycene. Chapter 8 presents new exciting challenges and proposes further promising research directions emerging from this work, while the last chapter provides a brief recapitulation.

In summary, this thesis is intended to illustrate the considerable research potential of single molecule studies for extending the knowledge of studied species and their environments. This is demonstrated on the example of porphycene, of which the vibrational structure was already a subject of detailed research.[32] Single molecule studies allowed for improving previous assignment of modes, including identification of combination bands and overtones. Moreover, rare behaviours or molecular forms could be witnessed. As already mentioned, this thesis aims also at discussing a more general issue: the influence of molecular properties on the detection sensitivity by the SERS technique. This was based on the comparison of differently substituted porphycenes. As the results presented here concern the fundamental phenomena related to SERS process, the outcome of this dissertation may be of considerable importance, especially from the analytical, both qualitative and quantitative, point of view. Finally, the reported temperature dependence indicates that altering the temperature may also affect the sensitivity of the SERS technique.

All implemented software and additional information can be found at `http://github.com/gitmajka/phd`.

Chapter 2

Theoretical background

This chapter provides a brief theoretical background of Raman scattering and surface-enhanced Raman scattering (SERS), key processes studied in this thesis. Here, however, we will limit ourselves to classical and simplified quantum description, which is required to understand the experimentally observed effects. The exhaustive treatment of Raman scattering, including resonance Raman scattering with its detailed quantum mechanical description has been provided by Long,[33] while all essential aspects of SERS were explored in the textbook of Le Ru and Etchegoin.[34]

Moreover, this chapter describes the history of single molecule SERS spectroscopy and provides its current status, including important issues such as the bi-analyte technique, intensity fluctuations, existence of a diffuse background, and photostability of molecules under SERS conditions.

2.1 Light-matter interaction

Spectroscopy, a study of the matter through its interactions with electromagnetic (EM) radiation, provides a wealth of information about an investigated system. In the classical description, electromagnetic waves interact with matter via charged

particles, which are being pushed and pulled by an oscillating electric field. Nevertheless, light-matter interactions could not be properly treated without quantum mechanics, in which light field acts to couple quantum states of the matter.

We will focus on interactions between molecules and electromagnetic radiation with a wavelength in the range of 300-800 nm (ultraviolet, visible and near-infrared radiation). Since a molecule may interact with electromagnetic radiation in different ways, we can distinguish light absorption, emission, and scattering.

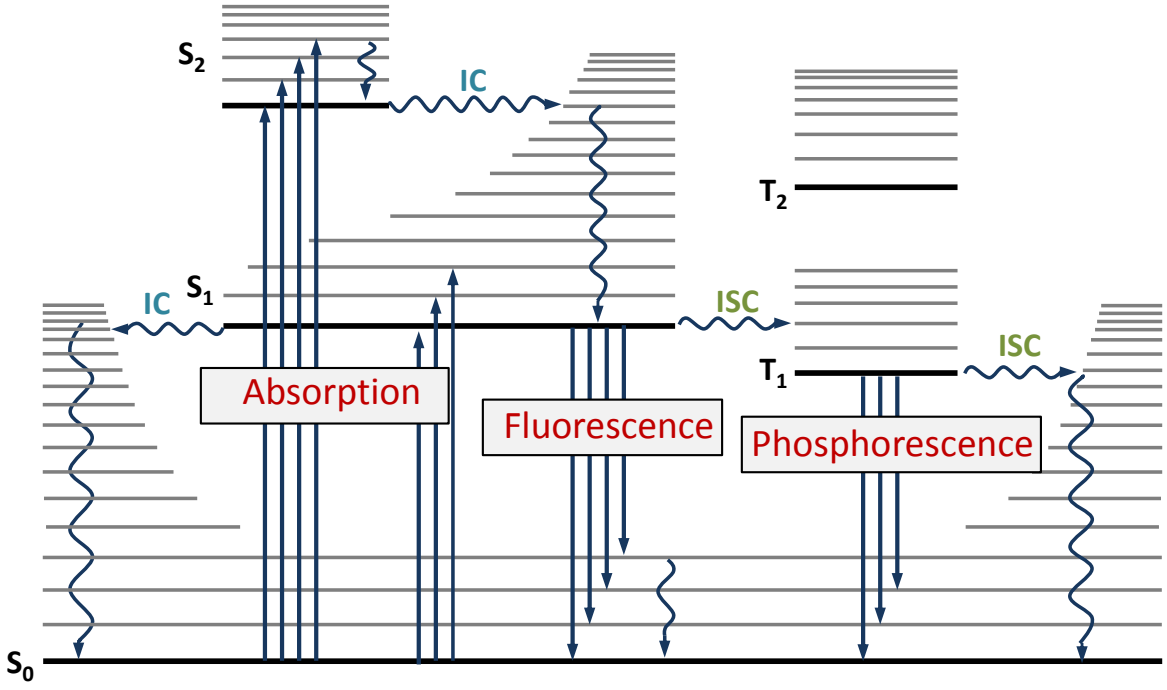

Figure 2.1: Perrin-Jabłoński diagram.

One of the most convenient ways to illustrate the electronic states of a molecule and possible photophysical processes, such as photon absorption and emission (fluorescence and phosphorescence), internal conversion (IC) and intersystem crossing (ISC), is a Perrin-Jabłoński diagram (Figure 2.1).[35] Radiative processes are indicated by straight arrows, while non-radiative processes by wavy ones. Singlet states are denoted as S_0 (the ground state), $S_1, \ldots$, while triplet states are marked as $T_1, T_2, \ldots$. Vibrational levels are related to each electronic state. There is also another family of photophysical processes, known as scattering. The main difference between scattering and absorption or emission, is that it is a two-photon

process. We can treat scattering as instantaneous absorption of an incident photon and emission of another one. Classically, scattered light might be considered as the light reradiated after electromagnetic wave encountered scattering matter (e.g., molecules). As such a wave interacts with the matter, the electron cloud of an atom or a molecule experiences periodic perturbation about its equilibrium position with the same frequency ω as that of the electric field of the incident wave. According to the laws of electromagnetism, oscillating charge emits EM radiation. This scattered light does not always have the same frequency as an incident wave. By the difference of energy between the incident and scattered photons, we can classify scattering processes as elastic or inelastic. If both photons have the same energy, we deal with elastic scattering. In the case of molecules this process is often called Rayleigh scattering. Its intensity strongly depends on the wavelength of light (it is inversely proportional to the fourth power of the wavelength) and the size of the scattering particle. Although this model also properly describes scattering from small particles (with the size up to a tenth of the wavelength of the incident light), it may not be applied to larger objects, such as nanoparticles. Such scattering, referred to as Mie scattering, is described by the Mie solution to the Maxwell's equations.[36] The proposed model applies to spherical particles with the size comparable to the wavelength of the incident radiation.

Apart from elastic scattering, light may also be inelastically scattered by the matter. This happens when the scattered photon has different energy than the incident one. In molecules, one of the most important cases of such process is Raman scattering. The energy difference between the two photons yields information about the internal energetic structure, on the ground that it corresponds to the molecular electronic, vibrational, or rotational transitions. This is not the case for elastic scattering, which leaves a molecule at the same energy level and therefore provides no insight into its internal structure.

2.2 Raman scattering

The Raman effect was theoretically predicted by Smekal in 1923,[37] and experimentally observed for the first time five years later by C. V. Raman and his

student K. S. Krishnan.[38] For this discovery Raman was awarded the Nobel Prize in Physics in 1930. Despite the importance of Raman spectroscopy, its use was seriously limited by the low intensity of inelastic scattering (approximately 1 out of 10^6 photons[1]) until the development of the first laser in 1960.[39] As lasers provide monochromatic and coherent light, they serve as an excellent source of excitation. In Raman spectroscopy the monochromaticity of light is of great importance, because what is measured is the difference between incident and scattered photons. Moreover, lasers emit high intensity radiation, which is crucial due to low Raman scattering intensity.

Although Raman scattering may seem similar to fluorescence, the nature of these two competitive processes is significantly different. Emission must be preceded by promotion of a molecule to an excited state, for instance via photon absorption. Raman scattering, however, is an instantaneous process and occurs independent of electronic state of a molecule. Therefore, even if incident light is not resonant with an electronic transition of a molecule, Raman scattering happens. However, if we excite a molecule in resonance, fluorescence is usually a few orders of magnitude stronger, hiding Raman features in the spectral range of emission.

The process of Raman scattering may be described either in the classical way, or by quantum mechanics, more specifically by the perturbation theory. However, for simplicity, also the latter approach treats electromagnetic radiation classically. Only the interacting molecule is described quantum-mechanically, with its states perturbed by the electric and magnetic fields.

The classical description of Raman effect was proposed by G. Placzek in 1934.[33] It is known that the electric field associated with incident radiation causes oscillations of the electron cloud resulting in periodic distortion of the charge, called induced dipole moment. Mathematically, the strength of the induced dipole moment (oscillating at the same frequency ω), $\boldsymbol{\mu}(\omega)$, may be expressed as

$$\boldsymbol{\mu}(\omega) = \boldsymbol{\alpha}\mathbf{E}(\omega), \tag{2.1}$$

where $\boldsymbol{\alpha}$ is the optical polarizability tensor, which fully characterizes the optical response of the molecule, and $\mathbf{E}(\omega)$ is the electric field of the incident wave. Polarizability, a property of matter, provides a measure of charge distribution distortion

in the presence of an external electric field. Since the induced dipole moment is not always parallel to the electric field of the incident wave, $\boldsymbol{\alpha}$ is a second-rank tensor. The highly polarizable molecules are the ones with 'free electrons', such as lone pairs or delocalized π electrons. There are a lot of organic molecules among them, especially dyes.

Naturally, molecular polarizability depends on the relative positions of the atoms, and therefore it changes during vibrations. Consequently, it can be expressed as a function of normal mode coordinates $Q_k, Q_l, \ldots$ associated with vibrational frequencies $\omega_k, \omega_l, \ldots$. Assuming that the displacement is very small (close to 0), each component of tensor $\boldsymbol{\alpha}$ can be expanded in a Taylor series with respect to the normal coordinates of vibration:

$$\alpha_{pq} = (\alpha_{pq})_0 + \sum_k \left(\frac{\partial \alpha_{pq}}{\partial Q_k}\right)_0 Q_k + \frac{1}{2}\sum_{k,l}\left(\frac{\partial^2 \alpha_{pq}}{\partial Q_k Q_l}\right)_0 Q_k Q_l + \ldots , \tag{2.2}$$

where $(\alpha_{pq})_0$ denotes the value α_{pq} at the equilibrium position. Assuming harmonic approximation, terms with powers of Q higher than the first can be neglected. Considering one specific normal mode of vibration Q_k, Equation 2.2 simplifies to

$$(\alpha_{pq})_k = (\alpha_{pq})_0 + \left(\frac{\partial \alpha_{pq}}{\partial Q_k}\right)_0 Q_k, \tag{2.3}$$

which can be phrased in vector notation as

$$\boldsymbol{\alpha_k} = \boldsymbol{\alpha_0} + \boldsymbol{\alpha_k'} Q_k. \tag{2.4}$$

Applying harmonic approximation for the oscillation, the time dependence of Q_k can be expressed as

$$Q_k = Q_{k_0} \cos(\omega_k t). \tag{2.5}$$

Therefore, we obtain

$$\boldsymbol{\alpha_k} = \boldsymbol{\alpha_0} + \boldsymbol{\alpha_k'} Q_{k_0} \cos(\omega_k t). \tag{2.6}$$

Since the electric field of the incident EM wave can be described as

$$\mathbf{E} = \mathbf{E_0} \cos(\omega_0 t), \tag{2.7}$$

the time-dependent induced dipole moment may be decribed by the equation

$$\boldsymbol{\mu} = \boldsymbol{\alpha_0}\mathbf{E_0}\cos(\omega_0 t) + \boldsymbol{\alpha}'_{\boldsymbol{k}}\mathbf{E_0}Q_{k_0}\cos(\omega_0 t)\cos(\omega_k t). \tag{2.8}$$

Finally, by applying trigonometric identities, we obtain

$$\boldsymbol{\mu} = \boldsymbol{\alpha_0}\mathbf{E_0}\cos(\omega_0 t) + \frac{1}{2}\boldsymbol{\alpha}'_{\boldsymbol{k}}\mathbf{E_0}Q_{k_0}\cos\left((\omega_0 - \omega_k)t\right) + \frac{1}{2}\boldsymbol{\alpha}'_{\boldsymbol{k}}\mathbf{E_0}Q_{k_0}\cos\left((\omega_0 + \omega_k)t\right). \tag{2.9}$$

As we can see from the above equation, the induced dipole has three separate frequency components. The first component corresponds to the incident frequency and accounts for Rayleigh scattering, while the next two are responsible for inelastic scattering, namely Raman scattering. The second component, which gives rise to radiation at frequency $\omega_0 - \omega_k$, explains the origin of Stokes scattering, and finally, the last one is referred to as anti-Stokes scattering: radiation at frequency $\omega_0 + \omega_k$. Moreover, according to the above equation, the necessary condition for Raman scattering related to molecular vibration of frequency ω_k is that at least one of the components $(\partial\alpha_{pq} \backslash \partial Q_k)_0$ is non-zero. Although classical theory predicts reasonably well the characteristic molecular vibrational frequencies, it cannot be applied to molecular rotations. Furthermore, it provides no information how $\boldsymbol{\alpha}'_{\boldsymbol{k}}$ depends on molecular properties, such as electronic energy levels, and therefore cannot explain the resonance Raman effect.

The quantum chemical approach provides a complete description of most aspects of Raman scattering, which allows us to determine the spectroscopic properties in both the ground and excited states. D. Long presented the quantum mechanical treatment based on perturbation theory, which includes derivation of the formula for the induced transition dipole moment $\boldsymbol{\mu}$ and hence the transition polarizability tensor $\boldsymbol{\alpha}$ for Rayleigh and Raman scattering.[33] In order to differentiate between the classical polarizability and the quantum mechanical one, which is defined in terms of wavefunction and discrete energy levels of a system, the latter is called the transition polarizability. The description of Raman scattering via Jabłoński-like diagram presented in Figure 2.2 requires introduction of the so-called virtual state, which is not a stationary state of a system. Since it is not a solution of a time-independent Schrödinger equation, it does not correspond to a well-defined

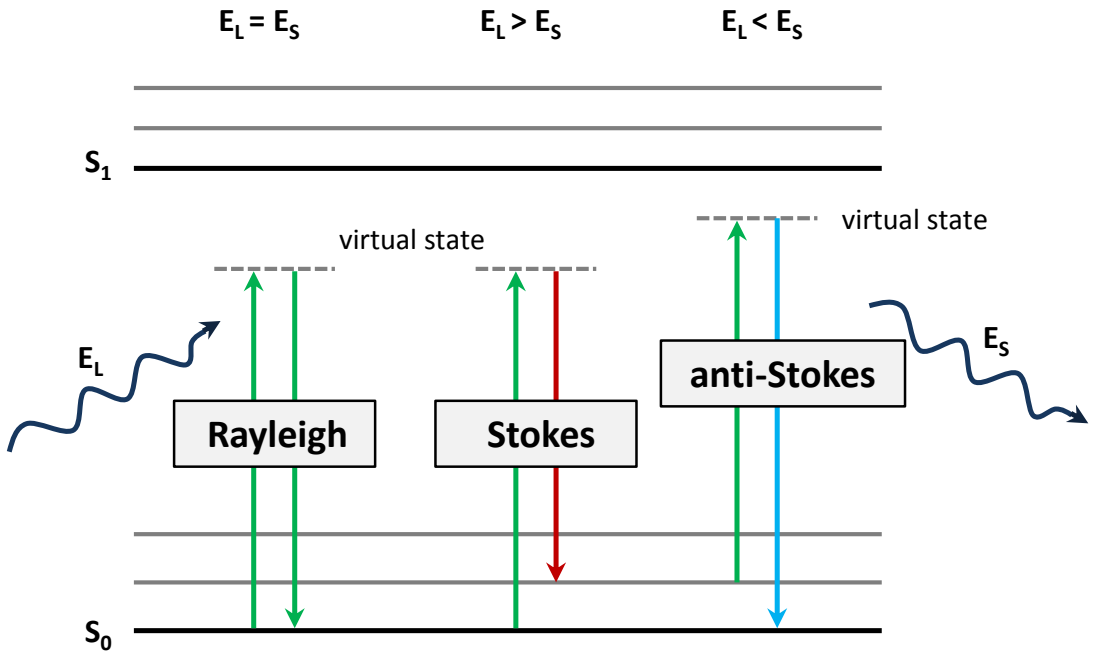

Figure 2.2: A simplified Jabłoński diagram illustrating scattering processes: Rayleigh and Raman (Stokes and anti-Stokes).

energy. The scattering is classified according to the relation between energies of the incident radiation, E_L, and the scattered one, E_S. Rayleigh scattering happens if both energies, E_L and E_S are equal. Stokes scattering appears when the energy of the incident photon is higher than the energy of the scattered one, contrary to anti-Stokes scattering, when the situation is opposite.

The quantum mechanical approach provides a formula for the transition polariability tensor $\boldsymbol{\alpha}$ for a transition between the initial state $|i\rangle$ and a final state $|f\rangle$:

$$\boldsymbol{\alpha}_{fi} = (\alpha_{pq})_{fi} = \frac{1}{\hbar} \sum_{r \neq i,f} \left[\frac{\langle f|\hat{\mu}_p|r\rangle\langle r|\hat{\mu}_q|i\rangle}{\omega_{ri} - \omega_1 - \mathrm{i}\Gamma_r} + \frac{\langle f|\hat{\mu}_p|r\rangle\langle r|\hat{\mu}_q|i\rangle}{\omega_{ri} + \omega_1 + \mathrm{i}\Gamma_r} \right], \tag{2.10}$$

where $\hbar = \frac{h}{2c}$ with h being the Planck constant and c the speed of light in vacuum, $\hat{\mu}_p$ denotes electric dipole moment operator, ω_1 is the frequency of the incident radiation, ω_{ri} is the frequency of a transition between states i and r, and $2\Gamma_r$ (rad s^{-1}) relates to the full width of the energy of state r. This full width $2\Gamma_r$ is related to the lifetime τ_r of the state r via the uncertainty principle, which results in an

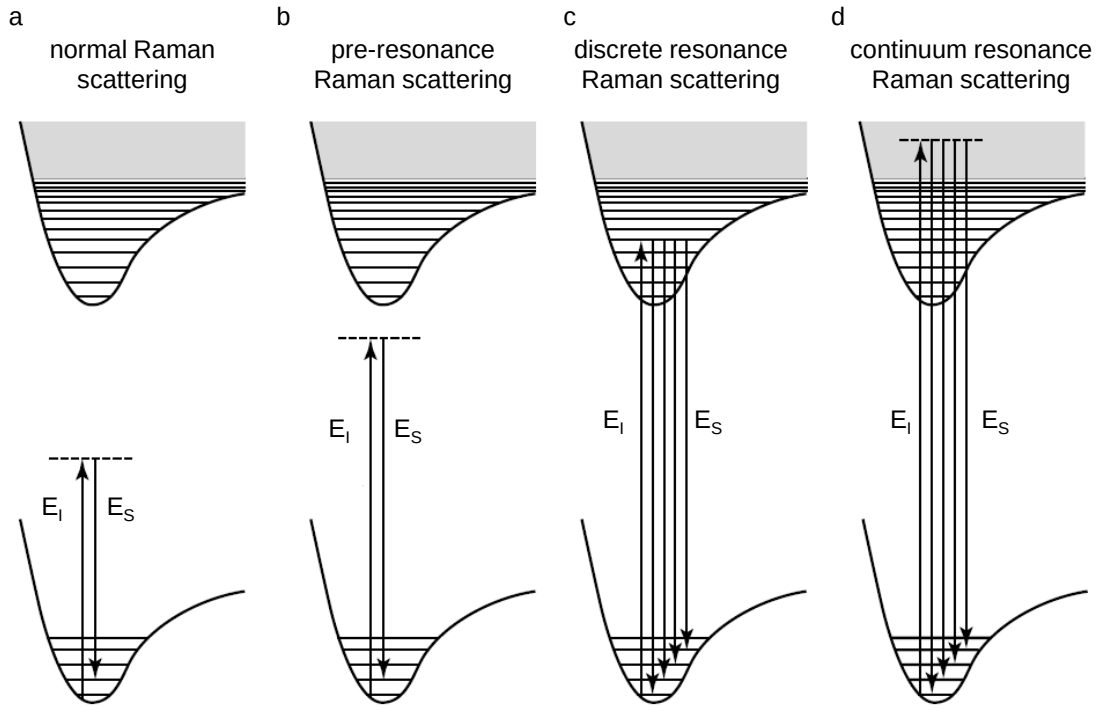

Figure 2.3: A simplified Jabłoński diagram illustrating Raman scattering processes classified according to the energy of the incident light E_I and molecular levels. E_S denotes the energy of the scattered photons.

equation $\tau_r = 1/2\Gamma_r$. For the initial and final states i and f their lifetimes can be assumed to be infinite, which gives $\Gamma_i = \Gamma_f = 0$.

The relationship between the frequency, ω, and the energy of the radiation, E, is given by the equation

$$E = \hbar\omega. \tag{2.11}$$

The expression 2.10 has singularities for every ω_1 giving the value of the denominator $(\omega_{ri} - \omega_1 - \mathrm{i}\Gamma_r)$ equal to 0. Therefore, Raman scattering may be classified according to the energy of the incident radiation $\hbar\omega_1$ with respect to the energy levels of a studied system. As the exciting frequency ω_1 is usually much lower than any molecular transition frequency of a studied system, i. e., for all states $|r\rangle$: $\omega_1 \ll \omega_{ri}$, then $\omega_{ri} - \omega_1 \approx \omega_{ri}$. Moreover Γ_r is much smaller than ω_{ri}, hence its influence can be neglected. Under such conditions, equation 2.10 has no singularity and the scattering is termed as normal Raman scattering.

If ω_1 approaches any of the absorption frequencies ω_{ri}, which is illustrated in Figure 2.3(b), the Raman scattering is classified as pre-resonance. As $\omega_1 \approx \omega_{ri}$, which is

shown in Figure 2.3(c), the singularities may occur. The value of the denominator $(\omega_{ri} - \omega_1 - \mathrm{i}\Gamma_r)$ tends to 0 and highly influences the transition polarizability tensor $\boldsymbol{\alpha}$. Such scattering is called resonance Raman. It may also happen that the energy $\hbar\omega_1$ is large enough to reach dissociative energy levels in a molecule, which is shown in Figure 2.3(d). Such process is called continuum resonance Raman scattering.

The intensity of resonance Raman scattering is usually a few orders of magnitude higher than for normal Raman scattering. This is due to components with the denominator $(\omega_{ri} - \omega_1 - \mathrm{i}\Gamma_r)$ close to 0, whose value drastically increases as their denominators approach 0.

The intensity, I, of radiation originating from an oscillating electric dipole induced in a molecule by incident light with frequency ω_0 along the direction forming an angle θ with the dipole axis is given by the equation

$$I = k'_\omega \omega_s^4 \mu_0^2 \sin^2\theta, \tag{2.12}$$

where μ_0 is the amplitude of the induced electric dipole with frequency ω_s (which might be different from ω_0) and k'_ω is a constant equal to

$$k'_\omega = \frac{1}{32\pi^2 \varepsilon_0 c_0^3}. \tag{2.13}$$

2.3 Surface-enhanced Raman spectroscopy

Although Raman spectroscopy gives insight into vibrational structure of the studied molecules, it suffers from low intensity due to low inelastic scattering cross-section, which limits its applicability. However, the intensity of Raman scattering by molecules adsorbed on metallic nanostructures or rough metal surfaces (mainly gold, silver, and copper) might be enhanced even by several orders of magnitude. This phenomenon, called surface-enhanced Raman scattering (SERS) was observed for the first time in 1974 by Martin Fleischmann et al. for pyridine adsorbed on an electrochemically roughened silver electrode.[2] Then, however the observed enhancement of the signal intensity was misinterpreted. It was wrongly attributed to higher concentration of scattering molecules owing to much larger

surface area of the fractal-like structures. The correct interpretation of the experimental data was provided only few years later. In 1977, two independent groups proposed mechanisms explaining the observed enhancement. Jeanmaire and van Duyne suggested the electromagnetic mechanism,[4] while Albrecht and Creighton proposed a charge-transfer effect.[3] The exact mechanisms and their contributions to the enhancement are still under debate in the literature, however the SERS community accepted electromagnetic and charge-transfer effects, with the former being much stronger.

Reports of an extraordinary sensitivity of the SERS technique, reaching a single molecule level, by two independent groups in 1997[5,6] attracted many researchers to this field. Since then we have witnessed an extremely rapid development in SERS spectroscopy, including advances in microscopy and nanofabrication. Nowadays, the SERS technique, due to its great analytical potential is the technique of choice in a wide range of disciplines: chemistry, physics, materials, and life sciences. Its numerous applications include identification of intermediates and the establishment of reaction mechanisms, sensing (e.g., pH, glucose), detection of mutations in DNA, and attempts to carry out DNA sequencing, protein localization in tissues and bacteria identification.[40]

2.4 SERS mechanisms

Raman intensities are proportional to the square of the amplitude of the induced electric dipole $\boldsymbol{\mu}(\omega) = \boldsymbol{\alpha}\mathbf{E}(\omega)$ (see Eq. 2.2). For that reason, two distinct effects contributing to the enhancement were naturally proposed: increase of the local electric field close to the nanostructure or change in the molecular polarizability due to the interaction with metal surface. The first mechanism, called electromagnetic enhancement, makes a major contribution to the overall enhancement, while the second one, chemical enhancement, results in an increase by up to two orders of magnitude. Both mechanisms are discussed in more detail below.

2.4.1 Electromagnetic enhancement

The electromagnetic theory explains an experimentally observed enhancement as a purely physical effect, which requires the existence of plasmonic nanostructures in order to efficiently couple photons. Only a few metals are suitable for SERS, among which gold and silver are the most commonly used. However, the electromagnetic enhancement has also been observed for different metals, such as copper and aluminium. The optical properties of these metals, different from the properties of standard dielectrics, are due to the presence of free conduction electrons forming free-electron plasma. Indeed, in the dielectric materials electrons are bound to the host atoms, while in metals they can move freely. The optical response in both cases can be modelled by simple harmonic motion due to the oscillatory character of the optical field. Such description is known as the Lorentz model for dielectrics and the Drude model for metals, described in more detail in the textbook of Le Ru and Etchegoin.[34] Although the Drude model predicts reasonably well frequency-dependent dielectric functions of metals, which is crucial to understand light-plasmon interactions, in some cases it needs to be extended. This simplest model, taking into account only intra-band transitions, fails if the inter-band transition is close to the plasma frequency, which is the case for gold.[34]

Considering a perfect metal, in the absence of an external perturbation the charge density of plasma is uniform with zero net charge. However, if we illuminate a metallic nanoparticle, localized surface plasmon resonances (LSPRs) can be excited, among which of greatest importance is the dipolar one (higher order multipolar resonances can be neglected for small nanoparticles). The surface plasmons are collective oscillations of the conduction electrons with respect to the ionic metal nuclei that result in charge separation.

In order to excite the localized surface plasmons the resonance condition must be fulfilled: the frequency of the incident radiation should match the natural frequency of the plasma oscillations, ω_p, which depends on the dielectric functions of the metal, $\varepsilon_{metal}(\omega)$, and the surrounding medium, $\varepsilon_{medium}(\omega)$. Moreover, it is sensitive to the size and shape of a nanoparticle. Typically, LSPR shifts to the red with an increasing size or nanoparticles aggregation. Furthermore, the curvature and

the aspect ratio of nanoparticles enormously influence the LSPR. Usually, largest enhancement of the electric field is observed for spikes and sharp edges.

Upon resonant excitation with light of frequency ω_{inc}, the oscillating electric field of the incident light drives free electrons in the metal forward and backward, creating a Hertzian dipole, which in turn is a source of electromagnetic radiation with the same frequency ω_{inc}. Thus, a metal nanoparticle may act as a nanoantenna emitting radiation at the same frequency as the incident light, ω_{inc}. As a result the local electric field, $\mathbf{E_{loc}}(\omega_{inc})$, close to the metal nanoparticle is modified with respect to the electric field of the incident radiation, $\mathbf{E_0}(\omega_{inc})$. Not only its magnitude changes, but also its direction. If a molecule is located in the vicinity of the metal surface, it interacts with this local field. Therefore the induced dipole moment is equal to $\boldsymbol{\mu} = \boldsymbol{\alpha}\mathbf{E_{loc}}(\omega_{inc})$. As it was previously described, due to vibrations, a molecule scatters not only in an elastic way. Considering one specific vibration with frequency ω_k, a molecule may also scatter at frequencies $\omega_{inc} - \omega_k$ and $\omega_{inc} + \omega_k$, which accounts for Stokes and anti-Stokes scattering, respectively. Finally, this frequency-shifted radiation may also excite LSPR of the metal nanostructure, leading to scattering at the same frequency. This is exactly the same mechanism as for the incident radiation, but this time for Raman-shifted photons scattered by a molecule.

In conclusion, the surface-enhanced Raman scattering may be considered as a five-step process, which involves:

1. excitation of localized surface plasmon resonance by the incident light,
2. elastic scattering off a metal nanostructure resulting in an enhancement of the local electric field,
3. Raman scattering by a molecule,
4. excitation of LSPR by Raman-shifted radiation,
5. elastic scattering of Raman-shifted radiation by a nanostructure into far-field.

Typically, the theoretical estimations of the electromagnetic enhancement are based on $|E|^4$-approximation.[41] This model separately treats the enhancements

of the incident radiation and inelastically scattered radiation. In view of Eq. 2.12, the intensity of the radiation emitted by oscillating electric dipole is proportional to $|\boldsymbol{\mu}|^2$. Hence, a change in electromagnetic field due to the presence of metallic nanostructure strongly affects the intensity of scattered radiation. This effect, known as local field enhancement, results in the amplification by a factor

$$M_{loc}(\omega_{inc}) = \frac{|\mathbf{E_{loc}}(\omega_{inc})|^2}{|\mathbf{E_{inc}}|^2}. \tag{2.14}$$

Moreover, metallic nanostructure additionally intensifies the radiation scattered by a molecule (already enhanced once). Since the Raman-shifted radiation has the frequency $\omega_R = \omega_{inc} \pm \omega_k$, its intensity is enhanced by a factor

$$M_{rad}(\omega_R) = \frac{|\mathbf{E_{loc}}(\omega_R)|^2}{|\mathbf{E_{inc}}|^2}. \tag{2.15}$$

Taking into account these two mechanisms, the EM enhancement factor might be expressed as

$$EF(\omega_{inc}, \omega_R) \approx M_{loc}(\omega_{ins}) M_{rad}(\omega_R) \approx \frac{|\mathbf{E_{loc}}(\omega_{inc})|^2}{|\mathbf{E_{inc}}|^2} \frac{|\mathbf{E_{loc}}(\omega_R)|^2}{|\mathbf{E_{inc}}|^2}. \tag{2.16}$$

Based on the additional approximation $\omega_{inc} \approx \omega_R$, which is more valid for low frequency vibrations, the EF might be estimated by $|E|^4$-approximation:

$$EF(\omega_{inc}) \approx \frac{|\mathbf{E_{loc}}(\omega_{inc})|^4}{|\mathbf{E_{inc}}|^4}. \tag{2.17}$$

We should, however, keep in mind that the plasmonic nanostructure also affects the radiation pattern, so in order to completely describe the enhancement factor, the directional properties (i.e., the polarization of the incident light and the direction of the detection) should be considered. Indeed, if the radiation is enhanced, but at the same time redirected, it may become undetectable.

Experimentally, the enhancement factor is given by

$$EF = \frac{I_{SERS}/N_{SERS}}{I_{Raman}/N_{Raman}}, \tag{2.18}$$

where I and N account for the intensity and the number of molecules contributing to the signal, while the subscripts *SERS* and *Raman* refer to the SERS experiment and the normal Raman (non-SERS) measurement, respectively.

One of the aims of introducing this measure was to compare the quality of the SERS substrates. In practice, however, it is not that simple, since it depends on the probe molecule, its orientation with respect to the surface, excitation laser line, etc..

The local field enhancement may dramatically vary according to the position. Therefore, for the same SERS substrate, the average enhancement factor may be a few orders of magnitude lower than the single-molecule EF, which corresponds to a specific position. The locations which exhibit extremely large local field enhancement are called 'hot-spots'.

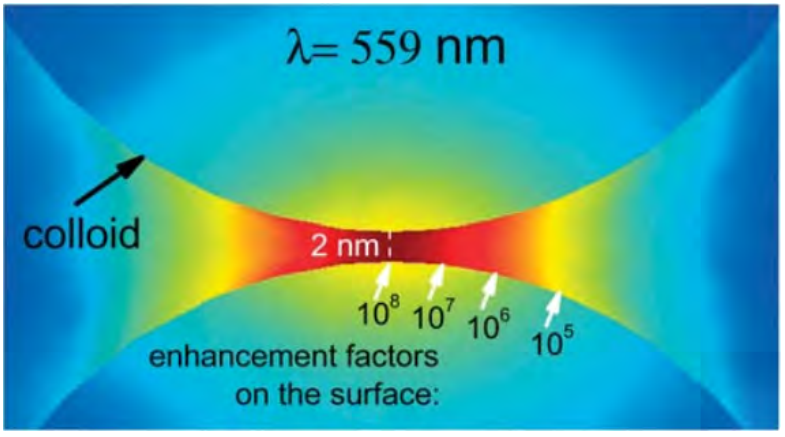

Figure 2.4: Distribution of the enhancement factor between two gold nanoparticles, each with a radius of 30 nm. Simulations were performed for $\lambda = 559$ nm, using electrostatic approximation. Adapted from[28].

On account of SERS being a distance-dependent phenomenon, the surface coverage should ideally be one monolayer or lower. Otherwise, the enhancement of Raman scattering from molecules located further would be lower and the proportionality of signal intensity to the number of molecules would be no longer maintained.

Since the electromagnetic enhancement is a purely physical effect, it should apply independent of the kind of a molecule that is adsorbed on a nanostructure. According to the commonly accepted models it decreases rapidly over a distance of 2-3 nm, which is demonstrated in Figure 2.4.

2.4.2 Chemical enhancement

It is commonly accepted that two separate mechanisms are involved in the enhancement of Raman scattering upon placing molecules in the proximity of plasmonic nanostructures.[34] Not all of the experimental observations could be explained exclusively by electromagnetic theory. For instance, the enhancement factor for molecules containing a lone pair of electrons, such as pyridine or piperidine was 10 up to 1000-fold higher than expected.[42] Other, difficult to explain, experimental data were obtained from measurements in electrochemical cells, which revealed that for different excitation wavelengths the maximum of SERS intensities is observed at different applied potentials.[43,44] Therefore, apart from the electromagnetic mechanism, chemical enhancement was postulated. Contrary to the former, which applies to all analytes, the chemical mechanism entirely depends on the adsorbate and in general is limited only to molecules with a direct contact with a metal surface. Therefore, it is also known as a first-layer SERS effect.[45]

For a long time, the chemical effect and its contribution to the enhancement was a matter of debate.[34] First, its influence on the enhancement is usually a few orders of magnitude lower than the contribution due to the electromagnetic mechanism. Second, other molecular features may affect the intensity of the SERS signal: affinity to a substrate surface (depending, among others, on the electrical charge), orientation in a hot spot, etc. If both mechanisms coexist, the observed enhancement results from multiplication of enhancements originating independently from electromagnetic and chemical effects.[34] Therefore, the determination of the absolute value of the chemical enhancement factor is a challenging task.

In general, any change in the Raman polarizability tensor $\boldsymbol{\alpha}$ upon adsorption onto a metal surface can be classified as chemical enhancement.[34] A particularly noticeable increase in polarizability occurs upon charge transfer (in the ground or in the excited state). This may happen if a molecule is bound to the metal surface. Nevertheless, already a close proximity of the metal surface affects molecular polarizability. Modification of $\boldsymbol{\alpha}$ naturally affects the SERS intensity, however the most spectacular changes are due to resonance process associated with new electronic transitions. In a molecule-metal system overlapping of molecular orbitals with metal states creates new electronic states, and therefore new transitions are

available. If they are in resonance or pre-resonance with the excitation laser line the SERS intensities benefit additionally from resonance enhancement, which is schematically shown in Figure 2.5. Consequently, the Raman scattering cross section is greatly enhanced.

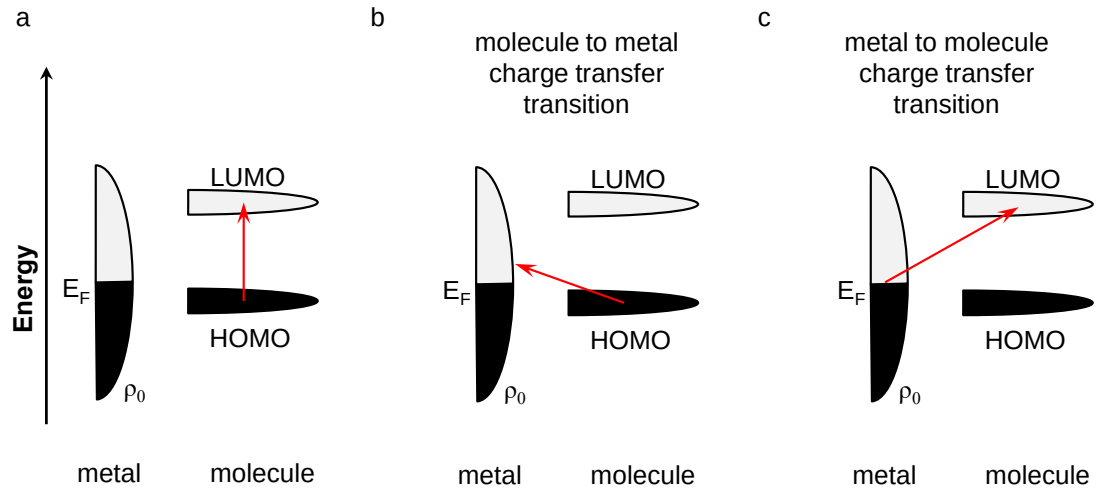

Figure 2.5: (a) Energy levels of a molecule-metal system. The discrete molecular levels broaden upon adsorption on metal. In metal the conduction band, whose width represents the density of available states ρ_0 is partially filled. The filled levels (black) range up to E_F, the Fermi level; above are unfilled levels (grey). (b) The scheme of molecule-to-metal charge transfer transition. (c) The scheme of metal-to-molecule charge transfer transition.

Different cases have been observed where the chemical enhancement was recognized (based on the discussion in the textbook of Le Ru and Etchegoin[34]):

(i) a molecule is located in the proximity of metal, but is not covalently bound to its surface; as a result, the electronic structure might be slightly perturbed, which influences the polarizability of the adsorbate and therefore affects the Raman scattering cross section

(ii) interactions between molecular orbitals of the adsorbate and metal states can lead to the charge transfer phenomenon already in the ground state (without help of light);[46] This results in a significant change in the intrinsic polarizability of an adsorbate. Typically, the charge transfer happens from the metal conduction band to unoccupied orbitals of an adsorbate. This charge transfer transition is modulated by molecular vibrations. The increase in intensities of Raman bands results from intensity borrowing from metal, which has high

scattering cross section. The theory behind this process was established by Lippitsch.[47] This mechanism occurs also for non-resonant excitation, i.e., if the energy of the incident photon does not match any of the allowed transitions. An additional enhancement due to resonance can appear independently. If the electronic structure is perturbed upon adsorption in such a way that the excitation wavelength, which is off resonance for non-adsorbed molecule, induces resonant-Raman scattering, the Raman scattering cross section is dramatically enhanced.

(iii) upon formation of a surface complex if the energy of the photon matches the difference between the Fermi level E_F and the molecular highest occupied orbital (HOMO) or the lowest unoccupied orbital (LUMO) of the adsorbate, photo-driven charge transfer may occur (charge transfer in the excited state); Figure 2.5 presents such a situation: while resonance Raman requires a higher energy photon (a), the charge transfer via metal states occurs at lower energies; there are two possibilities: molecule to metal transfer (an electron is transferred between the HOMO and unoccupied states above the Fermi level, scheme (b)) and metal to molecule transfer (an electron is transferred from the occupied states slightly below the Fermi level to LUMO, scheme (c)). This mechanism explains the earlier mentioned observation that the maximum of SERS intensity appears at different potentials for different energies of incident light. Indeed, the Fermi level might be 'tuned' to obtain the highest enhancement for a given laser line by applying the external potential. The theory behind this excited-state charge transfer mechanism was developed by Adrian[48] and Lombardi et al.[42] This is the only mechanism explaining the already mentioned behaviour in electrochemical cells: the maximum of the SERS signal intensity appears at different potentials depending on the used excitation wavelength.[43,44]

The distinction between the ground-state and excited-state charge transfer mechanisms can be made on the basis of the Raman excitation profile that is derived from a series of measurements using different excitation lines. If the ground-state charge transfer mechanism dominates the Raman excitation profile should reflect the profile of ordinary resonance Raman. Whereas, the occurrence of the excited-state charge transfer can be confirmed by the charge transfer peak in the Raman

excitation profile, associated with the transition between the Fermi level and the HOMO or LUMO level of the adsorbate. Its energy is specific to a given system.

The described situations, in which chemical enhancement may occur show how complex phenomenon it is. One of the major obstacles in the detailed investigation of this effect is the crucial role played by specific interactions, entirely depending on the investigated system. Moreover, it is often impossible to disentangle the contribution from the polarizability changes and the resonance enhancement. Coexisting electromagnetic enhancement makes the situation even more complicated.

2.4.3 Raman tensor

Classically, the electromagnetic radiation theory might be used to explain the scattering phenomenon. An oscillating electric dipole is a source of electromagnetic radiation of the same frequency. The induced dipole moment, $\boldsymbol{\mu}$, can be expanded in the power series

$$\boldsymbol{\mu}_{ind} = \boldsymbol{\mu}^{(1)} + \boldsymbol{\mu}^{(2)} + \boldsymbol{\mu}^{(3)} + \dots, \tag{2.19}$$

where

$$\boldsymbol{\mu}^{(1)} = \hat{\boldsymbol{\alpha}}\mathbf{E}, \quad \boldsymbol{\mu}^{(2)} = \frac{1}{2}\boldsymbol{\beta}\mathbf{E}\mathbf{E}, \quad \boldsymbol{\mu}^{(3)} = \frac{1}{6}\boldsymbol{\gamma}\mathbf{E}\mathbf{E}\mathbf{E}. \tag{2.20}$$

Provided the strength of the electric field is not high (which is not the case for non-linear optics), contribution from the terms $\boldsymbol{\mu}^{(2)}$ and $\boldsymbol{\mu}^{(3)}$ is negligible. It means that dielectric polarization linearly responds to the incident electric field $\mathbf{E}$:

$$\begin{bmatrix} \mu_x \\ \mu_y \\ \mu_z \end{bmatrix} = \begin{bmatrix} \alpha_{xx} & \alpha_{xy} & \alpha_{xz} \\ \alpha_{yx} & \alpha_{yy} & \alpha_{yz} \\ \alpha_{zx} & \alpha_{zy} & \alpha_{zz} \end{bmatrix} \begin{bmatrix} E_x \\ E_y \\ E_z \end{bmatrix}. \tag{2.21}$$

The tensor $\hat{\boldsymbol{\alpha}}$, called polarizability, is represented by a 3×3 matrix in Cartesian coordinates and fully characterizes the linear response of the system to an incident electric field. This response could not be described only by a vector, as $\boldsymbol{\mu}$ may not have the same direction as the electric field, $\mathbf{E}$. According to the definition, the polarizability tensor is real and symmetric. Therefore, it can be diagonalized, i.e., there exists an invertible matrix, Q, such that $Q^{-1}\hat{\boldsymbol{\alpha}}Q$ is a diagonal matrix. This procedure corresponds to a change of the coordinate system to new axes (x', y', z'),

called *principal axes*:

$$\begin{bmatrix} \mu_{x'} \\ \mu_{y'} \\ \mu_{z'} \end{bmatrix} = \begin{bmatrix} \alpha_{x'x'} & 0 & 0 \\ 0 & \alpha_{y'y'} & 0 \\ 0 & 0 & \alpha_{z'z'} \end{bmatrix} \begin{bmatrix} E_{x'} \\ E_{y'} \\ E_{z'} \end{bmatrix}. \tag{2.22}$$

The polarizability can be graphically represented as an ellipsoid with semi-principal axes of length $\alpha_{x'x'}, \alpha_{y'y'}$ and $\alpha_{z'z'}$ in this new coordinate system. In quantum-mechanical calculations the obtained polarizability tensor is expressed in coordinates attached to the molecule, for example the principal axes. Hence, in order to make calculations in practice, either the polarizability tensor must be expressed in laboratory fixed coordinates (e.g., Cartesian coordinates), or the electric field must be 'rotated'.

The Raman tensor is defined as

$$R_k(\omega_L) = \left(\frac{\partial \alpha_L(\omega_L)}{\partial Q_k} \right)_{Q_k=0}. \tag{2.23}$$

2.5 Single molecule spectroscopy

Most of the knowledge about chemical or biological systems has been obtained from ensemble measurements. However, this began to change as single-molecule sensitivity of optical detection was proved. This was a real breakthrough in the field of spectroscopy, as the possibility of performing single-molecule experiments promised to uncover information that was hidden so far. A single-molecule measurement, in contrast to a conventional bulk one, provides information on the properties of an individual molecule, whilst the values of parameters obtained in bulk experiments are averaged over a large number of molecules. Therefore, we lose the knowledge of the distribution of the measured parameter. In order to realize how much information we can obtain from single-molecule experiment as compared to the conventional one, suppose there is a sample in which we want to study the orientation of molecules in a thin film. Let us assume the molecules are oriented only in two possible ways: horizontal and vertical (Fig. 2.6). In such case, a single-molecule experiment will provide us with bimodal distribution, while from

a bulk measurement we will get only an averaged value - around 45°, provided the probabilities of these two orientations are equal.

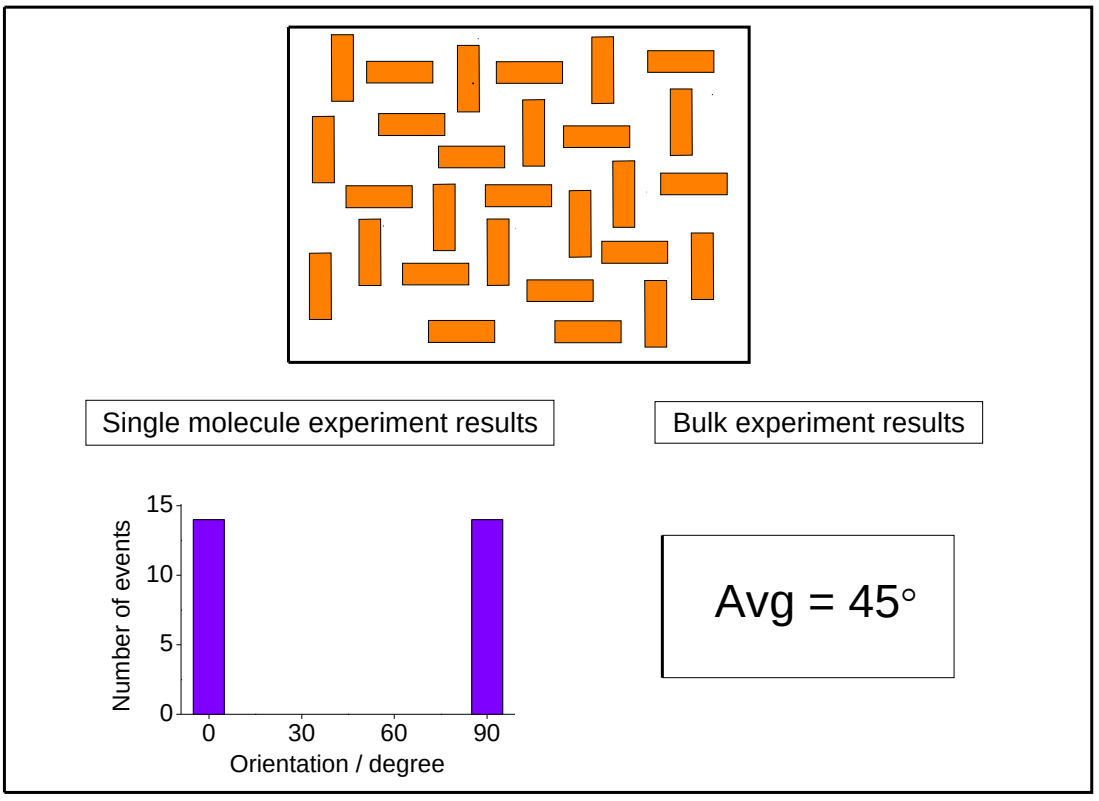

Figure 2.6: An example of the potential of single-molecule experiments. Above: a sample with differently oriented molecules (only horizontal and vertical orientations are possible). Below: the comparison of exemplary results from single-molecule experiment (the distribution of orientations), and bulk measurement (only the average angle).

This example illustrates the potential of single-molecule spectroscopy, thanks to which we may find answers to questions unanswerable by conventional experiments. The probability distribution function of the experimental parameters which we can obtain from single-molecule experiment is of great importance, especially for heterogenous systems, e.g., crystals, polymers or glasses. Moreover, a single molecule can be used as a local reporter of its "nanoenvironment". Indeed, not only a molecule itself can be studied, but also the environment (with its heterogeneity), with which it interacts. Furthermore, from monitoring the behaviour of an individual molecule in the time domain, conclusions about the dynamics may be drawn. For instance, any molecular changes such as tautomerism, protonation reactions or reorientation can be investigated.

Since single-molecule measurements might serve as an extremely valuable source of information, observation of individual molecules was the holy grail of spectroscopy for many years. The optical detection of single molecules in liquid dates back to 1976, when Hirschfeld first reported the observation of individual immobilized protein labelled with many fluorophores.[49] This was accomplished through reduction of the probe volume, which significantly limited the background signal. Despite this achievement, single chromophores were thought to be optically undetectable till 1989, when single molecules of pentacene in *p*-terphenyl were observed by Moerner and Kador. The absorption technique with a sophisticated frequency modulation scheme at liquid-helium temperatures was applied.[50] This experiment was soon followed by fluorescence detection from individual molecules in the same system (also under cryogenic conditions).[51] Since fluorescence generates less background than the absorption technique, it emerged as the method of choice in a rapidly growing field of single-molecule detection. Imaging of individual chromophores at room temperature (carbocyanine dye molecules immobilized in thin polymer films) was first done with near-field scanning optical microscopy by Betzig and Chichester.[52] Far-field microscopy (confocal microscopy or conventional wide-field microscopy) is also suitable for imaging of single molecules at room temperatures.[53] W. E. Moerner *et al.* provided a nice review about single-molecule spectroscopy: its history and main aspects.[54] It is worth mentioning that single-molecule detection in the condensed phase paved the way for further development of super-resolution techniques based on fluorescence microscopy, for which Eric Betzig, Stefan W. Hell, and William E. Moerner were awarded the Nobel Prize in Chemistry in 2014. Although single-molecule fluorescence microscopy is nowadays an extremely powerful technique, as much effort was put into designing efficient fluorophores, it also suffers from drawbacks. Mainly, detection on a single-molecule level is seriously hampered by the low emission quantum yield of a chromophore and photobleaching, which limits the number of photons emitted from a molecule. Moreover, the emission spectra do not provide detailed molecular information.

Fortunately, new opportunities occurred when single-molecule sensitivity of the SERS technique was reported.[6,5] In contrast to fluorescence, Raman spectra contain highly resolved vibrational information. Another important advantage, especially in investigating biological samples, is the possibility of infrared excitation.

The history and current status of single-molecule SERS (SM-SERS) is described in the next section.

2.6 Single molecule surface-enhanced Raman spectroscopy

Demonstration of single-molecule sensitivity of SERS by two independent groups in 1997[6,5] spurred a lot of interest and was a strong stimulus for the SERS field. Kneipp *et al.* studied SERS spectra of crystal violet in an aqueous silver colloid[6], while Nie et al. investigated Rhodamine 6G adsorbed on citrate-reduced silver nanoparticles immobilized on a glass surface[5]. Although these papers held considerable impact, the proof of single molecule detection was not incontrovertible. Therefore, it has been a subject to heated discussions and was seriously questioned.[14,22] In the early works the main argument for single-molecule detection was based on ultra-low dye concentration (below 1nM) with, on average, around 0.1 chromophore molecule per colloid particle. This might have been a source of errors, since the colloid concentration was estimated on the basis of the Ag mass used during the synthesis and the average nanoparticle size. Moreover, because of lack of control over the aggregation process, it was difficult to estimate its extent. Etchegoin *et al.* raised this issue, pointing out that usually only a small fraction of nanoparticles create aggregates and there is a possibility that on these active clusters more-than-average dye molecules were adsorbed.[27]

Another evidence of a single-molecule nature of the registered spectra presented by Kneipp *et al.* was the experimentally obtained Poisson distribution of the SERS intensities.[6] The presented statistical distribution of intensities of 100 SERS measurements was fitted with four Gaussian curves, corresponding to the detection of 0, 1, 2 or 3 dye molecules in the probe volume. Furthermore, the observed statistics followed the Poisson distribution with a fitting parameter 0.5, which means that on average there was 0.5 molecule in the probe volume. By contrast, the tenfold increase in crystal violet concentration resulted in Gaussian statistics, which replaced the Poisson one. This approach was heavily criticized a few years later by Etchegoin and his co-workers.[22] In fact, Kneipp *et al.* analyzed only 100 SERS

spectra, which were binned into 20 bins. Moreover, fitting such a small statistics with four independent Gaussian functions was questioned. For a reliable statistics many more spectra should have been taken into account. On the basis of simulations and experimental data, it was concluded that all of Poisson statistics in SM-SERS are just plain artefacts due to the limited sampling. Indeed, the problem with the Poisson distribution, which describes the probability of the occurrence of a given number of events within a fixed time interval, is that it does not take into account different intensities of the SERS signal. Using the Poisson distribution, one automatically assumes the same intensity for all the events. However, in SERS the variations of the enhancement factor are of the orders of magnitude due to its nature. Simulations proved that if the intensities vary by more than a factor of 2, the Poisson statistics is washed out.

According to Nie and Emory, a sufficient proof for single-molecule detection was the observation of sudden spectral changes interpreted as decomposition or photobleaching.[5] Despite blinking and bleaching being a conclusive argument for fluorescence originating from a single molecule, the observation of these phenomena as a proof of SM-SERS detection has been put in doubt.[27] In order to observe a Raman signal from a single molecule, it has to experience a huge enhancement of the electromagnetic field, which is not possible without the existence of a metallic nanostructure. Any change in this nanostructure, induced directly by light or indirectly by thermal heating, affects the SERS enhancement factor due to modification of the electromagnetic field distribution. This, in turn, influences all molecules adsorbed on that nanocluster. Hence, a sudden drop of intensity could be observed as a result of nanostructure change (for example through photo-oxidation) even if many molecules were adsorbed on it. Moreover, other photoinduced processes, such as desorption or dissociation may affect many molecules at the same time.

By combining SERS measurements with scanning electron microscopy (SEM) and atomic force microscopy (AFM) it was shown that colloidal aggregates (starting from a dimer) provide much higher enhancement compared to single nanoparticles. This was shown for two systems: Rhodamine 6G[10] and hemoglobin,[55] both adsorbed on silver nanoparticles. Indeed, single molecule spectra of these compounds were observed exclusively from aggregates consisting of at least two individual nanoparticles.

Although the single-molecule sensitivity of the SERS technique was reported almost twenty years ago, the observation on a single molecule level still remains a challenge. So far most of the molecules for which it was accomplished (less than 40) are dyes excited with resonant laser line, including Rhodamine 6G,[5,7,8,9,10,11,12,13,14,15] Rhodamine 800,[56] methyl ester version of Rhodamine 6G,[21,57] Nile blue,[20,21,14,11] crystal violet,[6,16,17,18] brilliant green,[19], malachite green isothiocyanate, cyanine dyes. However, the observation of single molecules has been claimed also for non-resonant conditions, for example for adenine,[58,59,60,61,62,63,64] DNA,[65,66] and fullerens.[67,68]

2.6.1 Photostability

Photobleaching of the fluorescence signal is a well documented phenomenon in the spectroscopy of dyes. This photochemical destruction of a molecule can be seen as fading of a fluorescence signal during an imaging experiment or a sudden disappearance of a signal while observing single molecules. Most often it is a problem, as it limits the number of emitted, and therefore collected photons from a single emitter before its destruction. In some cases, however, photobleaching may be exploited. One of the technique based on this phenomenon is fluorescence recovery after photobleaching (FRAP), which is useful in studies of diffusion through tissue or cells.[69] Numerous studies showed that the mechanisms responsible for photodestruction of fluorophores can be very diverse, and so far they have not been fully understood.[70,71,72,73,74] Nevertheless, in most of the cases the photobleaching occurs as a result of a reaction in the excited state: the long-lived triplet state T_1 achieved via transition from the singlet excited state S_1 opens new channels to photochemical reactions with surrounding molecules.[70,71,73] One of the most common paths is the interaction between an oxygen molecule and a fluorophore in the T_1 state, which creates very reactive oxygen radicals or oxygen in its singlet state, that can destroy the fluorescent moiety. Therefore, photostability depends both on photophysical properties, such as intersystem crossing yield and phosphorescence lifetime, and on environment (e.g., oxygen concentration). Photobleaching does not only affect the fluorescence signal, but also the Raman scattering, where it is manifested by decrease in the intensities of Raman peaks and often accompanied

by the appearance of new bands derived from a product, provided that its Raman cross section is comparable to that of the substrate. For instance, sometimes the characteristic broad band of amorphous carbon appears.[75,76] Under resonant conditions, however, the appearance of new bands is limited. When the excitation energy matches an electronic transition of a molecule, Raman scattering is greatly enhanced. Because of alteration of electronic structure upon irradiation, the used laser line may no longer be in resonance, hence the Raman scattering from the product can be even several orders of magnitude lower.

The proximity of metallic nanoparticles/surfaces influences photophysical properties, and hence photobleaching, but does not prevent it. Despite numerous studies utilizing electromagnetic enhancement derived from plasmonic nanostructures, not much attention was devoted to photostability of molecules located close to them. The investigations of this complex phenomenon ideally require a well-defined system. Only in 2014 the group of Le Ru proposed a simple theoretical description of photobleaching mechanism of molecules located close to plasmonic nanostructures by modifying the standard triplet-state mediated model.[77] It was experimentally verified using a common SERS probe, Nile blue uniformly adsorbed on nanolitographically prepared gold nanodisc arrays with tunable plasmon resonances. The measured photobleaching decay rates revealed nonexponential nature and ranged across several orders of magnitude. Moreover, these rates were strongly affected by the incident power and the wavelength of plasmon resonance. The obtained broad distribution of decay rates results from the long-tail nature of the enhancement factor distribution on SERS active substrates.[30] The authors observed also an anomalous photobleaching regime at higher powers, which was attributed to heating of plasmonic nanostructures as a consequence of plasmon-enhanced absorption in gold. The close proximity of the metal surface can make a molecule less vulnerable to photobleaching due to faster relaxation, which results in a lower probability of the excited state reaction. On the other hand, the presence of a metalic nanoparticles can enhance the intersystem crossing, which may lead to photochemical reaction in the triplet state ending with decomposition of a molecule. Moreover, charge transfer between a molecule and metal may occur, which also would affect photostability. There certainly exist other mechanisms that affect photobleaching, however, there were not extensively discussed in the literature.

2.6.2 Origins of fluctuations and blinking in SM SERS

Intensity fluctuations are very common for single molecule SERS and are even used as evidence for the observation of individual molecules. Since the enhancement of the electromagnetic field is highly anisotropic within a hot spot, single molecule SERS spectra are extremely sensitive to the position and orientation of a molecule. Therefore fluctuations may originate, either from reorientation of a molecule or its thermal diffusion in and out of a hot spot. There have been reported such large amplitude fluctuations that they even led to temporal vanishing of the Raman signal, which is known as blinking. This phenomenon has been frequently observed in single molecule fluorescence. The extensive studies of the mechanism of intensity fluctuations, including blinking, showed that it originates mostly from population of a metastable dark state (nonabsorbing or nonemissive, such as triplets or ions) via excited state upon resonant excitation.

However, in the case of Raman scattering, especially under non-resonant conditions, blinking and bleaching cannot be easily rationalized. For instance, Bjerneld *et al.* attributed spectral changes in single molecules of tyrosine to changes in the adsorption of a molecule at the surface.[78] On the other hand, Weiss and Haran imputed the observed fluctuations to the modulation of the CT contributions through the diffusion of a molecule on a SERS surface.[79]

2.6.3 SERS background

SERS spectra are often accompanied by a broad background underneath the Raman lines, which is often called *SERS continuum*.[80] Although the conventional Raman spectra are not background-free, which is attributed to the existence of impurities or residual intrinsic fluorescence, it is believed that in the case of SERS the observed background has a real physical origin.[34] Surprisingly, its source raised a lot more controversy than the mechanism of enhancement in SERS,[81] which has become established over the years and nowadays is widely accepted by the SERS community. To this day there is no clear consensus reached about this SERS continuum, which was initially ascribed to luminescence[82] or inelastic scattering.[83]

In general, the intensity of this structureless background increases upon adsorption of analyte molecules on SERS-active spots.[84] It was observed that the background is directly related to the enhanced Raman signal: both signals blink on and off together, i.e., disappear and reappear simultanously.[9,85] Michaels et al. suggested that the chemisorption of a molecule may trigger both the continuum background and enhancement of Raman scattering. Jiang et al. proposed that the simultanous intensity fluctuations reflect adsorption-desorption kinetics of the probe molecule.[85] Nevertheless, the continuum background is also observed in the absence of adsorbate (for example in metallic films prepared under ultrahigh vacuum conditions, which provides a clean surface).[86]

Many potential mechanisms underlying the broad continuum have been proposed, among which the most reasonable are:

(i) inelastic light scattering of electron-hole pairs in the intrasurface bands of metals observed already in the absence of adsorbate, which proves that it is an intrinsic property of the noble-metal substrates;[83,86,87] electronic Raman scattering in crystalline metals such as Ag is usually very weak, however atomic scale surface roughness may induce this process,[88,89]

(ii) electronic Raman scattering induced by surface defects enhanced by charge transfer between the metal surface and chemisorbed molecules,[9,45,85]

(iii) luminescence originating from radiative recombination of electrons in the conduction band with photocreated holes in the *d* band;[82,90,91] time-resolved studies provided evidence that the continuum background arises at least partially from nanoparticles luminescence,[92]

(iv) emission due to optical intraband transitions (electronic states in the same conduction band) mediated by localized surface plasmon, which provides the required extra momentum;[91] accounts only for background in the infrared region,

(v) fluorescence from adsorbed molecules,[93]

(vi) luminescence from a complex formed between chemisorbed molecules and surface metal atoms,[9,90]

(vii) radiative relaxation of the excited LSP.

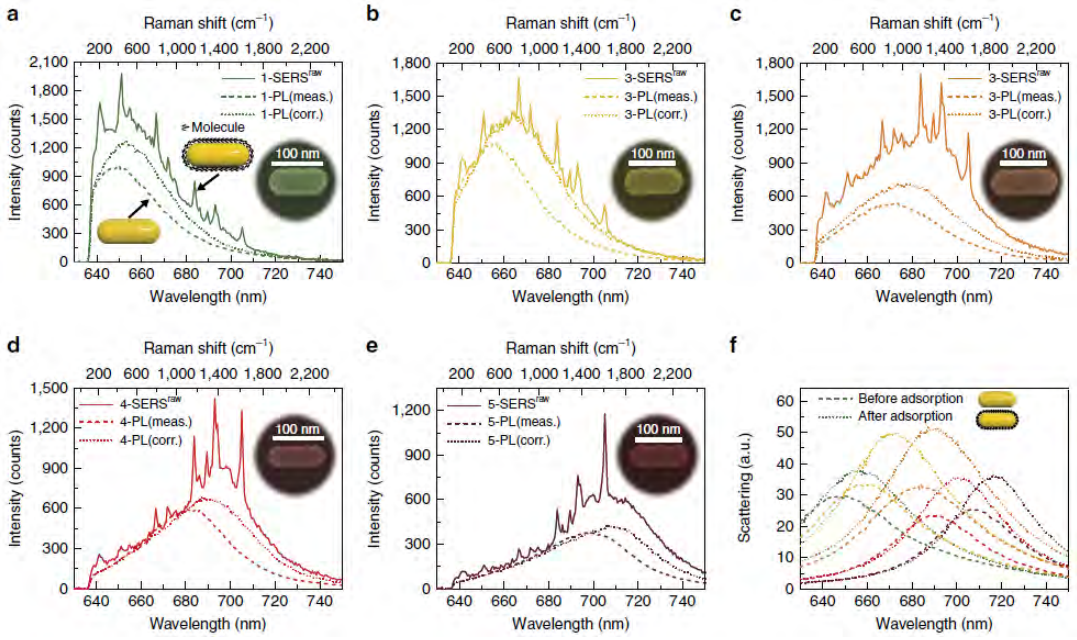

Figure 2.7: Quantitative correlation of the SERS background and photoluminescence (PL) for single gold nanorods. (a–e) Measured PL signal (dashed lines) of five gold nanorods with different aspect ratio in the absence of molecules and the corresponding SERS spectra (which include a spectrally broad background) after adsorption of the malachite green isothiocyanate (MGTIC) molecules (solid lines). All measurements were performed under 633 nm laser illumination. The dotted lines, PL(corr.), correspond to the PL after applying the correction which accounts for the influence of the molecules on the plasmonic resonance. The insets are the SEM images of the five nanorods. (f) Scattering spectra of the five gold nanorods measured before (dashed lines) and after (dotted lines) adsorption of the MGITC molecule. Adapted from[94].

Despite numerous studies, the issue of SERS continuum has not been completely resolved so far. Enumerating so many possible processes giving rise to the background demonstrates that it is a difficult problem and the experimentally observed background may have different contributions. Moreover, recently Lin *et al.*[94] postulated that this background may contain information about the local field, which, except being the main source of SERS enhancement, also modifies the relative intensities of bands in the original Raman spectra (known as plasmonic spectral shaping effect, PSSE). The comparison of the optical response of gold nanorods with different aspect ratios before and after adsorption of malachite green isothiocyanate (MGTIC) molecules revealed that photoluminescence (PL) understood

as the emission at smaller energies than the incident light makes the major contribution to the SERS continuum in the studied system. The experimental results including morphology of studied nanoantennas, SERS spectra upon adsorption of MGTIC, LSPR scattering measured by dark-field microscopy, and photoluminescence before addition of dye are presented in Figure 2.7. Indeed, the background of SERS spectra closely follows the spectral shape and intensity of photoluminescence measured in the absence of molecules, which is the intrinsic responce of a nanostructure. Based on that assumption Lin *et al.* proposed a method to retrieve the original relative intensities of Raman bands.[94]

2.6.4 Bi-analyte technique

The method called bi-analyte technique, developed in 2006,[27] was announced to be the first incontestable proof of single-molecule SERS. This simple approach is based on SERS measurement of a mixture composed of two different species with comparable Raman cross-sections. Furthermore, beyond confirming a single-molecule character of the measured signal, this method allows for estimating the concentration regime appropriate for observing single-molecule events. However, the reliability of this method strongly depends on differences in the Raman scattering cross-sections, the absorption spectra, and the surface binding affinity of the used analytes. Assuming equal probabilities of observing each of the species, the signal originating from many molecules most likely would be the superposition of spectra from both analytes. If n molecules contribute to the signal, the probability of observing pure signal (coming from only one species) is $(1/2)^n$ for each of the mixture components. Thus, with an increasing number of molecules, the chance of observing a spectrum which corresponds to only one species drops drastically, which is presented in Figure 2.8. If the vast majority of the spectra is purely of one type, it indicates that a single-molecule regime was achieved. Initially, this bi-analyte approach was successfully implemented for a mixture of two markedly different dyes: Rhodamine 6G and benzotriazole.[27] The use of two isotopologues, realized for Rhodamine 6G: R6G-d_0 and R6G-d_4 significantly improved its reliability.[23] While isotopic substitution should only hardly affect the

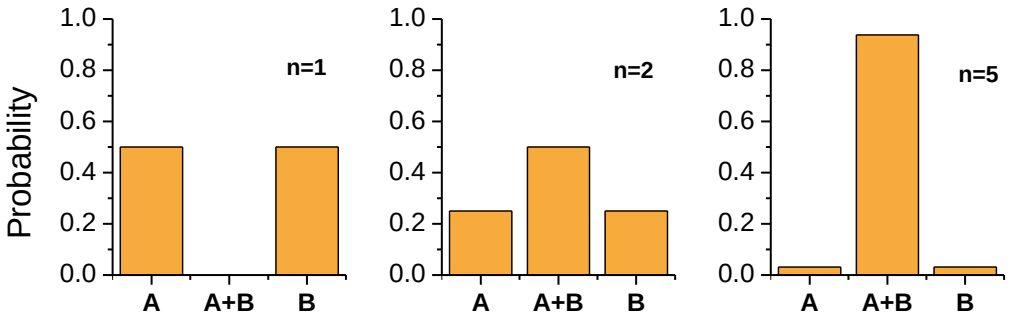

Figure 2.8: The probability distribution of observing pure spectrum of components A and B, and the superposition of A and B spectra for different number of molecules $n = 1$, $n = 2$ and $n = 5$ (assuming the same probability of observation for each of the species).

Raman cross-section, electronic structure, and leave the surface chemistry almost unchanged, the Raman spectra still allow for the distinction between species.

Despite full acceptance of the bi-analyte method among SERS community, it was shown in 2014 that under some conditions it may lead to incorrect conclusions.[26] It was proved that in the case of measurements in colloids, sample preparation plays an absolutely crucial role in the distribution of molecules throughout the sample. Two ways of sample preparation were compared. In the first method, called half-half dilution (HHD), 500 μl of colloid was mixed with 500 μl of dye and in the second method, named large factor dilution(LFD) 500 μl of colloid was mixed with 490 μl of water, followed by adding 10 μl of dye. Due to competition between dye adsorption and diffusion, the LFD method may result in high non-uniformity of molecular coverage per NPs: the faster the analyte adsorbs onto nanoparticles, the larger variation across the sample is present. Moreover, it was shown that because of such competition, the bi-analyte experiments performed for colloids can be trusted only if the dyes solutions were mixed before addition into colloids. In the case of sequential addition of dyes the bi-analyte approach may lead to wrong conclusions due to the violation of the implicit assumption about the uniformity of the analyte distribution.

2.7 Porphycene

Porphycene, a constitutional isomer of porphyrin (Fig. 2.9), was synthesized for the first time in 1986 by Vogel and coworkers,[95] and according to the common nomenclature of porphyrin analogs, it may be referred to as [18]porphyrin-(2.0.2.0)[96] indicating an 18 π-electron macrocycle containing four pyrrolic subunits linked alternately by two- or zero-carbon bridges.

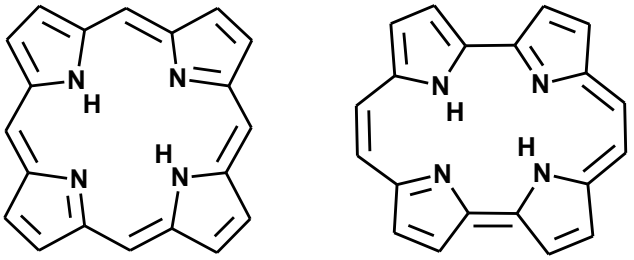

Figure 2.9: Chemical structures of porphyrin (left) and porphycene (right).

It is an attractive chromophore for SM-SERS studies since both, its photophysical properties and vibrational structure have been characterized in detail.[32] Not only standard techniques such as IR and Raman spectroscopy[97,32] were employed, but also matrix-isolation,[97,98] neutron scattering,[32] supersonic jets,[99,100] and superfluid helium nanodroplets[101,32] were used. With the support of quantum-mechanical calculations 106 out of 108 fundamental vibrations have been assigned.[32] Moreover, porphycene was already observed on a single molecule level by two techniques different than surface-enhanced Raman spectroscopy: fluorescence[102,103,104] and scanning tunneling microscopy (STM).[105,106,107]

X-ray studies revealed that porphycene, similarly to porphyrin is virtually planar,[95] however, it has lower symmetry (C_{2h} point group) compared to porphyrin (D_{2h}). The main difference between porphycene and porphyrin, which strongly influences their properties, is the shape of the inner cavity. In the case of porphycene it has an rectangular shape with the dimensions of 2.63 and 2.83Å.[95] Such geometry results in strong, close to linear NH$\cdots$H hydrogen bonds and therefore much lower tendency to form metal complexes compared to porphyrin. The formation of metal complexes for porphyrin molecules located on Ag and Au SERS substrates,

known as metallation has already been reported. DFT calculations (energies evaluated with BLYP/6-31G** for geometries optimized with BLYP/3-21G) predict that free base porphycene is more stable than porphyrin by about 1.5 kcal/mol.[108]

2.7.1 Tautomerism

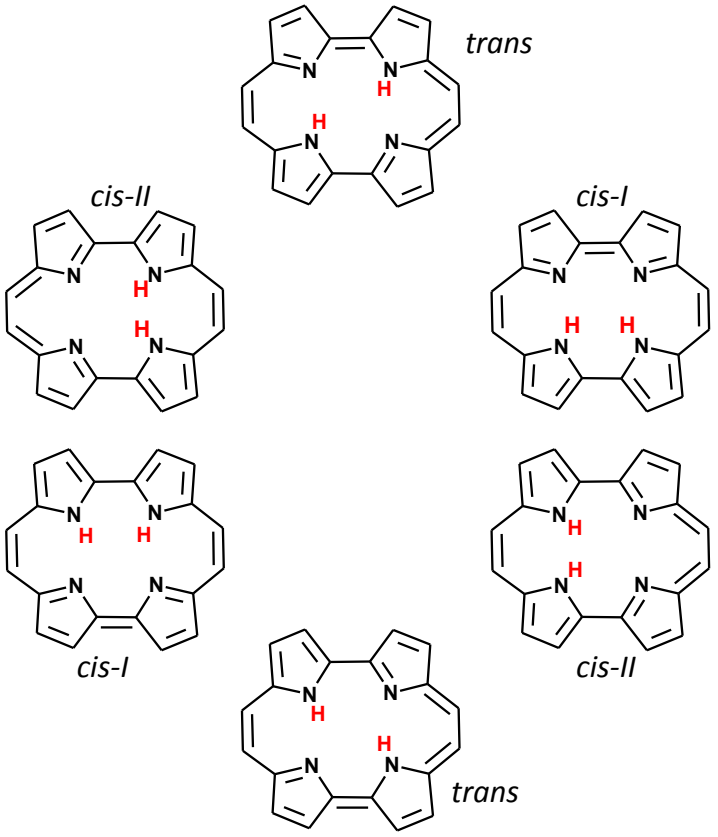

Figure 2.10: Tautomeric forms of porphycene (inner-hydrogen migration).

In porphycene, contrary to porphyrin, the existence of two chemically different *cis* tautomers is possible: *cis-I* and *cis-II* (Fig. 2.10). The *cis-I*-porphycene is predicted to be less energetically stable by 2 kcal/mol compared to the *trans* tautomer, while the second *cis* tautomer (structure *cis-II*) is predicted to be strongly destabilized with respect to the other ones.[109] Therefore, we will not hereafter consider this tautomeric form and as a *cis*-porphycene we will refer to the structure *cis-I*. Different proton positions in the tautomeric forms are accompanied by a change in the point group from C_{2h} for the *trans* form to C_{2v} for the *cis* tautomer. Since *cis*-porphycene is deprived of the inversion center, an exclusion principle is no longer applicable. Therefore, one might expect that both IR and

Raman spectra of the *cis* tautomer should be significantly more crowded. However, this is not the case. Surprisingly, the calculations predict close similarity in IR and Raman spectra of both forms. It seems that vibrations of the skeleton are hardly influenced by the actual position of the inner protons. Most of the transitions which become symmetry-allowed in *cis*-porphycene do not gain much intensity.[97] Despite such a strong similarity in the vibrational patterns predicted by quantum-mechanical calculations, careful experimental data analysis indicates that porphycene in the ground state exists in the *trans* form.[109] Moreover, variable temperature infrared studies revealed no evidence for an equilibrium between the *cis* and *trans* tautomers (no temperature dependence).[97]

Although the two *trans* tautomers are chemically equivalent, the orientation of the transition dipole moment of the S_0 to S_1 transition is different in both structures; these transition moments form an angle of 70-80°, which was determined from bulk fluorescence anisotropy measurements, both stationary[110] and time-resolved,[111] from transient absorption measurements[112] and from single molecule fluorescence studies.[102,103] Due to double-dipole character of porphycene it is possible to determine the 3D orientation of a single porphycene molecule based on the emission pattern, provided that properly polarized laser beams are used as excitation sources.

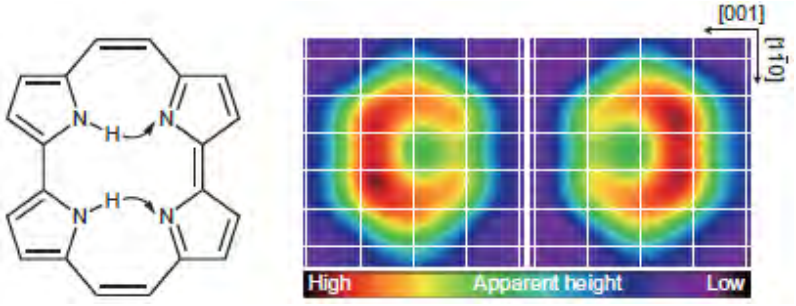

Figure 2.11: Schematic representation of hydrogen transfer during *cis-cis* tautomerization (left) and typical STM images of single porphycene molecules on a Cu(110) surface (right).[105]

Contrary to the situation in the gas phase and solution, if porphycene is located on a Cu(110) surface, the *cis* tautomer is the most stable, which was revealed by scanning tunnelling microscopy (STM).[105] Such behavior originates from the interaction between the non-hydrogenated nitrogen atoms and the copper atoms

forming the surface. Moreover, the *cis-cis* tautomerization rates can be tuned by precise positioning of a single copper atom in the vicinity.[105]

2.7.2 Electronic spectrum

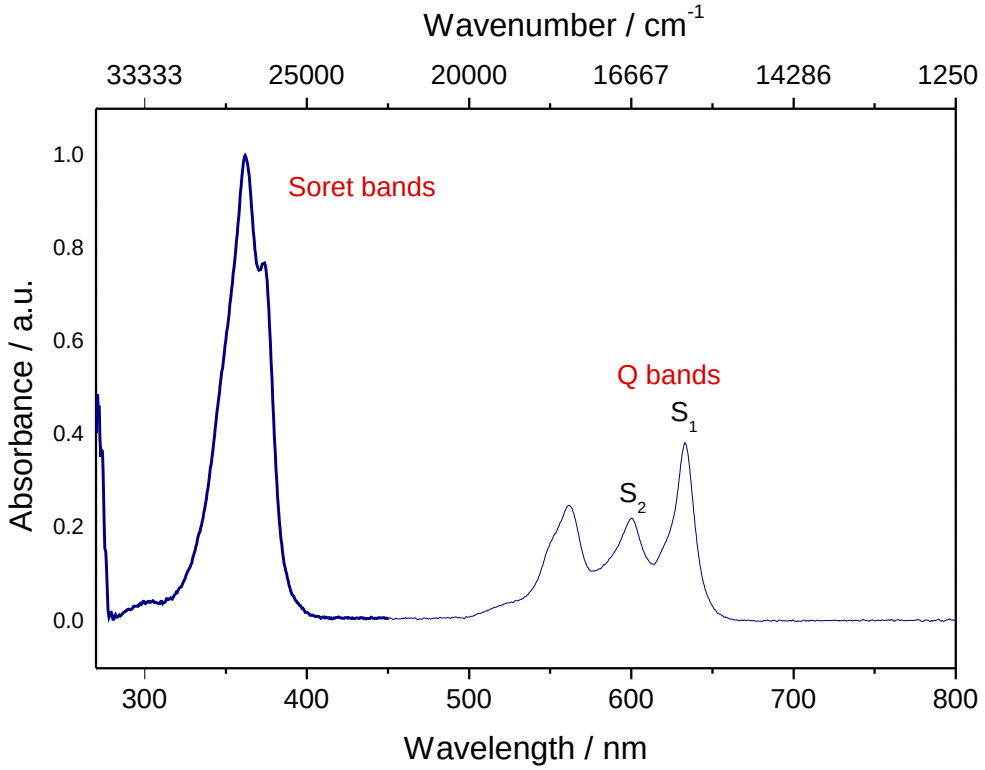

Figure 2.12: The absorption spectrum of porphycene in ethanol.

In the electronic spectrum of porphycene we can indicate three main groups of bands. The Q bands include electronic transitions to S_1 and S_2 excited states, Q_x and Q_y, respectively. They show up in the visible region, from 15000 to 20000 cm^{-1}. The assignment of the origin of the S_0 to S_2 transition was done based on the electronic absorption and fluorescence measurement in low-temperature nitrogen and rare gas matrices,[98] as well as by magnetic circular dichroism (MCD) studies.[113] In the case of nitrogen matrix the position of the $S_2(0-0)$ transition is at 16894 cm^{-1}, 882 cm^{-1} higher than the 0-0 position of $S_1 \leftarrow S_0$.

The Soret bands appear in the UV region and originate from electronic transitions to higher excited singlet states. They lie very close to each other and are characterized by higher absorption coefficients. The higher-energy bands related to electronic transitions to higher excited states are much less intense.

Chapter 3

Objective of the thesis

As already mentioned in the introduction, single molecule studies provide a wealth of information that cannot be obtained from bulk measurements. Therefore, our initial goal was reaching a single molecule level by means of surface-enhanced Raman spectroscopy, which served as a starting point for investigation of vibrational structure of porphycene and its behaviour close to metal nanostructures. To the best of our knowledge, porphycene is the only species studied on a single molecule level by three different techniques: fluorescence spectroscopy,[102,103,104] scanning tunneling microscopy,[105,106,107] and, now, by surface-enhanced Raman spectroscopy.[114,115] As single molecule sensitivity was reached, not only porphycene, but also its derivatives attracted our interest. It quickly turned out that differently substituted porphycenes may serve as probe molecules to study factors that govern the possibility of observation of chemical compounds on a single molecule level by the SERS technique. Such factors can be classified into two categories: intramolecular and external ones. Features such as electronic or spatial structure belong to the former group, while conditions such as the excitation laser line used or SERS substrate fall into the latter category. Here, however, we mostly focus on factors that influence detectability of individual molecules that are inherent to a molecule. Surprisingly, there were no systematic studies on this subject so far. The scarcity of knowledge in this field is most likely the result of the lack in the availability of chromophores differing only in one or a small number of parameters. An access to a family of chemically similar compounds: differently substituted porphycenes, which can be relatively easily observed on a single molecule level by

SERS spectroscopy, allowed us to face this challenge. As the understanding of how molecular features affect the detection sensitivity has the potential to significantly influence the broad field of surface-enhanced Raman spectroscopy, developing it became a parallel objective for us. In this thesis, a special attention was put on the investigation of an impact of presence of *tert*-butyl groups on SERS spectra and detectability on a single molecule level. One of the side effects of the presented studies is the extension of a collection of species observed on a single molecule level by the SERS technique. Last but not least, the temperature plays an important role in SERS spectroscopy. It affects both the intensities of Raman signal and photostability of molecules. Therefore, evaluation of an impact of temperature change on single molecule detectability is also one of the main goals of this thesis.

To be more specific, the key objectives of this thesis are following:

- broadening the knowledge about porphycene: its vibrational structure, tautomerism, photophysics, and behaviour in the close vicinity of plasmonic nanostructures by means of single molecules
- understanding the nature of intensity fluctuations commonly observed in SM-SERS studies
- contributing to better understanding of molecular features that influence single molecule sensitivity using differently substituted porphycenes
- elucidating the effect of lowering the temperature on photostability as well as on fluorescence and SERS signal intensities
- comparing various supports in terms of applicability in observation of single molecules by the SERS technique
- proposing further potential research directions

Chapter 4

Experimental methods

4.1 Materials

4.1.1 Solvents

All aqueous solutions were prepared with deionised water obtained from an ELIX system (Millipore). For preparation of ethanol solutions, ethyl alcohol (anhydrous, $\geqslant$ 99.8%, max water content 0.2%, POCh) was used.

4.1.2 Compounds

All of the chemical compounds studied in this thesis (except for deuterated porphycene) were provided by the supervisor of this thesis, prof. Jacek Waluk. These compounds include porphycene, *tert*-butyl-substituted porphycenes, and *meso*-substituted porphycenes. The synthesis and purification of porphycene,[116] *tert*-butyl-substituted porphycenes,[117] and *meso*-substituted porphycenes[118] were performed according to procedures described in the literature.

The perdeuterated porphycene (Pc-d_{12}, with all CH protons in the periphery substituted by deuterons) was obtained according to the following procedure: 20 mg of parent porphycene was dissolved in 3 ml of 98% D_2SO_4 (Sigma Aldrich, isotopic purity of 99.5 atom % D) and afterwards, 1 ml of D_2O (Sigma Aldrich, isotopic

purity of 99.9 atom % D) was added. Such obtained solution was kept at 180°C in the oil bath for 8 hours. After cooling the solution to room temperature, 20 ml of chloroform (Merck, spectroscopic grade) was added, followed by neutralization of the mixture by addition of 25% NaOD (Sigma Aldrich, isotopic purity of 99 atom % D) solution in D_2O. In order to transfer the product of reaction into an organic phase, extraction was performed. The aqueous phase was removed, while the organic phase was evaporated. In order to ensure high isotopic purity, the described procedure was repeated several times: the product from the previous step was used as a substrate. Finally, the obtained product in the form of a powder was rinsed several times with D_2O and *n*-hexane to remove polar and non-polar contaminations, respectively. Originally, all protons, including the inner ones, should be exchanged. However, in the air, the inner deuterons are easily exchanged by protons. Mass spectrometry with electrospray ionization (ESI-MS) allowed for determination of the degree of isotopic substitution for Pc-d_{12}. The described procedure provided the substitution of more that 90% of the outer protons by deuterons.

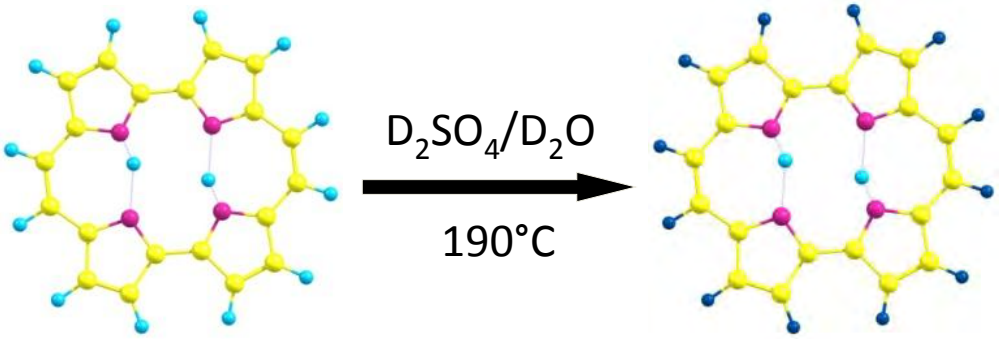

Figure 4.1: Scheme of deuteration of porphycene (left: Pc-d_0; right: Pc-d_{12}).

4.1.3 Nanoparticles

Large variety of gold, silver and copper nanoparticles have been tested. We have tried different preparation methods: physical (laser ablation), chemical, and electrochemical. Below we will describe the procedures that were the most successful

according to our needs, i.e., which provided a relatively broad range of enhancement and a large number of hot spots, which allowed for observation of a considerable number of single molecule events. We did not test the obtained SERS substrates for homogeneity across the whole sample.

4.1.3.1 Chemical synthesis

Chemical synthesis of silver nanoparticles stabilized by hydroxylamine was performed according to the literature.[119] In short, approximately 1 ml of 15 mM hydroxylamine hydrochloride (Aldrich) solution and 30 mM sodium hydroxide solution were added to 9 ml of 1.1 mM silver nitrate (Merck) solution under rapid stirring.

Copper nanoparticles were prepared by chemical reduction of cupric sulfate by borohydride in an aqueous citrate sodium solution according to the procedure described in the literature,[120] originally developed by Creighton.[121] In short, 5 ml of $2{\cdot}10^{-2}$ M aqueous solution of cupric sulfate was added into 60 ml of degassed $2.8{\cdot}10^{-3}$ M citrate solution, while stirring and being kept in an ice bath. Afterwards, 30 ml of freshly prepared $NaBH_4$ ($2{\cdot}10^{-2}$ M) in NaOH ($1.9{\cdot}10^{-2}$ M) was gradually added while bubbling the solution with nitrogen. The solution was stirred at the above-mentioned conditions for 10 min. Such prepared colloid was stable for several hours while kept at 4 °C. The measured extinction spectra of the colloid had a broad maximum at about 570 nm and a relatively high background due to scattering.

4.1.3.2 Laser ablation

Laser ablation allowed us to obtain chemically clean gold and silver nanoparticles. Colloids were obtained by irradiation of a small bar of gold (Mint of Poland, 99.99%) or a silver wire (Aldrich, 99.9%) mounted in a quartz cuvette filled with deionized water by a focused beam of a pulsed laser. No additional surfactant was added. Two types of lasers were used: (i) Lambda Physics LPX100 excimer laser (XeCl, 308 nm) with the energy tuned in the range of 10 - 90 mJ per pulse and its duration of 25 ns; (ii) PL 8000 (Continuum) Nd:YAG with two wavelengths:

the fundamental one (1064 nm) and the second harmonic (532 nm), with approximately the same energy of 20 mJ per pulse and 10 ns of pulse duration. The repetition rate of both lasers was 25 Hz, which allowed to produce metal colloids with sufficient concentration within a few minutes. This preparation method was implemented by Sylwester Gawinkowski and Aleksander Gorski (Institute of Physical Chemistry PAS). Unfortunatelly, it did not allow us to obtain high reproducibility, probably due to reablation processes. Better results using this method would require further optimization, which was not our main goal.

4.1.3.3 Gold nanorods

Among different colloids we have also used commercial nanoparticles, Nanopartz Bare Gold Nanorodz A12-25-600 and A12-25-650 with dimensions of 25 µm×47 µm and 25 µm×60 µm, respectively. Both colloids were prepared in deionised water and were stabilized by cetyl trimethylammonium bromide (CTAB). Different size of nanoparticles resulted in plasmonic resonance of colloids at 600 nm for smaller nanoparticles and 650 nm for bigger ones. Aggregation of nanoparticles induced by deposition of colloid on a glass coverslide and evaporation of water resulted in a significant broadening of plasmonic resonance, covering the spectral region from about 500 to 1200 nm. Before deposition of nanoparticles on glass, the excess of CTAB was removed by centrifugation. First, 1 ml of colloid was centrifuged for 10 minutes at 6000 rpm (2500 rpm for A12-25-650 colloid), then decanted, and redissolved in 1 ml of miliQ water. This procedure was repeated twice, however the final solution was not redissolved in water. Such concentrated solution was drop-cast on a microscope coverslide and left to evaporate under ambient conditions. Typically, 1-5 µl was used for one SERS substrate.

4.2 SERS substrates

4.2.1 Deposition of colloids

All colloids used to prepare the SERS substrates were characterized by measurements of extinction coefficients. Typically, as a SERS support we used nanoparticle

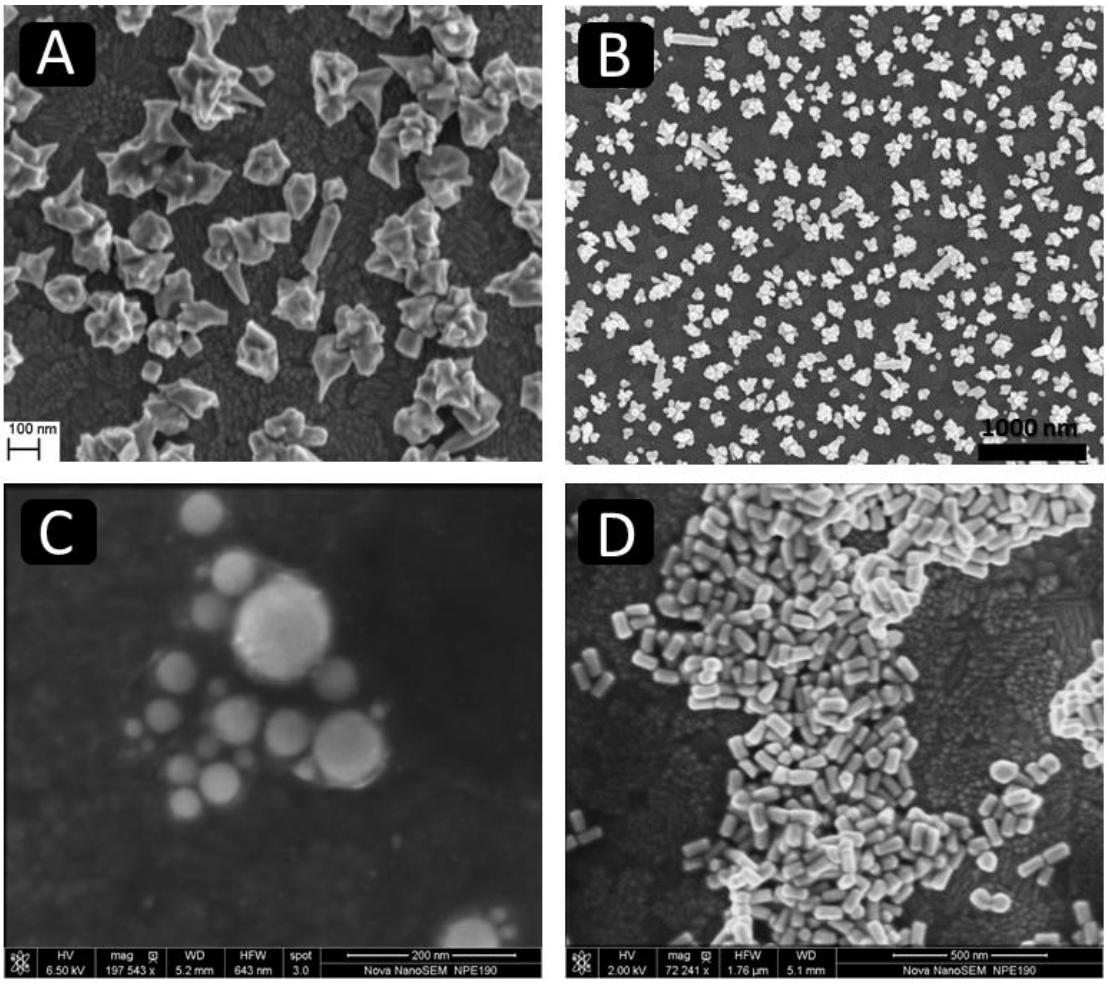

Figure 4.2: SEM images of different SERS substrates: (A) obtained by electrodeposition at a three-phase junction (image taken by I. Kamińska); (B) obtained by electrorefining using scanning electrochemical microscopy (image taken by W. Nogala); (C) Au nanoparticles obtained by laser ablation; (D) commercial 60x25 nm Au nanorods. Adapted from[115].

aggregates formed by colloid dropcasting (typically 1-5 µl) on a microscopic glass cover slide or a piece of silicon wafer, followed by solvent evaporation under ambient conditions. The surface on which a drop was cast was cleaned in advance by bathing for 15 minutes in a freshly prepared piranha solution (1:1 mixture of 96% H_2SO_4 and 30% H_2O_2, both from Sigma Aldrich) or rinsing several times with methanol (Sigma Aldrich, spectroscopic grade) and miliQ water to avoid the change of hydrophobicity of the glass. No capturing agent was used. Such obtained nanoparticle aggregates were characterized by AFM and SEM techniques. The samples for SEM imaging, however, were prepared by dropcasting colloids on an ITO surface (tin-doped indium oxide coated glass) in order to reduce charging

effects.

4.2.2 Electrodeposition at a three-phase juncion

A separate group of SERS substrates were electrochemically obtained gold nanoparticles attached to a surface of an ITO electrode (sheet resistivity 8-12 Ω per square, Delta Technologies Ltd.) by electrodeposition at a three-phase junction.[122] These substrates were produced by Izabela Kamińska and Joanna Niedziółka-Jönsson. In short, the ITO electrode was immersed in an electrochemical cell containing two immiscible phases. The organic one was composed of toluene (Chempur) containing 1 mM tetraoctylammonium tetrachloroaurate salt, which was obtained by anion exchange from tetraoctylammonium bromide (98%, Aldrich), toluene, and $HAuCl_4 \cdot 3H_2O$ (98%, Aldrich) dissolved in water. The aqueous phase contained 0.1 M KPF_6, which served as a supporting electrolyte. Particle deposition was achieved by means of a double-step chronoamperometry technique with a nucleation potential set to -1.0 V, applied for 50 ms and a growth potential 0 V, applied for 2500 s.

4.3 Instrumentation and experimental techniques

4.3.1 Raman microscopy

All Raman measurements, including mapping, were performed using a commercial InVia Renishaw system based on a Leica microscope equipped with a thermoelectrically cooled CCD detector with a matrix of 1024×256 pixels. The SERS or Raman signal was collected by a 100x Leica air objective (NA=0.85) and dispersed by 1200 grooves/mm or 1800 grooves/mm grating (in the visible and NIR range), which provided the spectral resolution of 4-6 cm^{-1} depending on the combination of an excitation laser and grating. In the case of the UV range, the holographic grating of 2400 grooves/mm was used. The wavelength accuracy was 2 cm^{-1}, which was calibrated with both the Rayleigh line and the characteristic band of silicon crystal at 520.6 cm^{-1}. As an excitation source four laser lines were

used: 325 nm (He-Cd, Kimmon), 514.5 nm (Stellar Pro argon Modu-Laser, LLC), 632.8 nm (HeNe, Renishaw), and 785 nm (HPNIR785). The cut-off filters allowed to register Stokes shifts down to 40 cm^{-1} for 514.5 nm excitation, about 100 cm^{-1} for 632.8 and 785 nm excitations, and to 200 cm^{-1} for the 325 nm laser line. The simultaneous measurements of Stokes and anti-Stokes signal excited with a 632.8 nm laser line was realized with the BragGate notch filter, which allowed for registration of spectral features as close as 10-15 cm^{-1} to the Rayleigh line. In order to minimize photobleaching or thermal destruction of the sample, the laser power was controlled by neutral density filters.

The Raman mapping was realized with a piezo stage with 100 nm steps in the XY direction and 200 nm steps in depth. Typically, raster scanning was done with a step of 1 µm in both X and Y directions.

The spectra of solutions were obtained using quartz cuvettes or glass flasks (the measured spectra revealed no differences).

4.3.2 Cryostat

The temperature studies were possible due to usage of a Linkam chamber which allows for cooling a sample down to liquid nitrogen temperatures and heat it to around 400℃. A long-working distance 50× objective was used for these studies.

4.3.3 Dye laser

The preliminary studies aiming at recording Raman excitation profile were done using coherent Innova ring laser with a liquid solution of sulforhodamine B (Kitton Red) and DCM as the lasing medium. This provides the emission in the range between 600 and 645 nm.

4.3.4 Absorption and emission spectra

Electronic absorption and excitation spectra in the UV/VIS range were recorded with a a Shimadzu UV 3100 spectrophotometer. Fluorescence spectra were obtained with an Edinburgh FS 900 spectrofluorometer. Fluorescence lifetimes were measured with an Edinburgh FL 900 spectrofluorometer equipped with a NBH NanoLED diode laser with a frequency of 1 MHz and a wavelength of 297 nm.

Fluorescence quantum yields were determined for ethanol solutions containing porphycenes, using as a reference porphycene dissolved in *n*-hexane, of which the fluorescence quantum yield was determined as 0.36.[123] Correction for the refractive index of the solvents was included.

4.3.5 Scanning electron microscope (SEM) images

Nanoparticles and SERS substrates were characterized by FEI Nova NanoSEM 450 with field emission gun (Schottky type).

4.4 Data analysis

The standard procedures used in the processing of Raman spectra, such as cosmic ray removal, quick preview of the registered spectra, background removal, etc., were provided by Renishaw Wire 3.3. software. If it is not mentioned explicitly, the spectra were not background-corrected. When the background correction was done, the cubic-spline interpolation was applied. Moreover, Renishaw Wire 3.3 software has implemented principal component analysis (PCA), a statistical method that allows for identification of linearly uncorrelated variables known as principal components, based on a set of observations, which might be correlated. In other words, this technique reduces the dimensionality of the data, typically to few components, where the first one has the largest variance, i.e., it accounts for maximum possible variability. In the spectral analysis, this method enables the distinction between different species or molecular forms and minimizes the impact of extraneous spectra, which might result from impurities. To be specific,

the components extracted from PCA represent the noise-filtered spectra of the investigated species.

Contrary to the data obtained from 'normal' Raman or SERS measurements, which typically do not need any sophisticated processing, usually not included in commercial software, the analysis of single molecule data requires some automation, mostly due to its size. Hence, implementation of procedures supporting the analysis of the obtained data was an important part of research. All software was written in Matlab, entirely by myself and can be found at http://github.com/gitmajka/phd. The typical procedures allow for averaging over a set of spectra, numerical integration over a selected interval by means of the trapezoidal rule, calculation of correlations between Raman bands intensities, graphical representation of time traces, and the statistical analysis. The Raman peaks were fitted by Lorentzian functions, as they provided better agreement than the Gaussian ones.

The Raman mapping of samples prepared for observation of single molecules produces thousands of spectra, of which typically only a few percent contain the signature of the investigated species, while the rest show exclusively bands originating from the SERS substrate. Hence, the discrimination between these spectra is one of the initial tasks during single molecule analysis. This selection was based on a condition that a maximum intensity in a specified interval was higher than the mean intensity in this range, increased by some threshold value. Naturally, this discrimination was not perfect and required further, typically manual, verification. Too high threshold resulted in rejection of spectra containing the Raman signs of investigated species, while too low values caused that the spectra containing only noisy background were not rejected automatically. Therefore, the values of the threshold were carefully selected. The distinction between spectra belonging to different species, like different isotopologues, was also attempted automatically, based on the Raman shifts of the recognized peaks. The preliminary categorisation was manually verified.

The graphical representation of the Raman tensors was implemented according to the description provided in Chapter 6.

4.5 Quantum mechanical calculations

Quantum mechanical calculations, including geometry optimizations and normal mode analysis were performed at the density functional theory (DFT) level with the hybid B3LYP[124,125,126] functional and 6-31G(d,p) basis set using Gaussian 09 software.[127] The resonance Raman spectra were predicted by Amsterdam Density Functional (ADF) software[128] also at the DFT level, but with the use of the generalized gradient approximation (GGA) BP86 functional[129,130] and double-zeta plus polarization (DZP) basis set.

The quantum chemical calculations provided Raman activities of normal modes. In order to simulate the Raman spectra intensities, I, which are sensitive to the temperature, T, (in K) and the exciting laser frequency, $\tilde{\nu_0}$, (in cm^{-1} units), the following formula[131] was used:

$$I_i = f\frac{S_i(\tilde{\nu}_0 - \tilde{\nu}_i)^4}{\tilde{\nu}_i(1 - \exp(\frac{-hc\tilde{\nu}_i}{kT}))}, \tag{4.1}$$

where S_i denotes the calculated Raman activity of the i-th normal mode, $\tilde{\nu_i}$ is the vibrational wavenumber of the i-th mode, k, c and h are universal constants, and f is the chosen normalization factor common for all of the vibrations. Additionally, Lorentzian broadening was applied to peaks with a bandwidth (FWHM) of 10 cm^{-1}.

Chapter 5

Single molecules of porphycene isotopologues

The purpose of this chapter it to prove that in the case of porphycene placed on nanoparicles acting as nanoantennas we have reached single molecule level. In addition to the bi-analyte approach, intensity fluctuations and step-like time evolution confirm observation of single molecules. At the beginning, however, we will briefly describe the spectral features of the investigated species, such as electronic absorption, emission, and Raman scattering.

5.1 Spectral characteristics of porphycene: electronic absorption, fluorescence, and Raman scattering

The electronic absorption and fluorescence of porphycene (Pc) are presented in Figure 5.1. The arrows pointing down indicate the excitation laser lines used for Raman and SERS measurements, whereas the grey areas refer to the respective Stokes Raman regions. The used laser lines correspond to the non-resonant excitation (785 nm), excitation into the S_1 state (633 nm), S_2 (514 nm), and into a higher

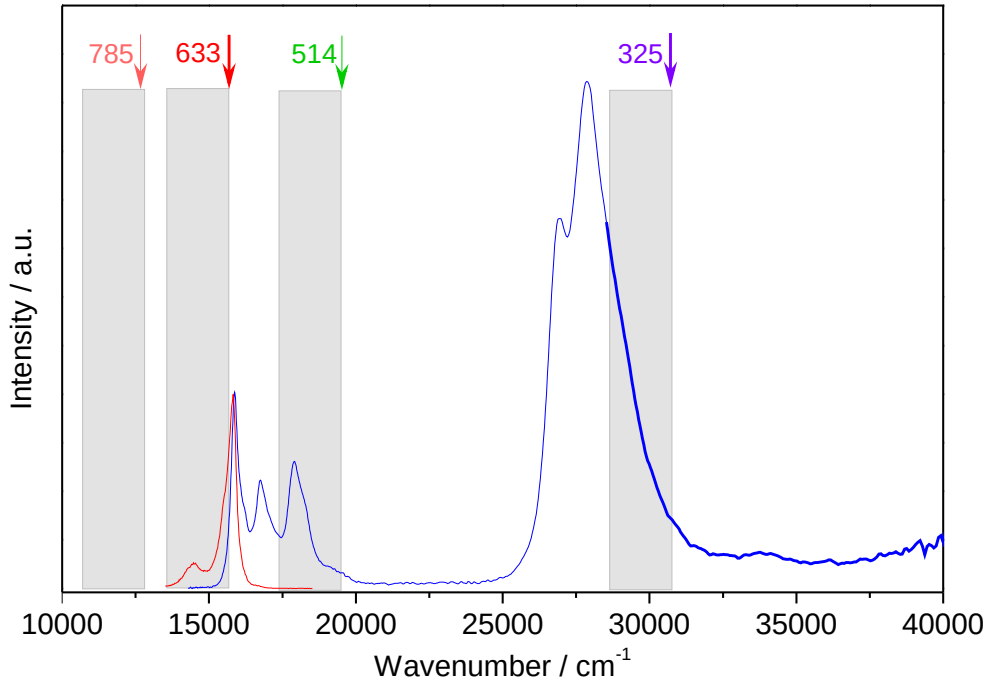

Figure 5.1: Absorption (blue) and fluorescence (red) spectra of porphycene-d_0 in tetrahydrofuran at room temperature. (Spectra measured by S. Gawinkowski)

electronic level (325 nm). The obtained Raman and SERS spectra of Pc-d_0 measured under different conditions, including various environments, temperatures, and excitation wavelengths are presented in Figure 5.2.

One of the reasons for investigation of porphycene under various experimental conditions was an attempt to verify whether it exists (in detectable amounts) in more than one tautomeric forms. Another reason for the investigation was an aim to compare the data obtained by quantum chemical calculations of resonance Raman spectra and the actual experimental results. Despite widespread availability of supercomputers and quantum mechanical software, such calculations are uncommon. Furthermore, methods for prediction of resonance Raman specta are only implemented in a very limited number of software packages (not even in the most popular among them: Gaussian). The accuracy of such calculations will be discussed in the next chapter.

Unfortunately, the Raman or SERS spectra of Pc could not be measured under any conditions. For instance, the Raman spectrum of Pc in solution excited by a 633 nm laser line was unattainable due to fluorescence, which strongly overlaps with the Raman bands (emission of porphycene has a very small Stokes shift).

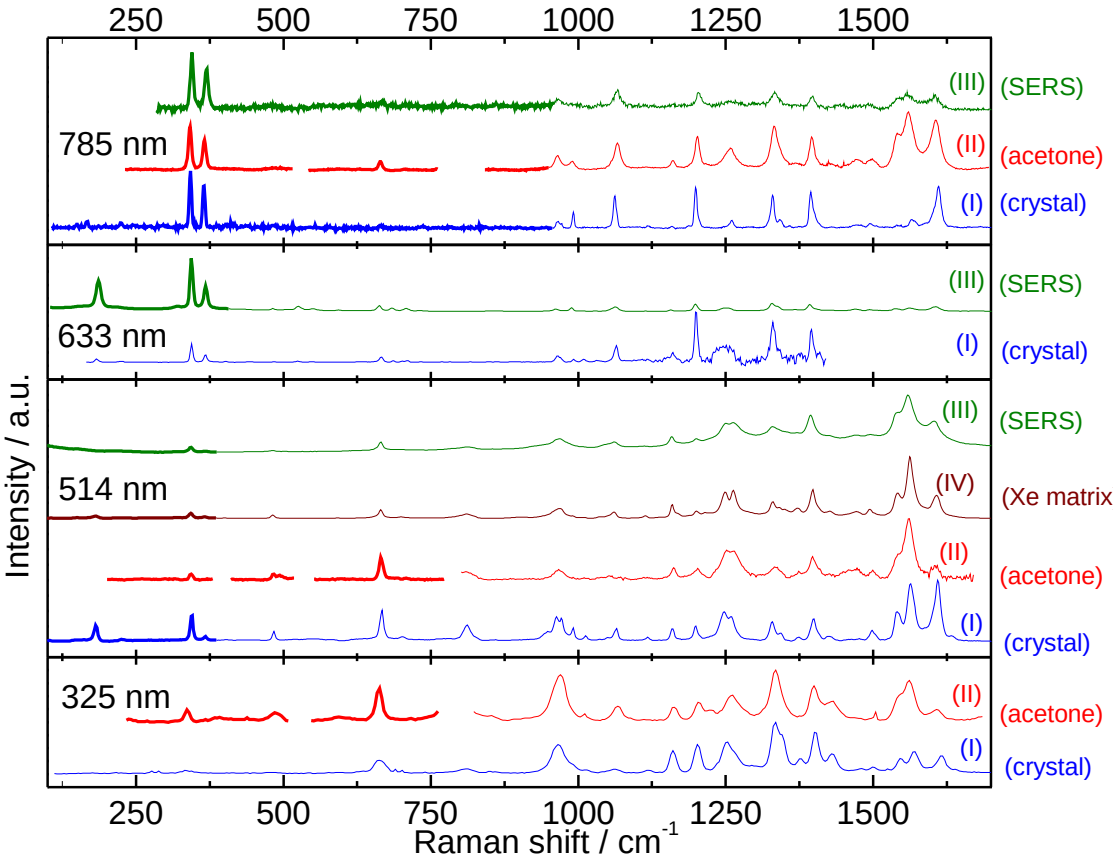

Figure 5.2: Backgorund corrected SERS and Raman spectra of Pc-d_0 excited with four laser lines under different conditions: (I) Raman spectra of a crystalline sample at 293 K; (II) Raman spectra in acetone solution recorded at room temperature; (III) SERS spectra on gold nanostructures measured at room temperature for 785 and 514, and at 77 K for 633 nm excitation; (IV) Raman spectra of Pc-d_0 in Xe matrix measured at 6 K. (Some of the spectra were measured by S. Gawinkowski)

High fluorescence quantum yield (0.36-0.49 depending on solvent) effectively prevented the observation of Raman spectrum. In the case of SERS, however, the proximity of metallic nanostructures efficiently quenched fluorescence, enabling us to observe Raman peaks. Nevertheless, we managed to obtain the resonance Raman spectrum of porphycene without deposition on metal nanoparticles. Namely, when porphycene molecules are organised in a crystal structure the strong fluorescence observed for chromophore molecules dissolved in solution is quenched and red-shifted. Typically, for such spectral changes aggregation is responsible and the crystal may be considered as an extreme case of a higher order aggregate. The emission of a porphycene crystal is shown in Figure 5.3. The decrease in temperature results in red shift of emission, which is better illustrated in Figure 5.4. This red shift of fluorescence allows us to measure the resonance Raman spectrum

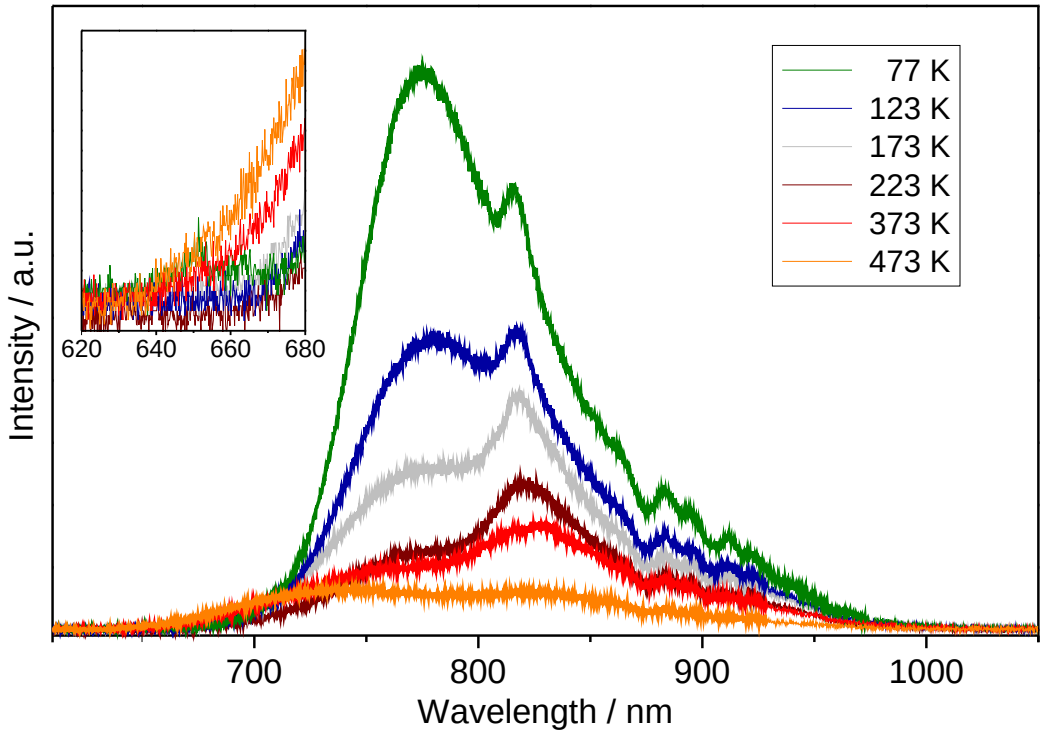

Figure 5.3: The emission of a porphycene crystal excited at 633 nm, registered at different temperatures.

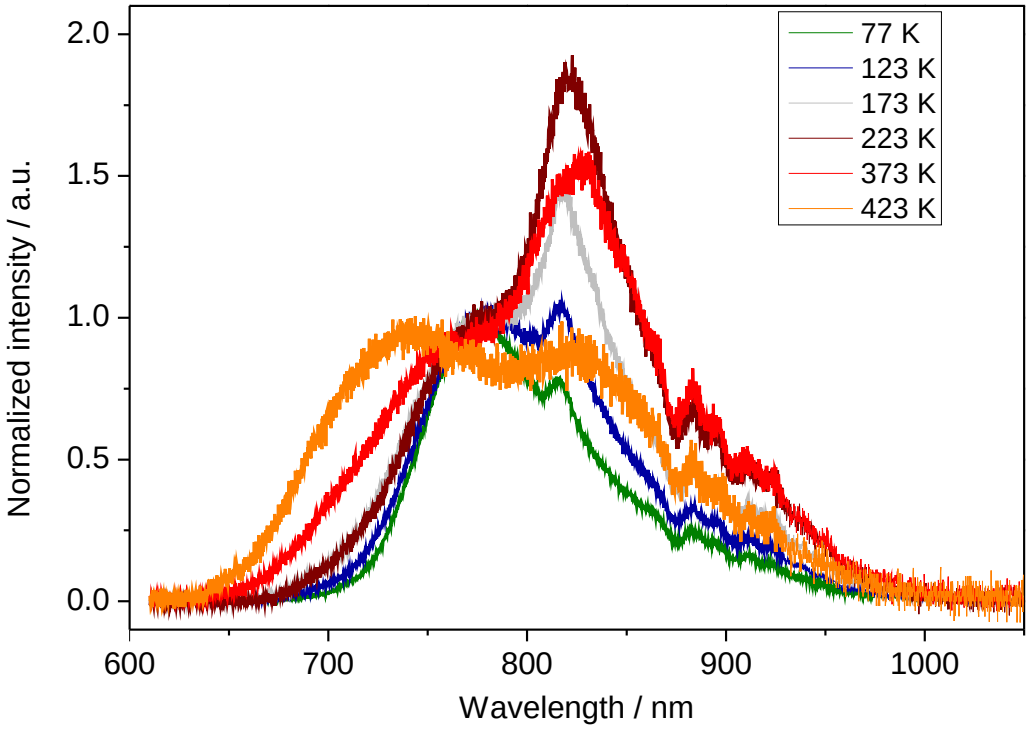

Figure 5.4: The emission of a porphycene crystal excited at 633 nm, registered at different temperatures normalized to the intensity of the first peak.

excited at 633 nm deprived of luminescence background up to 1000 cm^{-1}, which is shown in Figure 5.2. This background corrected spectrum shows significantly higher noise above 1000 cm^{-1} due to overlapping with fluorescence.

We have failed not only in measurement of Raman spectrum of Pc in solution using 633 nm laser line, but also in observing SERS spectra while exciting in the UV region. Insufficient enhancement is most likely due to damping of surface plasmon resonance by the metal interband transition absorption in this spectral region. Kneipp admits that her goup failed in UV-SERS measurements[132], but there were reports of SERS spectra excited by 325 nm laser line obtained for a number of species adsorbed on various transition-metal surfaces.[133,134]

Despite these difficulties, we have acquired a collection of Pc spectra measured under various conditions. In general, the number and position of peaks are very similar regardless of the excitation wavelength. Due to C_{2h} symmetry of Pc (*trans* tautomer) Raman-active are totally symmetric A_g modes and out-of-plane B_g modes. The obtained spectra are dominated by A_g vibrations, but B_g modes are present as well.[32] The relative peak intensities vary considerably while changing the excitation energy. However, considering a particular excitation laser line, the relative peak intensities are comparable for SERS and non-SERS spectra. The largest discrepancies are observed in the spectra obtained with 633 nm laser line, between the intensities of low and high frequency modes.

It is remarkable that among four used laser lines only the excitation at 633 nm revealed overtones and combination bands.

5.2 Bi-analyte approach

As described in the introduction, the bi-analyte approach has been widely accepted as providing the strongest argument for reaching single molecule regime. This approach requires SERS measurement of a mixture composed of two chromophores having similar properties, i.e., surface affinity, Raman cross section, etc. While the absorption spectra of isotopologues are virtually identical and a lot

of properties are similar, often their Raman spectra are distinguishable. Therefore, chromophores that differ only in isotopic substitution are perfect candidates for this method, ensuring the highest reliability. In order to apply the bi-analyte method, porphycene with all outer protons exchanged by deuterons (Pc-d_{12}) was prepared. As noted above, the extent of deuteration was determined by mass spectrometry, according to which more than 90% of compound was fully deuterated. In addition, porphycene-$^{15}N_4$ was analysed, however its Raman spectrum is almost the same as for Pc-d_0.

5.2.1 Absorption and Raman spectra of porphycene and its isotopologues

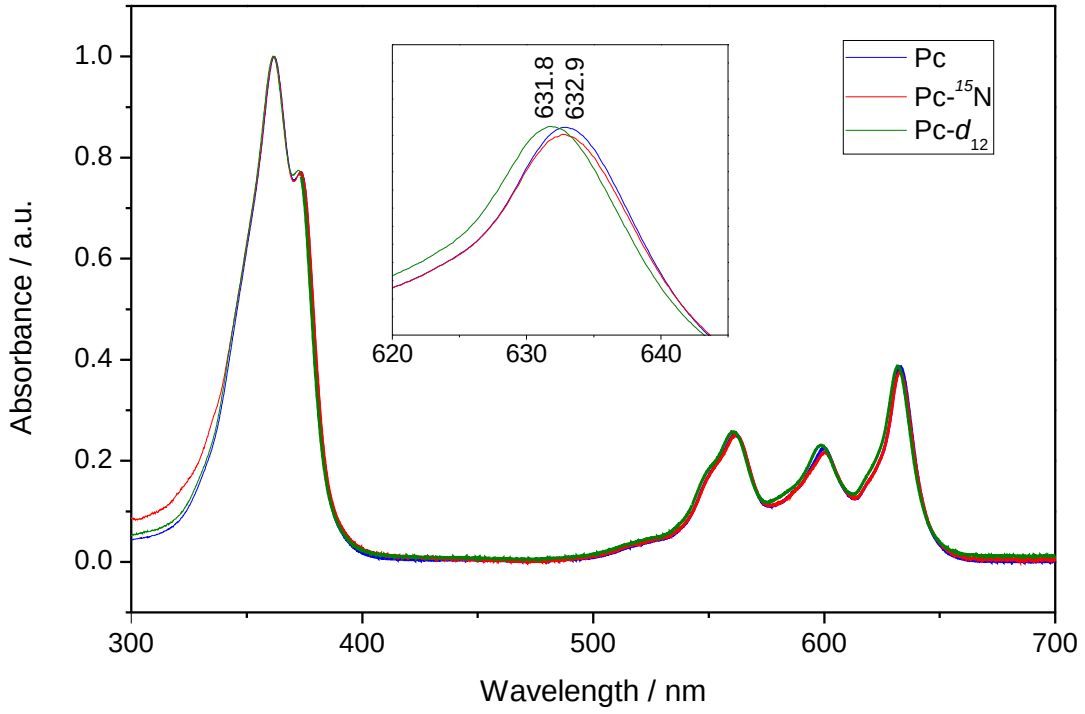

Figure 5.5: Absorption spectra of porphycene isotopologues: Pc-d_0, Pc-d_{12} and Pc-$^{15}N_4$ in toluene.

Figure 5.5 presents the absorption spectra of all three available isotopologues dissolved in toluene. The maximum of the Q_x band for Pc-$^{15}N_4$ is located exactly at the same energy as for porphycene, while for Pc-d_{12} it is slightly blue-shifted (by

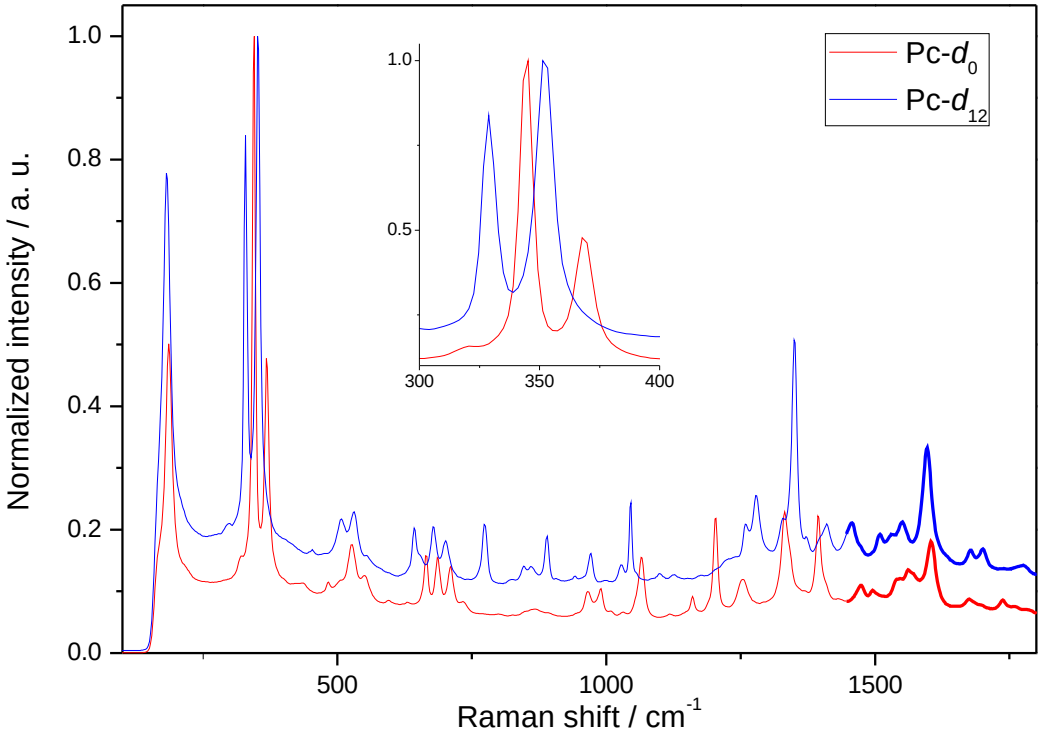

Figure 5.6: The averaged SERS spectra of Pc-d_0 and Pc-d_{12}. SERS substrate: 25 µm×47 µm gold NRs, laser excitation: 632.8 nm, laser power: 50 µW, room temperature, concentration of solutions: 10^{-8} M.

about 28 cm^{-1}), probably as a result of slightly higher S_0-S_1 zero point energy difference. In our single molecule experiments we use the laser line of 633 nm, which corresponds to the transition from S_0 to S_1, and therefore we take advantage of resonance enhancement of Raman scattering.

The SERS spectra of Pc-d_0 and Pc-d_{12} obtained for this excitation are presented in Figure 5.6. Upon deuteration some modes shift significantly, which allows for sharp distinction between species. The most diagnostic is the region between 300 and 400 cm^{-1}, where $3A_g$ and $4A_g$ modes occur,[32] as typically these bands are the most intense.

Figure 5.7 presents the influence of Pc concentration on the SERS spectra. As the concentration increases, the background becomes higher. It proves that the observed background originates from chromophore molecules adsorbed on nanostructures, more specifically from their fluorescence. The energy and spectral shape are consistent with the emission of porphycene. A significantly greater increase of the background compared to the increase of Raman bands intensities is most likely

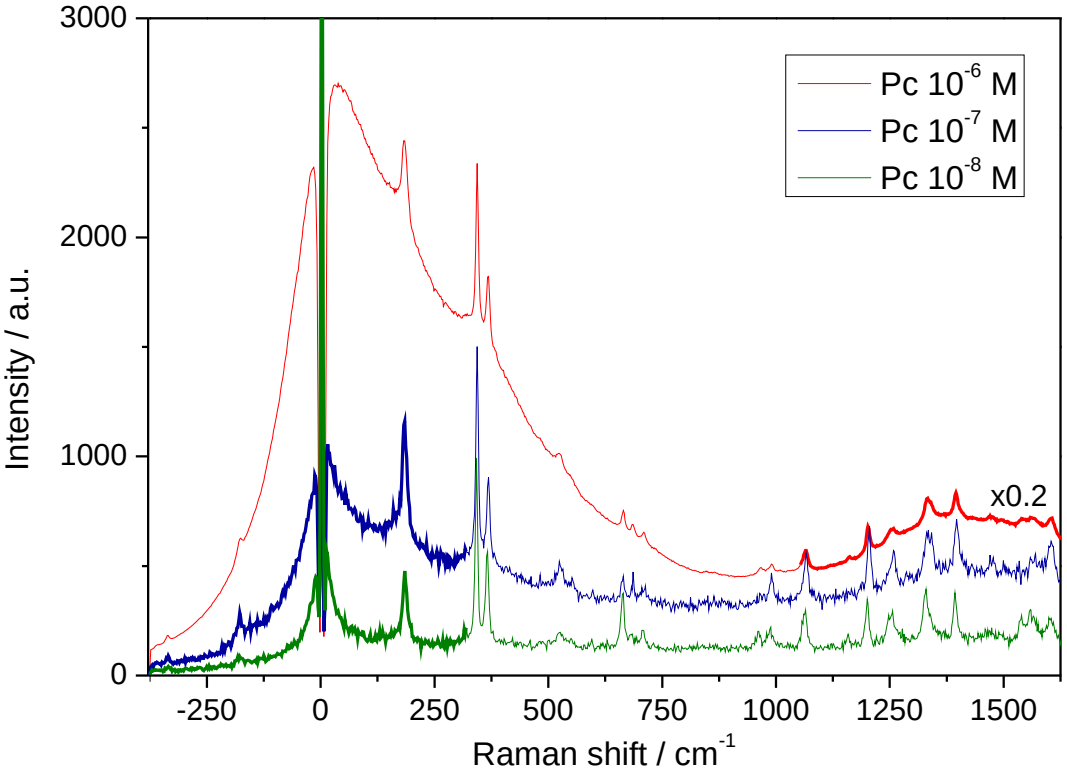

Figure 5.7: The averaged SERS spectra of Pc-d_0 measured at sample prepared from solutions of different concentrations. SERS substrate: Au NPs electrodeposited at three phase junction, laser excitation: 632.8 nm, laser power: 50 µW, room temperature.

caused by the fact that additional molecules are not as close to plasmonic nanostructures as the preceding ones. Therefore, their fluorescence is not that efficiently quenched. This experiment demonstrates that in the case of highly fluorescent dyes an increase in concentration may impede measurements of SERS spectra.

5.2.2 Procedure of sample preparation

For application of the bi-analyte technique, 1:1 mixture of two isotopologues: Pc-d_0 and Pc-d_{12} was prepared. In order to eliminate errors in the sample preparation, the solutions used for the experiment were prepared sequentially: the initial solution was obtained by mixing equal volumes of Pc-d_0 and Pc-d_{12} solutions (both of concentrations 5x10^{-6} M) and then, only the dilutions by addition of ethanol were done. First, the solution of total dye concentration of 10^{-6} M was obtained, which in turn served as an initial solution for further dilutions, etc. In a single step a

solution was diluted no more than ten times. Such way of preparation ensures the same relative concentration of Pc-d_0 to Pc-d_{12} in all solutions, provided that the same amount of both molecule types was adsorbed on the vessel walls. Such assumption seems very reasonable.

A drop of ethanol solution containing the same concentration of both chromophores was put on a SERS substrate. Then, after evaporation of ethanol (which took a few seconds), the Raman mapping was performed. The measured spectra were afterwards classified into three groups: 'pure Pc-d_0', 'pure Pc-d_{12}' and 'both' if there was any indication of coexistence of both chromophores. Relevant histograms were obtained for different concentrations of porphycene, ranging from 10^{-7} to 10^{-10} M (total concentration of dyes).

5.2.3 Results

The obtained histograms combined with the spectra averaged over the registered events are shown in Figure 5.8. Based on this data, we can estimate the limit of single molecule regime, which is indicated by a negligible number of 'two-chromophore' spectra with respect to 'one-chromophore' ones. In the case of samples prepared using 10^{-7} M solutions, the vast majority of spectra are superposition of Pc-d_0 and Pc-d_{12} SERS spectra, indicating that we are far from single molecule regime. A decrease in solution concentration by one order of magnitude results in comparable occurrence of all three kinds of events. By further lowering the concentration, the occurrence of both chromophores in a single spectrum becomes very rare. Therefore, single molecule regime may be estimated for 5×10^{-9} M. This limit, however, might be slightly shifted for different substrates, since it most likely depends on the hot spots density and the behaviour of a droplet: differences in wettability of SERS substrates affect local concentration. With a further decrease in concentration of the stock solution, the shape of histograms changes unexpectedly. Namely, the ratio between numbers of 'pure Pc-d_0' events to 'pure Pc-d_{12}' becomes remarkably higher than the expected 1:1 ratio. Indeed, for lower concentrations hot spots are preferentially occupied by non-deuterated molecules. Such unpredicted and surprising behaviour was confirmed for different SERS substrates (prepared by laser ablation as well as by electrochemical methods).

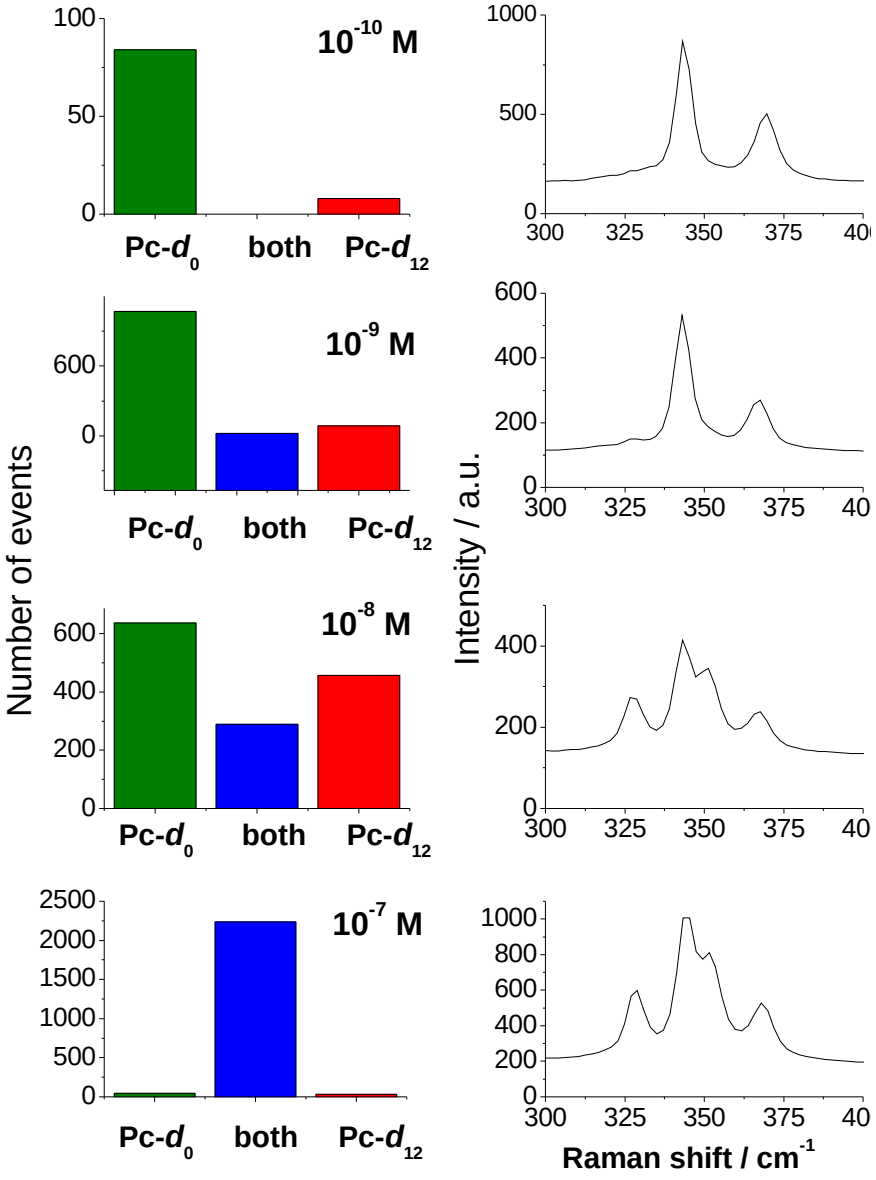

Figure 5.8: Left: histograms presenting the number of 'one-chromophore' vs 'two-chromophore' events obtained for 1:1 mixtures of Pc-d_0 and Pc-d_{12} for different total concentration of dyes (ranging from 10^{-7} to 10^{-10} M). Right: the averaged SERS spectra (spectra with no Raman peaks of Pc were discarded) for each concentration. SERS substrate: 25 µm×47 µm gold NRs, laser excitation: 632.8 nm, laser power: 50 µW, room temperature.

Relative contributions of both isotopologues Pc-d_0 and Pc-d_{12} to the averaged SERS spectra for samples prepared using more concentrated solutions ($10^{-7}-10^{-8}$ M, Figure 5.8) are roughly the same. Similarly, numbers of events corresponding to detection of 'pure Pc-d_0' and 'pure Pc-d_{12}' are comparable. Therefore, the observed imbalance between isotopologues emerging at lower concentration cannot

be simply explained by the difference in the enhancement factor and/or surface affinity. If that were the case, this ratio should be more or less constant in a broad range of concentrations, which is not observed. The obtained results may be justified by difference in diffusion coefficients of both isotopologues. Indeed, if the molecules are relatively far from the hot spots they have to 'compete' with each other to reach them. Then, even a small difference in diffusion coefficient may become detectable. This is only the case for low concentration regime, where the average distance to hot spots is appreciable. The influence of isotopic substitution on diffusion coefficient on the metal surfaces has not been widely investigated so far. Nevertheless, studies of molecular rotation of acetylene isotopologues adsorbed on Cu(100) surface at 8 K revealed significant differences.[135] Diffusion is often described by the Arrhenius equation:

$$D = D_0 \exp(-E_a/kT), \tag{5.1}$$

where E_a denotes the activation energy, k is the Boltzmann constant, T is the temperature. Upon isotopic substitution the activation energy might be modified due to the difference in zero-point energy, which naturally changes the value of the diffusion coefficient. Moreover, isotopic edition may also affect the interaction with the metal surface.

If the model described above applies, further decrease in concentration, reaching a situation when the number of molecules is much smaller than the number of hot spots, should again result in a comparable number of single molecule spectra for both isotopologues. However, we did not manage to obtain the reliable statistics for such a low concentration. Already at the concentration of 10^{-10}M we had to record a very large number of spectra, since only a very small fraction of them revealed Raman features. Unfortunately, the proposed hypothesis cannot be easily verified in a different way.

The model of 'molecules competing for hot spots', where difference in diffusion coefficient comes into play is one of the plausible hypotheses, which requires further verification. Diffusion of porphycene molecules on the metal surface seems very likely, especially at room temperature. This supposition is supported by the observation of mobility of porphyrins on the metal surface.[136,137,138,139] Although

the experimental conditions during SERS measurement are significantly different from the ones during measurements at ultra-high vacuum on atomically smooth metal surfaces deprived of water and carbon dioxide molecules, the comparison of surface diffusion coefficients of porphycene isotopologues performed by scanning tunnelling microscopy might shed light on the mobility modification upon deuteration. To this end, we plan to carry out systematic studies using SERS substrates of varying hot spot density. The control of this density, however, may not be that straightforward. The simplest idea would involve the use of differently concentrated colloids for substrate preparation. It should be noted that, a smaller number of hot spots would substantially increase the measurements' time.

5.3 Time traces

The characteristic features of single molecules are zero-one character of signal intensity and one-step bleaching, i.e., a sudden disappearance of the spectral signal. In fluorescence studies of chromophores embedded in polymer films, blinking and bleaching provide a conclusive proof for single molecule character. In SERS, however, the sudden disappearing of signal may result from hot spot degeneration. Nevertheless, at a single molecule level time traces always have a distinctive appearance, different from ones registered for bulk.

Figures 5.9 and 5.10 present temporal changes of Raman scattering intensity (integrated intensity of bands in the region between 330 and 390 cm^{-1}) in two cases: higher and lower concentration (three orders of magnitude difference). At higher concentration, time evolution resembles an exponential decay, which is most likely associated with photodecomposition of the chromophore. Even after long-term illumination the SERS spectrum of porphycene is clearly visible (the red spectrum in Figure 5.9).

The registered time evolution of the SERS signal originating from a single molecule looks completely different. It has zero-one character with some fluctuations. The spectra presented in Figure 5.10 at times $t = 10$ s and $t = 11$ s demonstrate a sudden bleaching of Raman scattering, and what remains is only the spectrum of the SERS substrate. The disappearance of the Raman signal may result either

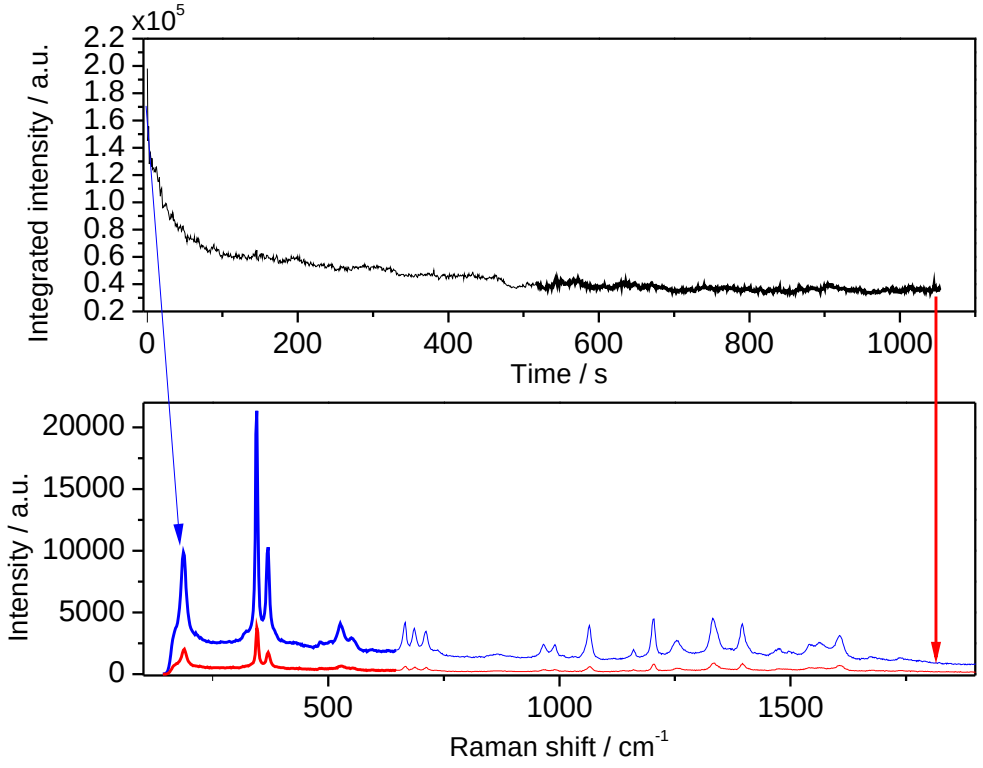

Figure 5.9: Top: time evolution of integrated Raman intensity (bands between 330 and 390 cm^{-1}) of Pc-d_0 on gold NPs (the concentration of the solution used for preparation was $5 \cdot 10^{-6}$ M). Bottom: SERS spectra registered at two different moments: $t = 0$ s and $t = 1100$ s. SERS substrate: 25 µm×47 µm gold NRs, laser excitation: 632.8 nm, laser power: 50 µW, room temperature.

from an escape of a molecule from a hot spot (probably via thermal motion) or from photodecomposition of a molecule itself. If the product of this reaction is no longer resonant with incident light, the enhancement may be not high enough to register its Raman signal. Another explanation, albeit rather unlikely considering low laser power and short acquisition time, is the change of the nanostructure morphology.

Time traces of Raman scattering recorded for molecules located in hot spots are similar to time traces of emission obtained for chromophores embedded in polymer films. The main difference is blinking frequency, which is much higher for the latter. In the case of SERS signal, blinking rarely takes place. Figure 5.11 presents a very unusual time trace, where blinking happened. The fluctuations of integrated intensity of the SERS signal in the region between 330 and 390 cm^{-1} are exceptionally large. The spectrum at the moment of $t = 137$ s (green) displays no Raman bands, similarly to the spectra after bleaching (for example at $t = 2182$

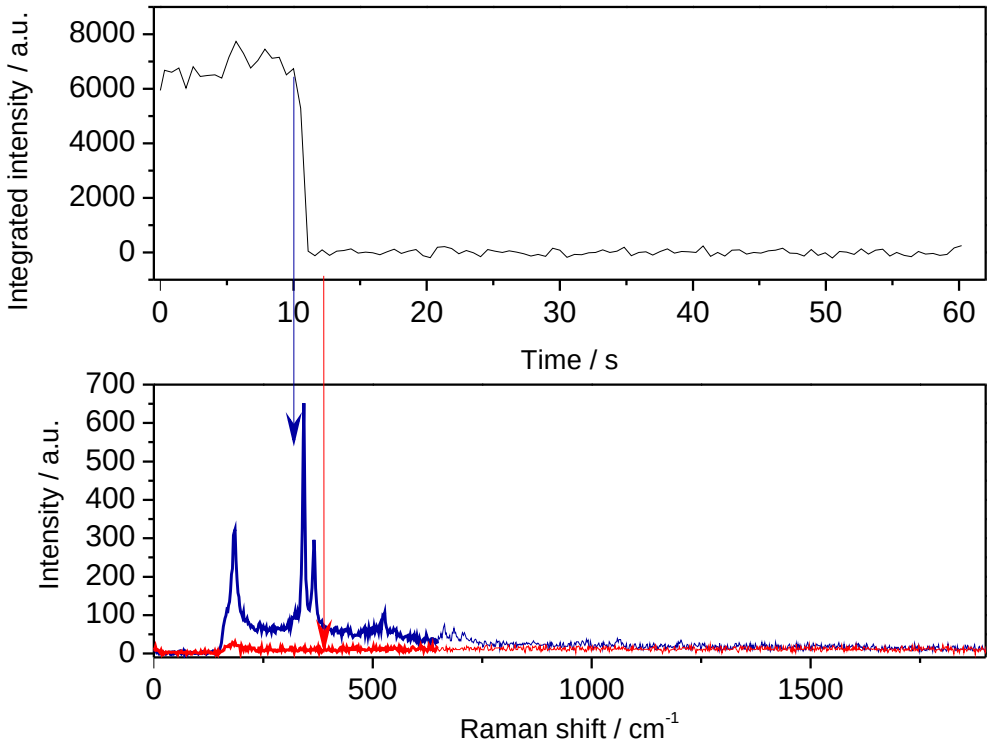

Figure 5.10: Top: time evolution of integrated Raman intensity (bands between 330 and 390 cm^{-1}) of Pc-d_0 on gold NPs (the concentration of the solution used for preparation was 10^{-9} M). Bottom: SERS spectra registered at two different moments: $t = 10$ s and $t = 11$ s. SERS substrate: 25 µm×47 µm gold NRs, laser excitation: 632.8 nm, laser power: 50 µW, room temperature.

s (red)). Such behaviour may originate from motions of a molecule in and out of a hot spot. In the case of SERS, sometimes it is practically impossible to distinguish between blinking and bleaching, as the recovery of signal occurs after long 'off' period, exceeding tens of seconds. The reappearance of the SERS signal may be caused by another molecule which entered a hot spot. We can be sure that such situation happened only if the recovered spectrum changed markedly compared to the original one, for example belonging to a different isotopologue. To make the situation even more complicated, reappearing of a signal may be caused by population of another hot spot within the laser focus. It is possible, because the latter is significantly bigger than the size of a hot spot.

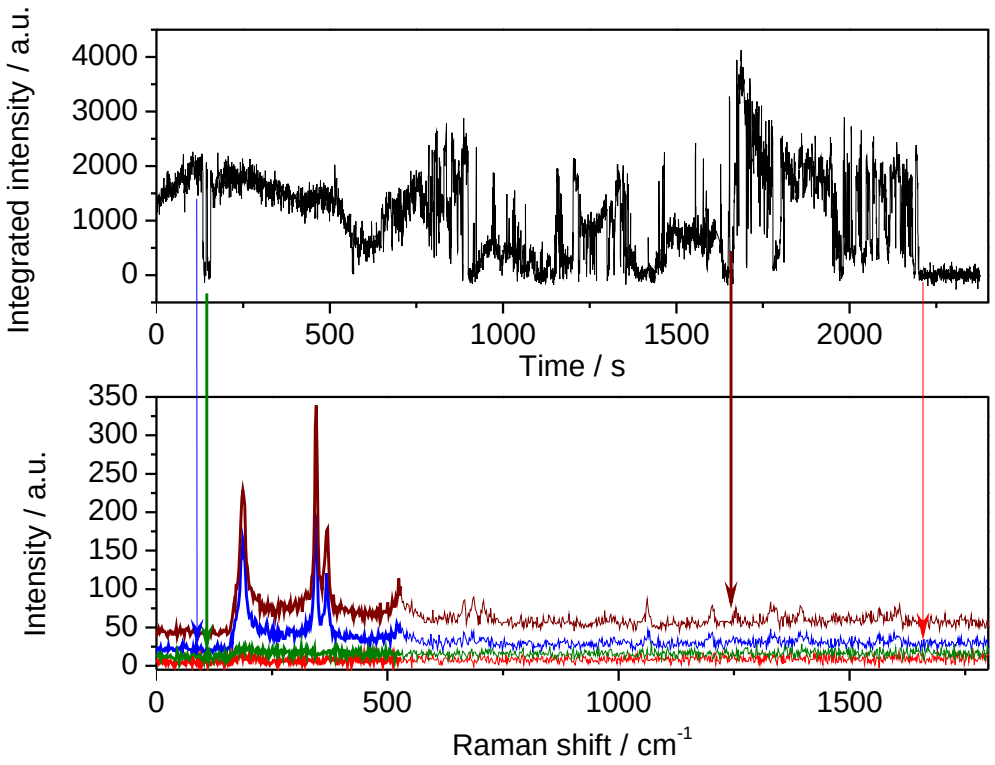

Figure 5.11: Top: time evolution of integrated Raman intensity (bands between 330 and 390 cm^{-1}) of Pc-d_0 on gold NPs (the concentration of the solution used for preparation was 10^{-9} M). Bottom: SERS spectra registered at four different moments: t = 133 s, t = 137 s, t = 1640 s and t = 2182 s. SERS substrate: Au nanoparticles obtained by electrodeposition at a three phase junction, laser excitation: 632.8 nm, laser power: 50 µW, room temperature.

5.4 Single molecule SERS spectra

Another essential feature of single molecule spectra is their uniqueness. Figure 5.12 shows a selection of single molecule SERS spectra of Pc-d_0 recorded at the same SERS substrate, but from different hot spots. The measured spectra reveal striking differences, especially in terms of bands intensities. In general, the highest variability is observed between the low and high frequency regions. For instance, among the spectra shown in Figure 5.12 the red and grey ones represent a situation in which modes in a broad region of frequencies are significantly enhanced. In the case of the green spectrum, low frequency modes are much more enhanced than the modes in the high frequency region, contrary to the orange and blue spectra. Such changes in relative intensities we attribute to differences in the hot spot structure, which greatly influence plasmon resonance. The modes which appear at

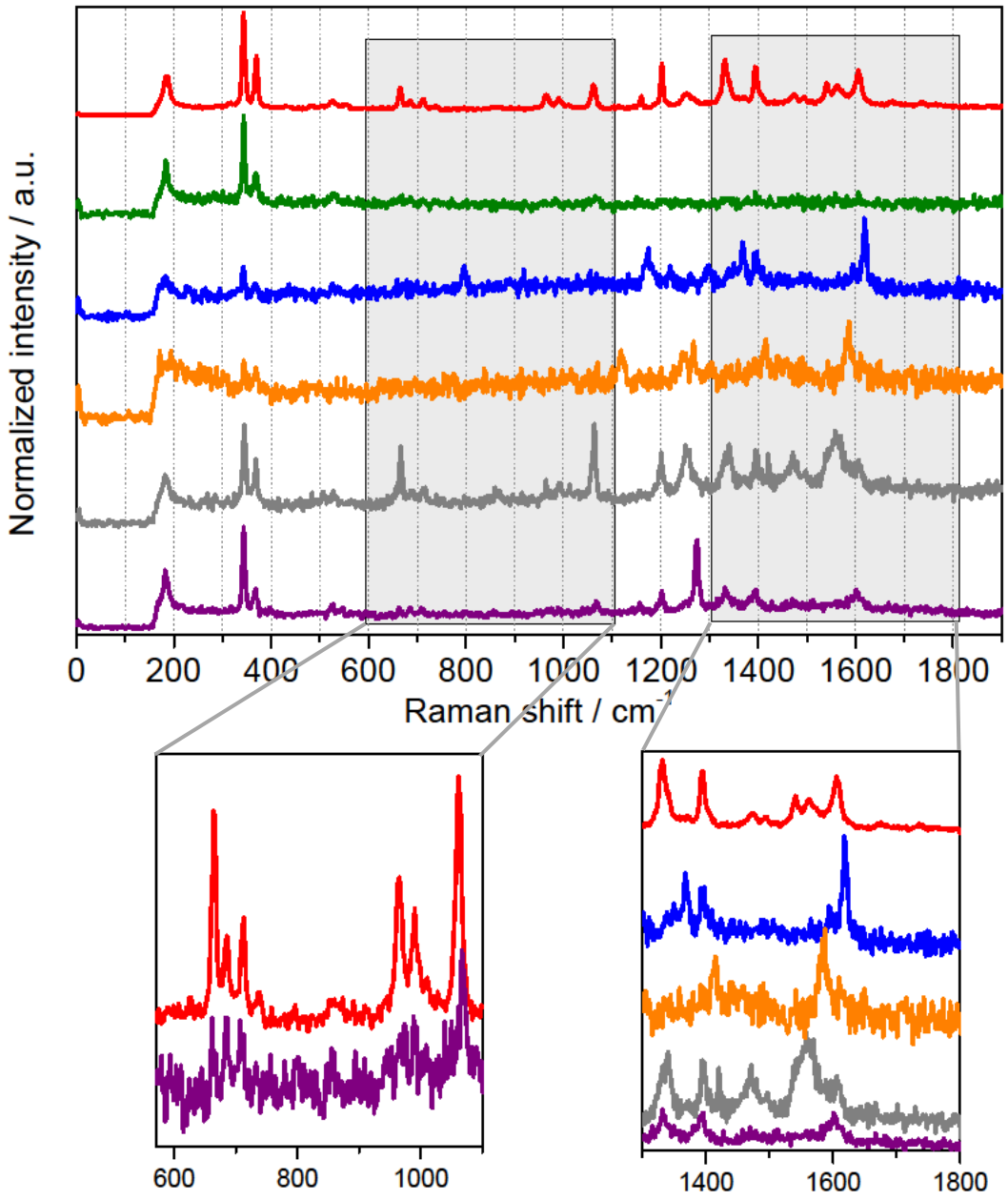

Figure 5.12: Single molecule SERS spectra of Pc-d_0 measured at different hot spots (the concentration of the solution used for preparation was 10^{-9} M). SERS substrate: Au nanoparticles obtained by electrodeposition at a three phase junction, laser excitation: 632.8 nm, laser power: 50 µW, room temperature.

the maximum of plasmon resonance experience the highest enhancement. Nevertheless, the relative intensities of peaks close to each other may change radically from hot spot to hot spot. This is illustrated by three closely lying bands around 700 cm^{-1} shown in Figure 5.12 (left bottom graph). The relative intensities of the first peak to the second or third one, which intensities are, by the way, comparable, vary considerably in the selected spectra. Such behaviour may be rationalized by different orientations of a molecule inside a hot spot. Since the enhancement of electromagnetic field inside a hot spot is highly directional, the intensities of Raman bands are very strongly related to the location and arrangement of a molecule. Figure 5.13 depicts the simplest model of a hot spot: two spherical nanoparticles separated by a few nanometers. A molecule inside can be arranged in infinitely many ways, of which three examples were shown. In addition, as long as a molecule is not chemically bound, as in the case of porphycene, it is highly probable that it can change its position. Even if its freedom is somehow limited, rearrangement of a molecule to some extent seems very likely.

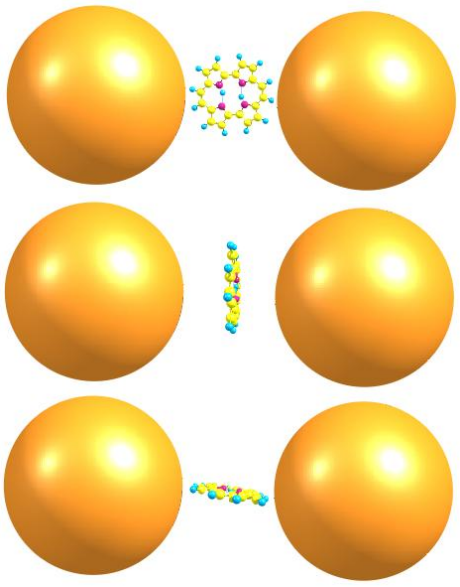

Figure 5.13: The simplest model of a hot spot and exemplary orientations of a molecule inside.

As for the position of the Raman bands, they are roughly the same. Brief analysis, for instance of the spectra presented in Figure 5.12 in the region between 1300 and 1800, may cause an impression that the bands shift distinctly. However, such illusion is caused by drastic changes in intensities: while some bands completely disappear, the others appear. Figure 5.14 presents the same single molecule spectra

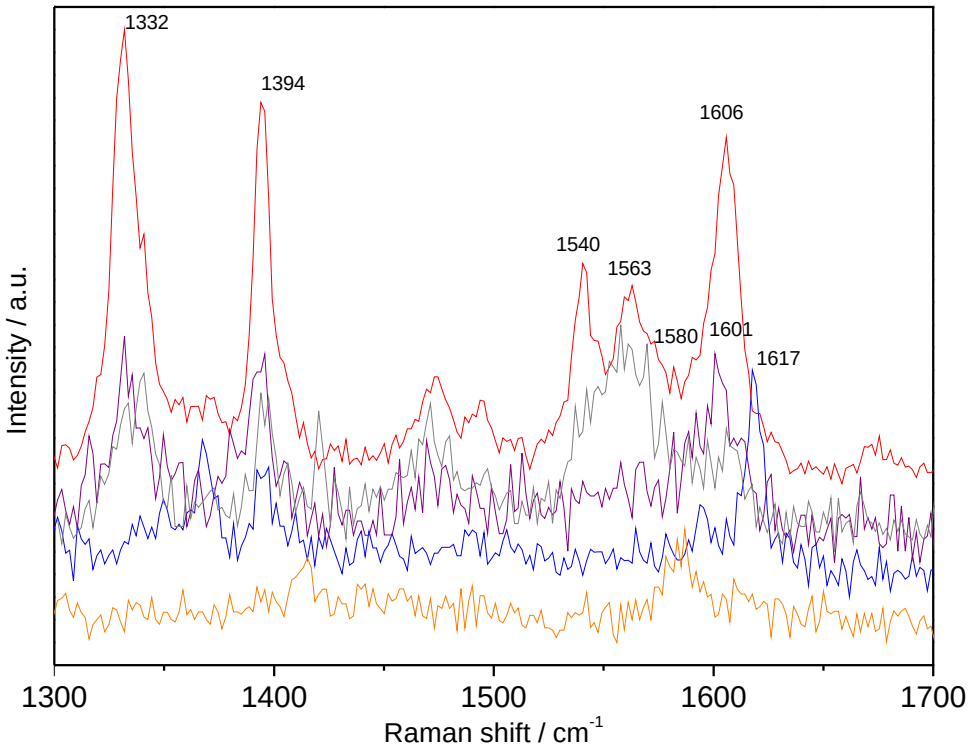

Figure 5.14: Single molecule SERS spectra of Pc-d_0 measured at different hot spots (the concentration of the solution used for preparation was 10^{-9} M), already shown in Figure 5.12. SERS substrate: Au nanoparticles obtained by electrodeposition at a three phase junction, laser excitation: 632.8 nm, laser power: 50 µW, room temperature.

of Pc-d_0 as in the Figure 5.12, but in such a way, that we can clearly see that bands shift only slightly. In the red spectrum in the region between 1500 and 1650 cm^{-1} three strong bands are present: at 1540, 1563 and 1606 cm^{-1}. There is also probably a band of low intensity at 1580 cm^{-1}. In the same region, in the grey spectrum two peaks can be recognized: around 1563 and 1606 cm^{-1}, while in the violet one, only a band at 1601 cm^{-1} is visible. In the orange spectrum we cannot see this band (maybe a trace around 1606 cm^{-1}), but an intense peak appears around 1580 cm^{-1}. The most surprising is the blue spectrum, in which peaks at 1594 and 1617 cm^{-1} are present. Since there is no clear evidence of any of these bands in the other spectra, their appearance may be due to a slight shift of the peaks observed in the aforementioned spectra. However, the described region is rich in various peaks, as the shapes of bands present in the red spectrum are quite complex: bands have some arms and do not have a pure Lorentzian (or Gaussian) shape. Again, single molecule spectrum of porphycene are highly affected by orientation of a molecule:

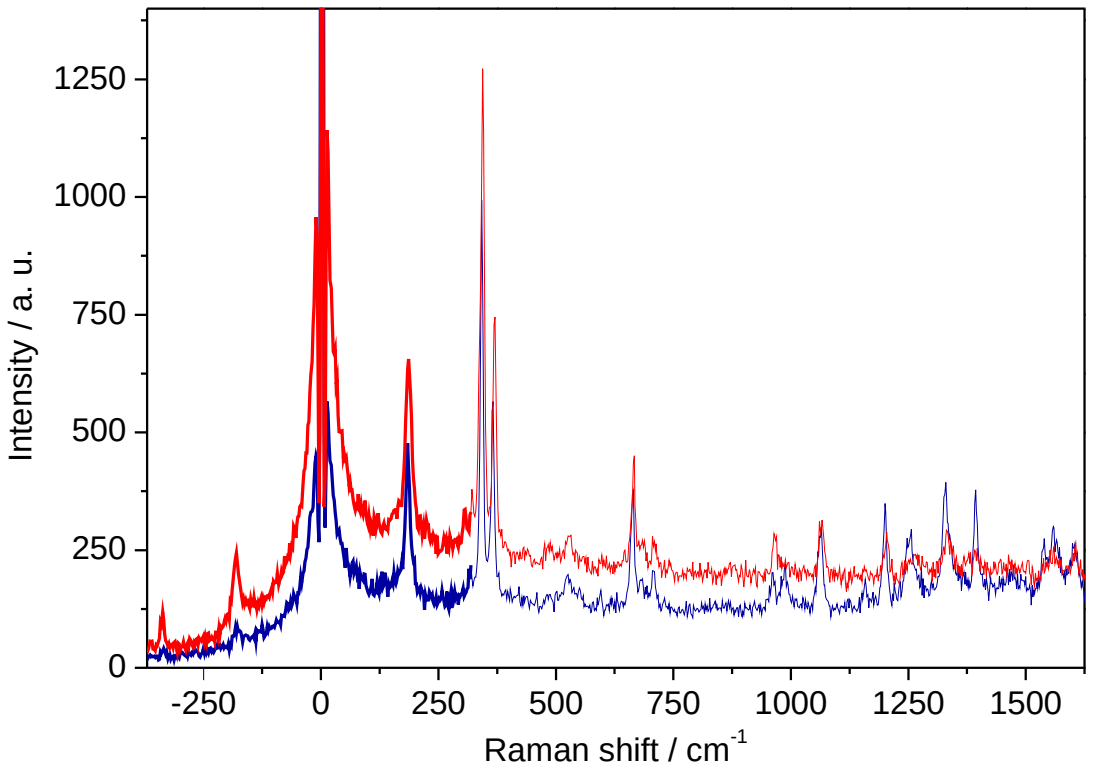

Figure 5.15: Single molecule SERS spectra of porphycene registered at different hot spots (the concentration of the solution used for preparation was 10^{-9} M). SERS substrate: Au nanoparticles obtained by electrodeposition at a three phase junction, laser excitation: 632.8 nm, laser power: 50 µW, room temperature.

this may lead to spectral shifts fluctuating in time and thus, to strange-looking band shapes.

Table 5.1: Integral intensities of the selected Raman bands presented in Figure 5.15, ratio of anti-Stokes to Stokes intensities and the corresponding temperatures.

spectrum	freq (cm^{-1})	area (a.u.)	anti-Stokes/Stokes	temperature (K)
red	180	9700	0.088	103
	-180	858		
	343	10680	0.022	124
	-343	236		
blue	180	5620	0.018	63
	-180	102		
	343	5862	0.018	119
	-343	108		

Fig. 5.15 illustrates an example of plasmon resonance shift. The two presented spectra were registered from the same sample, but at different hot spots. One should note differences in the relative intensities between the anti-Stokes and

Stokes intensities, which are listed in Table 5.1. These ratios can be translated into different temperatures, T, in the hot spots using the formula:

$$\frac{I_{AS}}{I_S} = \frac{(\nu_0 + \nu_i)^4}{(\nu_0 - \nu_i)^4} \exp\Big(-\frac{h\nu_i}{kT}\Big),$$

where I_S and I_{AS} denotes the Stokes and anti-Stokes Raman scattering intensity, respectively, ν_0 is the frequency of the incident light, ν_i is the frequency of the vibration, k stands for the Boltzmann constant and h for the Planck constant. This equation is derived from a Boltzmann distribution of the ground and first excited vibrational state populations.

For the $2A_g$ mode (at 180 cm^{-1}), the value of 0.088 was one of the highest ratios among the registered spectra. Surprisingly, it is significantly lower than the expected value for room temperature, which is 0.46. It is rather unique, as often under SERS conditions the unusually high ratio of anti-Stokes to Stokes intensities were observed.[140]. Santos *et al.* discussed the observed anomalies in the anti-Stokes to Stokes intensity ratios in single-molecule SERS spectra and attributed their fluctuations to the differences in plasmon resonance energies on the nanostructure.[19] Based on that, a method for estimation of plasmonic hot spot energy distribution across the SERS substrate was proposed.

Referring to the cited research, the observed variations in the relative anti-Stokes and Stokes intensities may origin from differences in surface plasmon resonance energies. Since plasmon resonance is broad, its shift can be confirmed by comparing relative intensities of Raman modes located away from each other. For instance, in the red spectrum, shown in Figure 5.15, the anti-Stokes bands are much stronger than in the blue one. However, the situation is exactly the opposite in the region above 1000 cm^{-1}, where the intensities of peaks in the blue spectrum distinctly prevail. Such behaviour indicates the difference in surface plasmon resonance energies related to the hot spots, from which these single molecule spectra originate.

5.5 *Cis-trans* tautomerization

According to the experimental and computational studies porphycene mainly exists in *trans* tautomeric form. However, when located on a crystal Cu(110) surface the *cis* form becomes more stabilized, which was revealed by STM.[106,105] Therefore, we carefully analyzed the registered spectra to check for the possible presence of different tautomeric forms.

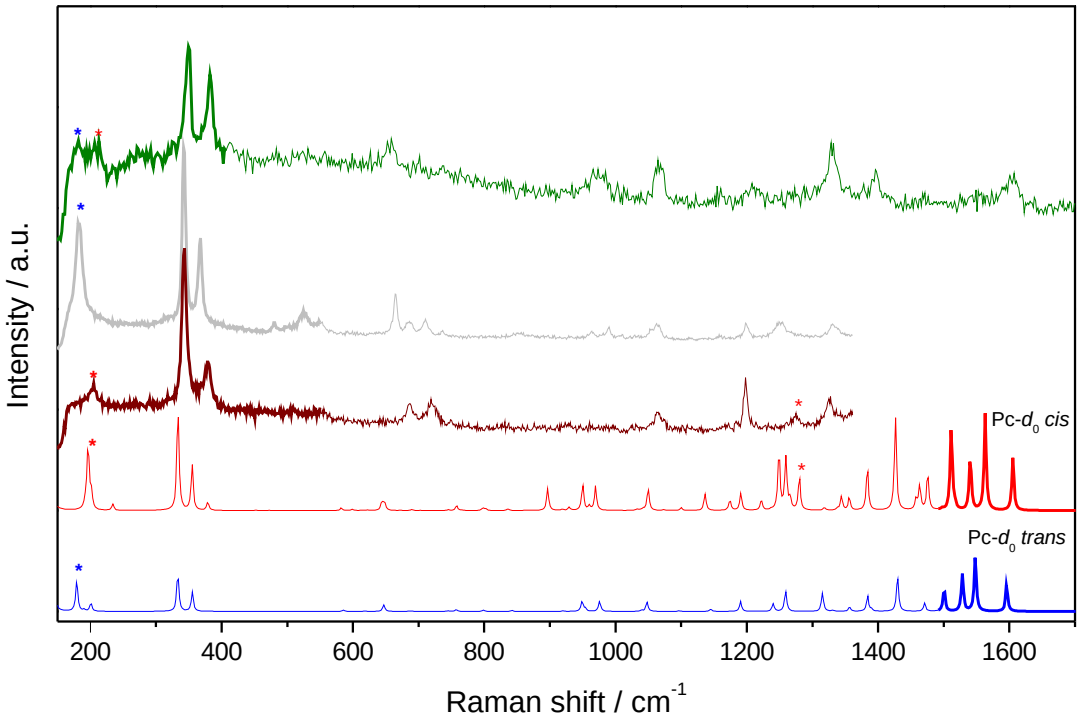

Figure 5.16: SM-SERS spectra of Pc-d_0 from different hot spots, compared with quantum-mechanical predictions for *trans* (blue) and *cis* (red) tautomeric forms (B3LYP/6-31G(d,p), frequencies scaled by 0.96, intensities corrected for 633 nm excitation and 298 K). The asterisks mark the bands that reveal different frequencies in the two isotopologues. SERS substrate: chemically synthesized Au NPs deposited on glass, laser excitation: 632.8 nm, laser power: 50 µW, room temperature.

Given the theoretical predictions of Raman activity for *cis* and *trans* tautomers of Pc-d_0 and Pc-d_{12}, presented in Figures 5.16 and 5.17, respectively, the distinction between these forms is not straightforward. One diagnostic band appears at 180 cm^{-1} in the *trans* tautomers of both isotopologues and shifts to the blue by about 20 cm^{-1} in the *cis* form. However, the frequencies of the other low frequency

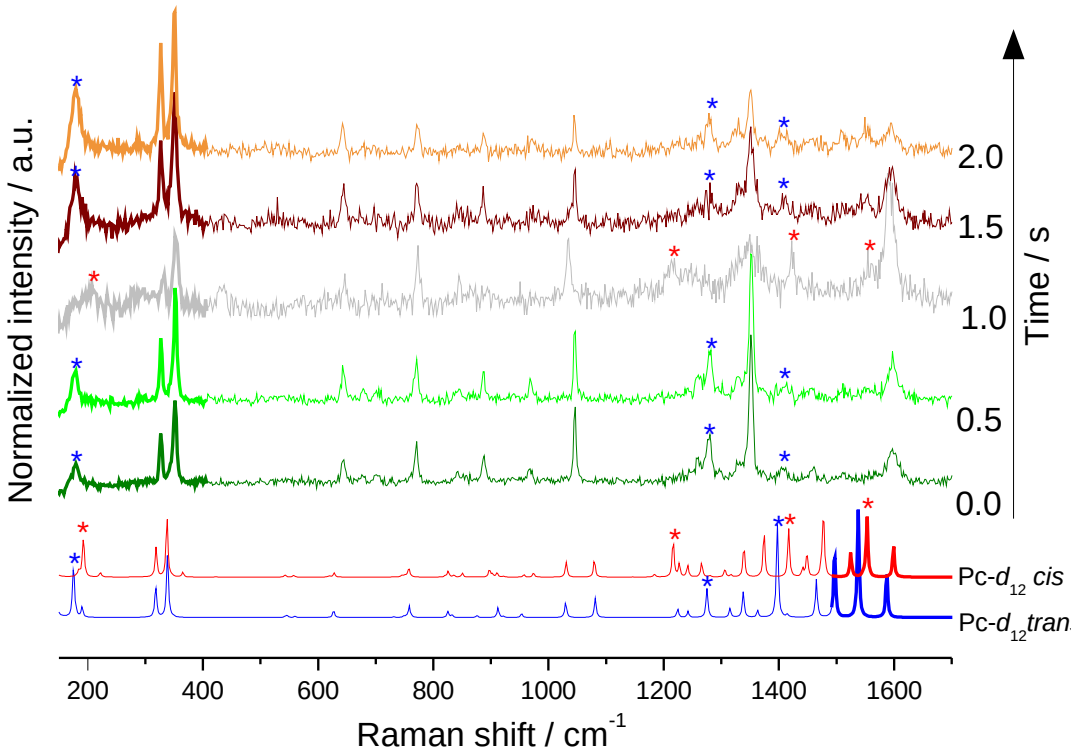

Figure 5.17: Consecutive SM-SERS spectra of Pc-d_{12} from the same sample point, compared with theoretical predictions. SERS substrate: chemically synthesized Au NPs deposited on glass, laser excitation: 632.8 nm, laser power: 50 µW, room temperature.

modes, which are usually the most intense in the single molecule spectra registered at excitation at 633 nm, remain almost unchanged.

Figure 5.17 presents successive spectra of a single Pc-d_{12} molecule. The observed reversible change suggests, in combination with quantum-chemical predictions, that a sequence *trans-cis-trans* tautomerization processes has been observed.

A completely convincing proof of existence of the *cis* structure would be provided by coupling of scanning tunnelling microscopy with Raman measurements, which would be possible using tip-enhanced Raman scattering (TERS).

5.6 Single molecule SERS spectra on different supports

While searching for SERS substrates that would allow us to observe single molecules we have prepared and tested a great variety of SERS substrates: nanostructures obtained by electrochemical methods and prepared from chemically synthesized or laser-ablated nanoparticles. Furthermore, we have used different metals including gold, silver, and copper. Since various criteria, such as reproducibility, uniformity, spectral intensity, stability, purity, etc., may be considered, reliable comparison between SERS substrates is a really challenging task. Despite a great deal of effort put in designing of efficient SERS substrates by many research laboratories, no reliable method for comparing them has been developed so far. Our goal was to prepare a platform with a high density of 'hot' hot spots, which facilitates reaching the single molecule level. Another important parameter was the reproducibility of SERS substrates, but we have not focused on homogeneity and uniformity.

A general conclusion out of long hours spent in the laboratory (including nights and weekends) is that single molecule spectra of porphycene may be registered on various SERS substrates. In the case of gold and silver, we succeeded in recording single molecule spectra from each type of support we investigated (but not from every single sample!), provided that the excitation was at 633 nm. None of the other three laser lines allowed us to obtain such extreme sensitivity. Most of the experiments were performed on solid supports, however we have also observed Pc single molecules on colloids. From each class we selected SERS supports that gave the best results and made semi-quantitative comparison. From among the tested supports the best results were obtained for gold nanorods, which ensured the highest hot spot density and enhancement factors. A considerable number of different nanorods configurations constructing fractal-like nanostructures resulted in broad plasmon bands, which indicates numerous hot spots with their individual plasmon resonances spectrally close to the excitation laser line. Moreover, the substrates based on these gold nanorods provided the best performance for excitation by 785 nm laser line, enabling measurement of SERS spectra for samples prepared from solutions with low Pc concentration (down to 10^{-7}).

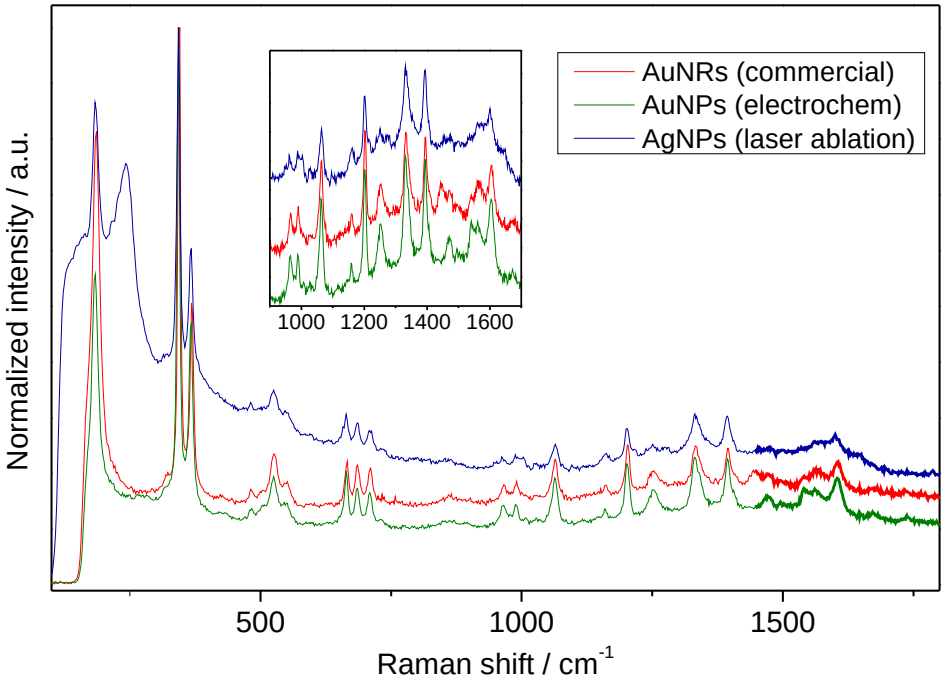

Figure 5.18: The spectra obtained by averaging of 75 single molecule SERS spectra of Pc-d_0 registered on different substrates: commercial 25 µm×47 µm gold nanorods (red), silver nanoparticles obtained by laser ablation (blue) and gold nanoparticles prepared by electrodeposition at a three phase junction (green). Laser excitation: 632.8 nm, laser power: 50 µW, room temperature.

Figure 5.18 presents the spectra obtained by averaging over single molecule SERS spectra of Pc-d_0 registered on different substrates: commercial gold nanorods, gold nanoparticles obtained by electrodeposition at a three phase junction, and silver nanoparticles obtained by laser ablation. Each spectrum was averaged over 75 independent spectra, registered at distinct hot spots. The obtained averaged spectra look very similar and the relative intensities of peaks are virtually the same. It was shown in Figure 5.12 that single molecule spectra are unique and may vary significantly; however, after averaging the results become reproducible. We have also checked whether the normalization of single molecule spectra before averaging makes any difference, and the changes were negligible. The obtained spectra resemble the SERS spectra of porphycene registered at higher concentration, shown for example in Figure 5.6.

The observed subtle differences originate from the background of the used substrates, which are presented in Figure 5.19. The main difference between the spectra registered from different platforms is the strong peak around 240 cm^{-1} in the

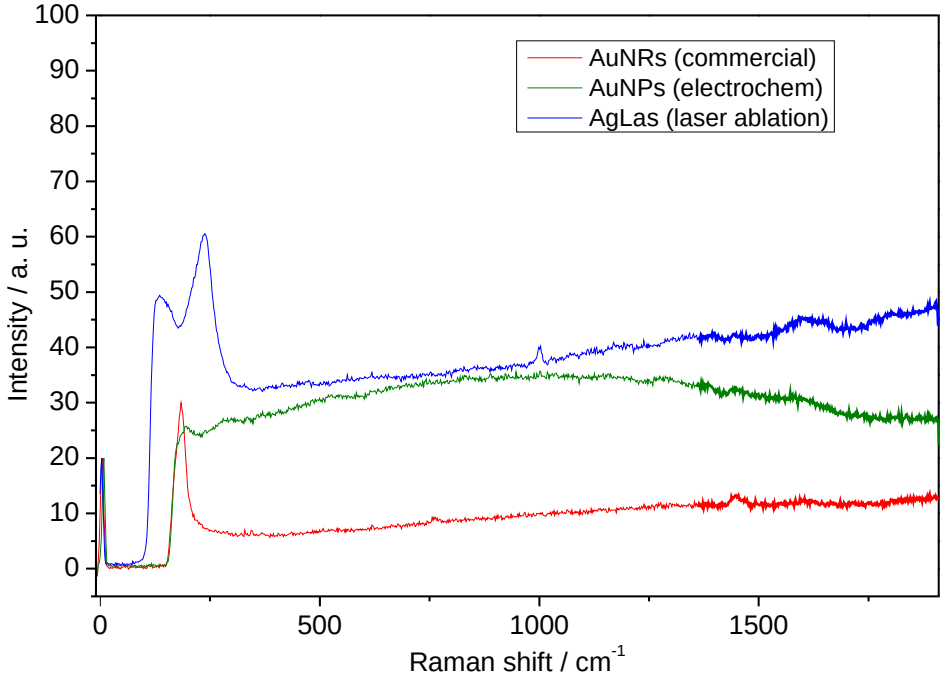

Figure 5.19: The spectra obtained by averaging of 300 SERS spectra of clean substrates: commercial gold nanorods (red), silver nanoparticles obtained by laser ablation (blue) and gold nanoparticles prepared by electrodeposition at a three phase junction (green). Laser excitation: 632.8 nm, laser power: 50 µW, room temperature.

case of substrate prepared using silver nanoparticles. This band originates from the substrate itself, in spite of the fact that nanoparticles obtained by laser ablation are chemically clean (no stabilizer was used). Moreover, the spectra measured from this substrate have a slightly higher background, which means that fluorescence was not that efficiently quenched as for the other tested substrates. The averaged spectra obtained on gold nanoparticles show almost no difference, except for the band at 180 cm^{-1}, of which the intensity is much bigger for commercial nanorods. This is caused by the fact that the substrate prepared using these nanorods has a band at this frequency. Accidentally, this band coincides with a band of porphycene, which increases artificially its intensity.

Unfortunately, we have failed in observing a 'normal' SERS spectrum from porphycene adsorbed on copper nanoparticles. At low concentration, the enhancement was insufficient, while at higher concentrations all Raman features were dominated by the emission background.

5.7 Mobility of molecules on nanostructures

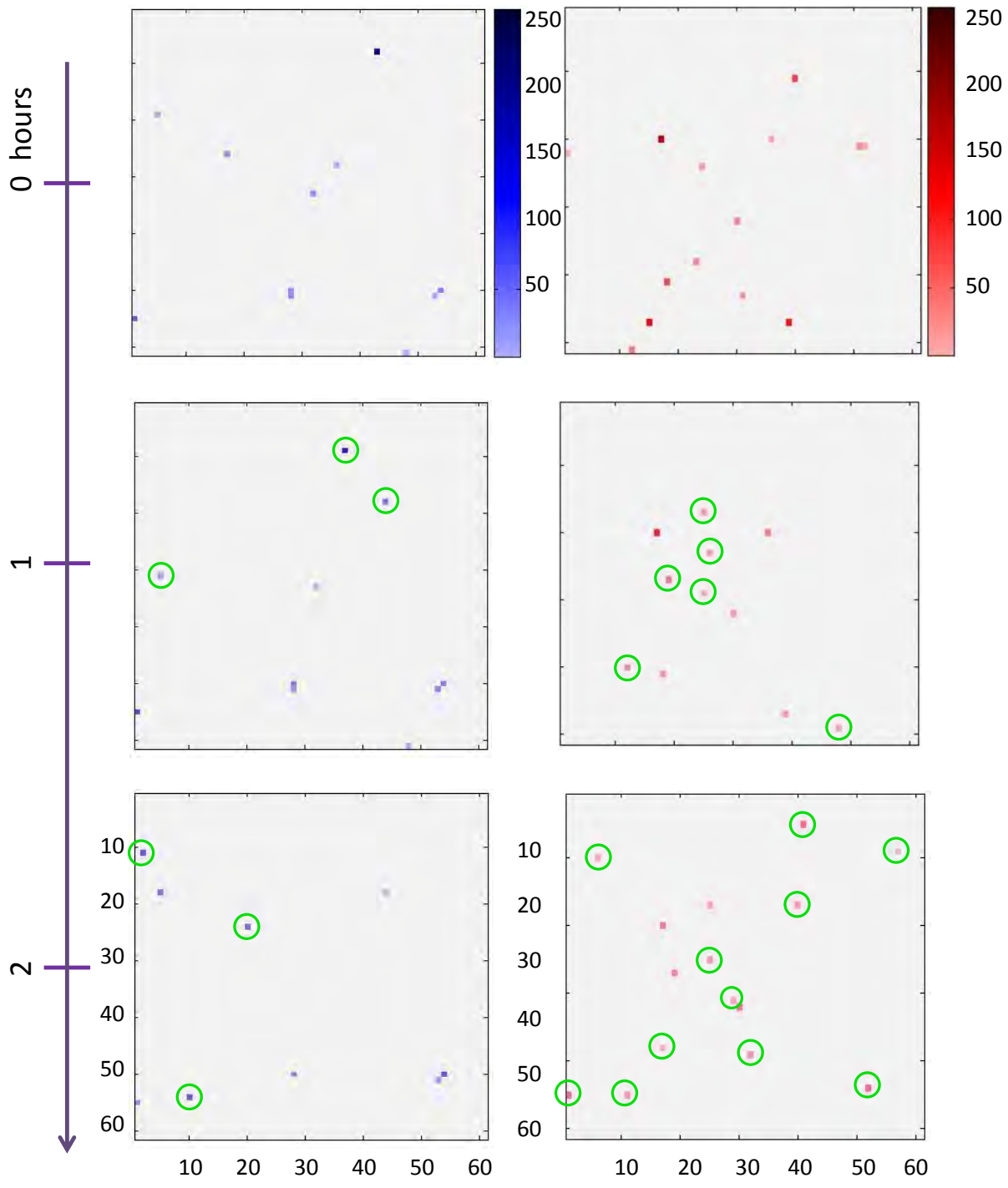

Figure 5.20: Localization of hot spots in three consecutive scans on two different SERS substrates (blue: electrochemicaly prepared substrate, green: silver nanoparticles prepared by laser ablation).

We have observed that molecules, even after evaporation of ethanol, can move on a surface at room temperature. These conclusions were drawn from series of consecutive Raman scans of the same sample area. Exemplary data presented in the Figure 5.20 show that single molecule SERS spectra sometimes occur from sample spots for which in the previous scan no Raman features were observed (marked with green circles). This means that either we have witnessed blinking or a hot spot was occupied only after some time passed. Based on numerous measured time traces of single porphycene molecule, we can conclude that blinking is a fairly rare event in our case. Therefore the observed appearance of a SERS signal after some time suggests that particles diffuse on our SERS supports. Moreover, once a molecule reaches a hot spot, it can remain there for a long time, from seconds to hours. This was observed for both illumination and non-illumination conditions.

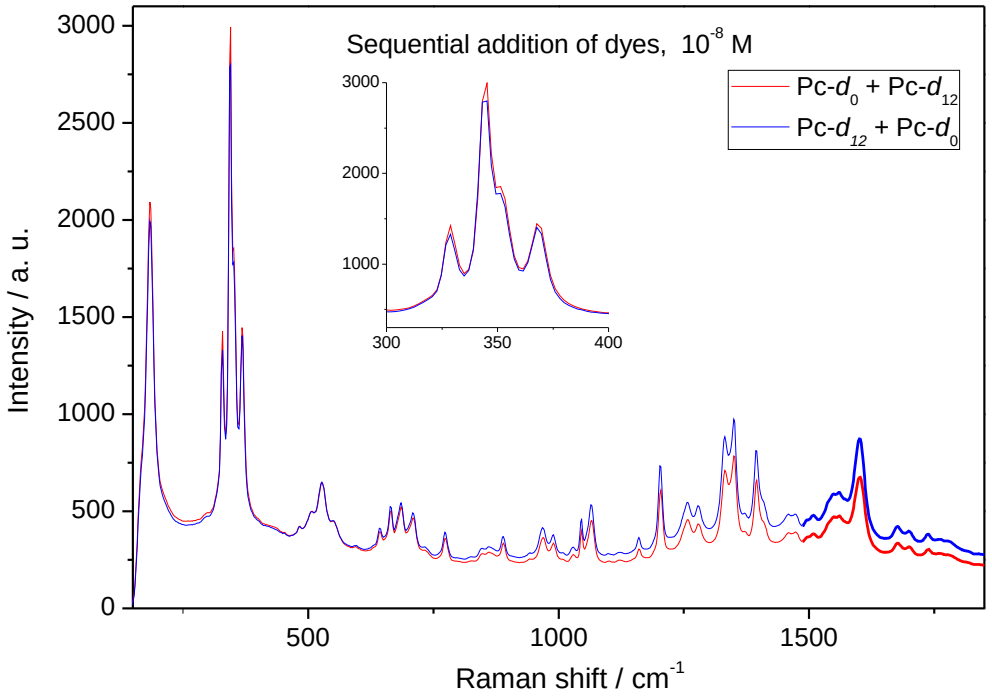

Figure 5.21: The SERS spectra from samples prepared by sequential addition of 10^{-8} M solutions of dyes: first Pc-d_0, then Pc-d_{12} (red) and first Pc-d_{12}, then Pc-d_0 (blue). SERS substrate: 25 µm×47 µm gold NRs, laser excitation: 632.8 nm, laser power: 50 µW, room temperature.

Since there are still many unanswered questions about the nature and strength of forces 'attracting' molecules to hot spots, we performed a relatively simple experiment based on sequential addition of dyes, i.e. a drop of solution containing

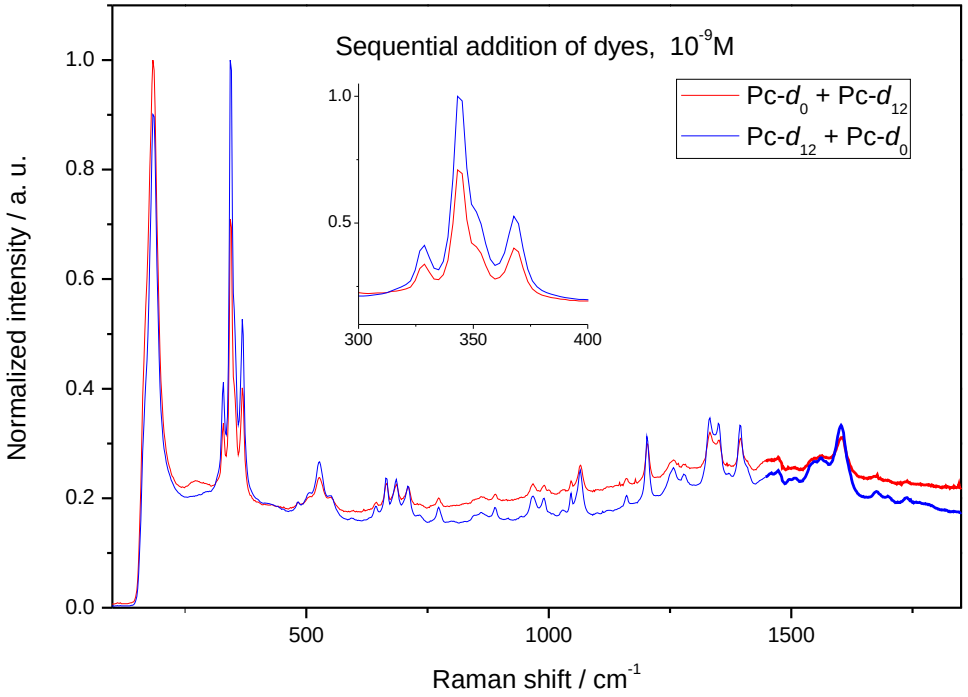

Figure 5.22: The SERS specta from samples prepared by sequential addition of 10^{-9} M solutions of dyes: first Pc-d_0, then Pc-d_{12} (red) and first Pc-d_{12}, then Pc-d_0 (blue). SERS substrate: 25 µm×47 µm gold NRs, laser excitation: 632.8 nm, laser power: 50 µW, room temperature.

only one dye was first put on a SERS substrate, followed by drop casting solution containing exclusively the second dye, after the solvent that contained the first one evaporated. In such a way both sequences were tested: Pc-d_0 followed by Pc-d_{12} and vice versa. The averaged spectra of such experiments performed for two different concentrations (10^{-8} and 10^{-9} M) are presented in Figures 5.21 and 5.22, respectively. We have observed no difference resulting from the order of dye addition. The relative contribution of both isotopologues is independent of the sequence. If molecules populated the hottest hot spots first, relative signal from species placed earlier should be stronger than the signal from species added later. This is not the case. We note, however, that while adding the second chromophore, solvent is added as well, which may displace the molecules from hot spots.

5.8 Calculation of the enhancement factor

The demonstration of ultra-high sensitivity of the SERS technique, reaching a single molecule level, provided a strong stimulus in designing and fabrication of an effective SERS platform. In view of the urgent necessity of introducing a parameter allowing comparison between the produced substrates, the enhancement factor started being commonly determined and it often serves as a measure of the quality of SERS substrates. It is defined as[34]:

$$EF = \frac{I_{\mathrm{SERS}} N_{\mathrm{Raman}}}{I_{\mathrm{Raman}} N_{\mathrm{SERS}}}, \tag{5.2}$$

where I_{SERS} and I_{Raman} are SERS and Raman signal intensities, respectively. These intensities must be normalized by the numbers of molecules contributing to the registered signal: N_{Raman} and N_{SERS}. Moreover, in case of measurements with different laser powers and acquisition times, normalization by factors $P_{\mathrm{Raman}}/P_{\mathrm{SERS}}$ and $t_{\mathrm{Raman}}/t_{\mathrm{SERS}}$, should be applied. For simplicity, let us denote the normalized Raman scattering intensity by I^*_{Raman}:

$$I^*_{\mathrm{Raman}} = H_{\mathrm{Raman}}/(t_{\mathrm{Raman}} P_{\mathrm{Raman}} N_{\mathrm{Raman}}), \tag{5.3}$$

where H_{Raman} is the intensity (counts) of the selected band, t_{Raman} is the acquisition time, P_{Raman} is the applied laser power on the sample, and N_{Raman} is the number of molecules in the microscope focal volume that contribute to the registered signal. Similarly, we can define the normalized intensity of surface-enhanced Raman scattering I^*_{SERS}. Then, the enhancement factor may be expressed as:

$$EF = I^*_{\mathrm{SERS}}/I^*_{\mathrm{Raman}}. \tag{5.4}$$

Despite a simple definition of the enhancement factor, its estimation is a challenging task. A particular difficulty is the determination of the number of molecules adsorbed on a SERS substrate which contribute to the signal. Ideally, there should be a monolayer of probe molecules, which is not always the case. Moreover, due to desirable roughness of a SERS substrate, molecules located in distinct locations experience significantly different enhancements. Furthermore, the results obtained

for different probe molecules may differ substantially. Therefore, in my opinion, we cannot speak of an 'absolute' enhancement factor. Calculations of electromagnetic field distribution, usually performed by finite-difference time-domain method (FDTD) provides the electromagnetic enhancement, however in real systems, the intramolecular features come into play. Therefore, while determining the enhancement factor for a given SERS substrate, the experimental conditions should always be emphasised, i.e., excitation wavelength, probe molecules, and the procedure used for sample preparation. While some substrates may provide high enhancement of SERS signal for some molecules, they may work very poorly for different ones.

We have not determined the enhancement factor for the SERS substrate we used. Our goal was not to prepare a homogeneous platform, but to obtain substrates with many strong hot spots enabling us the observation on a single molecule level. Therefore, we decided to determine the enhancement factor in the hottest hots spots (the ones which allowed us to observe single molecules). With that assumption, we overcame a problem of determining the number of molecules, that contribute to the signal: N_{SERS} is equal to one by definition.

In the case of Pc excited with He-Ne laser, which energy (633 nm) matches the energy of the $S_0 - S_1$ electronic transition, we obtain surface-enhanced resonance Raman scattering (SERRS) spectrum and the observed enhancement origins from two sources:

$$EF_{\mathrm{SERRS}} = EF_{\mathrm{RR}} \cdot EF_{\mathrm{SERS}}, \tag{5.5}$$

where EF_{SERRS} is the total SERRS enhancement factor, EF_{RR} is the enhancement due to resonance Raman effect, and EF_{SERS} stands for the enhancement factor due to SERS effect.

As a reference for Raman signal at non surface-enhanced conditions crystal or solution can be used. The most accurate estimation of the number of molecules in the focal volume is provided for a non-absorbing solution. Unfortunately, the measurement of resonance Raman spectrum of porphycene solution using laser line 633 nm is not possible. This excitation energy is in resonance with 0-0 transition and the fluorescence maximum is in the same spectral region as Raman scattering. Furthermore, the relatively high absorption coefficient of porphycene (50000 $\mathrm{M^{-1}cm^{-1}}$)

combined with significant quantum yield of fluorescence (0.36-0.49, depending on the solvent) results in the resonance Raman spectrum completely overlapped by many orders of magnitude higher fluorescence. It was shown on the examples of Nile blue and rhodamine 6G (R6G), that it is possible to determine the resonance Raman cross section by polarization techniques combined with long accumulation time, even if Raman peaks appear on a strong fluorescence background.[141,142,143] The described method was successfully applied to separate the Raman scattering from emission. In the case of porphycene excited by 633 nm laser line, however, this procedure was unsuccessful. The Raman peaks appear exactly in the region where emission is the strongest, contrary to R6G, where the Raman bands occur on the tail of fluorescence. Even very high number of acquisitions, extending the total time of accumulation to 78 h, was not enough to filter Raman features from the background.

Since we were not able to extract the Raman spectrum of porphycene solution excited by 633 nm laser line, we were left with a crystal as a non surface-enhanced reference.

In order to estimate the enhancements factors related to the resonance Raman effect EF_{RR} and the SERS effect EF_{SERS}, we measured Raman spectra under different conditions:

(a) single molecule SERRS (I^*_{SERRS}, molecule at a hot spot, excited at 633 nm)

(b) 'normal' Raman (I^*_{Raman}, crystalline Pc sample excited at 785 nm);

(c) resonance Raman (I^*_{RR}, crystalline Pc sample excited at 633 nm);

The above-mentioned enhancement factors can be expressed as the ratios between normalized signal intensities I^*:

$$\begin{aligned} EF_{\mathrm{RR}} &= k \cdot (I^*_{\mathrm{RR}}/I^*_{\mathrm{Raman}}) \cdot (\nu^4_{\mathrm{Raman}}/\nu^4_{\mathrm{RR}}), \\ EF_{\mathrm{SERS}} &= I^*_{\mathrm{SERRS}}/I^*_{\mathrm{RR}}, \end{aligned} \tag{5.6}$$

where ν^4_{Raman} refers to the frequency corresponding to 785 nm, ν^4_{RR} is the frequency corresponding to 632.8 nm and k is the experimental relative detection efficiency. The correction concerning differences in detection efficiencies and dependency of

scattering intensity on the wavelength should be included, as the resonance Raman and 'normal' Raman spectra were obtained with different laser lines. The relative detection efficiency denoted as k was experimentally determined in our setup for given laser lines as 1.1. Other effects related to measurements with distinct excitation laser lines, such as change in the refraction index, were neglected. For the determination of EFs, one of the strongest bands was chosen: $3A_g$ at 343 cm^{-1}.

The normalized signal intensity of a single molecule SERRS I^*_{SERRS} (a Pc molecule in a hot spot excited at 633 nm) was calculated according to the formula

$$I^*_{\mathrm{SERRS}} = H_{\mathrm{SERRS}}/(t_{\mathrm{SERRS}} P_{\mathrm{SERRS}} N_{\mathrm{SERRS}}). \tag{5.7}$$

After substitution of the experimental values (the height of the peak at 343 cm^{-1} $H_{\mathrm{SERRS}} = 2500$ counts, $t_{\mathrm{SERRS}} = 1$ s, $P_{\mathrm{SERRS}} = 0.01$ mW and the number of molecules contributing to the signal $N_{\mathrm{SERRS}} = 1$ molecule) we obtained $I^*_{\mathrm{SERRS}} = 2.5 \cdot 10^5$ counts/(s mW molecule).

Similarly, the normalized intensity of "normal" Raman scattering I^*_{Raman} (crystalline Pc sample excited at 785 nm) was determined according to the formula

$$I^*_{\mathrm{Raman}} = H_{\mathrm{Raman}}/(t_{\mathrm{Raman}} P_{\mathrm{Raman}} N_{\mathrm{Raman}}). \tag{5.8}$$

The values of peak height at 343 cm^{-1} H_{Raman}, the acquisition time t_{Raman}, and the power applied on a sample, P_{SERRS}, were directly taken from the Raman scattering measurements, whereas the number of molecules contributing to the signal N_{SERRS} was determined separately. In order to estimate this value, the effective focal volume of the used objective should be assessed. Often, the focal volume is assumed to be diffraction-limited, but this is rarely the case in experiments. Therefore we decided to determine it experimentally. One way of obtaining the effective focal volume is the proposed cutting-edge knife method[80,144] performed on a silicon wafer. This approach, however, assumes that the exciting and detecting foci are the same. We decided to determine the effective focal volume by performing lateral mapping and depth scanning of fluorescent nanospheres with a step of 100 nm. Based on these measurements we obtained the focal volume $V_{\mathrm{Raman}} = 9.2\,\mu\mathrm{m}^3$ for the 100× air objective used in the microscope.

The number of molecules that contribute to the registered signal N_{Raman} may be estimated according to the equation

$$N_{\mathrm{Raman}} = RV_{\mathrm{Raman}}, \tag{5.9}$$

where R stands for packing density in the crystal (taken from crystallographic data, for porphycene $R = 6.5 \cdot 10^8$ molecules/μm^3) and V_{Raman} is the effective focal volume. Upon substitution of the experimental values: $H_{\mathrm{Raman}} = 3500$ counts, $t_{\mathrm{Raman}} = 25$ s, P_{SERRS} =10 mW, and $N_{\mathrm{Raman}} = 6.5 \cdot 10^8$ molecules/μm$^3 \cdot 9.2\,\mu$m^3 = $6.0 \cdot 10^9$ molecules we obtained $I^*_{\mathrm{Raman}} = 2.3 \cdot 10^{-9}$ counts/(s mW molecule).

Finally, the intensity of resonance Raman scattering is described by the expression:

$$I^*_{\mathrm{RR}} = H_{\mathrm{RR}}/(t_{\mathrm{RR}} P_{\mathrm{RR}} N_{\mathrm{RR}}). \tag{5.10}$$

Again, the experimental values of the registered Raman intensity of the 3Ag band H_{RR}, the acquisition time t_{RR}, and the applied laser power on a sample P_{RR} can be taken directly from the experiment. This time however, while determining the number of molecules that contribute to the signal N_{RR} we should take into account that due to absorption of Pc at 633 nm only some fraction of light reaches the molecules located in deeper layers. As a result, the effective focal volume is smaller, which can be expressed by the formula:

$$V_{\mathrm{RR}} = bV_{\mathrm{Raman}}, \tag{5.11}$$

where b is the coefficient related to the depth of penetration of light into the crystal and V_{Raman} is the effective focal volume in the absence of absorption process. Assuming the absorption coefficient of the same value as for solution, we estimated b as 0.08. The determination of the number of molecules contributing to the signal may be done based on the equation

$$N_{\mathrm{RR}} = RV_{\mathrm{RR}} = RbV_{\mathrm{Raman}}, \tag{5.12}$$

where R is the packing density in the crystal (taken from crystallographic data). Upon substitution of values $R = 6.5 \cdot 10^8$ molecule/μm^3, $V_{\mathrm{Raman}} = 9.2\,\mu$m^3 and $b = 0.08$ we obtained $N_{\mathrm{RR}} = 4.8 \cdot 10^8$ molecules. The obtained experimental values

$H_{RR} = 173$ counts, $t_{RR} = 1$ s, $P_{RR} = 1$ mW, and $N_{RR} = 4.8 \cdot 10^8$ molecules resulted in $I^*_{RR} = 3.6 \cdot 10^{-7}$ counts/(s mW molecule).

Having determined the normalized intensities I^*_{SERRS}, I^*_{Raman} and I^*_{RR}, we can estimate the enhancement factors according to the equation 5.6: $EF_{RR} = 7.3 \cdot 10^2$, $EF_{SERS} = 6.9 \cdot 10^{10}$. Therefore, the total enhancement is equal to $EF_{SERRS} = 5.0 \cdot 10^{13}$.

The value of the enhancement factor originating exclusively from electromagnetic mechanism $EF_{SERS} \approx 10^{11}$ was obtained for the most intense single-molecule event, i.e., the "hottest" hot spot. Such a high value was observed only for a few single molecules of porphycene and is in a perfect agreement with the highest observed EF for non-resonant molecules: adenine, 1,2-di-(4-pyridyl)-ethylene and its benzotriazole derivative excited at 633 nm.[63] The same order of magnitude (10^{11}) of the maximum enhancement factor achievable through the presence of plasmonic nanostructures is predicted by calculations of electromagnetic field distribution.[55] Xu *et. al.* conclude that the reported enhancement factors exceeding this value, reaching $10^{14} - 10^{15}$, most likely involve additional enhancement mechanisms: chemical enhancement and resonance Raman effect. This is the case for porphycene, for which total enhancement factor EF_{SERRS} reaches $5.0 \cdot 10^{13}$. The contribution from resonance effect was estimated for $EF_{RR} \approx 10^3$. This value, however, is a lower limit, since it was determined by comparison of the intensities of the $3A_g$ mode (at 343 cm^{-1}) measured using two different laser lines: 633 nm (resonance Raman) and 785 nm. The latter wavelength corresponds, in fact, to pre-resonance conditions. Significant contribution of the enhancement related to the resonance Raman effect might explain why only for excitation at 633 nm single molecules of porphycene were observed.

5.9 Comparison of porphycene and Nile blue

We have also decided to compare porphycene to chromophores which were already observed on a single molecule level. Among the most extensively investigated chromophores, Nile blue was chosen as a molecule which is also resonantly excited at 633 nm. Its single molecule spectra were widely reported.[20,21,14,11] Figure 5.23

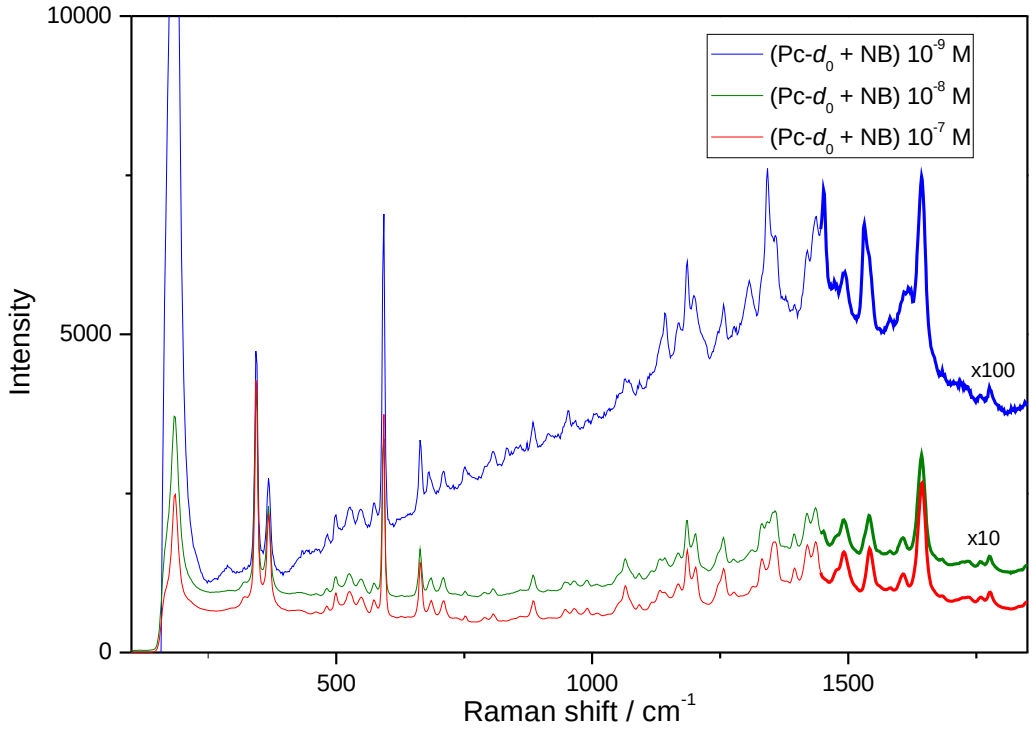

Figure 5.23: The SERS spectra from samples prepared by drop-casting of a 1:1 mixtures of porphycene-d_0 and Nile blue. SERS substrate: 25 µm×47 µm gold NRs, laser excitation: 632.8 nm, laser power: 50 µW, room temperature.

presents the averaged SERS spectra obtained from samples prepared by drop-casting a 1:1 mixture of porphycene and Nile blue on a substrate. The strongest band of Nile blue is at 590 cm^{-1}. Three different concentrations were tested, and to make the comparison easier, the spectra obtained from 10^{-8} M and 10^{-9} M mixtures were multiplied by 10 and 100, respectively. There is almost no difference between the spectra measured at samples prepared from 10^{-7} M and 10^{-8} M solutions, whereas lower concentrations resulted in a higher background. Most likely it originates from luminescence of the SERS substrate. At such a low concentration only small fraction of the recorded spectra contained features of porphycene or Nile blue, whereas all of them contained luminescence from nanoparticles. Even if it is very weak, after averaging over the whole map, it becomes clearly visible. Moreover, in the averaged spectra the relative height of peaks originating from Nile blue and porphycene changes upon decreasing their concentration, keeping equal amount of both species. Interestingly, the Raman scattering intensity scaled relatively well with changing concentration, a trait particularly noticeable for bands at 343 and 363 cm^{-1}.

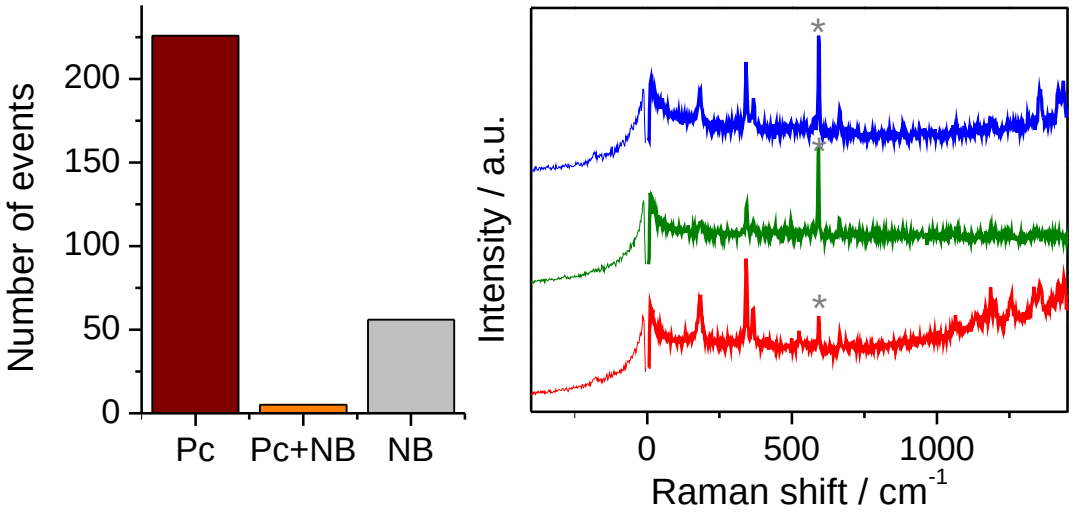

Figure 5.24: Left: histogram presenting 'single-chromophore' vs 'mixed-chromophore' events obtained for 1:1 mixture of Pc-d_0 and Nile blue of 10^{-8} M concentration. Right: selected spectra measured at different hot spots showing both chromophores. The asterisk indicates the most intense vibration of Nile blue at 590 cm^{-1}. SERS substrate: Au nanoparticles obtained by electrodeposition at a three phase junction, laser excitation: 632.8 nm, laser power: 50 µW, room temperature.

Figure 5.24 presents the results obtained by the bi-analyte method performed for a 1:1 mixture of porphycene and Nile blue (of the concentration of 10^{-8}M) in a form of histogram of 'single-chromophore' vs 'both-chromophore' events. Very low number of mixed events confirms the single molecule regime and may be considered as an independent proof for reaching a single molecule level in the case of porphycene. Surprisingly, the number of observed single molecules of Pc is significantly higher than for Nile blue. Such discrepancy may originate from a variety of factors, such as different surface affinities or enhancement factors. On the other hand, contribution of Nile blue to the averaged spectra shown in Figure 5.23 is significant. It would be worth to investigate this effect further, however we used Nile blue only as a reference and have not yet continued this topic. The spectra presented in Figure 5.24 show 'both-chromophores' events, where the relative intensity of porphycene and Nile blue varies considerably. The strongest mode of Nile blue at 592 cm^{-1} is indicated by an asterisk. The intensities of this band of Nile blue and a band of Pc at 343 cm^{-1} allowed us to estimate the relative enhancement factor between these dyes. Comparison of intensities of these peaks recorded with a 633 nm laser line under the same conditions (averaged over single

molecule spectra) with the intensities of the same bands measured with 785 nm laser line in acetone solution provided us with the relative enhancement factor about 30 times stronger for porphycene. Obviously, in these calculations differences in absorption coefficients and used concentrations were taken into account. However, the obtained value may be slightly overestimated, due to the differences in the onsets of the electronic absorption. In the case of Nile blue the absorption starts at 700 nm, while for porphycene, around 640 nm. Therefore, while 'exciting' by 785 nm laser line, intensities of the Raman bands of Nile blue benefit more from the pre-resonance effect. More accurate determination of relative enhancement factor would require measurements at longer wavelengths, for instance 1064 nm.

5.10 Low temperature SM-SERS spectra of porphycene

Low temperature measurements often reveal features unattainable at higher temperatures and help to better understand studied systems. For instance, in the case of tautomeric equilibrium the change in temperature may result in different percentage abundance, which may often help with assignment of spectral features to particular tautomers. The change in temperature may also affect photochemical parameters, such as fluorescence quantum yield. Typically, lowering of temperature results in rigidification of the environment (surrounding solvent molecules) and hampering non-radiative processes. As a result, fluorescence quantum yield increases. In high hopes for getting more knowledge about porphycene and its interaction with nanoparticles, we decided to perform measurements at different temperatures, ranging from liquid nitrogen temperature to about 150°C. With our chamber we could even reach 400°C, but at such temperature the morphology of SERS substrate would change.

The spectra presented in Fig. 5.25 were obtained at different temperatures: room temperature and -150°C (123 K). The inset presents the narrowing of the bands upon lowering the temperature: the full width at half maximum (FWHM) changes from 6.0 cm^{-1} to 4.5 cm^{-1}. As a consequence, closely lying bands might be better

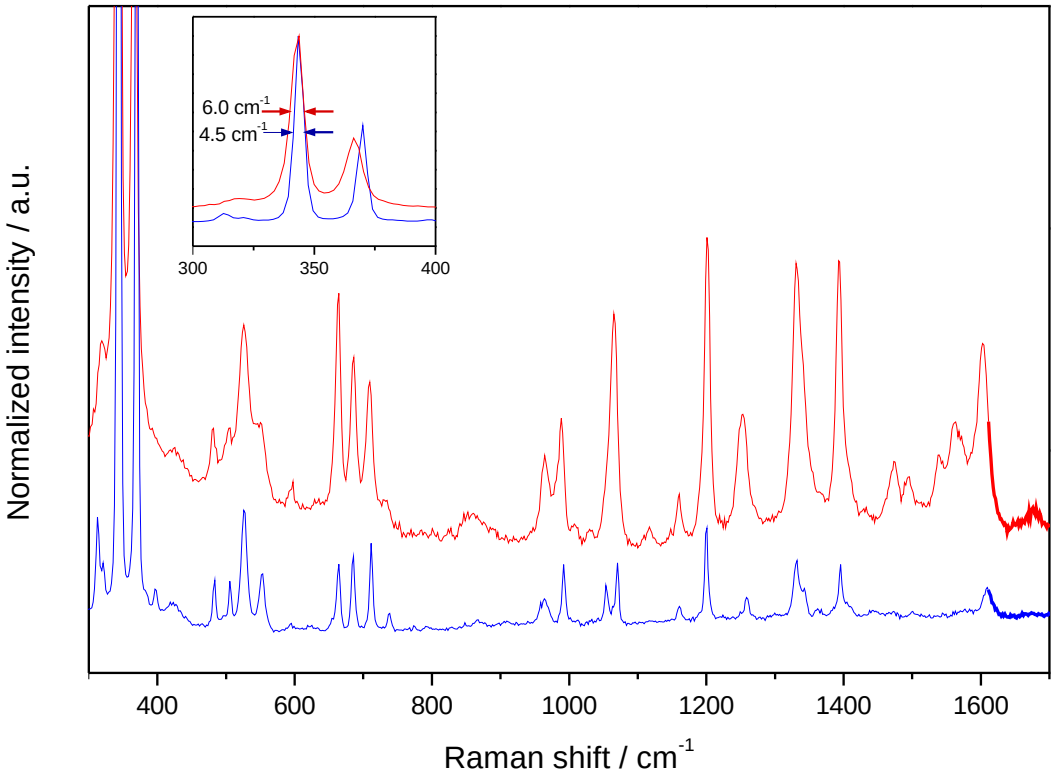

Figure 5.25: Spectra from two hot spots, averaged over 500 s, measured at different temperatures: 123 K (bottom, blue) and 293 K (top, red). SERS substrate: chemically synthesized Au NPs, laser excitation: 632.8 nm, laser power: 50 µW.

resolved. This is advantageous, for instance, in the region of combination bands and overtones, between 500 and 800 cm^{-1}. Moreover, in the case of low temperature measurements the background is significantly lower. Furthermore, the obtained spectra reveal marked differences, which are especially prominent in the region between 1400 and 1700 cm^{-1}. Their occurrence may be justified by the fact that not all molecular orientations are equally present in hot spots, at least at low temperature. Despite the really long time of averaging (500 s), the spectra look different. It seems that molecules cannot move freely inside a hot spot, which is manifested by the increased contribution of particular orientations to the averaged spectrum. In the next chapter we will investigate this phenomenon further by comparing spectra obtained by averaging over different time windows the time evolution of porphycene from the same hot spots.

Another advantage of low temperature measurements is the higher photostability of molecules in hot spots. Figure 5.26 presents the comparison of length of time traces (before bleaching) measured at two temperatures: 103 K (-170 ℃) and 293

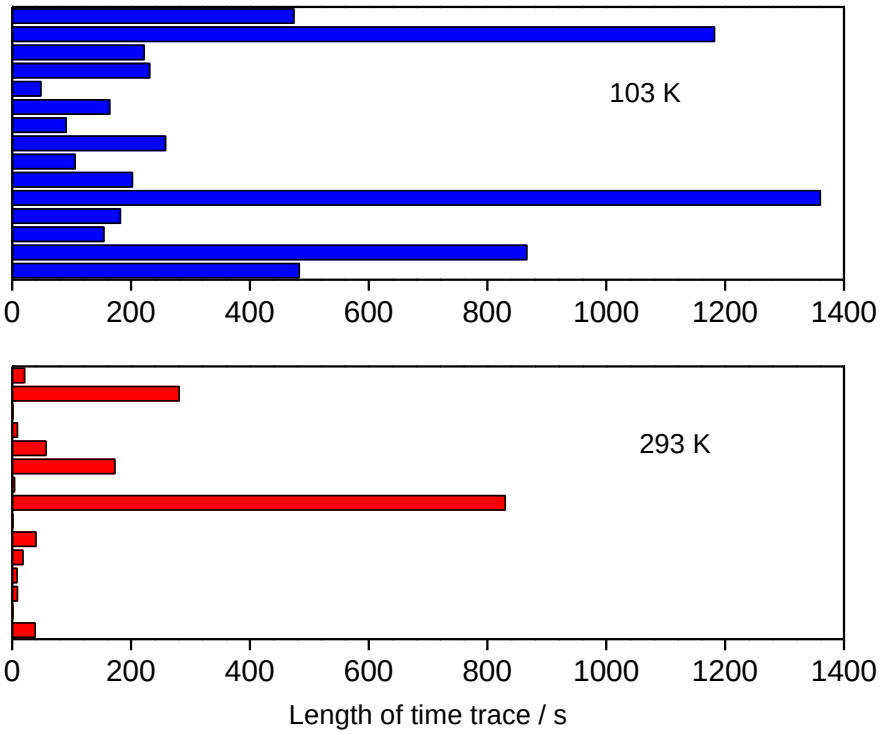

Figure 5.26: Length of time traces before bleaching. Spectra measured at different temperatures: 103 K (top, blue) and 293 K (bottom, red). SERS substrate: electrochemically synthesized Au NPs, laser excitation: 632.8 nm, laser power: 50 µW.

K (20 ℃). Both collections contain 15 independent time traces. This graph clearly illustrates the increased photostability at lower temperature. The average time before bleaching is 99.5 s at 293 K, and 401.5 s at 103 K. The reason for such discrepancy may be a different distance to the metal. At higher temperature, a molecule located in a hot spot may easier escape from it due to higher energy.

5.11 Conclusions

The data gathered and presented in this chapter, including SERS intensity fluctuations, one-step bleaching, and histograms of 'one-chromophore' vs 'two-chromophore' events for a mixture of two isotopologues confirm that in the case of porphycene single molecule level is reachable. When molecules are adsorbed on the investigated gold and silver nanostructures, the *trans* tautomer dominates, but we have also witnessed the existence of the *cis* form. Moreover, some time traces revealed

reversible tautomerization reaction: *trans-cis-trans*. The observation of such exotic species and behaviour was possible only thanks to single molecule sensitivity. On the other hand, the SERS spectra of Pc obtained at different tested substrates, after background substraction, are virtually the same. Nanoparticles efficiently quench fluorescence background, enabling observation of the SERS spectrum. In the absence of nanoparticles the measurement of Raman spectrum is much more difficult, and under some conditions even impossible. So far, out of four tested laser lines, only 633 nm allowed us to observe single molecule spectra. We suspect that the key lies in additional enhancement due to resonance with electronic transition, which we estimated as $EF_{RR} = 7.3 \cdot 10^2$. The total enhancement was estimated as $EF_{SERRS} = 5.0 \cdot 10^{13}$. Measuring the SERS excitation profile would be very helpful in gaining a better understanding of this phenomenon.

We have obtained rather unexpected results using the bi-analyte approach while further decreasing the concentration of the investigated species. The observed imbalance in the number of registered Pc-d_0 and Pc-d_{12} events, despite their equal concentration in the studied mixture may be caused by differences in diffusion coefficients. This demonstrates that quantitative analysis at such low concentrations is impossible, even for chemically very similar compounds, like isotopologues. Indeed, the histograms obtained for very low concentration wrongly suggest higher concentration of one of the isotopologues. The complete understanding of this phenomenon, however, requires further studies.

The uniqueness of single molecule spectra originates from their sensitivity to both the environment (a hot spot) and to the orientation of the molecule inside. The kind of metal and structure of a hot spot influences its surface plasmon energy, which directly affects the enhancement profile. When it shifts, the relative intensities of Raman modes vary considerably. This applies especially to bands which are relatively far from each other. In contrast, large relative intensity fluctuations of bands lying closely may be rationalized by changes in molecular orientation.

The change in temperature has an impact on SERS spectra. In particular, lowering of temperature results in narrowing of the Raman bands, which provides better spectral resolution. Another considerable advantage is the reduction of fluorescence

background and the substantial enhancement of photostability, which allows for longer time acquisition and accumulation of longer time traces.

Chapter 6

Investigation of correlations between different vibrational modes in porphycene

Undoubtedly, single molecule spectra contain a wealth of information, which is often not directly accessible. Only the use of statistical methods, which are designed to study the relationships between data sets (or a data set and simulated data based on a proposed model) allows for extraction of dependencies of interest. In this chapter we examine correlations between intensities of different Raman-active modes based on the measured single molecule spectra. Such dependencies may be acquired on the basis of intensity fluctuations, which are characteristic for single molecule signals. As the electromagnetic field in a plasmonic hot spot is highly anisotropic, the SERS spectra are very sensitive to both the position of a molecule and its orientation. One of the sources of the observed fluctuations might be thermal motions: due to extremely high electromagnetic field gradients even slight movement can cause significant change in the SERS signal intensities. Moreover, as each normal mode has its own Raman scattering tensor, molecular rotation affects differently intensities of various vibrations.

Potentially, the measured relative intensities of Raman modes combined with the exact knowledge of their Raman tensors allows us to infer the approximate orientation of a molecule in a hot spot. Furthermore, the time evolution of SM-SERS

spectra can provide information about dynamics of a molecule situated in a hot spot.

In this chapter, we present a method that allows us to study the linear dependence between intensities of vibrations for two kinds of data sets: a collection of spectra obtained from different hot spots (naturally, originating from different molecules) and measured time traces (typically, each describing behaviour of one specific molecule). In our case we will focus on porphycene, however due to versatility of this method, it can be successfully applied to any molecule. By means of such analysis we were able to amend the now recognized assignment of modes.[32]

6.1 Raman tensor and its graphical representation

Each normal mode k has its own Raman tensor, $R_k(\omega_{Inc})$ defined as

$$R(\omega_{Inc}) = \left(\frac{\partial\alpha(\omega_{Inc})}{\partial Q_k}\right)_{Q_k=0}, \tag{6.1}$$

where Q_k is the normal coordinate and $\alpha(\omega_{Inc})$ is the optical polarizability. It describes the change in polarizability resulting from displacement of atoms according to the molecular vibrational pattern of a given normal mode k.

A convenient way of graphical representation of a diagonalizable tensor is an ellipsoid. An ellipsoid with the principal axes coincident with the axes of a Cartesian coordinate system and its centre at the $(0, 0, 0)$ point is described by the equation[33]

$$\frac{x^2}{a^2} + \frac{y^2}{b^2} + \frac{z^2}{c^2} = 1. \tag{6.2}$$

The line segments between the origin of the coordinate system and the points $(a, 0, 0), (0, b, 0)$ and $(0, 0, c)$ lying on the surface are called *semi-principal axes*, since a, b, c are half the length of the principal axes.

One of the examples of a diagonalizable tensor is a polarizability tensor $\boldsymbol{\alpha}$ defined as[33]

$$\boldsymbol{\alpha} = \begin{vmatrix} \alpha_{xx} & \alpha_{xy} & \alpha_{xz} \\ \alpha_{yx} & \alpha_{yy} & \alpha_{yz} \\ \alpha_{zx} & \alpha_{zy} & \alpha_{zz} \end{vmatrix}. \tag{6.3}$$

In the case of molecules the polarizability tensors are always diagonalizable, as they are symmetric,[145] e.g., $\alpha_{xy} = \alpha_{yx}$, $\alpha_{xz} = \alpha_{zx}$ and $\alpha_{yz} = \alpha_{zy}$. Therefore, each polarizability tensor may be graphically represented by a polarizability ellipsoid given by the equation[33]

$$\alpha_{xx}x^2 + \alpha_{yy}y^2 + \alpha_{zz}z^2 + 2\alpha_{xy}xy + 2\alpha_{yz}yz + 2\alpha_{zx}zx = 1. \tag{6.4}$$

The center of such defined polarizability ellipsoid is at the origin of the coordinate system, while its principal axes may not be coincident with the axes of the coordinate system. However, the coordinate system may be transformed in such a way that the new axes denoted as X, Y, Z coincide with the principal axes of the polarizability ellipsoid. The polarizability tensor defined with respect to these new axes has a much simpler diagonal form in which $\alpha_{XY} = \alpha_{YZ} = \alpha_{XZ} = 0$:

$$\boldsymbol{\alpha'} = \begin{vmatrix} \alpha_{XX} & 0 & 0 \\ 0 & \alpha_{YY} & 0 \\ 0 & 0 & \alpha_{ZZ} \end{vmatrix}. \tag{6.5}$$

Then, the equation of the polarizability ellipsoid simplifies to

$$\alpha_{XX}X^2 + \alpha_{YY}Y^2 + \alpha_{ZZ}Z^2 = 1. \tag{6.6}$$

The semi-axes of such defined ellipsoid have the length of $\alpha_{XX}^{-1/2}$, $\alpha_{YY}^{-1/2}$ and $\alpha_{ZZ}^{-1/2}$. At first such definition of polarizability ellipsoid may seem counterintuitive, since a long semi-axis corresponds to low polarizability, and vice versa. Indeed, the physical meaning of such defined polarizability ellipsoid does not directly reflect the ability of changing the charge distribution by any external electric field in a given direction, but the energy required to polarize the crystal in various directions. The lower the polarizability, the higher the required energy. Such defined polarizability ellipsoid can be experimentally obtained by applying different electric fields.

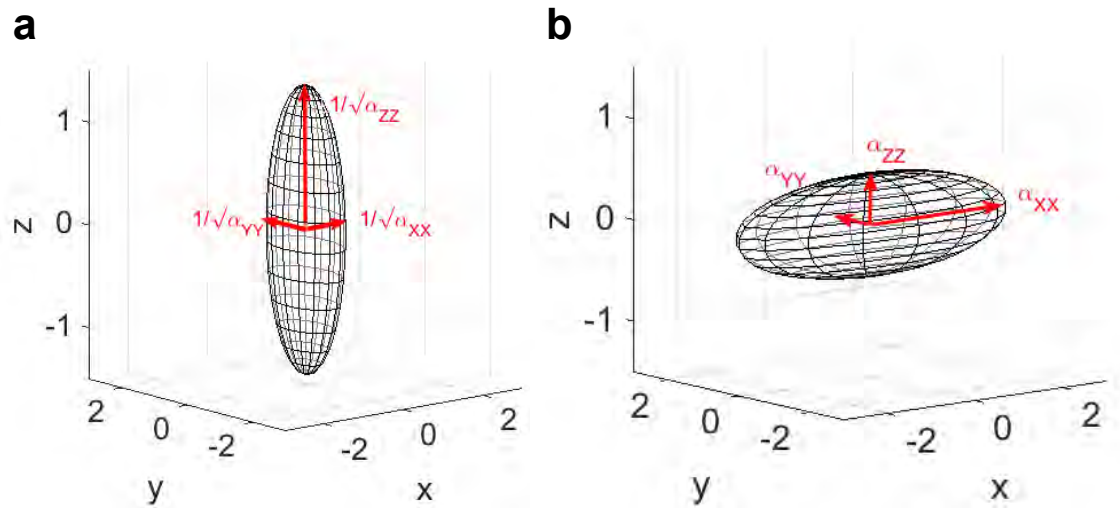

Figure 6.1: The comparison between two definitions of polarizability ellipsoid: (a) with semi-axes equal to $\alpha_{XX}^{-1/2}, \alpha_{YY}^{-1/2}$, and $\alpha_{ZZ}^{-1/2}$; (b) with semi-axes equal to α_{XX}, α_{YY}, and α_{ZZ}. In the presented example $\alpha_{XX} = 3, \alpha_{YY} = 1, \alpha_{ZZ} = 0.5$.

In this thesis, however, we will stick to the definition of polarizability ellipsoid used by Kęcki,[146] where the semi-axes have the length of α_{XX}, α_{YY} and α_{ZZ} instead of $\alpha_{XX}^{-1/2}$, $\alpha_{YY}^{-1/2}$ and $\alpha_{ZZ}^{-1/2}$. Figure 6.1 presents the comparison between these two ways of defining the polarizability ellipsoid. In our opinion, the latter definition is more intuitive, as longer semi-axes correspond to higher polarizability along a specified direction.

The new coordinate system $\{XYZ\}$, in which the polarizability tensor $\boldsymbol{\alpha}$ has a diagonal form may be found via matrix diagonalization, i.e. the procedure of constructing a matrix P, so that

$$\boldsymbol{\alpha} = PDP^{-1}, \tag{6.7}$$

where D is a diagonal matrix. Matrix diagonalization is equivalent to finding eigenvectors and corresponding eigenvalues of $\boldsymbol{\alpha}$. These eigenvectors create a new coordinate system, in which $\boldsymbol{\alpha}$ assumes a diagonal form. The corresponding eigenvalues are equal to the elements on the diagonal, while the eigenvectors construct matrix P, which defines a change of basis set and is called the *transition matrix*. To be precise, let us consider a vector space V of dimension n and its two distinct

sets of basis vectors

$$B_1 = \{\mathbf{v_1}, \mathbf{v_2}, \ldots, \mathbf{v_n}\}, \quad B_2 = \{\mathbf{u_1}, \mathbf{u_2}, \ldots, \mathbf{u_n}\}. \tag{6.8}$$

The vectors of basis B_2 can be expressed as linear combinations of vectors of basis B_1:

$$\begin{aligned} \mathbf{u_1} &= p_{11}\mathbf{v_1} + p_{21}\mathbf{v_2} + \ldots + p_{n1}\mathbf{v_n}, \\ &\cdots \\ \mathbf{u_n} &= p_{1n}\mathbf{v_1} + p_{2n}\mathbf{v_2} + \ldots + p_{nn}\mathbf{v_n}. \end{aligned} \tag{6.9}$$

The matrix P defined as

$$P = \begin{bmatrix} p_{11} & p_{12} & \cdots & p_{1n} \\ p_{21} & p_{22} & \cdots & p_{2n} \\ \vdots & \vdots & \ddots & \vdots \\ p_{n1} & p_{n2} & \cdots & p_{nn} \end{bmatrix} \tag{6.10}$$

is called the *transition matrix* (from base B_1 to B_2) and its columns contain coordinates of the new basis B_2 expressed in basis B_1. The transition matrix from base B_2 to B_1 is equal to P^{-1}.

If the coordinates of a given vector $\mathbf{q}$ in a basis B_1 are equal to $q_1, q_2, \ldots, q_n$, its coordinates in a basis B_2 are given by the equation

$$\begin{bmatrix} q_1^{'} \\ q_2^{'} \\ \vdots \\ q_n^{'} \end{bmatrix} = P^{-1} \begin{bmatrix} q_1 \\ q_2 \\ \vdots \\ q_3 \end{bmatrix}. \tag{6.11}$$

In our case B_1 is the standard basis, i.e. the set of unit vectors pointing in the direction of the axes of a Cartesian coordinate system: $B_1 = \{(1,0,0), (0,1,0), (0,0,1)\}$, and B_2 is a basis set in which the tensor has a diagonal form. The polarizability ellipsoid can be drawn in a few steps. First, diagonalization of the tensor $\boldsymbol{\alpha}$ defines a new coordinate system $\{XYZ\}$, in which $\boldsymbol{\alpha}$ takes a diagonal form. Next,

using the equation of the ellipsoid the points belonging to $\boldsymbol{\alpha}$ can be calculated: $E^{'} = \{(x_1^{'}, y_1^{'}, z_1^{'}), \ldots, (x_n^{'}, y_n^{'}, z_n^{'})\}$ Finally, the points corresponding to $E^{'}$, but in a Cartesian coordinate system should be drawn. Their coordinates (x_i, y_i, z_i) can be obtained according to the equation

$$\begin{bmatrix} x_i \\ y_i \\ z_i \end{bmatrix} = P \begin{bmatrix} x_i^{'} \\ y_i^{'} \\ z_i^{'} \end{bmatrix} . \tag{6.12}$$

To better visualize the whole procedure, let us consider an example where

$$\boldsymbol{\alpha} = \begin{bmatrix} 1 & 0 & 2 \\ 1 & -2 & 0 \\ 1 & 0 & 1 \end{bmatrix} . \tag{6.13}$$

This matrix can be represented as a product of matrices according to an equation $\boldsymbol{\alpha} = QDQ^{-1}$:

$$\boldsymbol{\alpha} = \begin{bmatrix} 0 & 0.8029 & -0.7259 \\ 1 & 0.1819 & -0.4578 \\ 0 & 0.5677 & 0.5133 \end{bmatrix} \cdot \begin{bmatrix} -2.0000 & 0 & 0 \\ 0 & 2.4142 & 0 \\ 0 & 0 & -0.4142 \end{bmatrix} \cdot \begin{bmatrix} -0.4286 & 1.0000 & 0.2857 \\ 0.6228 & 0 & 0.8807 \\ -0.6888 & 0 & 0.9741 \end{bmatrix} .$$

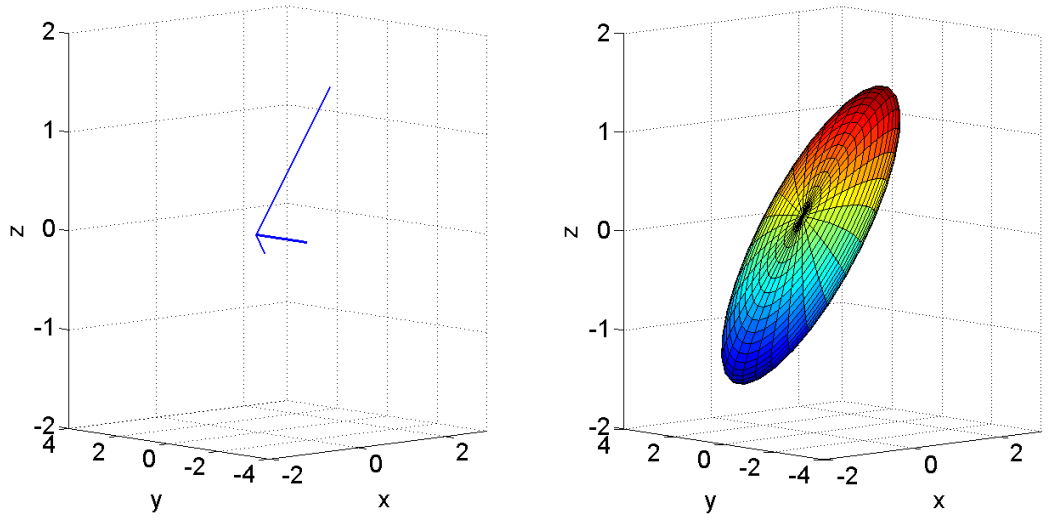

Figure 6.2: The unit vectors $\mathbf{u_1}, \mathbf{u_2}$ and $\mathbf{u_3}$ of a new coordinate system, in which tensor $\boldsymbol{\alpha}$ has a diagonal form and its visualisation.

The axes of a new coordinate system, where $\boldsymbol{\alpha}$ has a diagonal form are stored as columns in matrix Q: Figure 6.2 presents these axes and the polarizability ellipsoid obtained for the given tensor $\boldsymbol{\alpha}$. These vectors are orthogonal, as evidenced by scalar products of each pair equal to zero. In a such defined coordinate system the polarizability tensor is represented by a diagonal matrix $D = \{d_{mn}\}$. Therefore, the semi-axes of polarizability ellipsoid are equal to $d_{11} \cdot \mathbf{u_1}, d_{22} \cdot \mathbf{u_2}, d_{33} \cdot \mathbf{u_3}$, where $\mathbf{u_1}, \mathbf{u_2}$ and $\mathbf{u_3}$ are the unit vectors of a new coordinate system. The points (x', y', z') belonging to this polarizability ellipsoid can be calculated according to the equation:

$$\frac{x'^2}{d_{11}^2} + \frac{y'^2}{d_{22}^2} + \frac{z'^2}{d_{33}^2} = 1. \tag{6.14}$$

Finally, it should be taken into account that the coordinates (x', y', z') refer to a coordinate system defined via vectors $\mathbf{u_1}, \mathbf{u_2}, \mathbf{u_3}$. The coordinates (x, y, z) of these points in the standard Cartesian coordinate system may be calculated according to the equation

$$\begin{bmatrix} x \\ y \\ z \end{bmatrix} = Q \begin{bmatrix} x' \\ y' \\ z' \end{bmatrix}. \tag{6.15}$$

When considering Raman scattering, instead of the polarizability tensor, which is directly related to Rayleigh scattering, the Raman tensor should be considered. Let us call this graphical representation *Raman ellipsoid* or *polarizability derivative ellipsoid*. The length of an axis along a given direction corresponds directly to the change in polarizability during normal mode k, and therefore, to its Raman scattering intensity. All Raman tensors were plotted using the above-described procedure, proposed for graphical representation of the polarizability tensor $\boldsymbol{\alpha}$.

6.2 Vibrational modes of porphycene

As already mentioned, directional properties of Raman tensors for different modes are very important in the analysis of single molecule SERS studies. Indeed, the

electromagnetic field in a hot spot is highly uniaxial, which is predicted by finite-difference time-domain (FDTD) calculations. For instance, in the case of the smallest aggregate, i.e. a dimer, the enhancement of the electric field is along the direction of the axis between nanoparticles. Therefore, the analysis of Raman tensors for porphycene vibrations may help us to understand the observed positive and negative correlations between the intensities of Raman bands.

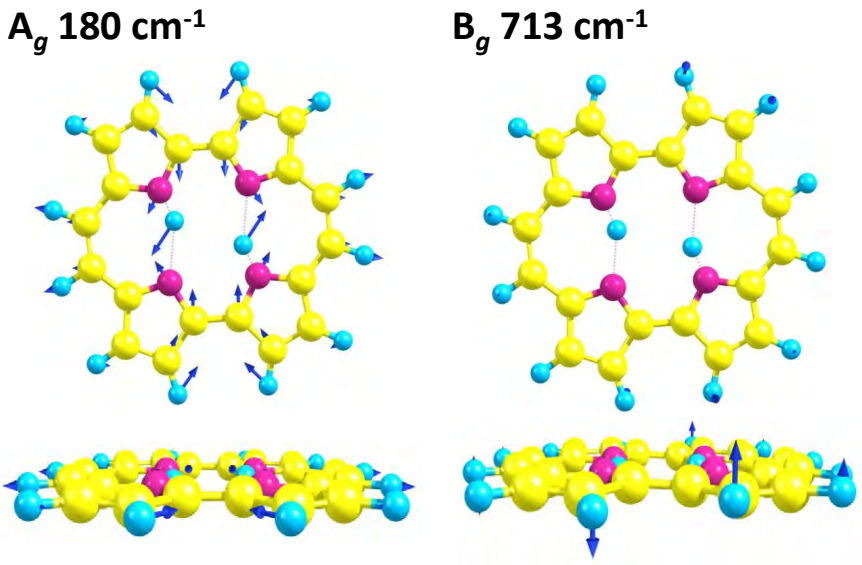

Figure 6.3: Displacement vectors of the two selected Raman active modes of porphycene obtained using DFT at the B3LYP/6-31G(d,p) level.

The *trans* tautomer of porphycene belongs to the C_{2h} point group. As it possesses a centre of symmetry, the rule of mutual exclusion applies. Both A_u and B_u modes are IR-active, contrary to in-plane A_g modes and out-of-plane B_g modes, which are Raman-active. Figure 6.3 presents examples of such modes.

Each vibrational mode has its own Raman tensor, and in order to fully understand the SERS spectra, their directional properties should be taken into consideration. In fact, the exact knowledge of the Raman tensor is required to predict Raman scattering intensities along specified directions. Only in the case of an isotropic Raman tensor, which is represented by the sphere-shaped ellipsoid the scattering intensity is independent of the direction. The shape of the Raman tensor for a given mode is strongly associated with the form of atomic displacement vectors. In the case of porphycene, vast majority of tensors are two-dimensional, i.e., their sizes in the third dimension are much smaller compared to the other two dimensions.

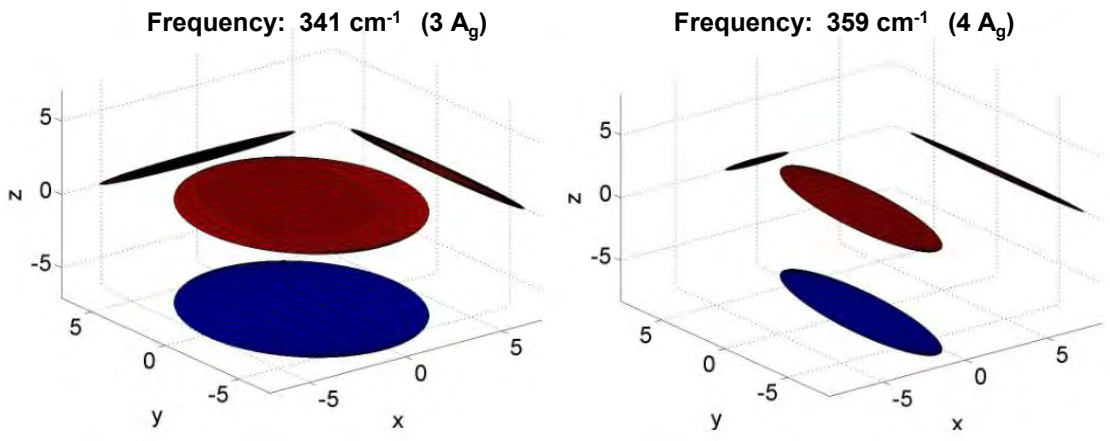

Figure 6.4: The tensors predicted for selected A_g modes of porphycene by DFT at the BP86/DZP level for non-resonant excitation.

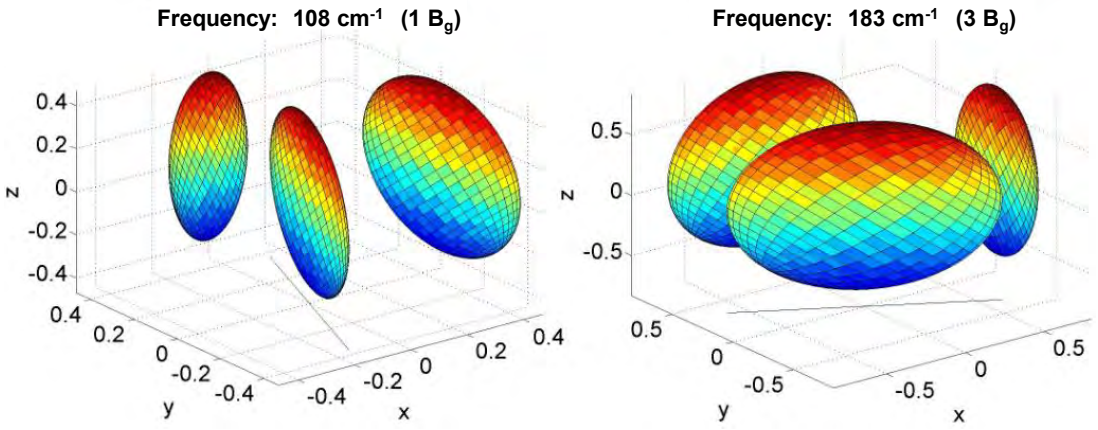

Figure 6.5: The tensors predicted for selected B_g modes of porphycene by DFT at the BP86/DZP level for non-resonant excitation.

Therefore they resemble differently oriented ellipses. Tensors corresponding to A_g modes are located in the molecular plane (xy), with a negligible z component. Tensors for B_g modes, however, are orthogonal to them, which results in substantial z component. The examples of Raman tensors describing A_g and B_g modes are presented in Figures 6.4 and 6.5, respectively. In order to better visualize them, the projections onto the xy, yz and xz planes were shown additionally. The colors used in these plots refer to the z direction.

The Raman tensors, their size and orientation, are very sensitive to the excitation wavelength. As our intention was to compare the simulations with the experimental spectra measured for resonance conditions, the quantum chemical calculations of

resonance Raman spectra had to be performed as well. These calculations were performed by prof. Jacek Waluk.

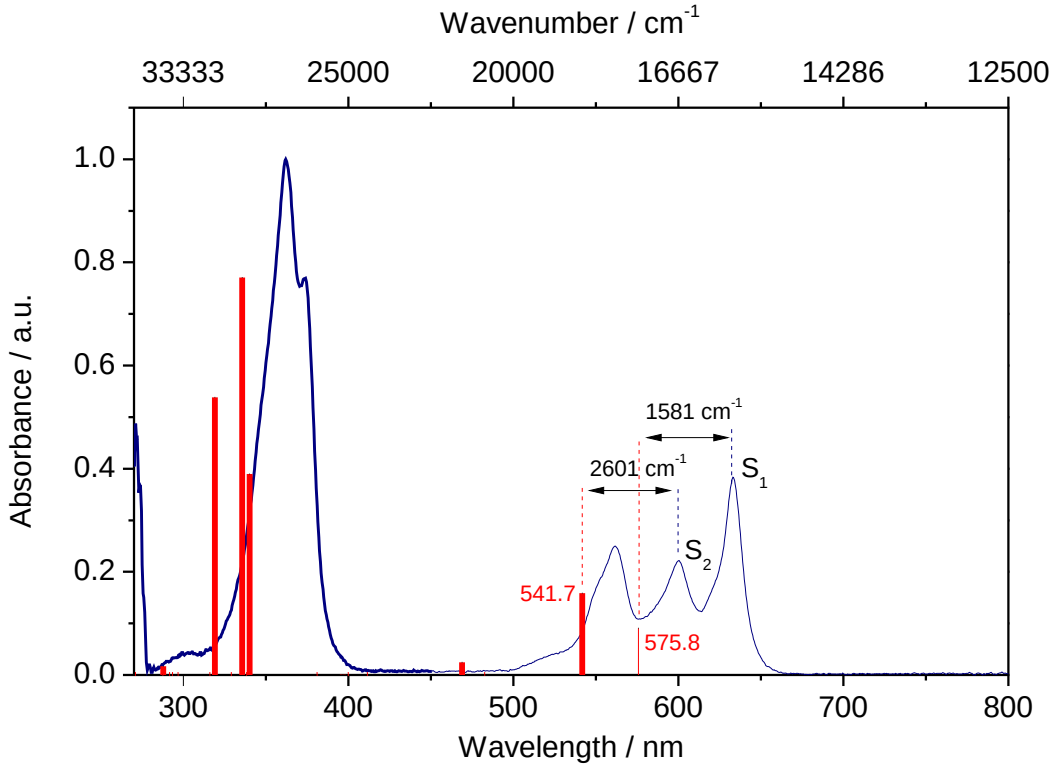

Figure 6.6: The absorption spectrum of porphycene measured in acetone and predicted by time-dependent density functional theory (TDDFT), BP86/DZP.

First, to determine the theoretically predicted energies of the electronic transtions, time-dependent calculations were performed. Figure 6.6 presents the measured and simulated electronic spectra of porphycene. According to the quantum chemical calculations the S_0-S_1 transition occurs at 17367 cm^{-1} (575.8 nm), while the S_0-S_2 transition at 18460 cm^{-1} (541.7 nm). These values are blue-shifted compared to the experimentally obtained energies equal to 16012 cm^{-1} and 16894 cm^{-1},[98] respectively, which is shown in Figure 6.6. Consequently, the resonance Raman calculations were performed for excitation energies corresponding to theoretically predicted values: 575.8 nm and 541.7 nm. Although the energies of the electronic transitions have not been predicted accurately, the calculated energy difference between S_0-S_1 and S_0-S_2 transitions equal to 1093 cm^{-1} is consistent with the experimental value (882 cm^{-1}). The electronic transition moments related to these transitions are indicated by arrows in Figure 6.7

Figure 6.7: Directions of S_0-S_1 and S_0-S_2 electronic transition moments predicted for porphycene (adapted from[123]).

Figures 6.8 and 6.9 illustrate on examples of three arbitrarily selected fundamental A_g modes ($3A_g$, $7A_g$, and $10A_g$) how strongly the Raman tensors depend on the excitation wavelength. As in-plane-modes are oriented in the molecular plane (xy), for simplicity their projections onto this plane were shown. The Raman tensors for all of the active modes are gathered in the supplementary materials attached in the electronic form (`http://github.com/gitmajka/phd`). In the presented figures, below the schemes of displacement vectors, their Raman tensors obtained for non-resonance conditions are shown. To clarify, as a non-resonance calculations we refer to simulations taking into account exclusively the ground electronic state of a molecule. Whereas all calculations considering the influence of the excited electronic states are denoted as pre-resonance or resonance, depending on the excitation energy. Unfortunately, no strict rule is applicable for the prediction of the shape of the Raman tensor. Nevertheless, it seems that often its orientation is to some extent related to atoms involved in a given vibration, i.e., the tensor is often oriented along atoms exhibiting large displacement from the equilibrium position. On the right, Raman tensors for different excitation energies are plotted. Since resonance Raman process involves absorption, the related tensors are composed of real and imaginary parts, which are shown separately (figures are marked in the upper right corners). Figure 6.8 contains tensors predicted for excitation at 785 nm and 633 nm, both corresponding to a pre-resonance Raman. Figure 6.9, on the other hand, presents tensors calculated for resonance Raman with excitation at 576 nm and 542 nm, which correspond to the S_0-S_1 and S_0-S_2 transitions, respectively.

In the case of pre-resonance Raman, the real and imaginary tensors resemble

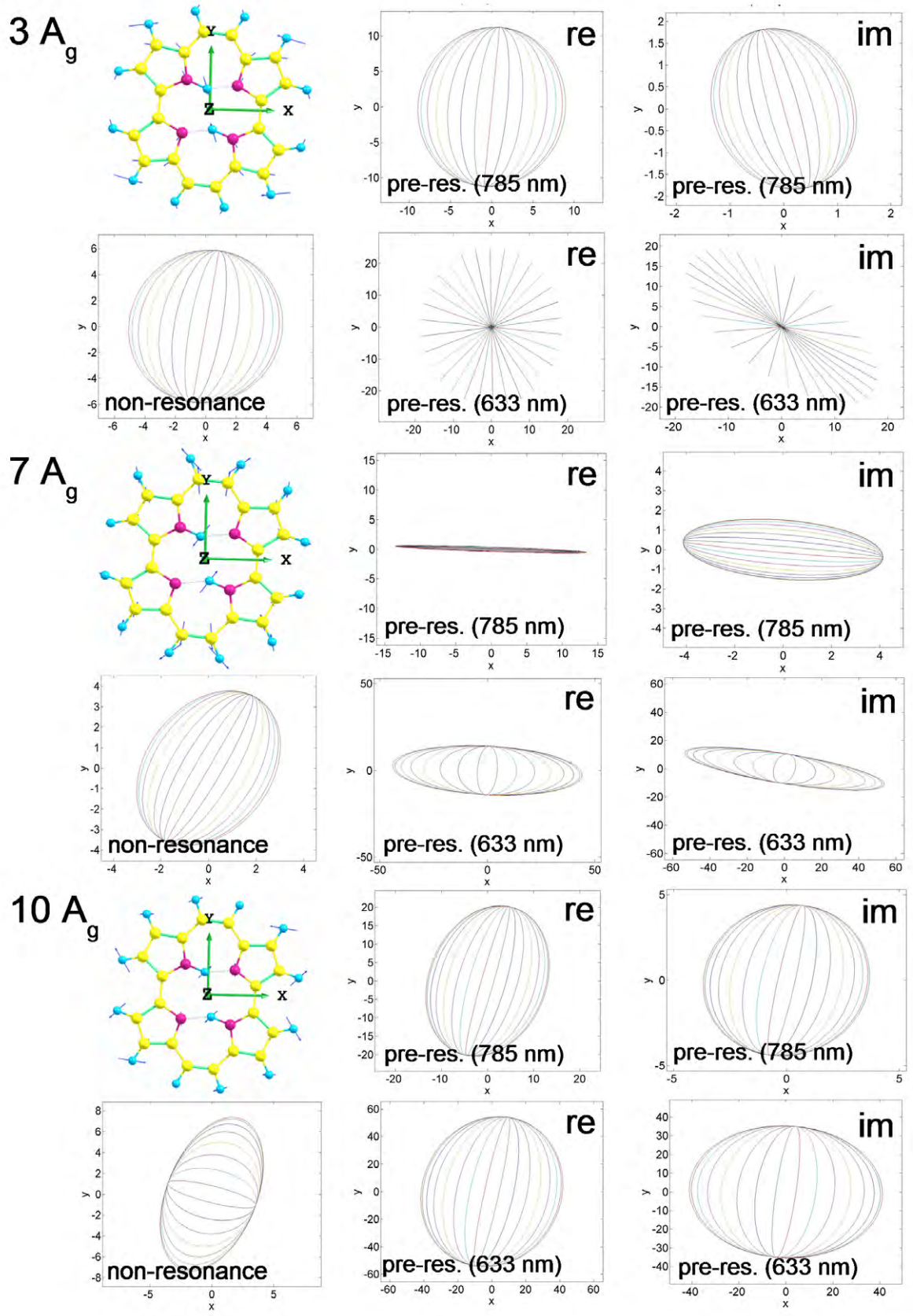

Figure 6.8: The displacement vectors and xy projections of Raman tensors obtained for non-resonance conditions (no imaginary part) and pre-resonance conditions with excitation wavelengths equal to 785 nm and 633 nm, respectively (BP86/DZP) for three selected modes.

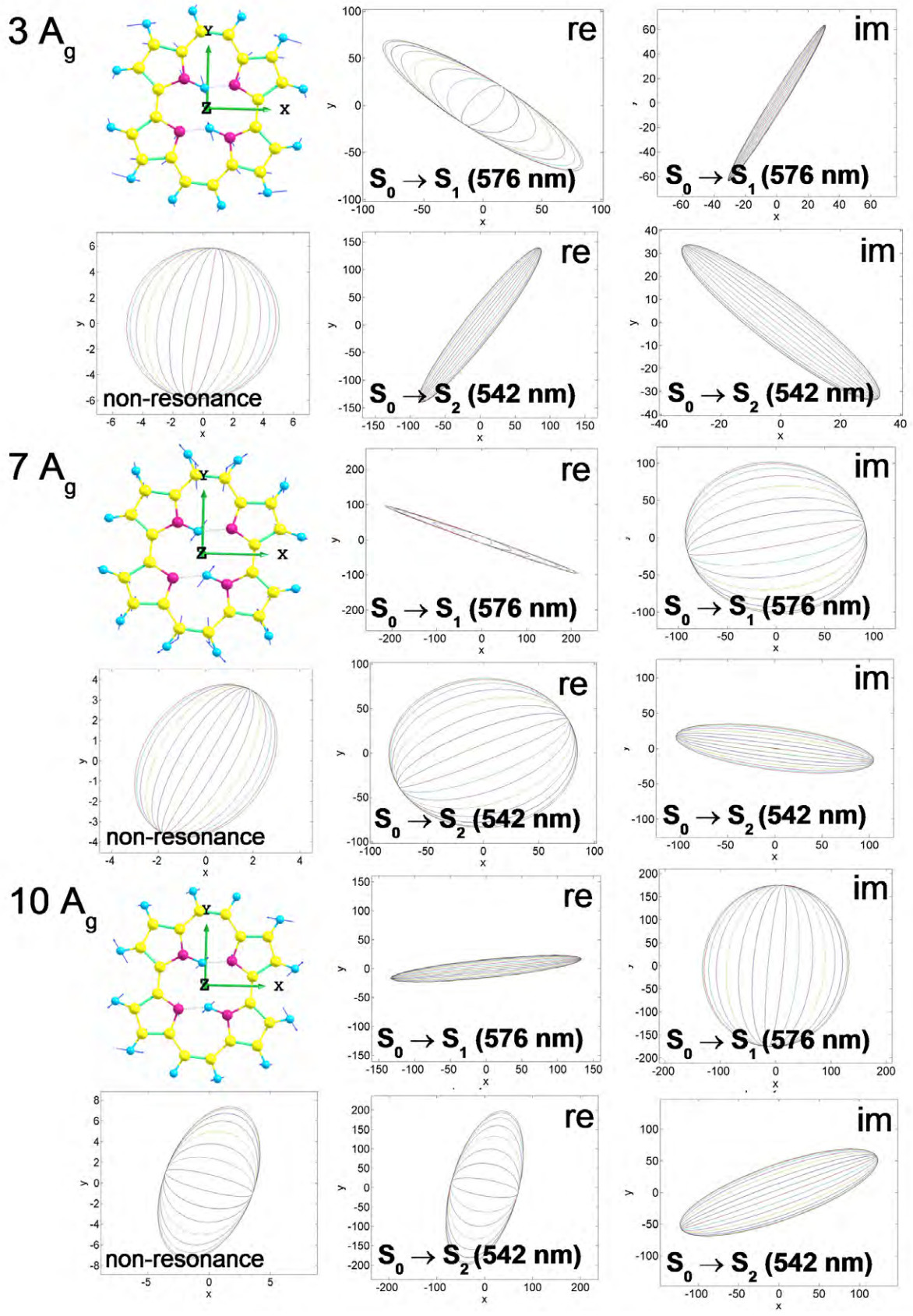

Figure 6.9: The displacement vectors and xy projections of Raman tensors obtained for non-resonance conditions (no imaginary part) and excitation wavelengths corresponding to the energy of S_0-S_1 and S_0-S_2 transitions, respectively (BP86/DZP) for three selected modes.

each other, being very similar to the tensors obtained for non-resonance conditions, which are composed exclusively from real parts. The closer to resonance, the contribution of the imaginary part becomes more substantial. While at 785 nm typically the imaginary part is a few times lower than the real one, at 633 nm, which corresponds to the experimental value of about 700 nm, the contributions from both real and imaginary parts are comparable.

The situation changes when the excitation wavelength matches the energy of an electronic transition. In general, the predicted tensors become more directional compared to those obtained for non-resonance and pre-resonance conditions. Moreover, most of the real tensors are oriented along the related transition moment. Interestingly, this does not apply to the imaginary part, which is quite often differently oriented. At the studied excitation energies, the contributions from both real and imaginary parts are comparable. The presented variety of shapes and orientations of Raman tensors may account for large fluctuations of bands intensities.

6.2.1 Simulations of resonance Raman spectra

The analysis of Raman tensors is based on quantum-mechanical predictions of resonance Raman intensities. Their reliability can be roughly assessed by comparison of the predicted spectra with the experimental data. Fig. 6.10 shows such a set for an excitation energy corresponding to the S_0-S_1 transition (633 nm for the experimental spectra and 576 nm for DFT calculations). While the Raman shifts of modes are reproduced relatively well, their relative intensities, especially for strongly distant bands do not coincide with experimental values. Contrary to the calculations, the intensities of low-frequency modes prevail over those of high-frequency modes. Nevertheless, the relative intensities of neighbouring bands are predicted quite correctly. In the case of excitation corresponding to the energy of the S_0-S_2 transition the agreement is significantly better, which is illustrated in Figure 6.11.

Figure 6.12 presents the predicted intensities upon changing the excitation wavelength. It it clearly visible that some modes are very sensitive to the resonant conditions.

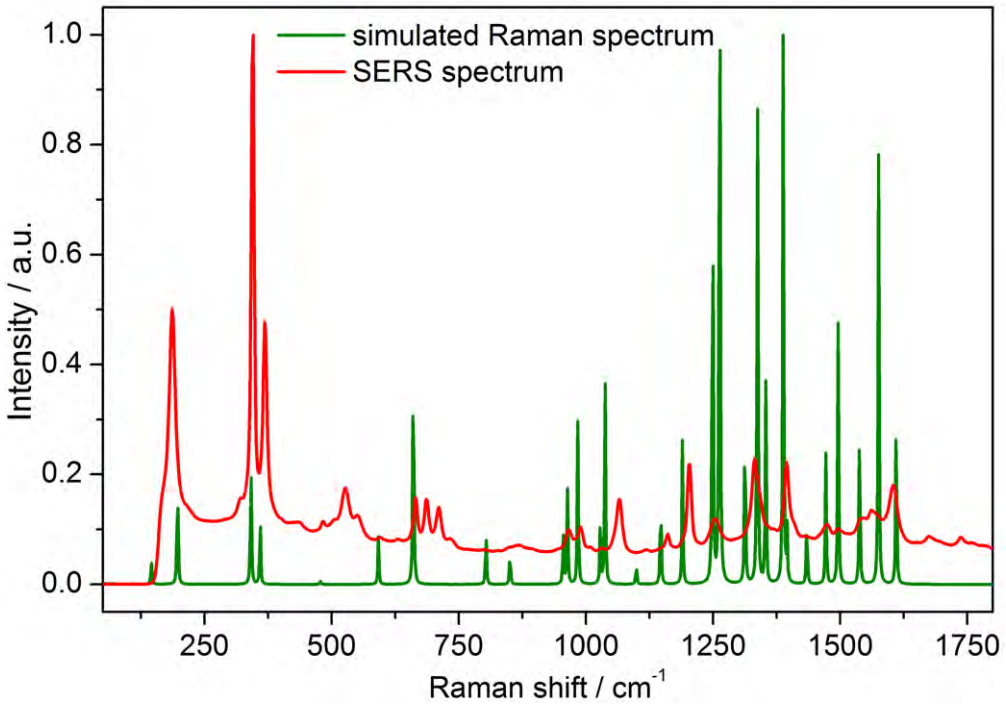

Figure 6.10: The simulated resonance Raman spectrum obtained for excitation wavelength corresponding to the energy of S_0-S_1 transition (BP86/DZP) and the corresponding experimental SERS spectrum. SERS substrate: 25 µm×47 µm gold NRs, laser excitation: 632.8 nm, laser power: 50 µW, room temperature.

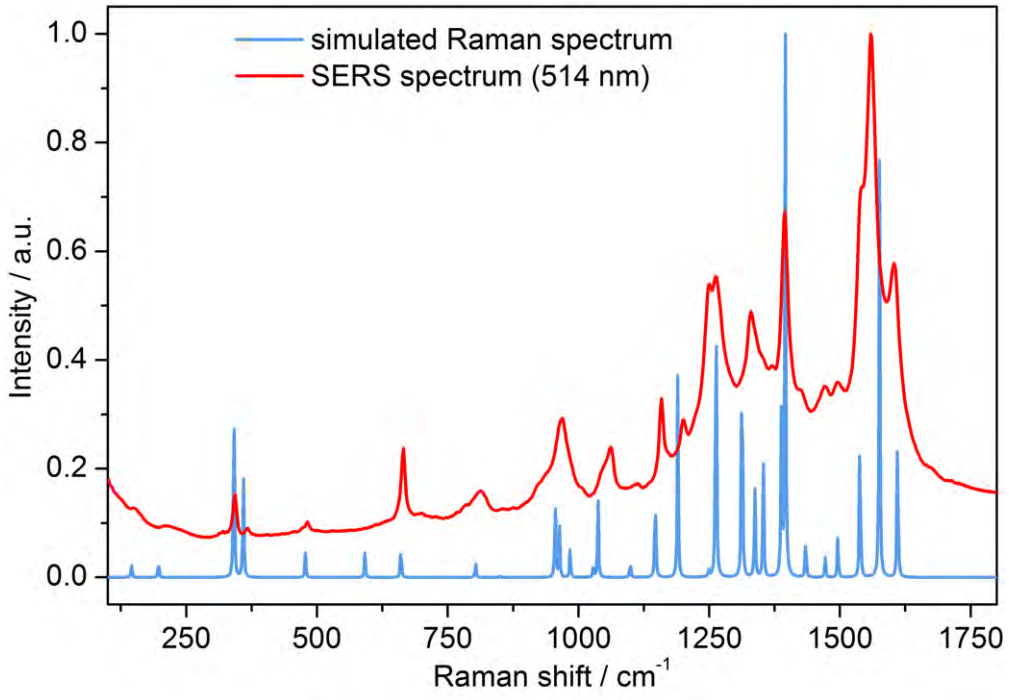

Figure 6.11: The simulated resonance Raman spectrum obtained for excitation wavelength corresponding to the energy of S_0-S_2 transition (BP86/DZP) and the corresponding experimental SERS spectrum. SERS substrate: 25 µm×47 µm gold NRs, laser excitation: 514 nm, laser power: 50 µW, room temperature.

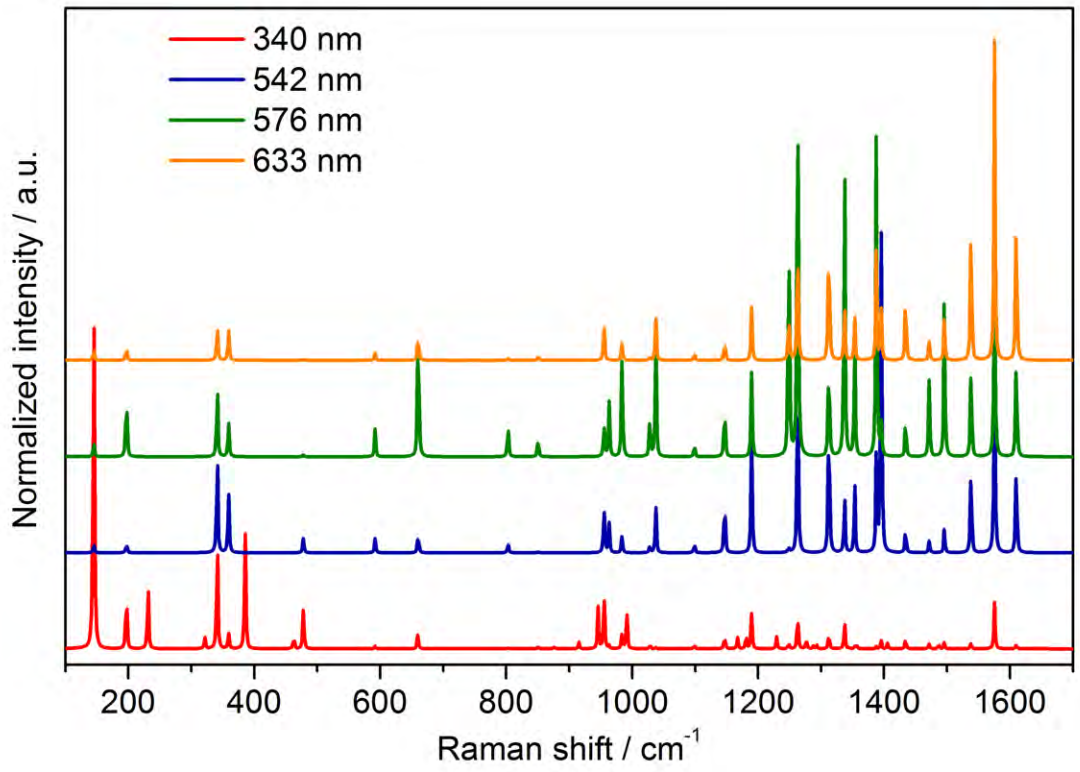

Figure 6.12: The comparison of simulated Raman spectra obtained for different excitation wavelengths: pre-resonance conditions (633 nm), the energy of S_0-S_1 transition (576 nm), the energy of S_0-S_2 transition (542) and the energy of the transition to the higher electronic state (340 nm).

6.2.2 Assignment of vibrational modes

The assignment of Raman modes of porphycene was reliably done by Gawinkowski et al.[32] by means of isotopic substitutions of porphycene and quantum mechanical calculations. The geometry optimization, followed by prediction of IR and normal Raman spectra were performed using density functional theory with B3LYP functional and 6-31G(d,p) basis set. As already mentioned, for our needs the quantum chemical calculations of non-resonance Raman were not sufficient. As a result, resonance Raman calculations were performed, but with different functional (BP86) and basis set (DZP) than those used by Gawinkowski *et al.*[32] Consequently, the corresponding vibrations had to be identified, which was achieved on the basis of atomic displacement pattern. The detailed description of the character of vibrations can be found in the above-cited work.

Table 6.1: Modes of gerade symmetry predicted by calculations for porphycene in vacuum for non-resonant conditions (B3LYP/6-31G(d,p)) and resonant conditions with excitation energy equal to the energy of the S_0-S_1 transition (BP86/DZP) compared with experimentally observed Raman-active modes of porphycene placed on gold nanostructures, excited at 633 nm.

Calculated						**Observed**	
B3LYP/6-31G(d,p)			BP86/DZP			SERS exc. 633 nm	
Symm	ν/cm^{-1}	int	ν/cm^{-1}	int(normal)	int(RR)	ν/cm^{-1}	assign.
1 B_g	119	0.5	108	0.3	6.1		
2 B_g	137	5.3	126	3.1	2.8		
1 A_g	150	31.2	145	30.9	719.5		
2 A_g	187	23.6	197	22.0	4386.7	182	2 A_g
3 B_g	198	1.3	183	0.8	6.0		
4 B_g	209	7.3	194	3.9	2.4		
						323	1 A_g + 2 A_g
3 A_g	347	75	341	65.4	15344.9	343	3 A_g
4 A_g	370	41.4	359	51.7	11674.2	365	4 A_g
5 B_g	399	0.7	383	0.5	25.8		
						425	3x1 A_g
5 A_g	491	0.2	478	0.2	1736.2	483	5A_g/1A_g + 3A_g
6 B_g	493	0.1	475	0.4	38.2		
						505	1 A_g + 4 A_g
						524	2 A_g + 3 A_g
						550	2 A_g + 4 A_g
6 A_g	610	5.6	592	4.0	9517.5	597	6 A_g
						629	1 A_g + 5 A_g
7 B_g	644	1.8	620	0.1	18.0		
8 B_g	673	10.2	644	1.0	0.2		
7 A_g	674	23.2	660	25.2	67790.0	665	7 A_g
						686	2x3 A_g

Continued on next page

Table 6.1 – *Continued from previous page*

Calculated						**Observed**	
B3LYP/6-31G(d,p)			BP86/DZP			SERS exc. 633 nm	
Symm	ν/cm^{-1}	int	ν/cm^{-1}	int(normal)	int(RR)	ν/cm^{-1}	assign.
						710	3 A_g + 4 A_g
						733	2x4 A_g
9 B_g	713	1.4	677	0.6	66.1		
10 B_g	718	1.3	689	0.008	108.5		
11 B_g	775	3.6	743	1.1	27.6		
12 B_g	789	10.5	753	0.9	11.4	796	12 B_g/1 A_g + 7 A_g
13 B_g	832	5.4	795	0.06	0.4		
8 A_g	833	2.2	803	5.7	14669.5		
9 A_g	877	6.7	850	9.0	12067.9	850	9 A_g
14 B_g	897	0.4	857	0.06	51.1		
15 B_g	904	0.3	861	0.3	37.0		
16 B_g	933	0.4	953	0.03	2.2		
17 B_g	958	3.8	920	0.4	155.6		
10 A_g	989	81.4	955	61.0	56994.0	960	10 A_g
11 A_g	994	23	963	58.9	39344.9		
12 A_g	1016	84.5	984	41.2	60102.1	986	12 A_g
						1006	3 A_g + 7 A_g
						1030	4 A_g + 7 A_g
13 A_g	1083	10.3	1028	0.9	26253.8	1148	13 A_g
14 A_g	1092	84.9	1037	41.8	88106.5	1063	14 A_g
15 A_g	1142	6.8	1099	3.5	26577.2	1116	15 A_g
16 A_g	1193	22.6	1147	32.2	93031.6	1159	16 A_g
17 A_g	1240	107.9	1190	56.4	115008	1201	17 A_g
18 A_g	1292	86.9	1249	62.9	209205	1247	18 A_g
19 A_g	1312	236.6	1263	100.8	585447	1254	19 A_g
20 A_g	1370	225.2	1312	56.3	393452	1331	20 A_g
21 A_g	1387	13.9	1337	5.8	291125	1355	21 A_g
22 A_g	1413	56.6	1353	27.8	163760	1368	22 A_g
23 A_g	1442	205.8	1388	72.2	500130	1393	23 A_g

Continued on next page

Table 6.1 – *Continued from previous page*

Calculated						**Observed**	
B3LYP/6-31G(d,p)			BP86/DZP			SERS exc. 633 nm	
Symm	ν/cm^{-1}	int	ν/cm^{-1}	int(normal)	int(RR)	ν/cm^{-1}	assign.
24 A_g	1448	27.8	1395	77.6	140727	1408	24 A_g
25 A_g	1489	514	1434	346.9	103884	1428	25 A_g
26 A_g	1532	118.2	1472	60.8	76714	1473	26 A_g
27 A_g	1563	341.6	1495	252.0	167766	1492	27 A_g
28 A_g	1592	567.1	1538	313.0	294999	1539	28 A_g
29 A_g	1613	905.5	1575	412.9	656530	1560	29 A_g
30 A_g	1663	440.5	1610	254.3	366973	1604	30 A_g
31 A_g	2895	4.7	2427	3.6	268276		
32 A_g	3165	102.1	3078	94.4	2812.9		
33 A_g	3184	745.3	3094	797.0	5021.2		
34 A_g	3236	266.9	3143	206.1	2193.6		
35 A_g	3250	266.7	3163	371.9	1444.2		
36 A_g	3256	498	3165	519.4	3115.0		
37 A_g	3268	617.4	3184	588.5	6478.7		

Table 6.1 contains a concise summary of this data, supported by experimentally observed surface-enhanced Raman scattering peaks. As the harmonic approximation was used, neither overtones nor combinational bands were predicted. The Raman shift of some of the peaks was determined from the spectra measured at liquid nitrogen temperature, which allowed us to obtain higher resolution and improve signal to noise ratio. Furthermore, as shown in the previous chapter, the SERS spectra of porphycene measured on gold and silver are very similar.

The SERS spectrum of porphycene is dominated by fundamental A_g modes. This is in line with simulations of resonance Raman spectrum excited at the energy corresponding to the S_0-S_1 electronic transition. The intensities of A_g modes are expected to be at least one order of magnitude higher than the intensities of B_g modes. Calculations predict that among B_g modes the most intense is the 17 B_g mode. For comparison, the intensity of this vibration is predicted to be two orders of magnitude lower than for the 3 A_g mode. Moreover, the 5 A_g band, which is

very weak in the SERS spectra is expected to be ten times higher than a peak corresponding to the 17 B_g mode, the strongest among B_g vibrations. In light of predicted intensities of Raman-active modes, the assignment of a small peak at 796 cm^{-1} appearing in both SERS and Raman spectra to 12 B_g, as in the previous assignment,[32] is very doubtful. The intensity of a band corresponding to this mode is expected to be even ten-fold lower than of the 17 B_g mode, which is already not visible. Therefore, it is far more probable that the peak at 796 cm^{-1} corresponds to the combinational band: 1 A_g + 7 A_g (150 + 674 = 824 cm^{-1}).

Compared to the Raman spectrum of porphycene crystal, the SERS spectrum of porphycene is richer in combinations and overtones of fundamental in-plane modes, for instance the peaks corresponding to $1A_g + 4A_g$, $3A_g + 4A_g$, $2x4A_g$, $4A_g + 7A_g$ are present exclusively when porphycene is placed on plasmonic nanostructures. This is a quite common phenomenon in SERS.[147,148]

6.3 Raman scattering of a molecule with fixed orientation

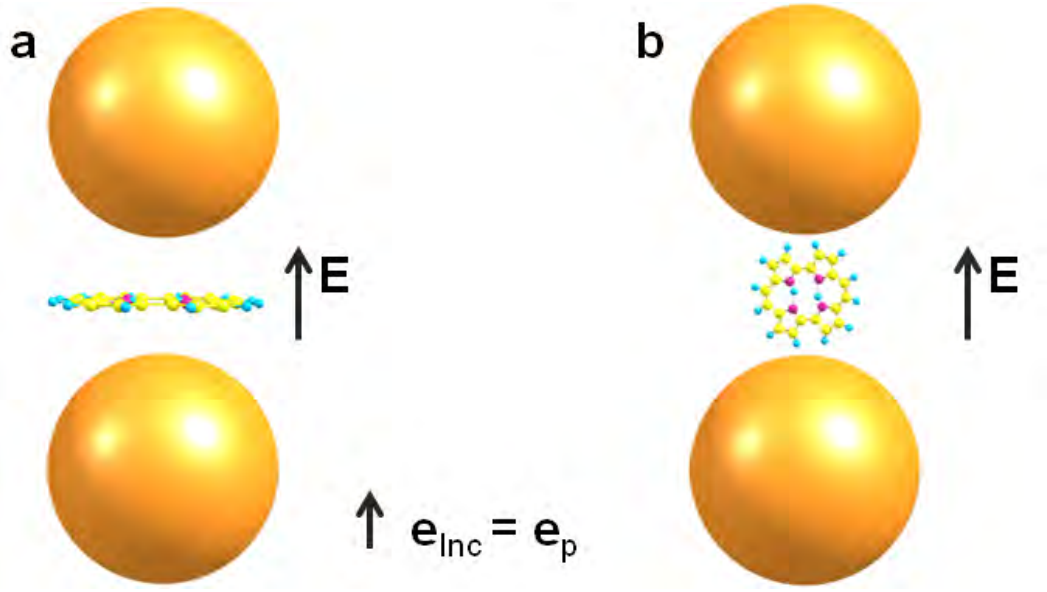

Figure 6.13: A simple model of a hot spot with two possible orientations of a porphycene molecule. The vector **E** indicates the direction of the electromagnetic enhancement.

Let us consider a molecule with fixed orientation, irradiated with light polarized along $\mathbf{E_{Inc}}$. The intensity of back- or forward- or 90°-scattered light, I, detected with a polarizer placed in front of the detector is proportional to

$$I \sim |\mathbf{e_p} \alpha \mathbf{e_{Inc}}^T|^2 |\mathbf{E_{Inc}}|^2, \tag{6.16}$$

where $\mathbf{e_{Inc}}$ is the unit vector along the incident polarization $\mathbf{E_{Inc}}$, α is the polarizability tensor and $\mathbf{e_p}$ is the unit vector along the polarizer axis.[34] In the case of Raman scattering α denotes the Raman tensor. For instance, the intensity of light scattered along y by a molecule irradiated with light polarized along x (propagating in the z direction) and detected behind a polarizer placed with axis along x is proportional to $|\alpha_{xx}|^2$.

Figure 6.13 presents a simple model of a hot spot: two spherical gold nanoparticles separated by a few nanometers. As mentioned earlier, under such conditions, the enhancement of the electric field occurs dominantly along one direction: the axis between nanoparticles, which is labeled by $\mathbf{e_{Inc}}$. This affects both, the incident and scattered radiation. Therefore, in order to calculate the intensity of the scattered light by a molecule immobilized in a hot spot, equation 6.16 should be applied with $\mathbf{e_{Inc}} = \mathbf{e_p}$ (unit vector along $\mathbf{E}$). Thus, only the modes with tensors having a non-zero component along the axis between nanoparticles experience electromagnetic enhancement. Since we are interested only in the relative intensities of different Raman-active modes and their changes upon rotation of a molecule, the magnitude of incident electric field can be assumed, for the sake of simplicity, to be equal to one: $|\mathbf{E_{Inc}}| = 1$.

It is worth to remind, that in the case of resonance conditions Raman tensors are complex, i.e., are composed of real and imaginary parts. As a result, the value of $\mathbf{e_p} \alpha \mathbf{e_{Inc}}$ is also a complex number. Let us denote it by $a + \mathrm{i}b$. Its squared modulus is then equal to $|a + \mathrm{i}b|^2 = a^2 + b^2$.

Let us now consider an orientation of a molecule of porphycene in a hot spot. The studies of porphycene located on atomically smooth metal surfaces, such as copper revealed that at liquid helium temperatures porphycene interacts with metal via its nitrogen atoms.[106] Therefore, it is probable that porphycene in a hot spot prefers the orientation perpendicular to the axis between nanoparticles, shown in

Figure 6.13a. Then, out-of-plane Raman-active modes should experience significantly higher enhancement compared to in-plane-modes. Under such conditions, however, the Raman scattering signal does not benefit from enhancement due to the resonance effect, as both the S_0-S_1 and S_0-S_2 electronic transition moments are oriented in the molecular plane, as shown in Fig. 6.7. On that account, the intensity of the SERS signal originating from molecules arranged in this way is most likely much lower compared to molecules oriented along the axis between nanoparticles, as presented in Fig. 6.13a. Therefore, in the simulations of single-molecule Raman spectra, for the reasons of simplicity we will limit the modelling to such an orientation of the porphycene molecule and its rotation only in a molecular plane.

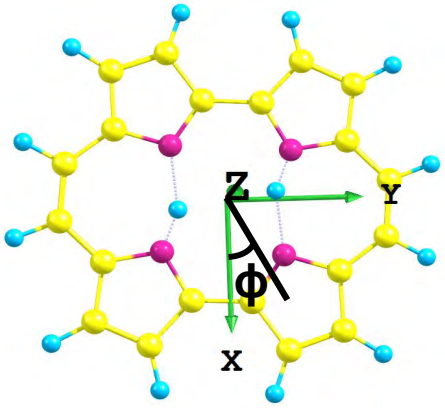

Figure 6.14: Definition of rotation angle around C_2, ϕ .

In order to properly describe the rotation of a molecule two angles should be considered. As porphycene is planar and disk-shaped, the rotation in the molecular plane seems the most probable. Hence, only an angle ϕ describing the rotation around C_2 axis, defined in Figure 6.14 will be considered. Nevertheless, in the case of porphycene the situation is more complicated due to the possibility of inner hydrogens motions. The vast majority of single molecule spectra originate from the *trans* tautomer, with the *cis* tautomer very rarely observed. However, we cannot exclude the possibility of *trans-trans* tautomerization, schematically depicted in Figure 6.15. Although both forms are chemically equivalent, such process results in the change of a direction of S_0-S_1 transition moment by $74 \pm 3°$, which was determined from bulk stationary fluorescence anisotropy measurements[110] and

time-resolved studies, including fluorescence anisotropy[111] and transient absorption measurements.[112] This was further confirmed by single molecule fluorescence studies using polarized light.[102]

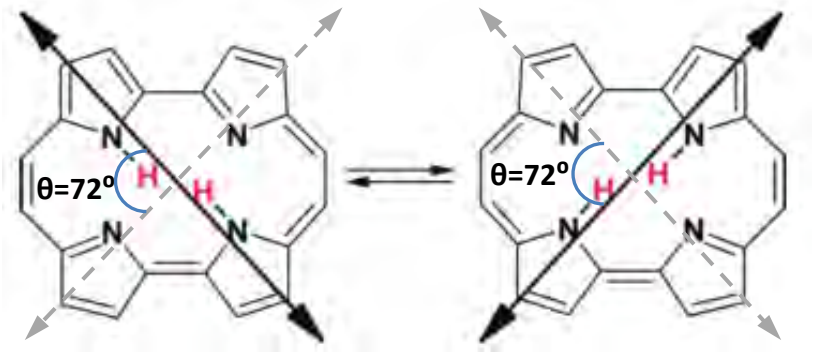

Figure 6.15: The scheme of *trans-trans* tautomerization in porphycene accompanied by a change in the direction of the S_0-S_1 electronic transition moment.

Tautomerization may additionally affect some Raman tensors, since it corresponds to a reflection in a plane perpendicular to the molecular plane σ, shown in Figure 6.16. Studies of porphycene isolated in supersonic jets[149] and in condensed phase[150] revealed that in the case of porphycene this double hydrogen-transfer process involves tunnelling. This was concluded on the basis of the observed splitting of the vibronic lines in laser-induced fluorescence excitation spectra, which disappears upon deuteration. Temperature dependence obtained from ^{15}N NMR studies confirmed the key role of tunnelling in this process, and provided an estimation of a barrier to be about 32 kJ/mol.[151] The calculations at the density functional theory level (B3LYP/TZ2P) suggest that the *trans-trans* tautomerization happens via a two-step mechanism that involves a *cis*-porphycene intermediate.[109] The energy of the *trans-cis* barrier (excluding zero-point effects) is estimated as 4.9 kcal/mol and the height of the reverse *cis-trans* barrier as only 2.5 kcal/mol. Such low values indicate that the inner hydrogens are very mobile, even at low temperatures and the experimental observation of *cis*-porphycene is highly unlikely. This suggests that, most likely, tautomerization happens also when porphycene is placed on plasmonic nanostructures. In order to include this reaction into simulations of Raman spectra, the contributions from both *trans* tautomers should be taken into account: the original one and its mirror image over a plane σ.

To find the tensors related to the second *trans* tautomer, an equation of a plane σ should be derived, followed by reflection of the components of tensors for the

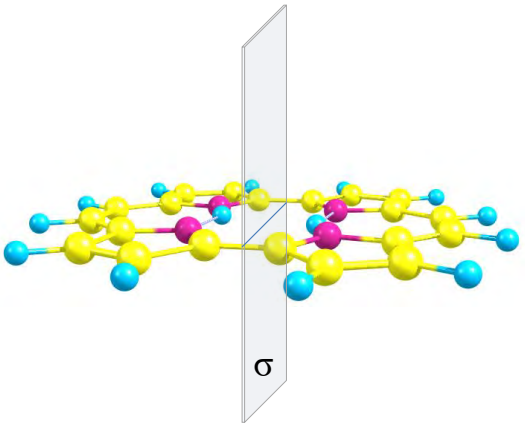

Figure 6.16: The transition between two *trans* tautomers in porphycene can be described as a result of a reflection over a plane marked as σ , which is perpendicular to the molecular plane.

initial *trans* tautomer over the defined plane. As the z components of A_g modes of Pc are negligible, our considerations can be limited to the xy plane. With such simplification, the reflection happens over a line resulting from the intersection of the molecular plane and the σ plane.

Figure 6.17 illustrates the procedure of calculating the coordinates of point $P' = (p', q')$ appearing upon reflection of a given point $P = (p, q)$ over a line $f(x) = ax + b$. These values can be obtained in the following steps:

- construction of a line $g(x)$ perpendicular to $f(x)$ that goes through the point P;
- finding the intersection point M of lines $f(x)$ and $g(x)$;
- calculation of the values of Δx and Δy, defined as the distance between the points P and M in x and y directions, respectively;
- doubling the values of Δx and Δy starting from the point P, which results in the point P'.

With a view to obtain analytical formulation, let us denote the line $g(x)$ as $g(x) = cx + d$. It is perpendicular to $f(x) = ax + b$ if and only if $c * a = -1$. Therefore $c = -1/a$. The condition that the line $g(x)$ passes through the point P is fullfield by the equation

$$g(x) = -\frac{1}{a}x + q + \frac{p}{a}. \tag{6.17}$$

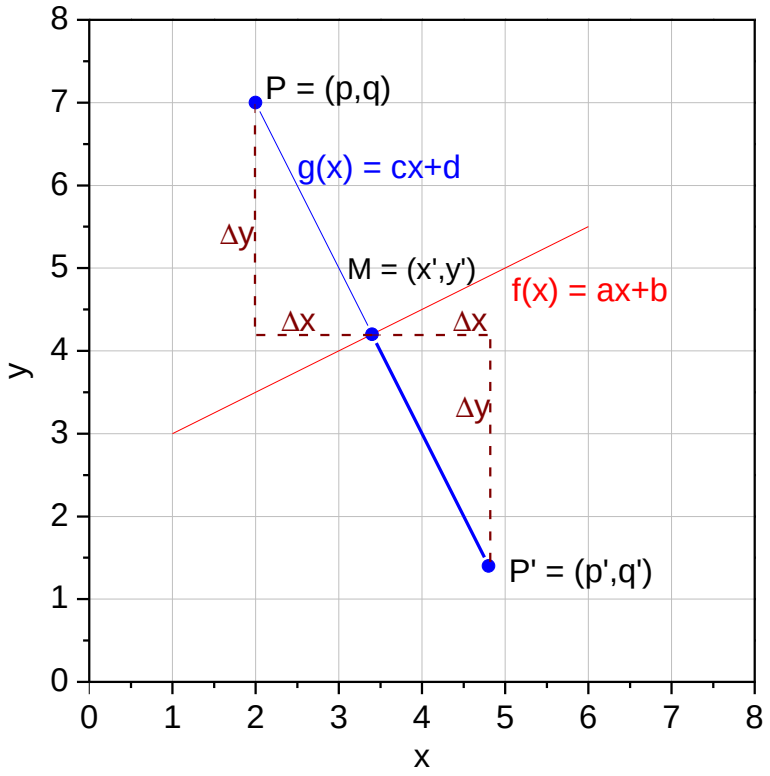

Figure 6.17: Pictorial representation of reflection of a given point P over a line $f(x)$.

The coordinates of the intersection point $M = (x', y')$ can be calculated by solving the equation $f(x') = g(x')$:

$$\begin{cases} x' = \dfrac{aq - ab + p}{a^2 + 1}, \\ y' = \dfrac{a^2 q + ap + b}{a^2 + 1}. \end{cases} \tag{6.18}$$

The values of Δx and Δy are equal to:

$$\begin{aligned} \Delta x &= p - x' = p - \frac{aq - ab + p}{a^2 + 1}, \\ \Delta y &= q - y' = q - \frac{a^2 q + ap + b}{a^2 + 1}. \end{aligned} \tag{6.19}$$

Finally, the coordinates of the point $P' = (p', q')$ are equal to

$$\begin{cases} p' = p - 2\Delta x = \dfrac{-a^2 p + 2aq - 2ab + p}{a^2 + 1}, \\ q' = q - 2\Delta y = \dfrac{a^2 q + 2ap + 2b - q}{a^2 + 1}. \end{cases} \tag{6.20}$$

If the reflection line goes through the center of a coordinate system, i.e., the $(0, 0)$ point, it takes a form $y = ax$ and the equation for coordinates of the point P' simplifies to

$$\begin{cases} p' = \dfrac{(1 - a^2)p + 2aq}{a^2 + 1}, \\ q' = \dfrac{2ap + (a^2 - 1)q}{a^2 + 1}. \end{cases} \tag{6.21}$$

On that account, the new tensor A' resulting from a mirror image of a tensor A over a line $y = ax + b$ can be calculated according to the equation

$$A' = QAQ^T, \tag{6.22}$$

where Q denotes a reflection matrix

$$Q = \frac{1}{1 + a^2} \begin{bmatrix} 1 - a^2 & 2a & 0 \\ 2a & a^2 - 1 & 0 \\ 0 & 0 & 1 \end{bmatrix}. \tag{6.23}$$

The mirror images of all of the predicted tensors were calculated using the above formula. Figure 6.14 shows the orientation of a porphycene molecule with respect to the Cartesian coordinate system upon geometry optimization in the performed calculations. The line of reflection is given by an equation $f(x) = -0.1x$, which was determined from the positions of the nitrogen atoms. The mirror image of an arbitrarily selected tensor over this line is illustrated in Figure 6.18.

Another basic operation on tensors, also shown in Figure 6.18, is the rotation about the z axis by an angle ϕ. The tensor A' resulting from rotation of a tensor A can be calculated according to the formula

$$A' = QAQ^T, \tag{6.24}$$

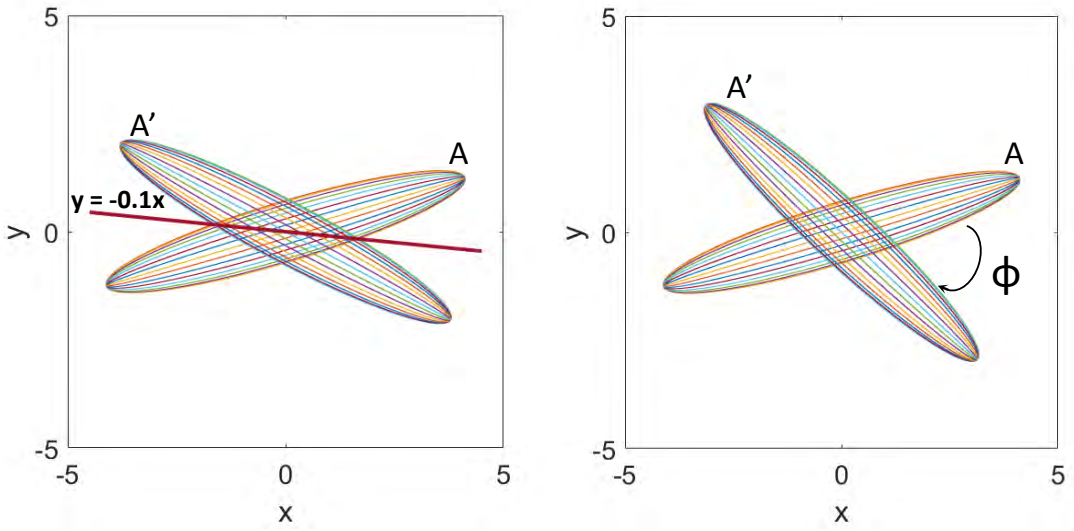

Figure 6.18: Examples of basic operations on tensors: left, reflection over a line $y = -0.1x$; right, rotation by angle ϕ.

where Q denotes a rotation matrix

$$Q = \begin{bmatrix} \cos\phi & \sin\phi & 0 \\ -\sin\phi & \cos\phi & 0 \\ 0 & 0 & 1 \end{bmatrix}. \tag{6.25}$$

This equation allows us to simulate changes in the Raman spectra resulting from reorientation of a single porphycene molecule located in a hot spot. Obviously, the arrangement of Raman tensors follows the molecular movements. The Raman activity, A, of a given vibration, which is directly related to its intensity, is predicted by the equation (6.16) extended by rotation by an angle ϕ around z axis described by formula 6.24:

$$A \sim |\mathbf{e_p}(Q\alpha Q^T)\mathbf{e_{Inc}}^T|^2 |\mathbf{E_{Inc}}|^2, \tag{6.26}$$

where α represents the related Raman tensor and Q is the rotation matrix defined by equation 6.25. Moreover, due to the nature of the hot spot $\mathbf{e_p} = \mathbf{e_{Inc}}$. For the reasons of simplicity, we can assume $\mathbf{e_p} = \mathbf{e_{Inc}} = [0 \quad 1 \quad 0]$ and $|\mathbf{E_{Inc}}|^2 = 1$. Typically, the predicted intensity, not Raman activity, is directly compared with the experiment results. Therefore, the obtained activity should be transformed according to the equation 4.1 given in Chapter 4, taking into account the excitation energy and temperature.

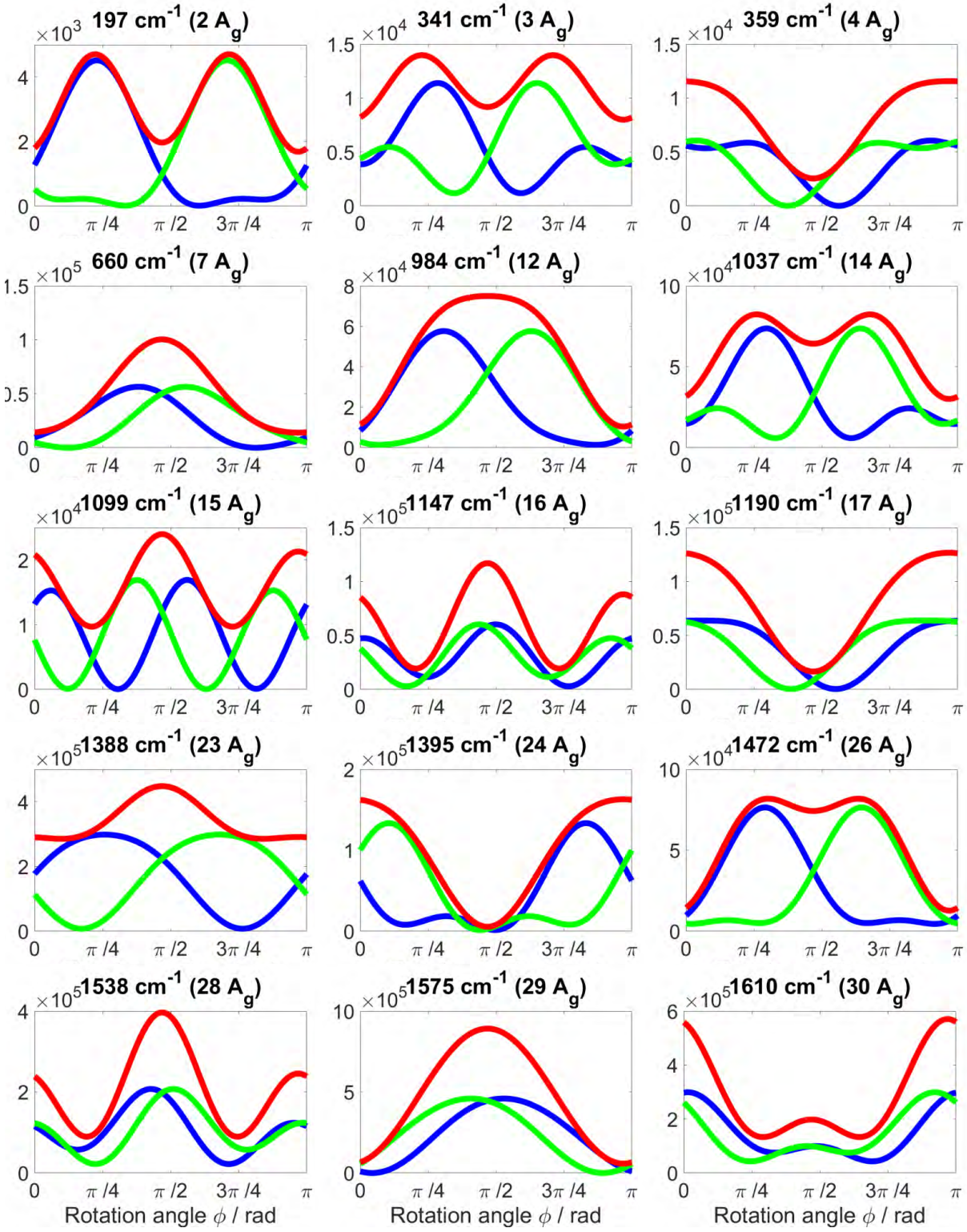

Figure 6.19: Dependence of the Raman activity on the rotation angle ϕ about the C_2 axis calculated for different porphycene vibrations: for both *trans* tautomers (blue, green) and their averaged sum (red); the shapes of Raman tensors were predicted by ADF software at the BP86/DZP level.

The dependence of the Raman activity of a given mode on the rotation angle ϕ is strongly related to the shape and orientation of the corresponding Raman tensor. Figure 6.19 presents this dependence for the selected modes. The red curves depict the situation with fast double-hydrogen transfer included, i.e., both *trans* tautomers contributing equally, whereas the blue and green curves denote predictions of the changes upon rotation separately for each *trans* tautomer. These simulations allowed us to calculate correlation coefficients for each pair of modes, which is described in the next section. Nevertheless, already a brief analysis indicates that some pairs of modes are strongly correlated, i.e., behave similarly: when the intensity of one peak increases, the same happens to the other one. This is the case for $7A_g$ and $29A_g$ modes when considering simulations including tautomerism (red curves). On the other hand, there are also modes exhibiting negative correlations. The bands assigned as $4A_g$ and $7A_g$ may serve as an example: when the former becomes more intense, the intensity of the latter decreases and *vice versa*. Furthermore, there are also modes, like $23A_g$, that are only slightly sensitive to molecular rotation.

In summary, Figure 6.19 illustrates that the Raman spectra are very sensitive to the molecular orientation. Moreover, the intensities of different vibrations do not behave in the same fashion. This can be also demonstrated in a more convenient way, namely as a collection of spectra simulated for different molecular arrangements. Figure 6.20 contains such predictions compared to the experimental data. The top panel shows the measured SERS spectra of a single molecule of porphycene averaged over 50 s (two different time windows were selected). Despite such a long averaging time, the measured spectra show clear differences. This means that if molecular rotation happens, its time range exceeds seconds. Moreover, the rotation might be not uniform. Below the experimental spectra shown in Figure 6.20, Raman spectra simulated for a porphycene molecule oriented as in Figure 6.13b, but differing in an angle ϕ: $\phi = 0, \phi = \pi/4, \phi = \pi/2$ and $\phi = 3\pi/4$ are presented. Specifically, Figure 6.20b presents the results of simulations assuming fast *trans-trans* tautomerization, while Fig. 6.20c does not include this double-hydrogen transfer. In the simulated spectra the broadening with a Lorentzian function was used with a parameter specifying the with, $\Gamma = 8$ cm^{-1}.

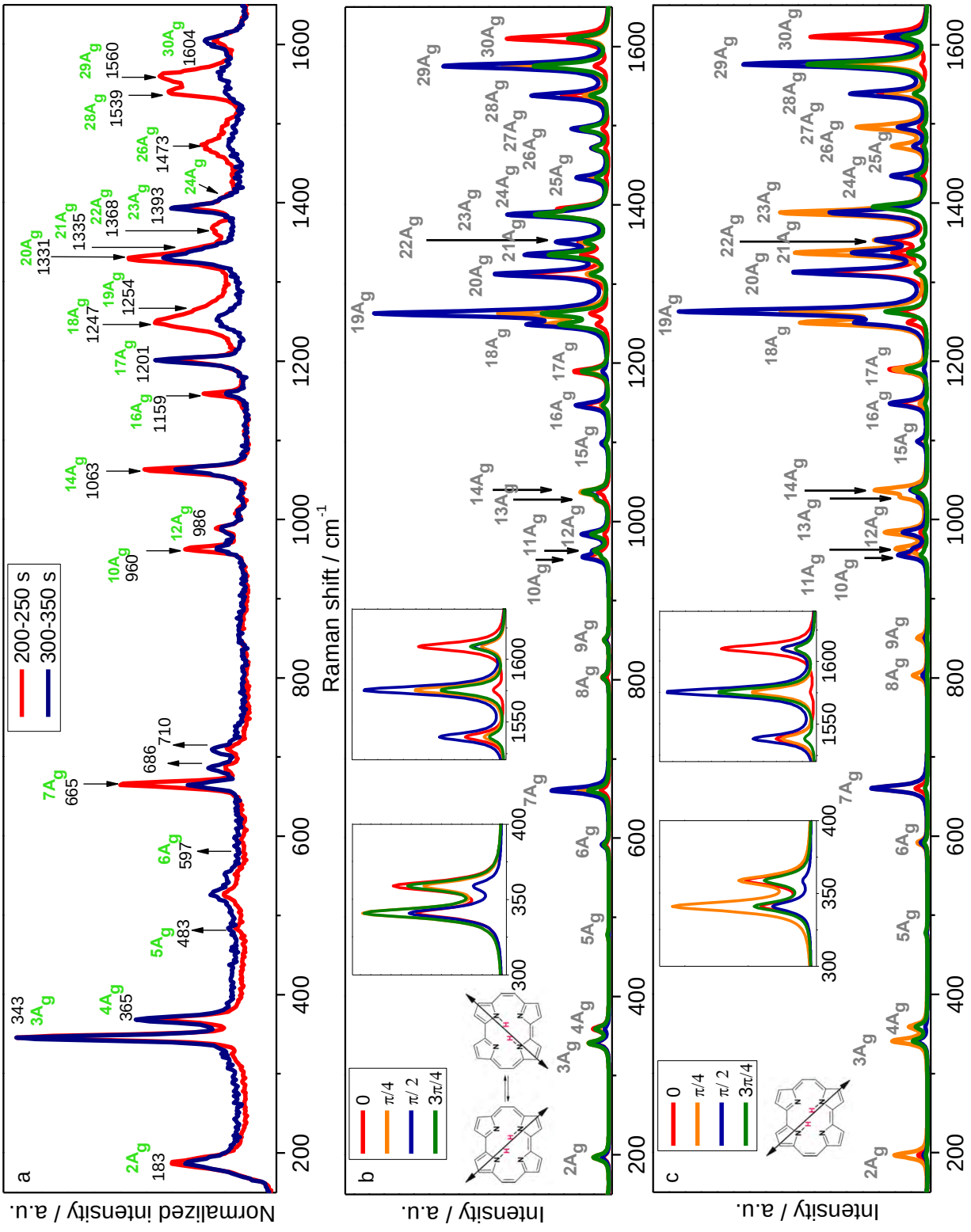

Figure 6.20: The comparison of experimental and simulated Raman spectra: (a) the SERS spectra obtained from the time trace shown in 6.24 averaged over different time windows, (b) the Raman spectrum of porphycene predicted on the basis of Raman tensors obtained from quantum chemical calculations at the DFT level (BP86/DZP) for different molecular orientations including *trans-trans* tautomerization and (c) excluding it.

In general, the calculated spectra that include fast tautomerism exhibit significantly lower variability of band intensities upon rotation. In the insets, the intensities predicted for $3A_g$ and $4A_g$ modes are shown. Their ratio in the measured spectra does not vary significantly: for the arbitrarily selected experimental single-molecule spectra presented in Figure 6.21 it changes from 1.4 for the green spectrum to 2.3 for the red one. The calculations, however, predict much broader distribution of this value, as shown in Table 6.2. For some orientations, for instance $\phi = 0$, the intensity of $4A_g$ mode is even higher than for $3A_g$, which has never been observed experimentally. Nevertheless, when hydrogen transfer is included, the relative changes are significantly lower, being at the same time closer to the experimental values. This suggests, that in the case of porphycene located on plasmonic nanostructures the fast tautomerism does occur.

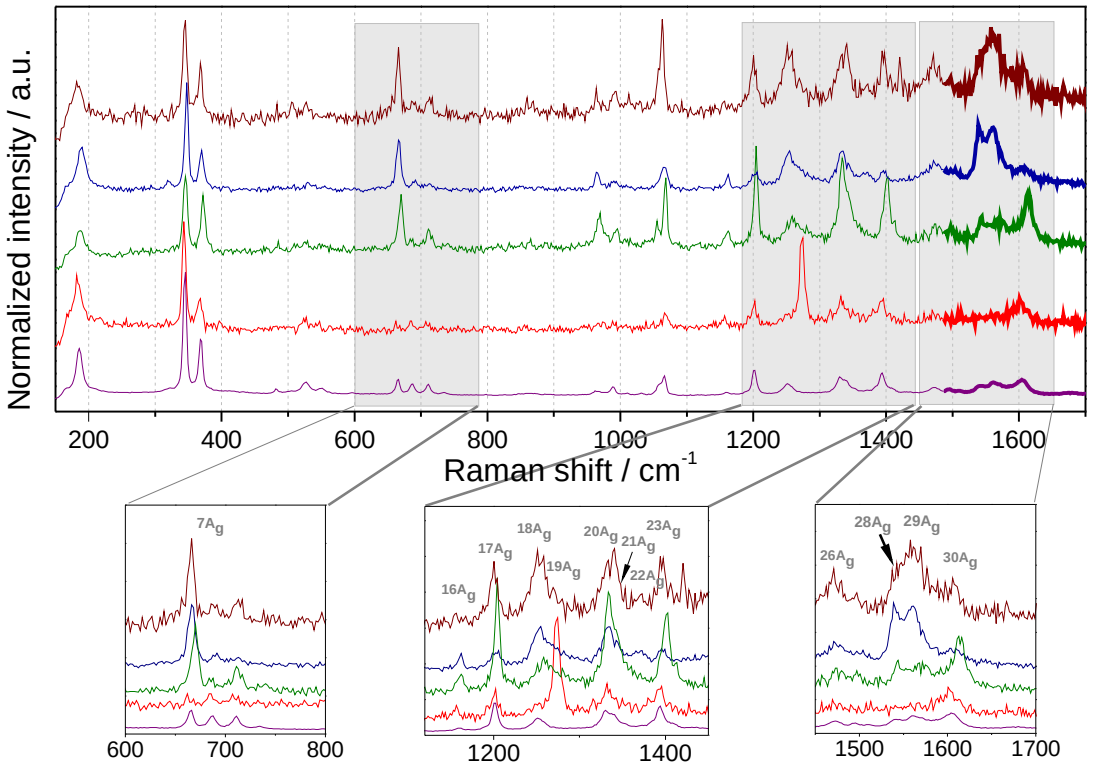

Figure 6.21: Single molecule SERS spectra of porphycene measured at different hot spots.SERS substrate: Au nanoparticles obtained by electrodeposition at a three phase junction, laser excitation: 632.8 nm, laser power: 50 µW, room temperature.

Another evidence confirming such hypothesis can be provided by the comparison of the experimental and predicted values of the ratio between the intensities corresponding to $2A_g$ and $3A_g$ fundamental modes. For the measured spectra shown in

Table 6.2: The predicted ratios of integral intensities of $2A_g$ and $3A_g$, and $3A_g$ and $4A_g$ modes obtained for different orientations of a porphycene molecule.

	tautomerism		no tautomerism	
Angle ϕ	$2A_g/3A_g$	$3A_g/4A_g$	$2A_g/3A_g$	$3A_g/4A_g$
0	0.47	0.76	0.71	0.74
$\pi/4$	0.71	1.95	0.87	2.11
$\pi/2$	0.47	4.05	0.37	6.17
$3\pi/4$	0.71	1.54	0.10	1.25

Figure 6.21 its value varies from 0.5 for the purple spectrum to 0.8 for the red one, whereas the simulations predict its change in the range of 0.5-0.7 when including the double-hydrogen transfer, and 0.1-0.9 when excluding it. Hence, the range of results obtained from simulations taking *trans-trans* tautomerization into account is much closer to the experimental values.

A further argument supporting the presence of tautomerization is based on the shape of a band originating from $23A_g$ and $24A_g$ modes, which hardly changes in the experimental spectra. Only its intensity fluctuates. The simulations excluding double-hydrogen transfer, however, predict the modification of its shape upon rotation, caused by alteration in the relative intensities of modes forming this band. On the contrary, the simulations that include tautomerism, forecast simultaneous variations in the intensities of bands corresponding to $23A_g$ and $24A_g$ modes, their ratio remaining unchanged.

The same situation occurs when considering a band originating from closely lying $18A_g$ and $19A_g$ modes. In the case of predictions including tautomerism its shape should not change, as the relative intensity of the $18A_g$ and $19A_g$ modes in not sensitive to the molecular orientation, which is not the case in simulations excluding *trans-trans* tautomerism. In the experimental spectra, usually only the intensity of a band formed by these modes changes, not its shape. Nevertheless, there occur some exceptions, like the red spectrum shown in 6.21. It might be due to an orientation of a porphycene molecule other than those we consider. Another plausible explanation is a very large decrease of the tautomerization rate, by many orders of magnitude, caused by the specific interactions with the environment. As we are examining single molecules, some very exotic behaviour might be observed.

The example of theoretical predictions of the intensities of the $18A_g$ and $19A_g$ modes shows that, as might have been expected, the simulations do not fully reflect the experimentally obtained relative intensities of the Raman-active modes. Under SERS conditions, typically the $18A_g$ mode is more intense than the $19A_g$, which has not been correctly predicted. Nevertheless, for most vibrations the simulations describe quite well their relative intensities. For instance, the simulations forecast large fluctuations of the intensities corresponding to the $7A_g$, $17A_g$ and $26A_g$ modes, which was confirmed experimentally, and is illustrated in Figure 6.21. Moreover, large variations in the intensities of the already mentioned $18A_g$ and $19A_g$ modes was predicted. In conclusion, quite a good agreement of predictions with the experimental data indicates that the calculations can be considered quite reliable.

Finally, it will be demonstrated that it is relatively easy to estimate the orientation of a single porphycene molecule from its SERS spectrum. This can be achieved on the basis of the region around 1600 cm^{-1}, where three modes, $28A_g$, $29A_g$, and $30A_g$ appear. Interestingly, the predicted spectral shape in this region is hardly affected by the presence of tautomerism. Both, the simulations and experimental data exhibit in this region significant variability. For instance, in the purple, red and green spectra, shown in Figure 6.21 the peak corresponding to the $30A_g$ mode is the most intense, which according to the simulations indicates that the angle ϕ defined in Figure 6.14 is close to 0. In the dark blue spectrum, however, the intensity of the $29A_g$ mode prevails, which, based on the calculations, gives $\phi \approx 3\pi/4$. Finally, in the case of the brown spectrum, the intensities of the $28A_g$ and $29A_g$ modes are comparable, which indicates $\phi \approx \pi/2$. Most likely, more accurate determination of an orientation of a molecule in a hot spot is possible based on a greater number of vibrations.

6.4 Analysis of time traces

The careful analysis of time evolution of SERS spectra originating from a single molecule can provide us a great deal of relevant information. First, the changes in both molecular structure and orientation can be inferred. Moreover, its interactions

with the environment can be followed. Second, the close-lying bands, which are not well resolved can be distinguished under the condition that they follow different fluctuations patterns. Third, the values of correlation coefficients between different modes, supported by quantum chemical calculations may be helpful in assignment of vibrational modes. These examples demonstrate that temporal evolution of single molecule spectra deserve thorough investigation.

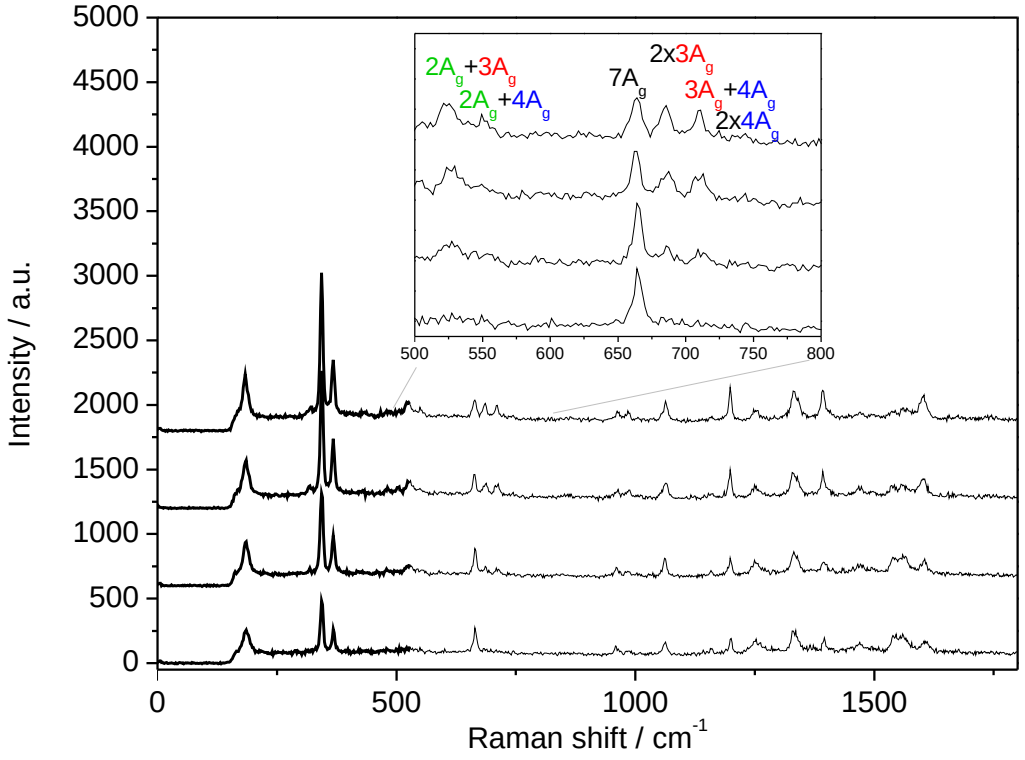

Figure 6.22: Single molecule SERS spectra of Pc-d_0 recorded from the same hot spots at different moments. Inset, enlarged spectral region with marked overtones and combination bands. SERS substrate: Au nanoparticles obtained by electrodeposition at a three phase junction, laser excitation: 632.8 nm, laser power: 50 µW, room temperature.

In the case of porphycene, the relative changes in intensity are very different for different modes. One of the regions with the highest intensity variability is the range of 650-750 cm^{-1} for Pc-d_0 and, respectively, 630-730 cm^{-1} for Pc-d_{12}. In this spectral range four peaks may be distinguished, although their intensities vary so drastically that sometimes only the mode at the lowest Raman shift ($7A_g$) is observed, which is demonstrated in Figure 6.22. The analysis of numerous time traces of porphycene revealed that the intensities of some modes fluctuates much

more than the others. To the group of bands showing the largest changes in intensity belong overtones and combinations. Indeed, in the discussed region only one out of four peaks (at 665 cm^{-1}) originates from a fundamental mode ($7A_g$) and its intensity changes are significantly smaller than those of the others. The remaining three peaks in the spectrum of Pc-d_0 observed at 686, 710, and 733 cm^{-1} correspond to $2x3A_g$, $3A_g + 4A_g$, and $2x4A_g$respectively. These three bands have not been assigned so far, despite their presence in fluorescence and Raman spectra.[32] For Pc-d_{12}, the corresponding frequencies are 654, 678, and 701 cm^{-1} and the $7A_g$ transition appears at 642 cm^{-1}. It is remarkable that these combinations and overtones are intense only when the excitation energy corresponds to the S_0-S_1 electronic transition. They are, however, practically not detectable when the excitation energy matches the S_0-S_2 electronic transition.

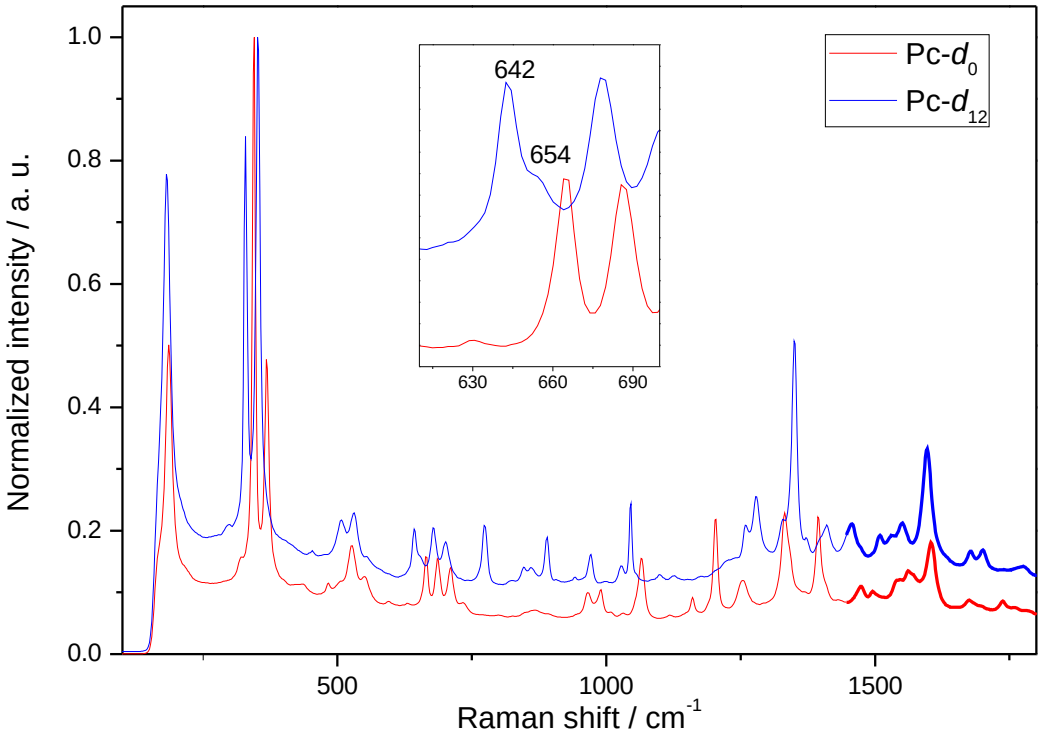

Figure 6.23: The averaged SERS spectra of Pc-d_0 and Pc-d_{12}. SERS substrate: 25 µm×47 µm gold NRs, laser excitation: 632.8 nm, laser power: 50 µW, room temperature, concentration of solutions: 10^{-8} M.

In normal Raman spectra, overtones and combinations are rarely observed, whereas they often appear in SERS. The observation that overtones and combinations manifest large intensity fluctuations combined with observed strong relative intensity changes confirms the previous assignment of a mode at 323 cm^{-1} as $1A_g + 2A_g$.[32]

In the spectra registered at non single-molecule regime this band is observed as a shoulder of the strong $3A_g$ mode and cannot be well resolved. In single molecule spectra, however, its intensity vary that significantly that at some moments it appears as a band with distinct maximum. Such behaviour is pictured in Figure 6.22. Similar situation happens for bands at 642 and 654 cm^{-1} observed for Pc-d_{12}. They are difficult to distinguish in the average spectrum (Figure 6.23). Their separation is possible based on different characteristics of intensity fluctuations. Such a surprising use of single molecule spectroscopy in detecting and assigning of molecular vibrations demonstrates its great potential in fundamental studies. A combination nature could also be confirmed for yet another transition in Pc-d_0, observed at 317 cm^{-1}. It was previously assigned to $2A_g + 2B_g$.

6.5 Correlations between modes in time traces

In order to measure the degree of correlation between variables, several correlation coefficients were introduced, among which the most commonly used is the Pearson correlation coefficient, which is sensitive only to linear relationship, i.e., when variables X and Y are related to each other by equation $Y = aX + b$, where a and b are constants. For two variables $X = x_1, x_2, \ldots, x_N$ and $Y = y_1, y_2, \ldots, y_N$ the Pearson correlation coefficient r_{XY} is given by the equation

$$r_{XY} = \frac{\sum_{i=1}^{N}(x_i - \bar{x})(y_i - \bar{y})}{\sqrt{\sum_{i=1}^{N}(x_i - \bar{x})^2}\sqrt{\sum_{i=1}^{N}(y_i - \bar{y})^2}}, \tag{6.27}$$

where $\bar{x}$ and $\bar{y}$ are mean values of variables X and Y, respectively.

Its value ranges from -1 to 1, where -1 indicates a perfect negative relationship (if the value of one variable increases, the value of another one decreases), 1 indicates a perfect linear correlation (the values of both variables increase or decrease simultaneously). The value of r_{XY} close to 0 means that the tested variables are independent. According to the definition $r_{XY} = r_{YX}$ and $r_{XX} = 1$.

After calculating the correlation coefficient the statistical significance should be examined. In statistics, hypothesis testing is of key importance and the so-called

'null hypothesis' is a fundamental concept. It refers to a general statement that the two investigated processes are independent. In other words, there is no relationship between them. The rejection of such hypothesis, which means that there exists a relationship between the investigated processes is nowadays a primary task in science, especially is experimental research. When testing the hypothesis the significance level α, called also alpha level is an important parameter. It defines the probability of rejecting the null hypothesis if it is true and typically is set to 0.05. The value $\alpha = 0.05$ indicates that if we claim that there exists a relationship in a given population, it will be present among at least 95 samples out of 100. In order to verify whether the calculated value r_{XY} is statistically significant, a critical value table for Pearson's Correlation Coefficient should be used. It contains the minimum correlation coefficient which ensures that in 95% cases from the whole population the relationship exists. It depends, however, not only on α, but also on the number of degrees of freedom, which is lower by 2 than the number of tested subjects. For instance, for 95 spectra, the number of degrees of freedom is 93, and the critical value (for $\alpha = 0.05$) is 0.2017.

As we are interested in finding correlations between intensities of different modes, the correlation coefficients should be determined for each pair of the Raman shifts (ν_X, ν_Y), more specifically the corresponding intensities (X, Y). Therefore it is convenient to represent each measured spectrum s_i as an n-dimensional vector $s_i = (x_i, y_i, z_i, \ldots)$, where n is a number of Raman shifts $(\nu_X, \nu_Y, \nu_Z, \ldots)$ for which the intensities $x_i, y_i, z_i, \ldots$ were recorded. Then, the variable X denotes the intensities at the Raman shift ν_X obtained in a collection of spectra, for instance in a time trace: $X = (x_1, x_2, \ldots, x_m)$. The subscript indicates the spectrum number. Similarly, the variable Y stands for the measured intensities in the same spectra, but at the Raman shift ν_Y: $Y = (y_1, y_2, \ldots, y_m)$.

The analysis of correlations between intensities of different modes based on time traces is limited only to those consisting of at least few tens of spectra, preferably several tens/hundreds. Fortunately, due to the enhanced photostability of porphycene molecules located close to a metal surface, we were able to record long time traces, lasting from seconds up to even hours (in very few cases).

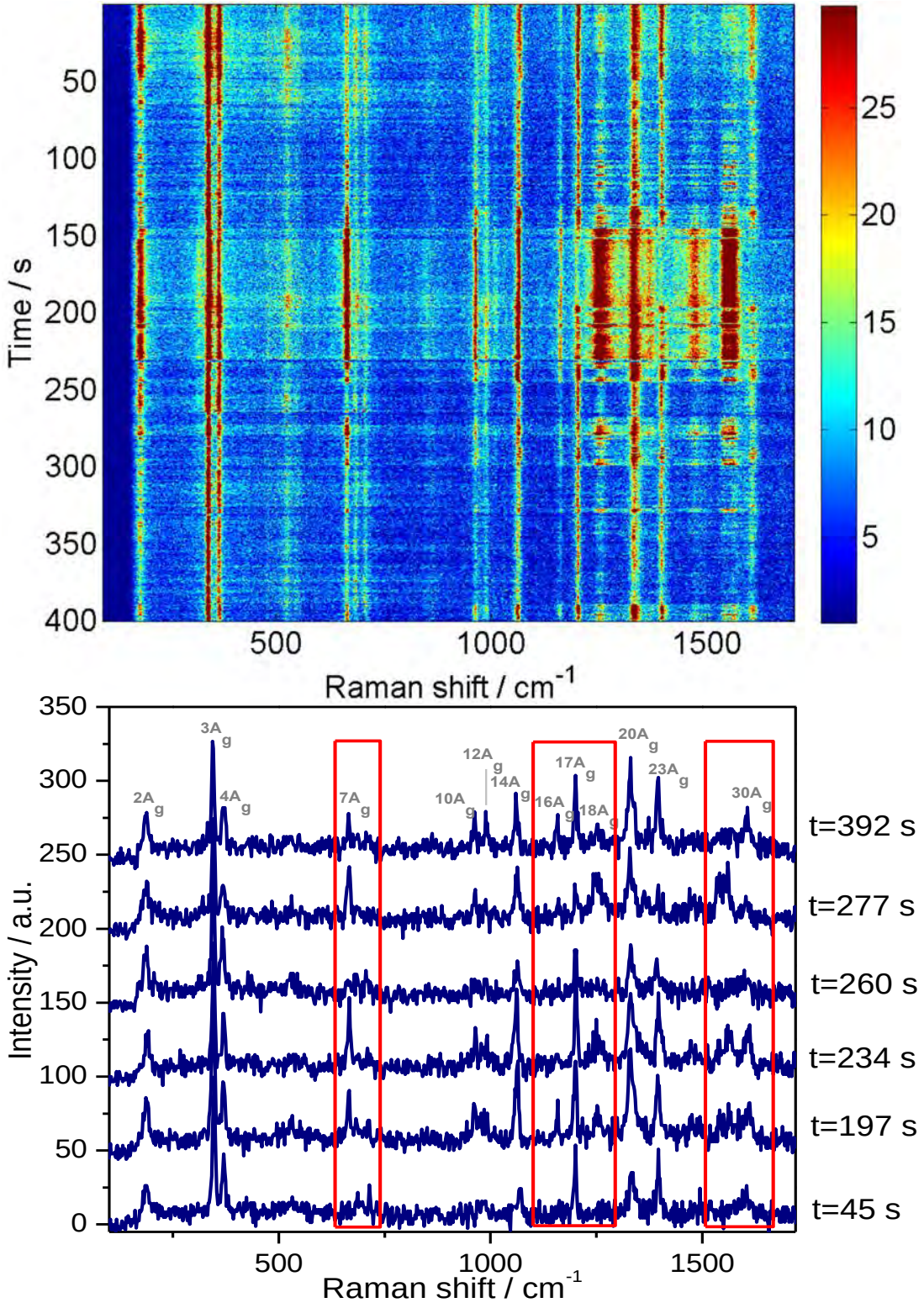

Figure 6.24: A sequence of SERS spectra of a single Pc-d_0 molecule located in a hot spot. Below, selected spectra registered at different moments; the regions of the highest variability are indicated by red rectangles. SERS substrate: 25 µm×47 µm gold NRs, laser excitation: 632.8 nm, laser power: 50 µW, room temperature, acquisition time: 500 ms/spectrum.

First 400 s of one of such long time traces is shown in Figure 6.24. It lasted almost 600 s and ended by photobleaching: sudden vanishing of the Raman signal. Although the graphical representation of a time trace in a form of a map with colors corresponding to signal intensity is convenient and gives a general overview of signal fluctuations over time, it is often helpful to look closer at the spectra registered at different moments. Hence, below the map, a few selected spectra are shown. Typically, the Raman shifts remain almost unchanged, contrary to the intensities of different modes, which vary significantly. Nevertheless, not all of the peaks behave in same fashion. While the intensities of some of the modes only slightly fluctuate, the intensities of the others vary drastically. For instance, the peaks corresponding to $2A_g$, $3A_g$ and $4A_g$ do not exhibit large variations. Similarly, the relative intensities for the $20A_g$ and $23A_g$ modes remain more or less the same. On the other hand, the band at 665 cm^{-1} ($7A_g$) changes significantly, sometimes even completely disappears (at $t = 45$ s). Similarly, the peak corresponding to the $16A_g$ mode exhibits large variations. This illustrates that there are a lot of modes to be traced. Hence, as the amount of information hidden in such a time trace is huge, the statistical analysis is required to extract as much as possible.

Therefore, having measured the time evolution, like the one shown in Figure 6.24, the Pearson correlation coefficient for each pair of Raman shifts can be calculated. Their values can be determined either for the entire collection of spectra, or for different time windows: for instance 20 or 50 s time intervals. The latter approach might be rationalized by the fact that at distinct time intervals a molecule located in a hot spot may behave in various ways, i.e., it may start rotating along a different axis or even stop rotating at all. Taking into account the time scale of rotational and translational movements of molecules, which are of the order of tens to hundreds picoseconds for small organic molecules, we are still extremely far from the time resolution enabling us to follow such dynamics. However, the motions of a molecule immobilized in a hot spot might be slowed down by the non-covalent interactions with the surface of nanoparticles. Our time resolution, which is limited to 300 ms, allows only for the observation of slow movements, with times ranging from seconds to minutes. Therefore, with a view to extract the dynamics of faster movements or processes it would be worth to improve the time resolution of our setup. Nevertheless, it will be inevitably limited by the signal to

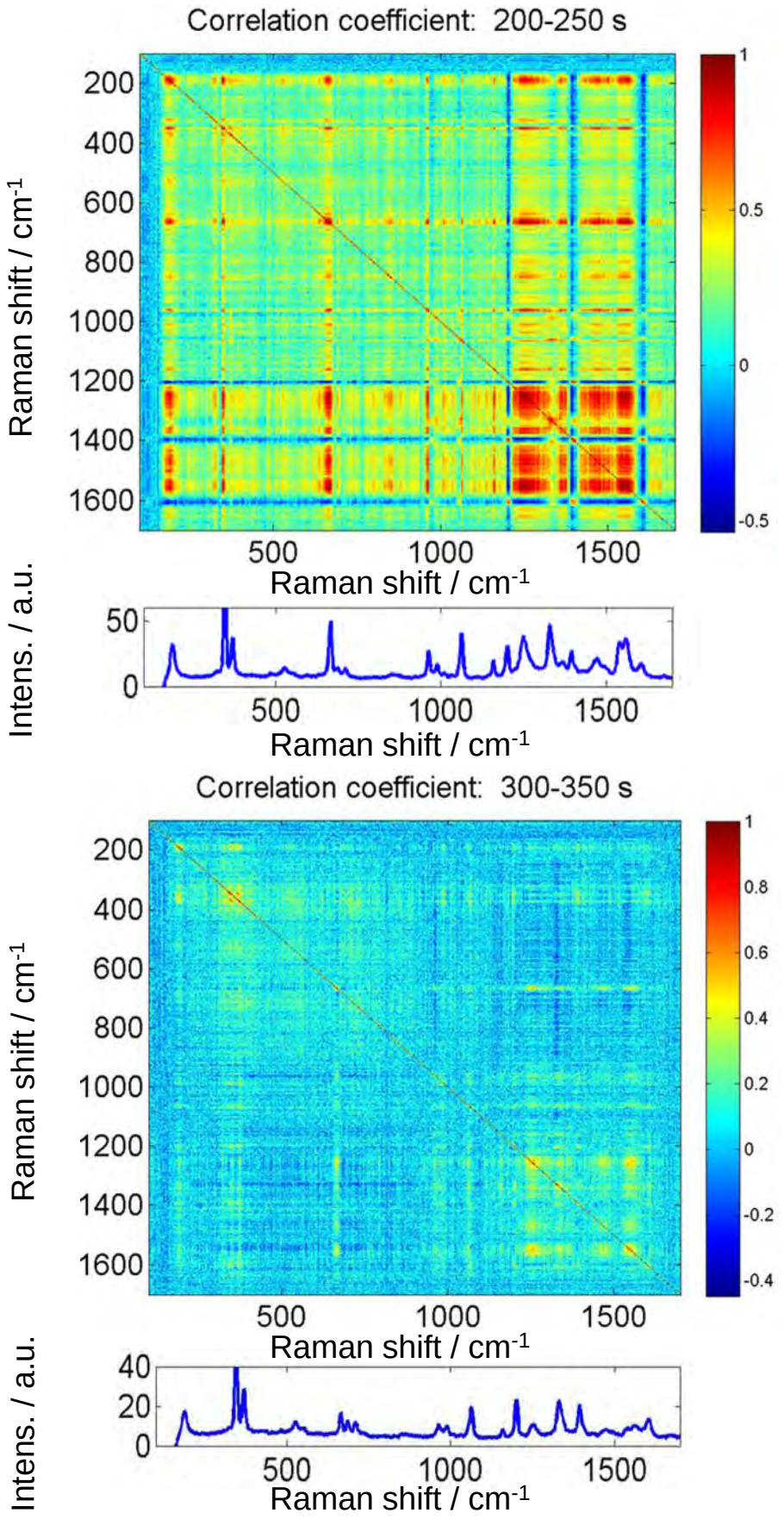

Figure 6.25: Maps of correlations between intensities in the SERS spectra calculated for the time trace presented in Fig. 6.24, calculated for two different time windows, each of 50 s duration. Below each of the maps, the spectra averaged over the selected time intervals are shown.

noise ratio.

It turned out that the nature of movements of a molecule changes over time, which is illustrated in Figure 6.25. It presents two maps of Pearson correlation coefficients calculated for the time trace presented in Figure 6.24, but for two different time windows, each of 50 s duration. The acquisition time of a single spectrum was set to 0.5 s, but due to the presence of some delays in the experimental setup each of the presented map is constructed from 95 spectra. Since $r_{XY} = r_{YX}$ and $r_{XX} = 1$ each matrix is symmetric, with the values on a diagonal equal to 1. Surprisingly, the maps obtained from the same single molecule, but for distinct time intervals look completely different. For the time window 300-350 s there is only one strong correlation: between $3A_g$ and $4A_g$. There are also pairs of modes, which exhibit weaker correlations: $2A_g$ and $3A_g$, $2A_g$ and $4A_g$, $7A_g$ and $18/19A_g$, $7A_g$ and $28/29A_g$, and $18/19A_g$ and $28/29A_g$. The other pairs of vibrations do not exhibit neither positive, nor negative correlations. The situation is entirely different in the case of time interval 200-250 s. First of all, a large number of modes are strongly correlated, e.g., $2A_g$ and $3A_g$, $7A_g$ and $28A_g$, $28A_g$ and $29A_g$. Furthermore, there occur negative correlations between some modes, which is rather uncommon. The Pearson correlation coefficients between the intensities of selected pairs of vibrations obtained for the time window 200-250 s are collected in Table 6.3. To remind, for a given number of spectra, the correlation is statistically significant, if the absolute value of the corresponding correlation coefficient is above 0.20. Thus, most of the found relationships are not accidental.

The obtained values of the correlation coefficients suggest that the most pronounced vibrations in the SERS spectra of porphycene can be divided into four differently behaving groups:

I: $2A_g$, $3A_g$, $7A_g$, $10A_g$, $16A_g$, $17A_g$, $18A_g$, $22A_g$, $26A_g$, $28A_g$, $29A_g$,

II: $12A_g$, $14A_g$, $20A_g$,

III: $17A_g$, $24A_g$, $30A_g$.

IV: $4A_g$.

Table 6.3: The values of Pearson correlation coefficients for the selected frequencies obtained for a time-trace shown in Fig. 6.24 (time wndow: 200-250 s).

	$2A_g$	$3A_g$	$4A_g$	$7A_g$	$10A_g$	$12A_g$	$14A_g$	$16A_g$	$17A_g$	$18A_g$	$20A_g$	$22A_g$	$24A_g$	$26A_g$	$28A_g$	$29A_g$	$30A_g$
$2A_g$	1	0.85	0.68	0.80	0.68	0.49	0.62	0.68	**-0.41**	0.83	0.50	0.60	**-0.34**	0.76	0.78	0.82	**-0.39**
$3A_g$	0.85	1	0.76	0.87	0.71	0.71	0.71	0.76	**-0.35**	0.85	0.60	0.66	**-0.31**	0.82	0.81	0.84	**-0.26**
$4A_g$	0.68	0.76	1	0.54	0.39	0.62	0.43	0.43	0.26	0.47	0.46	0.34	0.29	0.53	0.37	0.41	0.14
$7A_g$	0.80	0.87	0.54	1	0.82	0.83	0.78	0.81	**-0.37**	0.90	0.58	0.75	**-0.40**	0.87	0.92	0.93	**-0.39**
$10A_g$	0.68	0.71	0.39	0.82	1	0.47	0.64	0.74	**-0.30**	0.74	0.60	0.66	**-0.30**	0.80	0.82	0.79	**-0.26**
$12A_g$	0.49	0.71	0.62	0.83	0.47	1	0.58	0.49	0.12	0.46	0.61	0.45	0.18	0.47	0.47	0.46	0.07
$14A_g$	0.62	0.71	0.43	0.78	0.64	0.58	1	0.65	0.10	0.69	0.70	0.54	0.20	0.64	0.55	0.55	0.23
$16A_g$	0.68	0.76	0.43	0.81	0.74	0.49	0.65	1	**-0.27**	0.76	0.65	0.59	**-0.16**	0.75	0.78	0.75	**-0.22**
$17A_g$	**-0.41**	**-0.35**	0.26	**-0.37**	**-0.30**	0.12	0.10	**-0.27**	1	**-0.49**	0.33	**-0.37**	0.86	**-0.35**	**-0.52**	**-0.47**	0.78
$18A_g$	0.83	0.85	0.47	0.90	0.74	0.46	0.69	0.76	**-0.49**	1	0.49	0.70	**-0.47**	0.86	0.91	0.92	**-0.40**
$20A_g$	0.50	0.60	0.46	0.58	0.60	0.61	0.70	0.65	0.33	0.49	1	0.48	0.44	0.50	0.45	0.44	0.31
$22A_g$	0.60	0.66	0.34	0.75	0.66	0.45	0.54	0.59	**-0.37**	0.70	0.48	1	**-0.30**	0.68	0.71	0.67	**-0.22**
$24A_g$	**-0.34**	**-0.31**	0.29	**-0.40**	**-0.30**	0.18	0.20	**-0.16**	0.86	**-0.47**	0.44	**-0.30**	1	**-0.35**	**-0.50**	**-0.49**	0.78
$26A_g$	0.76	0.82	0.53	0.87	0.80	0.47	0.64	0.75	**-0.35**	0.86	0.50	0.68	**-0.35**	1	0.86	0.87	**-0.29**
$28A_g$	0.78	0.81	0.37	0.92	0.82	0.47	0.55	0.78	**-0.52**	0.91	0.45	0.71	**-0.50**	0.86	1	0.94	**-0.46**
$29A_g$	0.82	0.84	0.41	0.93	0.79	0.46	0.55	0.75	**-0.47**	0.92	0.44	0.67	**-0.49**	0.87	0.94	1	**-0.49**
$30A_g$	**-0.39**	**-0.26**	0.14	**-0.39**	**-0.26**	0.07	0.23	**-0.22**	0.78	**-0.40**	0.31	**-0.22**	0.78	**-0.29**	**-0.46**	**-0.49**	1
$1A_g + 2A_g$	0.62	0.65	0.47	0.56	0.51	0.49	0.54	0.48	-0.29	0.60	0.30	0.45	-0.25	0.57	0.61	0.57	-0.20
$2A_g + 3A_g$	0.56	0.59	0.54	0.46	0.38	0.36	0.45	0.51	-0.07	0.48	0.37	0.34	0.0	0.45	0.42	0.41	-0.14
$1A_g + 3A_g$	0.42	0.39	0.26	0.41	0.38	0.18	0.23	0.39	-0.25	0.42	0.25	0.32	-0.28	0.36	0.35	0.46	-0.17
$2x3A_g$	0.60	0.66	0.60	0.59	0.31	0.32	0.55	0.51	-0.08	0.44	0.29	0.30	-0.05	0.49	0.55	0.41	-0.05
$3A_g + 4A_g$	0.49	0.47	0.58	0.43	0.33	0.41	0.44	0.36	0.0	0.38	0.42	0.24	0.09	0.43	0.34	0.38	-0.02
$2x4A_g$	0.35	0.46	0.37	0.41	0.25	0.20	0.38	0.32	-0.25	0.34	0.16	0.37	-0.22	0.38	0.36	0.43	-0.18

Each of these groups is marked with a different color in Table 6.3. Most of the correlation coefficients within the formed groups are above 0.7. The lowest values of correlation coefficients occur in the group II and range from 0.58 and 0.70. These not so high values indicate that the changes in intensities of the $12A_g$, $14A_g$, and $20A_g$ modes do not follow exactly the same pattern. Interestingly, the modes classified into the group I, and only these modes, exhibit negative correlations with vibrations from the group III. Therefore, despite considerable similarities between the vibrations form both groups: I and II, they can be distinguished on the basis of the values of correlation coefficients with modes from the group III. The $4A_g$ mode cannot be easily classified, as it reveals similarities to both the I and II groups. Its behaviour is the closest to the behaviour of the $2A_g$ and $3A_g$ modes, which is confirmed by the relatively high correlation coefficients: 0.68 and 0.76, respectively. On the other hand, the values of the correlation coefficient obtained for the other modes belonging to the same group are markedly lower, being at the same time significantly below the average in this group. Furthermore, the values of the correlation coefficients between this $4A_g$ mode and the vibrations belonging to group II, which range from 0.43 to 0.62 point to certain similarities. As a result, the $4A_g$ mode is classified into a separate group.

Such classification of modes in the SERS spectrum based on the values of correlation coefficients was performed for several time traces. The most interesting is the fact that there are identified only few patterns of classification, i.e., the groups determined for different time evolutions are often made up of the same vibrations. After analysing numerous time traces, it can be concluded that the most common is the situation when almost all of the modes are correlated with each other. Such behaviour might be rationalized by the translational movement of a molecule, i.e., it moves in and out of a hot spot, which results in experiencing different electromagnetic field enhancement. If a molecule does not change its relative orientation with respect to the direction of an electromagnetic field, the relative change in the intensities of Raman modes should be the same for all of the vibrations, providing strong correlations. The negative correlations, however, like in the time trace 6.24 in a time window 200-250 s (Figure 6.25) occur very rarely. Nevertheless, if they occur, the corresponding maps of correlations usually look strikingly similar. To support this observation, another time trace originating from a single

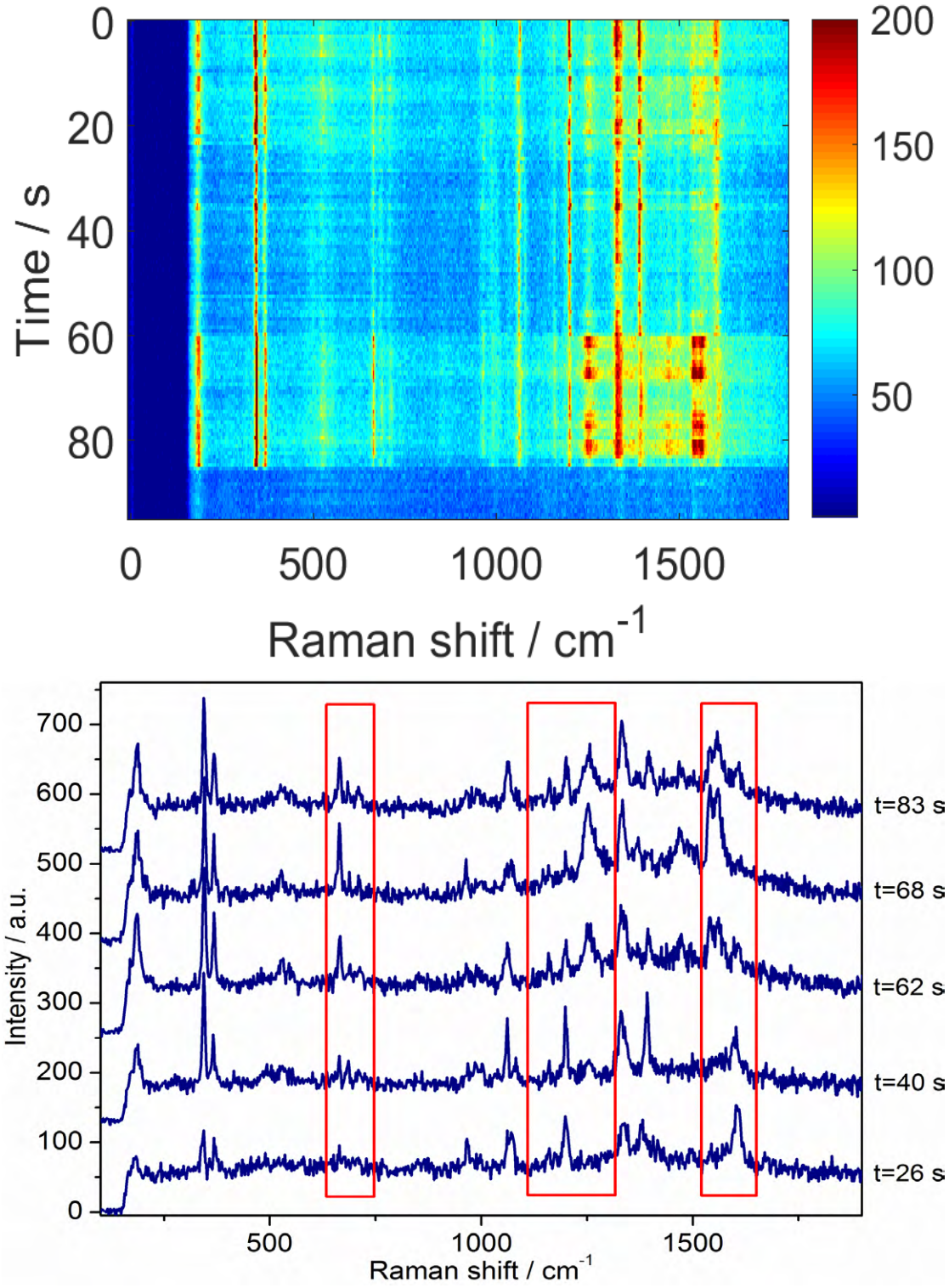

Figure 6.26: A sequence of SERS spectra of a single Pc-d_0 molecule located in a hot spot. Below, selected spectra registered at different moments; the regions of the highest variability are indicated by red rectangles. SERS substrate: 25 µm×47 µm gold NRs, laser excitation: 632.8 nm, laser power: 50 µW, room temperature, acquisition time: 500 ms/spectrum.

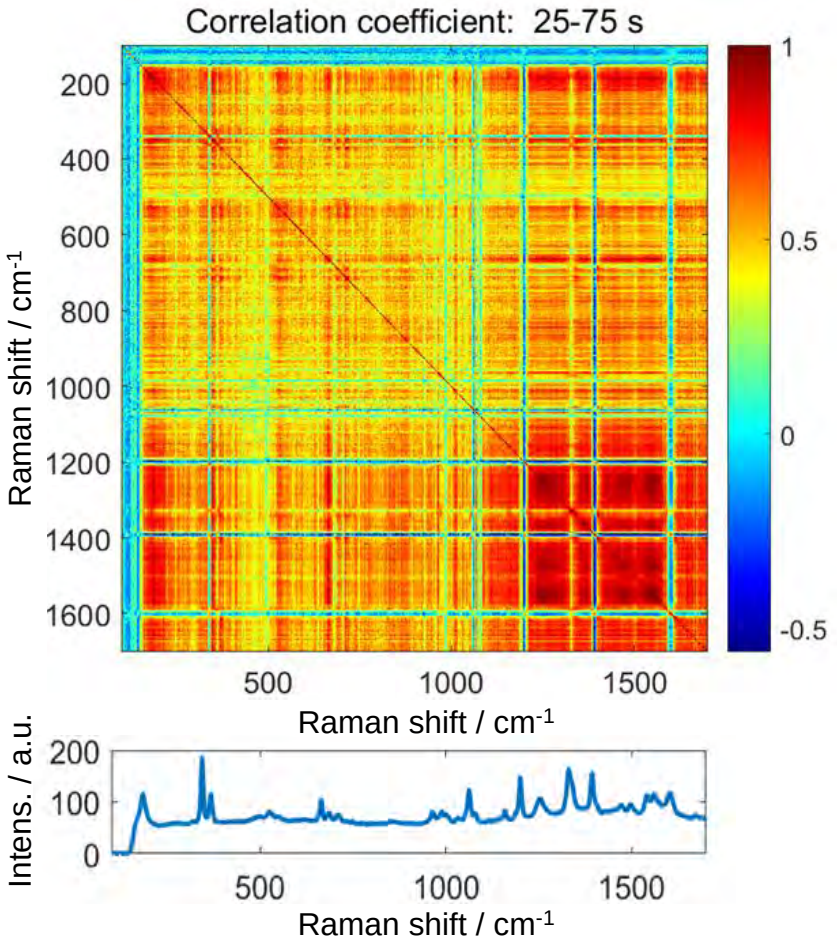

Figure 6.27: Map of correlations between intensities in the SERS spectra calculated for the time trace presented in Fig. 6.26, calculated for the time window of 25-75 s. Below, the spectrum averaged over the selected time interval is shown.

porphycene molecule revealing negative correlations is shown in Figure 6.26. The corresponding map of correlations calculated for a time window of 50 s length, as in the previous case, is presented in Figure 6.27. As one can see, it is remarkably similar to the correlation map shown in Figure 6.25. It means that the groups of vibrations behaving in the same fashion are composed of the same modes in both cases. This observation is of a great importance, as it indicates that the obtained classification of modes is not caused by a hot spot structure, but results from features inherent to porphycene. Therefore, it contains information about a probed molecule itself. Hence, it is worth to compare the classification of vibrations based on the experimental data with the theoretically predicted values of correlation coefficients for intensities of Raman-active vibrations, which are presented in Figure 6.28. To be more specific, for each pair of modes m, n the correlation

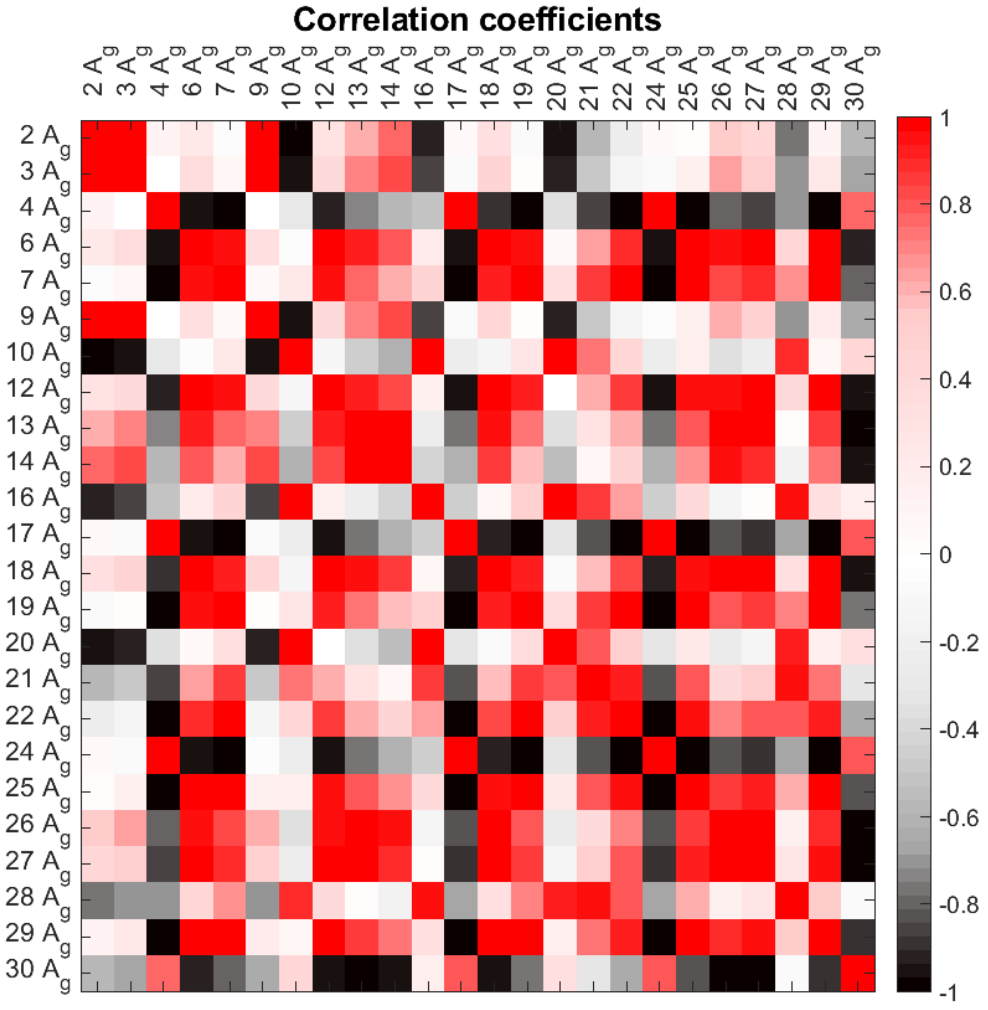

Figure 6.28: Map of theoretically predicted correlation coefficients for different modes.

coefficients were calculated for two series: $\{I^m(0), I^m(\phi), I^m(2\phi), \ldots I^m(N\phi)\}$ and $\{I^n(0), I^n(\phi), I^n(2\phi), \ldots I^n(N\phi)\}$, where $I^k(\alpha)$ denotes the Raman activity of the k-th mode of a porphycene molecule rotated by an angle α and $N+1$ is the length of series. As previously, only rotation around the C_2 axis was considered. To remind, Figure 6.20 shows how the intensities of different Raman-active modes fluctuate upon such rotation. The correlation coefficients gathered in Figure 6.28 were calculated taking into account fast *trans-trans* tautomerism, i.e., the simulated intensities stem from equal contributions of both tautomers. The obtained values of correlation coefficients are independent of a probing step (angle of rotation ϕ) of the Raman activity, until the series cover the full turnover of a molecule,

which happens for $N\phi > 2\pi$. In the case of a map shown in Figure 6.28 the Raman activities were sampled at intervals equal to 0.03 rad ranging from 0 to 2π.

The map shows that while some pairs of modes are strongly positively correlated, the other pairs exhibit strong negative correlations. Based on these values the vibrations can be classified into four groups:

A: $2A_g$, $3A_g$, $9A_g$,

B: $6A_g$, $7A_g$, $12A_g$, $13A_g$, $14A_g$, $18A_g$, $19A_g$, $21A_g$, $22A_g$, $25A_g$, $26A_g$, $27A_g$, $29A_g$,

C: $4A_g$, $17A_g$, $24A_g$, $30A_g$,

D: $10A_g$, $16A_g$, $20A_g$, $28A_g$.

The colors refer to the classification based on the experimental time traces of single porphycene molecules. Some of the Raman-active modes have not been assigned, as their intensities are typically very low in the SERS spectra and therefore the obtained correlation coefficients are unreliable.

As could have been expected, the theoretical predictions of correlation coefficients do not fully agree with the experimentally found relationships between modes. At first glance, the classification based on calculations significantly differs from the one provided by experimental data, but the careful analysis shows that the proposed model describes the measured time-traces relatively well. First of all, both experimental and simulated data indicate strong correlations between the $17A_g$, $24A_g$ and $30A_g$ modes (marked in purple) and their significantly different behaviour from the other vibrations. Secondly, simulations predict the experimentally observed negative correlations between these modes and the $7A_g$, $16A_g$, $18A_g$, $22A_g$, $26A_g$, $28A_g$ and $29A_g$. Furthermore, both calculations and measured time-traces exhibit very strong correlation between intensities of the $2A_g$ and $3A_g$.

The most striking difference between both classifications is that vibrations assigned on the basis of the experimental data to one group (denoted as I, marked in gray) are classified by theoretical model into three distinct groups. It should be emphasized, however, that these groups were separated using some minor features.

For instance, intensities of modes from groups A and B fluctuate quite similarly, but the correlation coefficients within a group composed of the $2A_g$, $3A_g$ and $9A_g$ modes are close to 1. Therefore these vibrations were extracted to a separate group named as A. On the other hand, vibrations assigned to group D behave differently, giving negative correlation coefficients with some modes, especially from group A, which is not the case in the measured time-traces. Hence, it seems that their fluctuations were wrongly described by the proposed mode. Similarly, theoretical predictions fail at describing the behaviour of the $4A_g$ mode. Its intensity does not follow the fluctuation pattern of bands corresponding to the $17A_g$, $24A_g$ and $30A_g$ modes, as calculations suggest.

Finally, let us consider the $12A_g$, $14A_g$, and $20A_g$ modes, which were classified according to the measured time-traces to the same group (denoted as II, marked in yellow). Despite not very high correlation coefficients within this group, ranging from 0.6 to 0.7, these vibrations are classified together, as all the correlation coefficients between these bands and others are non-negative. Based on simulations, the $12A_g$ and $14A_g$ modes were classified as belonging to the same group, while the $20A_g$ vibration was assigned to a different fluctuation pattern. The calculations incorrectly predict that the $20A_g$ mode behaves differently. On the other hand, the correlation coefficients determined for measured time-traces are quite high for vibrations belonging to the theoretically predicted group D ($10A_g$, $16A_g$, $20A_g$, $28A_g$). The lowest value equal to 0.45 was found for the $20A_g$ and $28A_g$ modes. This finding demonstrates that even if some modes were classified differently upon theoretical predictions, still the intensities of vibrations within proposed groups are correlated.

To conclude, even such a simple model, taking into account rotation of a porphycene molecule only around one axis reproduces reasonably well the experimentally found relationships between vibrations. Some incompatibilities may arise from not entirely correct calculations of resonance Raman, which is revealed by the discrepancy between predictions and experimental Raman spectra obtained for different excitations. This naturally affects the shapes of Raman tensors. Nevertheless, a group of vibrations behaving significantly differently from the others and giving negative correlations ($17A_g$, $24A_g$ and $30A_g$) was correctly identified. Only

the finer features on which the classification was based were not fully correctly predicted.

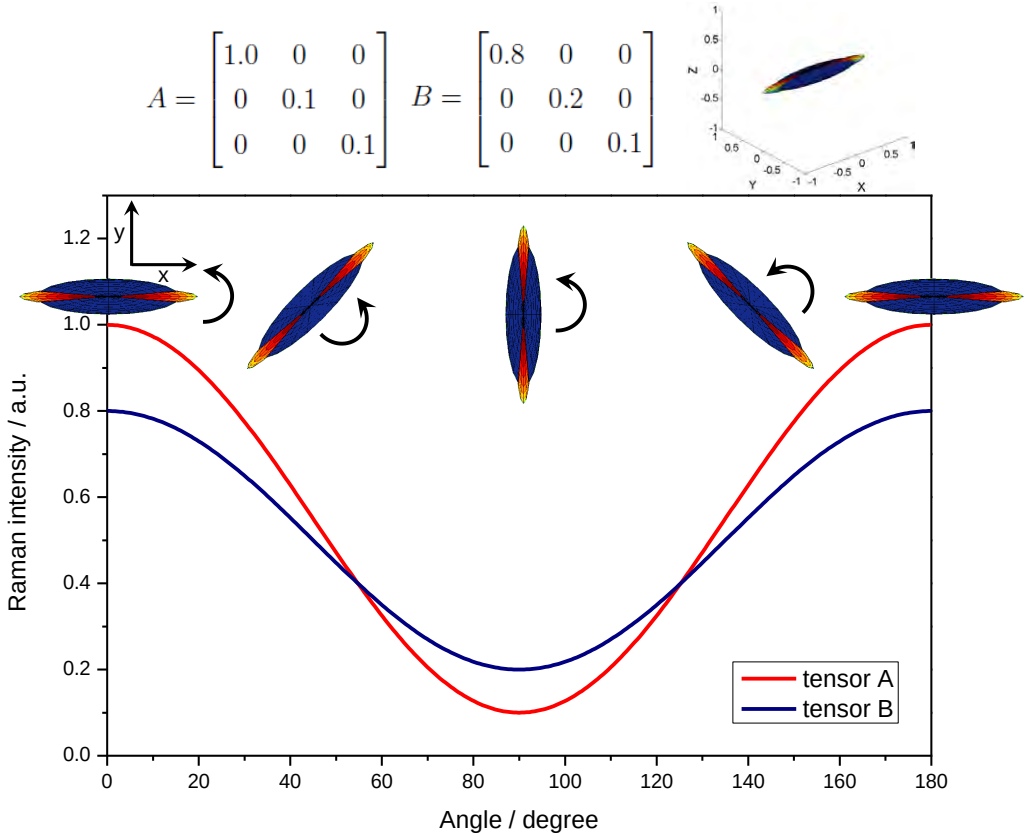

Figure 6.29: The intensity of Raman scattering of two exemplary tensors (parallel) upon rotation along z axis. Above the plot, the selected tensors A and B are given.

Figures 6.29 and 6.30 explain the possible appearance of positive and negative correlations between the intensities of different modes. As a molecule is immobilized in a hot spot, the enhancement of the electromagnetic field occurs mainly along one direction: the axis between nanoparticles, let us assume the x direction. Therefore, the intensity of the Raman scattering is determined by the x components of Raman tensors. Naturally, the rotation of a molecule results in the rearrangement of the Raman tensor, which, combined with the uniaxial nature of electromagnetic field enhancement, often results in a modification of the x component. Figure 6.29 presents two arbitrarily taken tensors A and B, with similar shapes and orientations. As one can see, the intensities of Raman scattering upon rotation change similarly in both cases, which corresponds to high correlation coefficients. However, the positive correlations might also origin from translational movement of a molecule. Then, only the value of electromagnetic field changes, not its direction

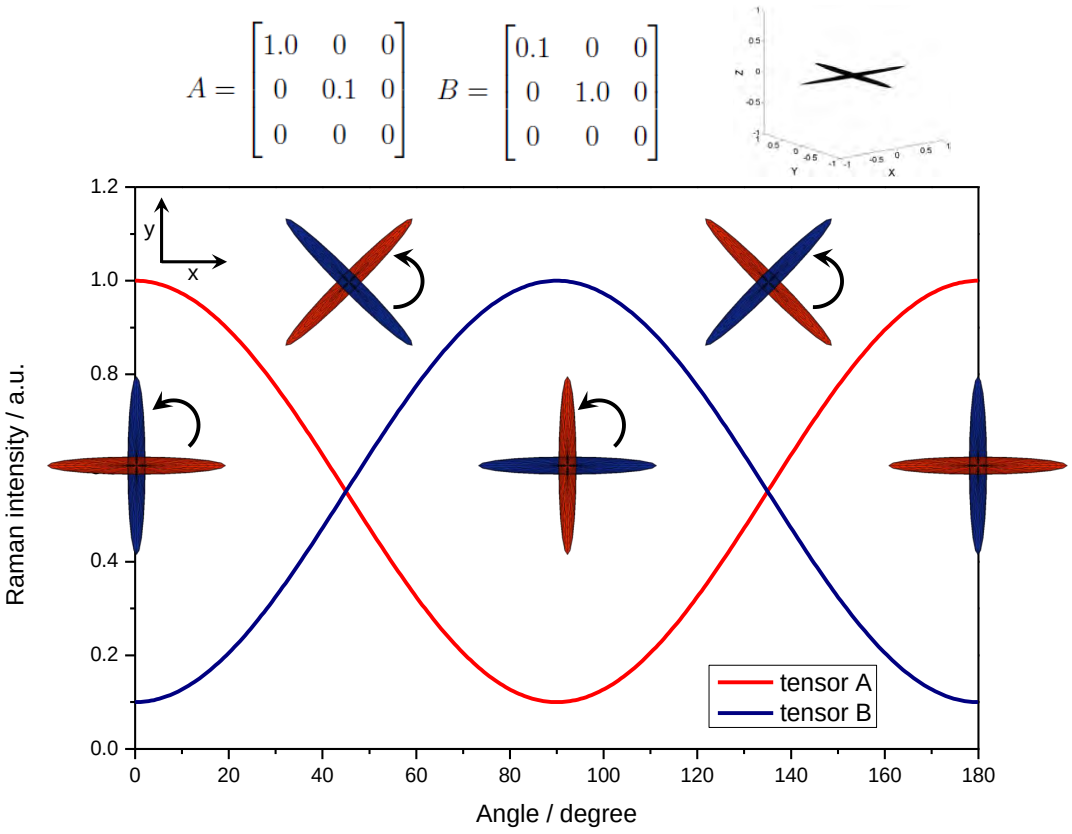

Figure 6.30: The intensity of Raman scattering of two exemplary tensors (orthogonal) upon rotation about the z axis. Above the plot, the selected tensors A and B are given.

regarding the orientation of a molecule, and therefore the corresponding Raman tensors. As a result, the intensities of all of the modes change simultaneously.

The opposite situation is presented in Figure 6.30, where the selected tensors are almost orthogonal. While the intensity determined by one tensor increases, the intensity of the other one decreases, and *vice versa*. Such opposite behaviour is recognized as a negative correlation. This indicates that the presence of negative correlations is a good indicator of the rotation of a molecule in a hot spot.

As it could be expected, this simplified model taking into account rotation only around one axis does not explain all of the observed time evolutions of SERS signal. Figure 6.31 shows one of the recorded time-traces that exhibit a different correlation pattern than previously described. The maps of correlation coefficients obtained for two distinct time windows: 170 - 220 s and 350 - 400 s are shown in Figure 6.32. They indicate different molecular behaviour in these two time windows. While in the former exclusively positive correlations are found, in the

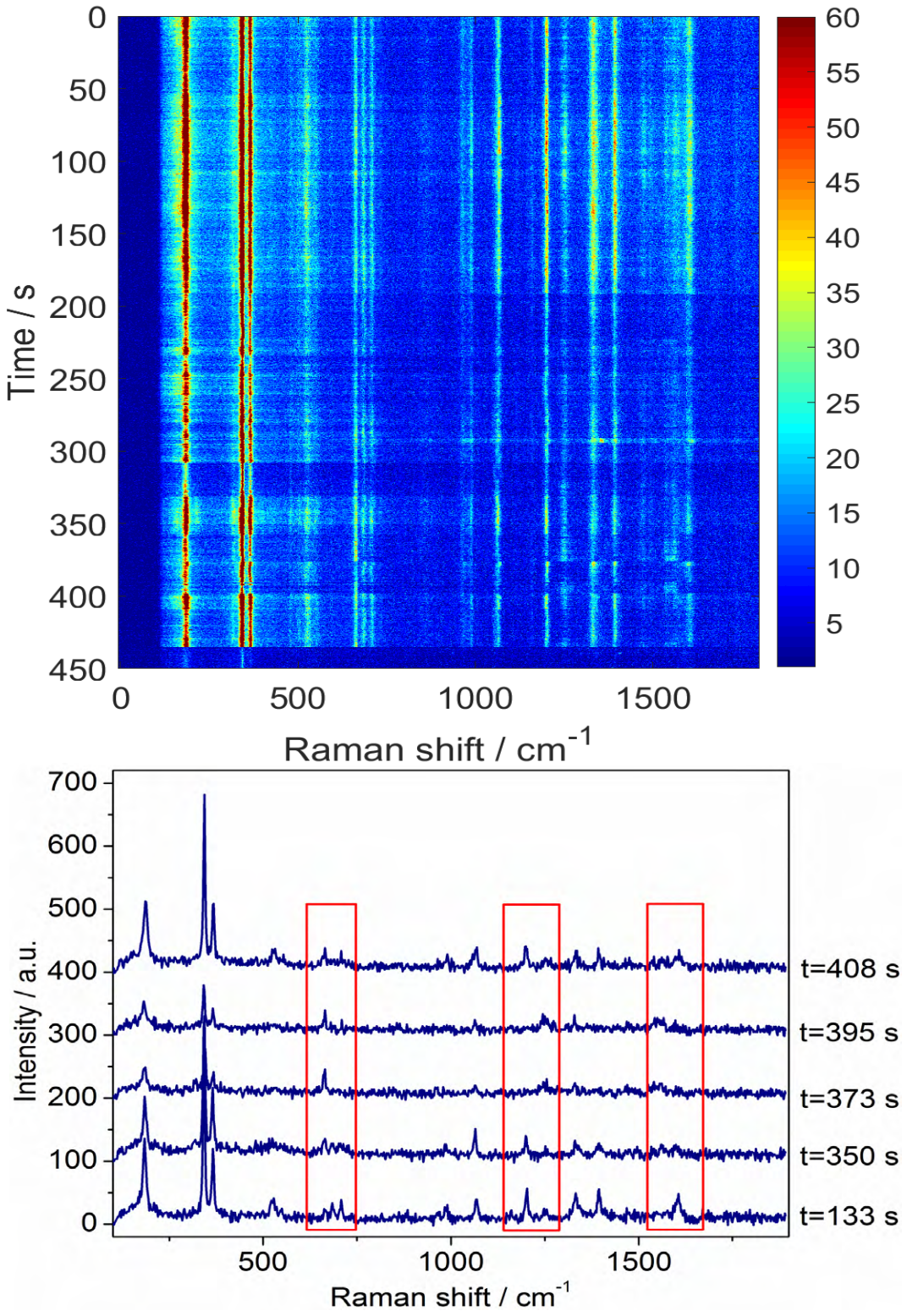

Figure 6.31: A sequence of SERS spectra of a single Pc-d_0 molecule located in a hot spot. Below, selected spectra registered at different moments; the regions of the highest variability are indicated by red rectangles. SERS substrate: 25 µm×47 µm gold NRs, laser excitation: 632.8 nm, laser power: 50 µW, room temperature, acquisition time: 500 ms/spectrum.

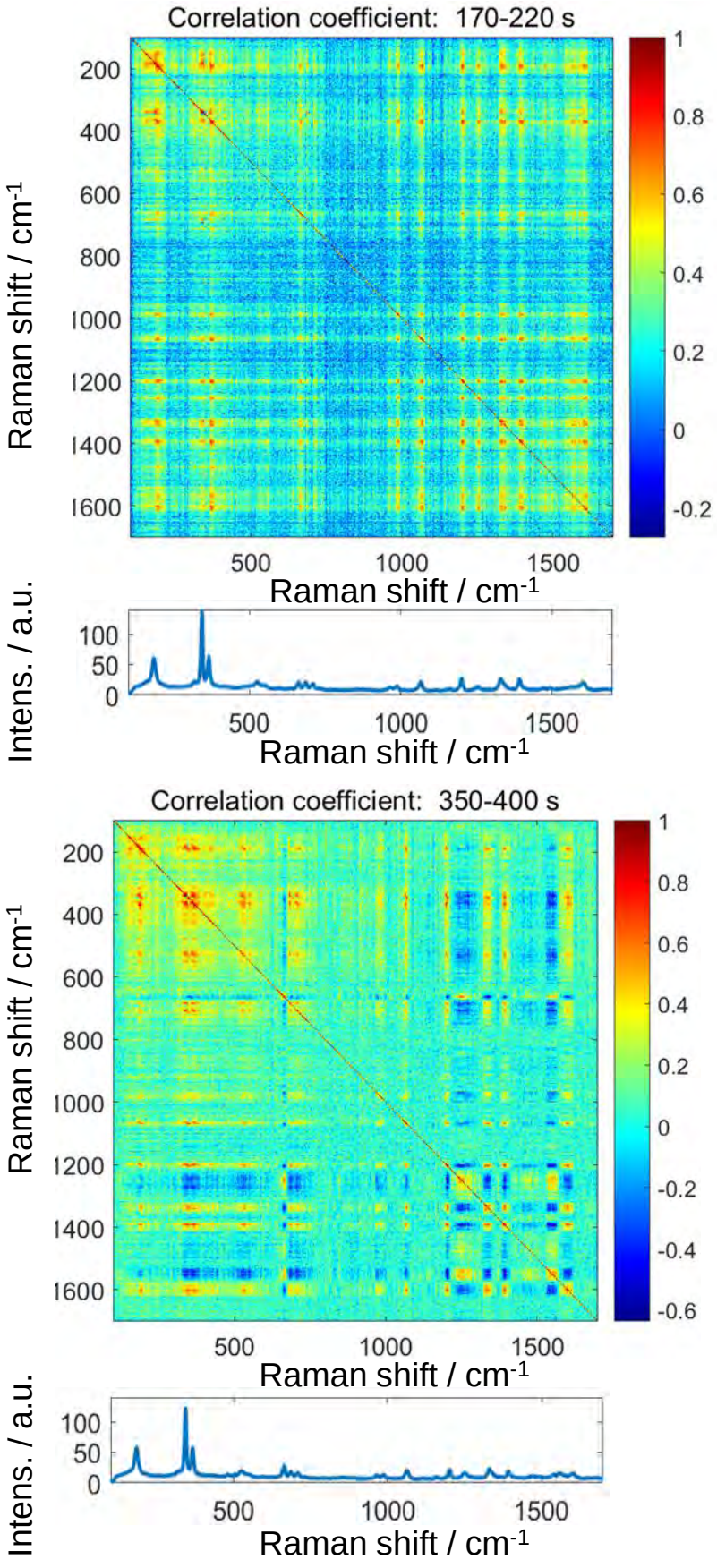

Figure 6.32: Maps of correlations between intensities in the SERS spectra calculated for the time trace presented in Fig. 6.31, calculated for two different time windows, each of 50 s duration. Below each of the maps, the spectra averaged over the selected time intervals are shown.

latter strong negative correlations appear. According to the values obtained the modes can be classified into two groups:

I: $2A_g$, $3A_g$, $4A_g$, $10A_g$ (very weak), $12A_g$, $14A_g$, $16A_g$, $17A_g$, $20A_g$, $24A_g$, $30A_g$

II: $7A_g$, $18A_g$, $22A_g$, $26A_g$, $28A_g$, $29A_g$.

6.6 Analysis of time correlations

There exist several mathematical tools designed for studying equally-spaced time series, which aim at finding temporal relations or answer a question whether a given data set was generated from a random process. Among them, autocorrelation function is one of the most commonly used.

6.6.1 Autocorrelation function

Autocorrelation function provides information about the correlation between points separated by various time delays. Specifically, its value for a time delay τ is equal to the Pearson correlation coefficient determined for values of a given signal $I(t) = \{x_1, \ldots, x_{N-1}, x_N\}$ and its copy delayed by τ:

$$R(\tau) = \frac{\frac{1}{N}\sum_{t=1}^{N-\tau}(x_t - \mu)(x_{t+\tau} - \mu)}{\frac{1}{N}\sum_{t=1}^{N}(x_t - \mu)^2} = \frac{\frac{1}{N}\sum_{t=1}^{N}(x_t - \mu)(x_{t+\tau} - \mu)}{\sigma^2},$$

where σ denotes the standard deviation of a given sequence and μ is its mean value. In spectroscopy, such function is called the autocorrelation function of the signal fluctuation. It can be also defined with a different normalization factor.

Another function, commonly used among the spectroscopists community, is the autocorrelation function of the intensity $I(t)$ defined as:

$$g(\tau) = \frac{< I(t)I(t+\tau) >}{< I(t) >^2}, \tag{6.28}$$

where <> denotes the averaging over time. Hence, it can be written as

$$g(\tau) = \frac{< I(t)I(t+\tau) >}{< I(t) >^2} = \frac{\frac{1}{N-\tau}\sum_{t=1}^{N-\tau} x_t x_{t+\tau}}{\mu^2}. \tag{6.29}$$

Although definitions of $g(\tau)$ and $R(\tau)$ are similar, they are not exactly the same. The relation between them can be determined on the basis of simple transformations:

$$\begin{aligned} R(\tau) &= \frac{\frac{1}{N}\sum_{t=1}^{N-\tau}(x_t-\mu)(x_{t+\tau}-\mu)}{\frac{1}{N}\sum_{t=1}^{N}(x_t-\mu)^2} = \frac{\frac{1}{N}\sum_{t=1}^{N-\tau}(x_t-\mu)(x_{t+\tau}-\mu)}{\sigma^2} = \\ &= \frac{\frac{1}{N}\Big[\sum_{t=1}^{N-\tau} x_t x_{t+\tau} - \mu\sum_{t=1}^{N-\tau}(x_t + x_{t+\tau}) + \mu^2(N-\tau)\Big]}{\sigma^2} \approx \\ &\approx \frac{\frac{1}{N}\sum_{t=1}^{N-\tau} x_t x_{t+\tau} - 2\frac{(N-\tau)}{N}\mu^2 + \frac{N-\tau}{N}\mu^2}{\sigma^2} = \frac{\frac{1}{N}\sum_{t=1}^{N-\tau} x_t x_{t+\tau} - \frac{N-\tau}{N}\mu^2}{\sigma^2}. \end{aligned}$$

As a result, the autocorrelation function of the intensity $g(\tau)$ and the autocorrelation function based on the Pearson correlation coefficients are linked via equation

$$g(\tau) \approx 1 + \frac{N}{N-\tau}\frac{\sigma^2}{\mu^2}R(\tau). \tag{6.30}$$

The equality occurs in the case of stationary time series, i.e., when all statistical parameters, such as mean values, variance etc. do not change with time. Equation 6.30 shows that only for $\tau << N$, which happens for long time traces the values of functions $g(\tau)$ and $R(\tau)$ are linked via linear transformation. This is not the case for the time traces obtained for porphycene, as $N/(N-\tau)$ is not always close to 1. For instance, for $N = 100$ and $\tau = 30$: $N/(N-\tau) = 1.43$. Therefore, for the measured time traces both autocorrelation functions $g(\tau)$ and $R(\tau)$ have been calculated.

Figure 6.33 shows the autocorrelation functions for the intensities of the SERS signal at 343, 483, and 665 cm^{-1} taken from a hot spot presented in Figure 6.24. For a comparison, two distinct time windows were selected: 200 - 250 s and 300 - 350 s. Obviously, the autocorrelation functions differ significantly for these selected time

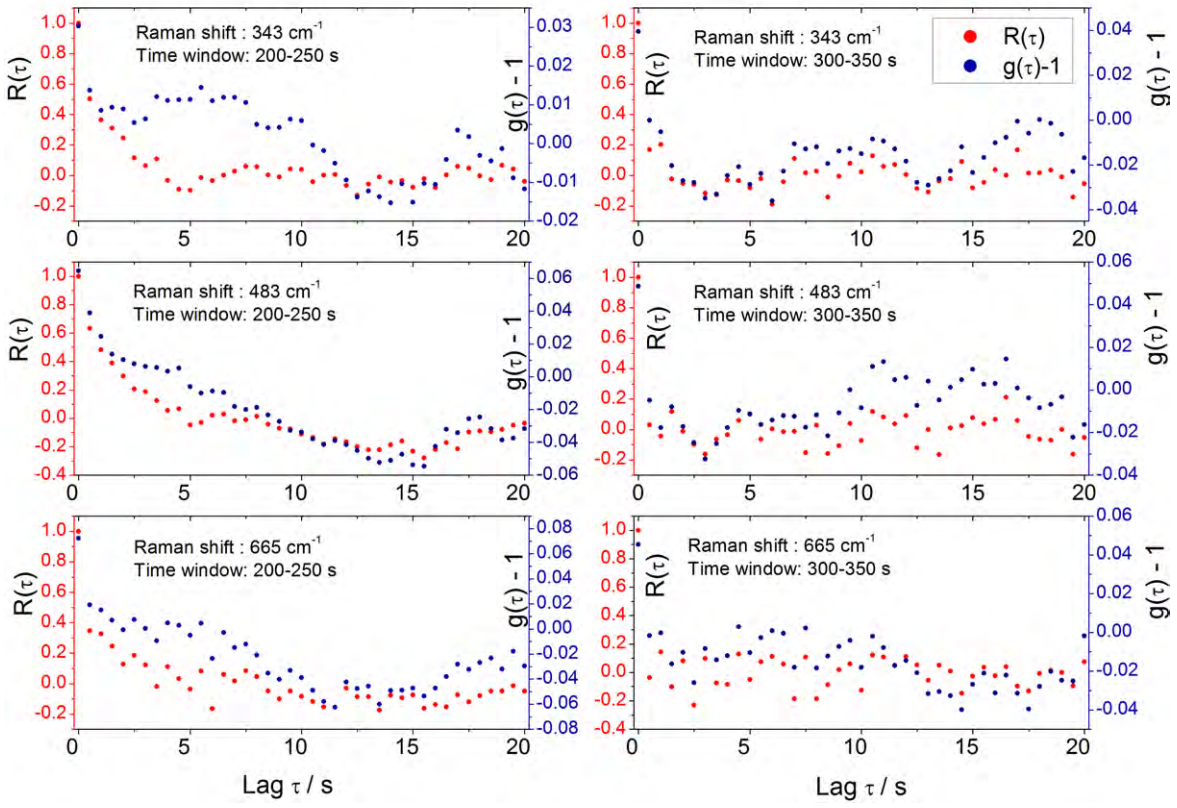

Figure 6.33: The comparison of autocorrelation functions obtained for the time trace presented in Figure 6.24 at 343, 483, and 665 cm^{-1} for two different time windows: 200 - 250 s and 300 - 350 s.

domains. This finding offers another strong evidence that a porphycene molecule behaves differently during these two distinct time windows. The analysis of the signal intensities in the time domain of 200 - 250 s shows that the correlation extends over a few seconds. On the other hand, in the time window 300 - 350 s the values of the autocorrelation function immediately reach values close to 0. This is typical for a sequence generated from a random process. Such behaviour may suggest that in the time window 200 - 250 s molecular rotation happens, while the fluctuations of the intensities in the period of 300 - 350 s originate mostly from fast translational diffusion. Nevertheless, without a proper model these autocorrelation functions do not provide direct information about physical parameters, such as rotational diffusion time. Unfortunately, according to our knowledge there is no model describing the behaviour of a Raman signal upon rotation of a molecule. The model relating rotational motion to the autocorrelation function of the fluorescence signal[152] cannot be applied to the Raman scattering signal. As was already shown,

the intensities of different Raman modes change differently upon molecular rotation due to the tensorial nature of Raman scattering. For instance, the intensity of a mode described by a spherical Raman tensor is completely insensitive to the molecular orientation. At the same time, the intensity of Raman modes described by the elongated Raman tensors can be extremely sensitive to the molecular orientation. Therefore, the autocorrelation function strongly depends on the vibrational mode, more specifically on the related Raman tensor. Figure 6.34 presents the theoretically predicted autocorrelation functions of intensity fluctuations $R(\tau)$ upon rotation of porphycene around C_2 axis. For a comparison, three vibrational modes combined with two different sampling steps referring to an angle of rotation ϕ at which Raman activity was probed. Each time trace is composed of $N = 100$ points

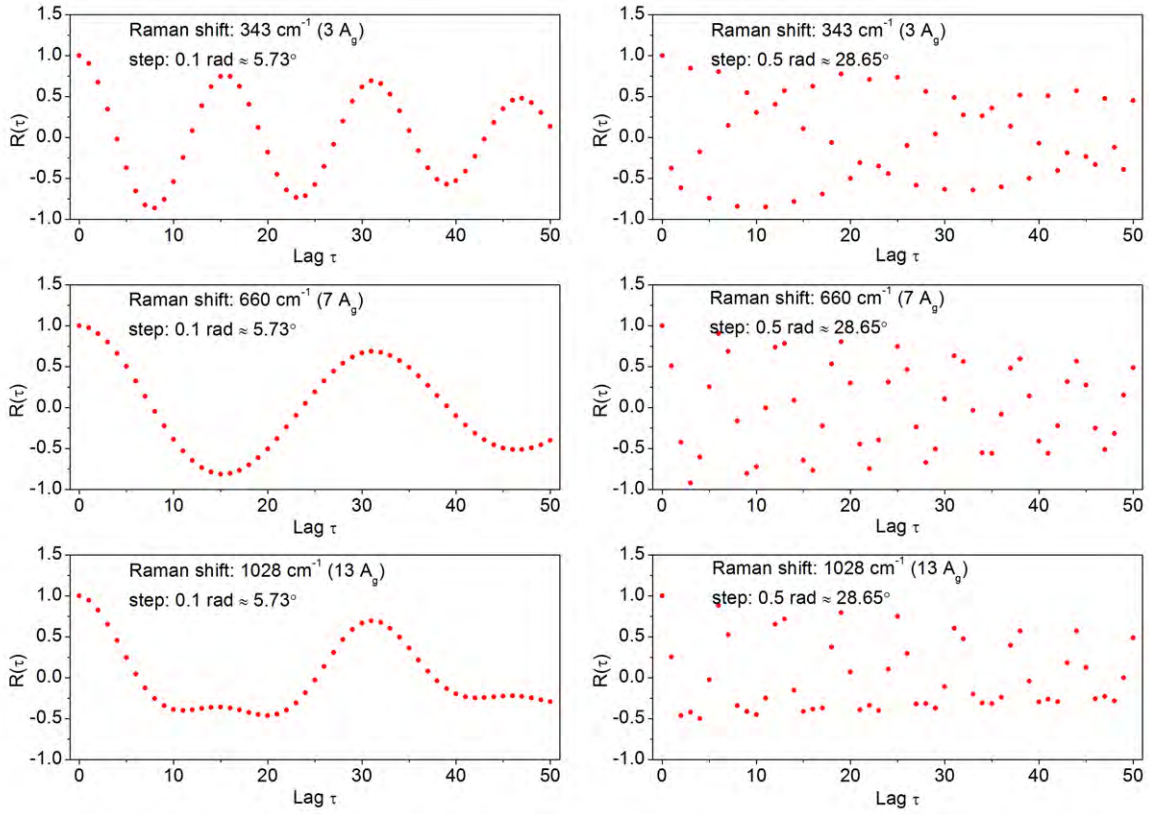

Figure 6.34: The comparison of autocorrelation functions calculated for fluctuations of intensities of three selected Raman modes upon rotation of porphycene (two different rotation steps were considered).

and was generated under assumption that a molecule rotates at a constant speed, which is rather unlikely in the case of a molecule immobilized in a hot spot. The autocorrelation function depends on both the shape of the Raman tensor and the sampling angle. As the angle between successive sampling points is getting bigger,

the autocorrelation functions exhibit larger variability. This shows that in order to analyze the experimentally obtained autocorrelation functions, the knowledge of Raman tensors is required. Moreover, in the real systems for larger time lags τ the autocorrelation functions tends to 0 as the rotational speed is fluctuating and the data are affected by the noise. To conclude, the careful investigation of autocorrelation functions aimed at extracting parameters such as rotational diffusion time seems challenging. But still, such studies might provide a deeper insight into the dynamics of a molecule located in a hot spot.

6.6.2 Fourier transform

Another approach to investigate the temporal patterns in time series is provided by Fourier analysis, which provides a tool for decomposing a signal into oscillatory components. Such transformation is extremely useful, as it reveals periodicities in the input data and determines the relative weights of periodic components. In the case of a discrete signal, i.e., a time series consisting of a finite sequence, which may be obtained by sampling a continuous-time signal, discrete Fourier transform (DFT) can be applied. It transforms a sequence of N complex numbers $\{x_0, x_1, \ldots, x_{N-1}\}$ into another sequence of complex numbers $\{X_0, X_1, \ldots, X_{N-1}\}$ according to the equation

$$X_k = \sum_{n=0}^{N-1} x_n \omega_N^{kn} \quad (k = 0, 1, \ldots, N-1), \tag{6.31}$$

where $\omega_N = \exp\left(-i\frac{2\pi}{N}\right)$. It is related to conversion from a time domain to a frequency domain.

Figure 6.35 presents the results of Fourier transformation obtained for sequences composed of intensities of the SERS signal from a time trace shown in Figure 6.24. Three different Raman shifts were selected: 343, 483, and 665 cm^{-1} and two time windows: 200 - 250 s and 300 - 350 s. The obtained results prove that there is no periodicity in the fluctuations of the SERS signal intensity over time on a larger scale, as no frequency with a relatively high amplitude is present in the spectrum upon Fourier transform. Therefore, if the rotation happens, which is very probable,

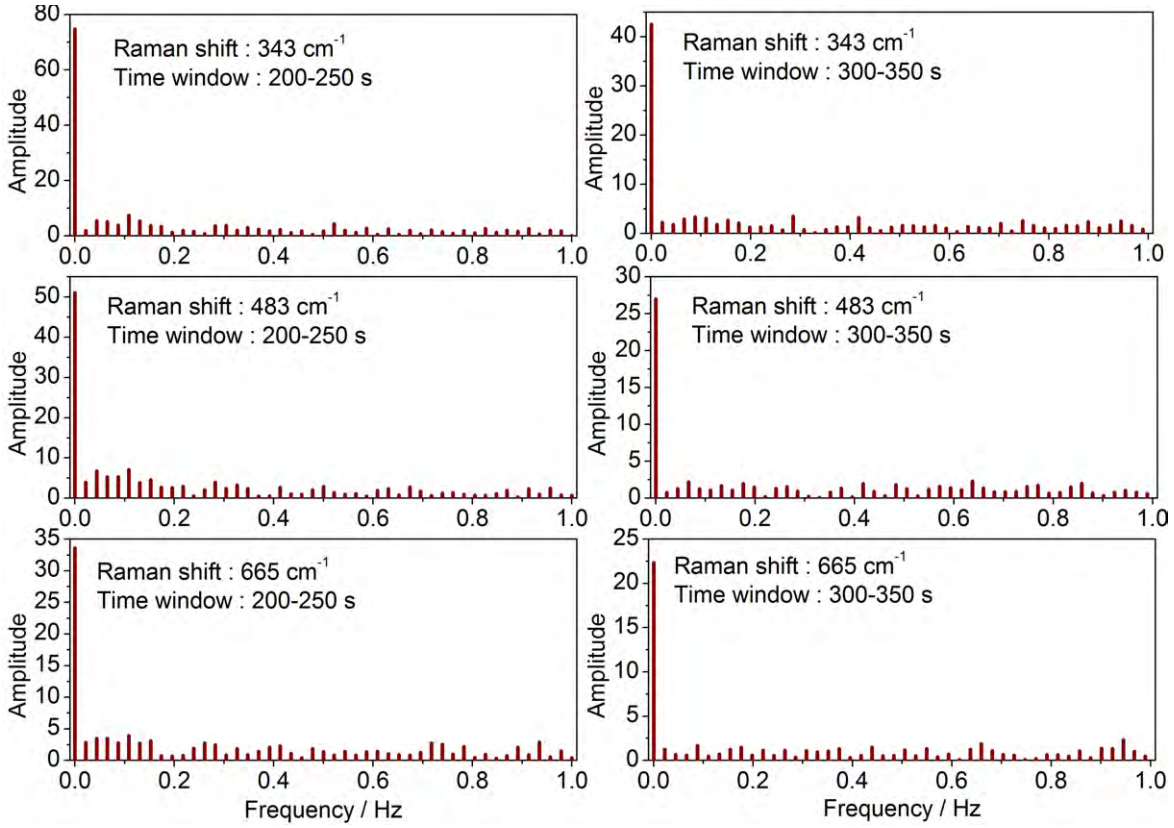

Figure 6.35: The comparison of Fourier transforms obtained for time trace presented in Figure 6.24 at 343, 483 and 665 cm^{-1} for two different time windows: 200-250 s and 300 - 350 s.

its velocity is not constant over time. Moreover, it most likely coexists with the translational diffusion.

6.7 Correlations between modes based on spectra recorded from different hot spots

The previously described analysis is limited to relatively long time traces. Unfortunately, only a small percentage of the recorded time evolution profiles fulfill this condition, since vast majority of them consists of only a few spectra. On the other hand, we have gathered an extensive collection of spectra from different hot spots, containing several thousand items. Therefore, a method to extract information about the relationships between intensities of vibrations based on such

data set would be eminently desired. Moreover, such approach would provide results averaged over the hot spot structures, since each spectrum corresponds to a slightly different arrangement of nanoparticles. However, this leads to a problem: the associated LSPRs are slightly changed, since they are extremely sensitive to size and shape of nanoparticles. This, in turn, results in various enhancement in different regions of the spectrum. While in some hot spots the low frequency modes are much more strongly enhanced with respect to high frequency ones, the other hot spots may exhibit completely different distribution of the enhancement factors. This effect is illustrated in Fig. 6.36. In the first spectrum the enhancement is comparable in the whole region, in the second one low energy bands are more enhanced than the bands around 1300 cm^{-1}, while in the third spectrum the situation is reversed.

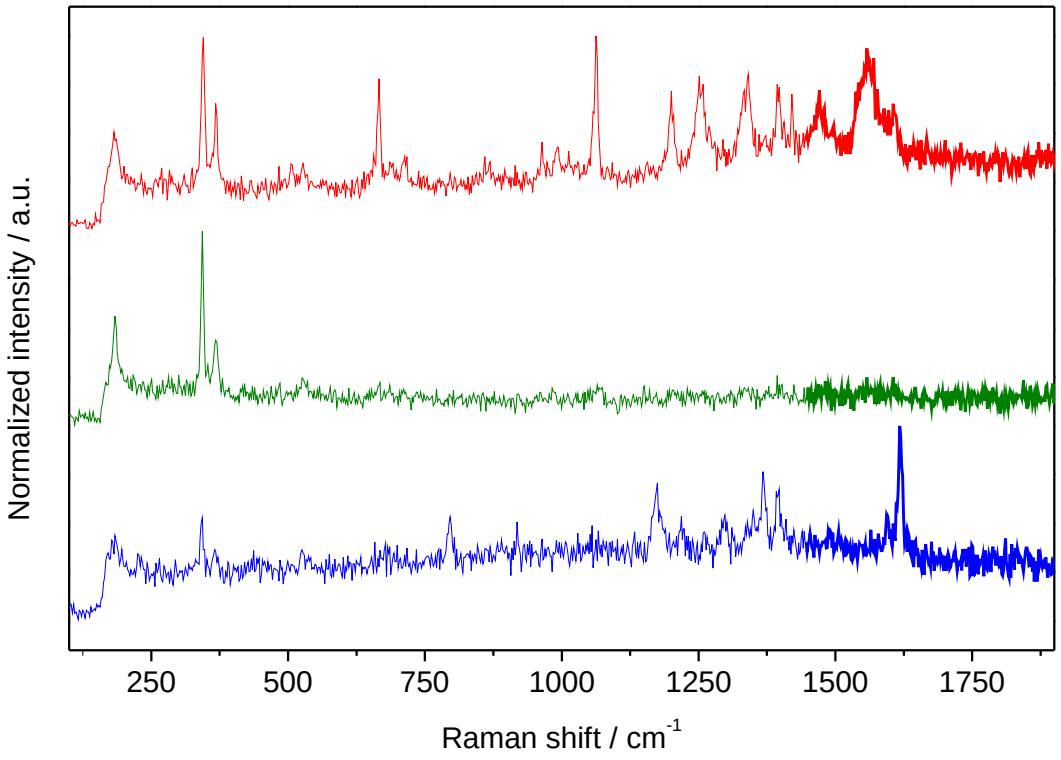

Figure 6.36: SERRS spectra of single molecules of porphycene obtained from different hot spots. SERS substrate: Au nanoparticles obtained by electrodeposition at a three phase junction, laser excitation: 632.8 nm, laser power: 50 µW, room temperature.

In order to avoid the influence of LSPR shift, the whole spectra cannot be analyzed at once. Since the closely lying bands are hardly affected by this effect (LSPR are

usually quite broad), the whole spectral region should be divided into smaller parts, which should be tested separately.

After selecting a region, we can fit the part of a spectrum with the specified number of Lorentzian-shaped functions, which provide better results than Gaussians. An example of fitting in given in Fig. 6.37. The curve fitting was done automatically with the help of a computer program. In the case of error above 10% the performed fitting was discarded, and the spectrum was not included into further analysis. Then, the relative ratios of peaks area for each pair of bands was calculated. The histograms of the obtained ratios for three selected peaks are shown in Figure 6.38.

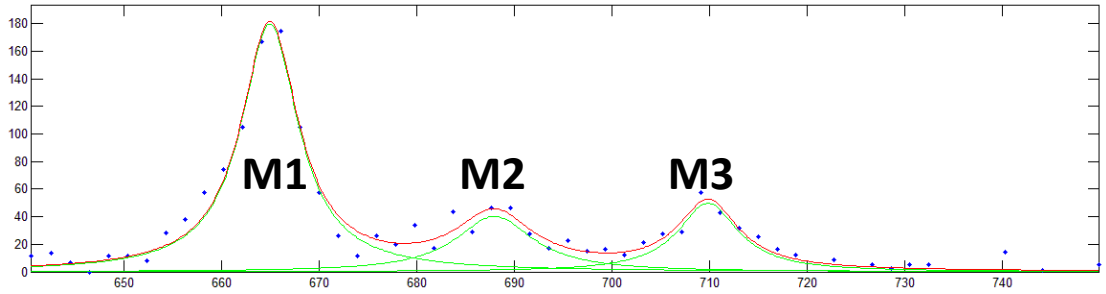

Figure 6.37: Example of fitting experimental points (blue dots) in the region 640-750 cm^{-1} with Lorentzian-shaped peaks.

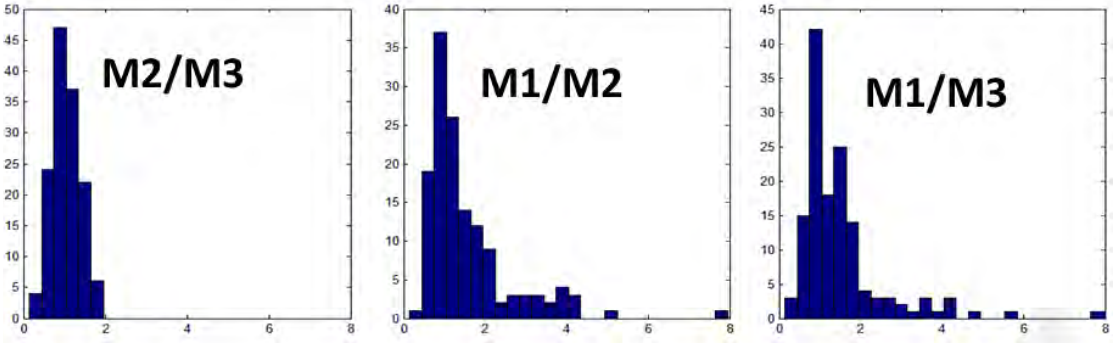

Figure 6.38: Histograms of values of relative surfaces of selected modes: 664, 684 and 708 cm^{-1} calculated for spectra from different hot spots. From left side: M2/M3, M1/M2 and M1/M3 intensity ratios.

We can see that the shape of distribution of values $M2/M3$ is completely different than for $M1/M2$ or $M1/M3$, it is much narrower. Such shape of histogram indicates strong correlation between the integral intensities of $M2$ and $M3$. At the same time the distribution of values $M1/M2$ and $M1/M3$ is much broader, revealing no strong dependencies between these pairs of Raman intensities.

6.8 Conclusions

The intensity of Raman scattering strongly depends on the polarizability of a molecule, which is mathematically described as a tensor α and can be graphically represented by an ellipsoid. Moreover, the enhancement of the electromagnetic field in a hot spot is highly anisotropic. Therefore, as it was shown in this chapter, intensity fluctuations observed in single molecule spectra may provide a wealth of information.

First, the approximate orientation of a molecule immobilized in a hot spot can be inferred from the relative intensities of Raman modes. Second, with the help of theoretical predictions, some Raman-active modes can be assigned. In the case of porphycene, the previous assignment was improved.

Finally, in the case of porphycene placed in plasmonic environment, the presence of fast *trans-trans* tautomerization reaction was confirmed. This conclusion was drawn on the basis of the experimental spectra combined with the spectra predicted for various molecular orientations, including and excluding tautomerization. One of the key indicator was the intensity ratio between the bands corresponding to 2 A_g and 3 A_g modes. The experimental values were much closer to the predicted ratios for different orientations.

In this chapter two approaches to the investigation of correlation coefficients between Raman peaks intensities were presented: directly from time traces of single molecules or from spectra recorded from different time-traces. The measured time-traces revealed that the observed correlation patterns may change over time, which may result from various molecular movements. For instance, start of rotation. Moreover, the same correlation patterns were observed for porphycene molecules immobilized in different hot spots, which indicates that they contain information of porphycene molecule itself. Furthermore, the experimentally observed negative correlations between some vibrations cannot be easily justified by simple translation of a molecule within a hot spot. Such behaviour may be rationalized by the presence of rotations. Finally, the spectra predicted using a simplified model of porphycene rotating around the C_2 axis agree reasonably well with the experimental data.

Chapter 7

The influence of *tert*-butyl substituents on single molecule SERRS spectra

The aim of this chapter is to compare detectability on a single molecule level within the family of porphycenes substituted on the pyrrole rings with *tert*-butyl groups.

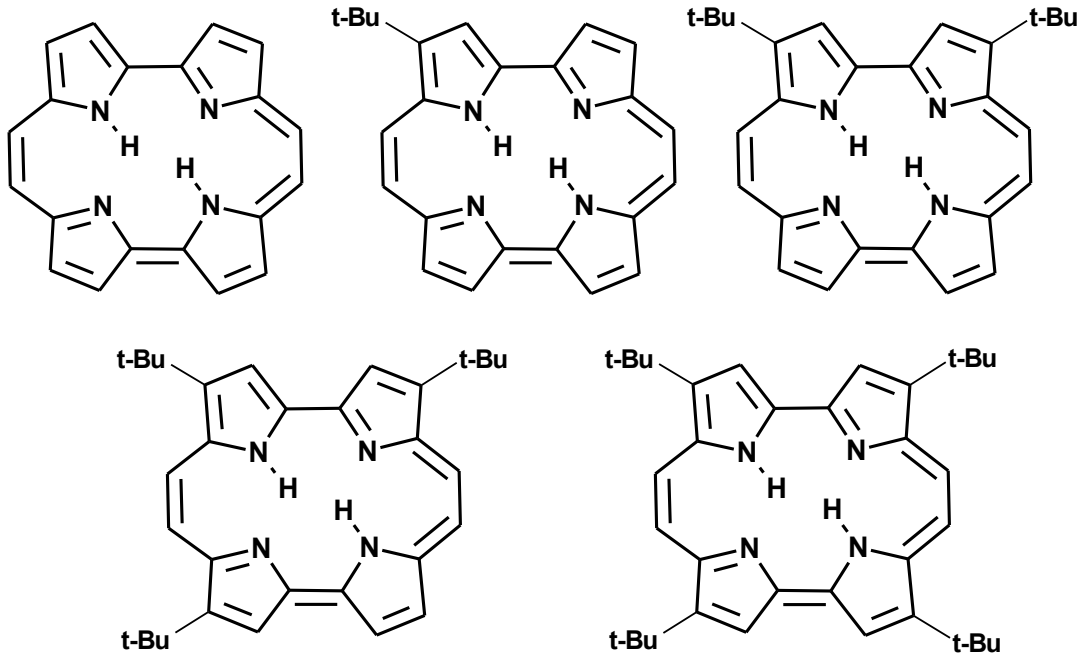

Figure 7.1: Structures of the investigated *tert*-butyl porphycenes.

The enhancement of Raman scattering close to a metallic nanostructure originates from both the electromagnetic mechanism and charge transfer effect. It it very difficult to disentangle these two contributions. Moreover, if the incident light is in resonance with an electronic transition, the Raman signal is significantly enhanced, which considerably facilitates the observation of molecules on a single molecule level. This is the case for porphycene excited by 632.8 nm laser line, which energy corresponds to S_0-S_1 transition. The enhancement due to resonance in porphycene was estimated as $7.3 \cdot 10^2$. However, under such conditions, not only Raman scattering is enhanced, but also fluorescence occurs, which, on the other hand, is efficiently quenched by metal surface. Competition between Raman enhancement and fluorescence quenching determines the detectability of the SERRS spectrum over the enhanced/quenched fluorescence background.

Within the family of *tert*-butyl substituted derivatives, the electronic structure is almost unchanged, therefore the contribution to the enhancement due to resonance may be considered of the same value. It is this underlying assumption that makes it possible to relate the number of observed single molecule events for each of the species with their relative "detectability", provided 1:1 ratio of the investigated compounds is used (the same concentration of each of them). As a result, we can determine the impact of steric hindrance on both SERS spectra and fluorescence quenching efficiency.

7.1 Photophysical and spectroscopic characteristics of *tert*-butyl porphycene derivatives

Fundamental photophysical properties, including absorption and emission spectra, and quantum yields in the family of *tert*-butyl porphycenes are very similar, as shown in Figure 7.2 and Table 7.1.

Figures 7.3, 7.4, 7.5 and 7.6 present the Raman spectra of the investigated compounds excited with 514 and 785 nm laser lines. They do not differ much due to high similarity in molecular structure, however the intensity ratio between modes observed around 1550 and 1610 cm^{-1} is markedly different, not only for distinct

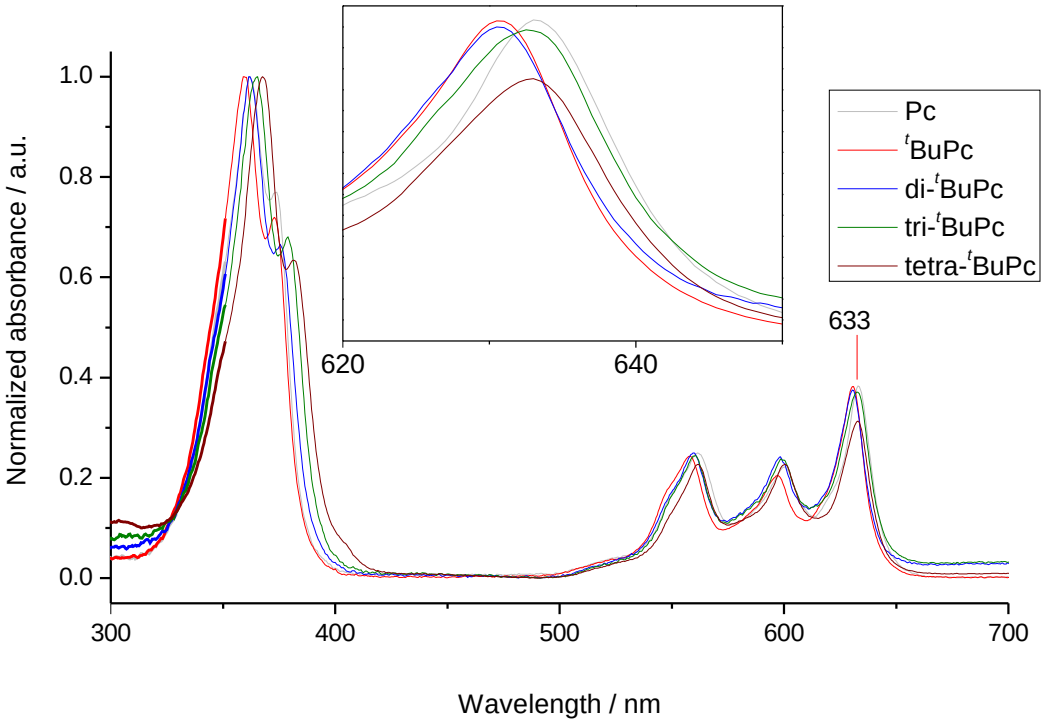

Figure 7.2: The absorption spectra of *tert*-butyl substituted porphycenes in ethanol solution.

Table 7.1: Absorption and emission peaks, and fluorescence quantum yields for *tert*-butyl porphycenes. The experiments were carried out at 293 K in ethanol solutions.

	λ_{abs} (nm)	λ_{em} (nm)	Φ_{fl}
Pc	633.0; 600.0; 561.0; 362.0	630	0.40
^{t}BuPc	630.5; 597.0; 558.0; 360.0	632	0.39
di-^{t}BuPc	630.5; 598.5; 559.5; 362.0	633	0.34
tri-^{t}BuPc	632.5; 598.5; 560.5; 365.0	636	0.35
tetra-^{t}BuPc	633.0; 600.5; 562.0; 367.5	636	0.32

species, but also for various laser lines. The low frequency region is not shown for mono-*tert*-butyl porphcyene and di-*tert*-butyl porphycene excited at 785 nm due to overlay with the tail of fluorescence. Moreover, strong fluorescence hampered observation of Raman spectrum excited with 633 nm laser line. As far as SERS spectra (excited with 633 nm laser line) are concerned, the most diagnostic region allowing the distinction between species in the family of *tert*-butyl substituted porphycenes is the low frequency region. Figure 7.7 presents the SERS spectra

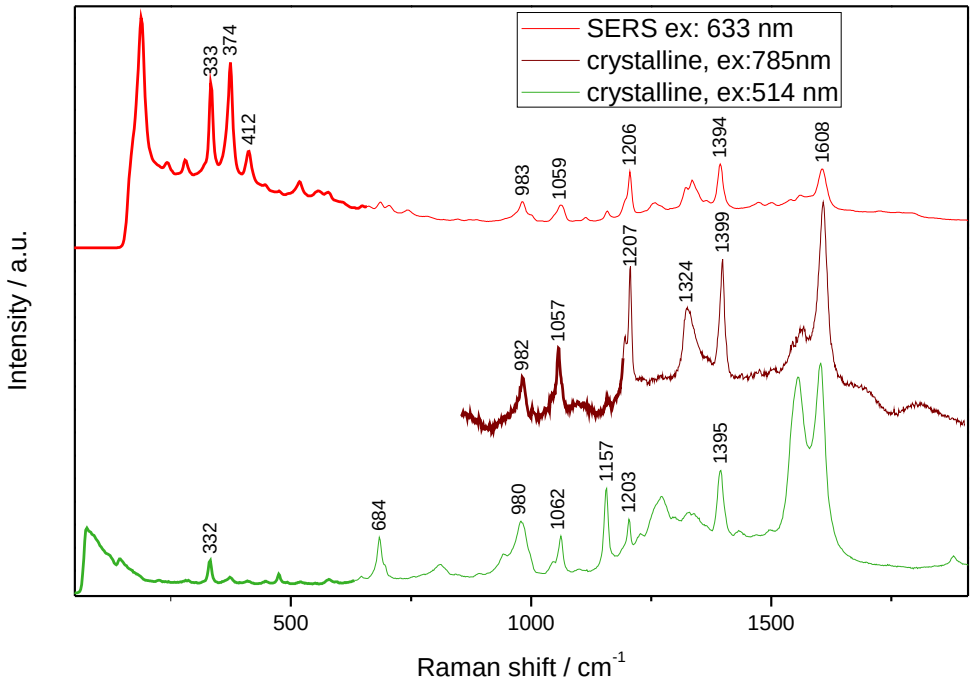

Figure 7.3: SERS spectrum of mono-*tert*-butylporphycene (SERS substrate: 25 µm×47 µm gold NRs, laser excitation: 632.8 nm, laser power: 50 µW, room temperature) and Raman spectra of a crystalline sample excited at 785 and 514 nm.

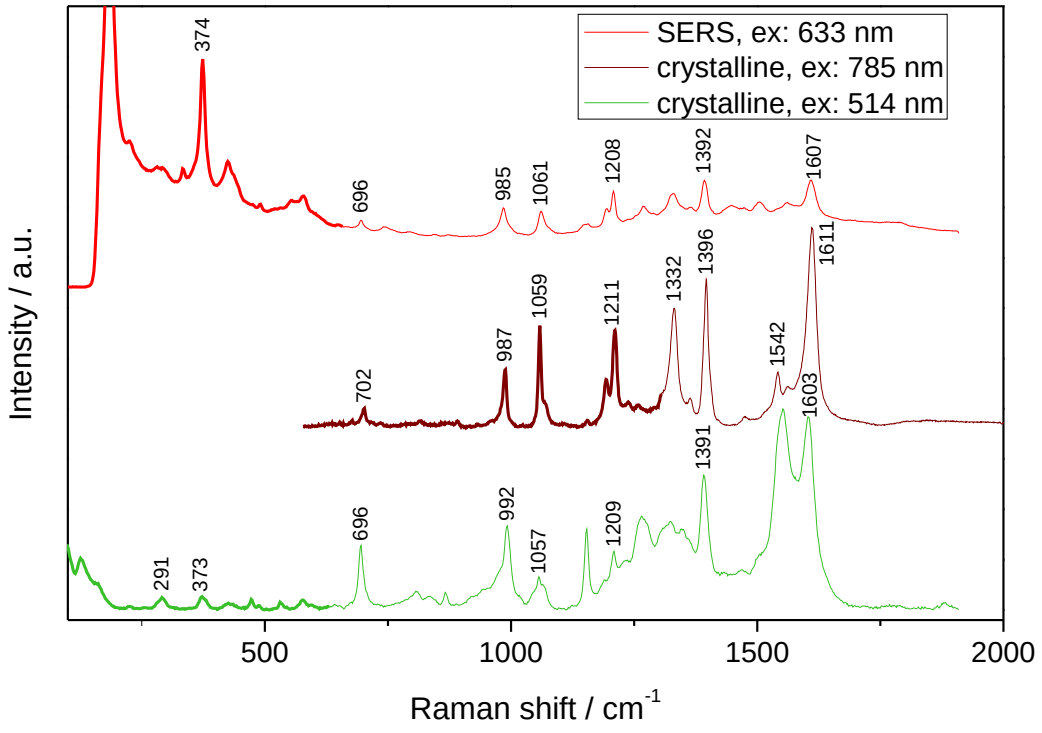

Figure 7.4: SERS spectrum of di-*tert*-butylporphycene (SERS substrate: 25 µm×47 µm gold NRs, laser excitation: 632.8 nm, laser power: 50 µW, room temperature) and Raman spectra of a crystalline sample excited at 785 and 514 nm.

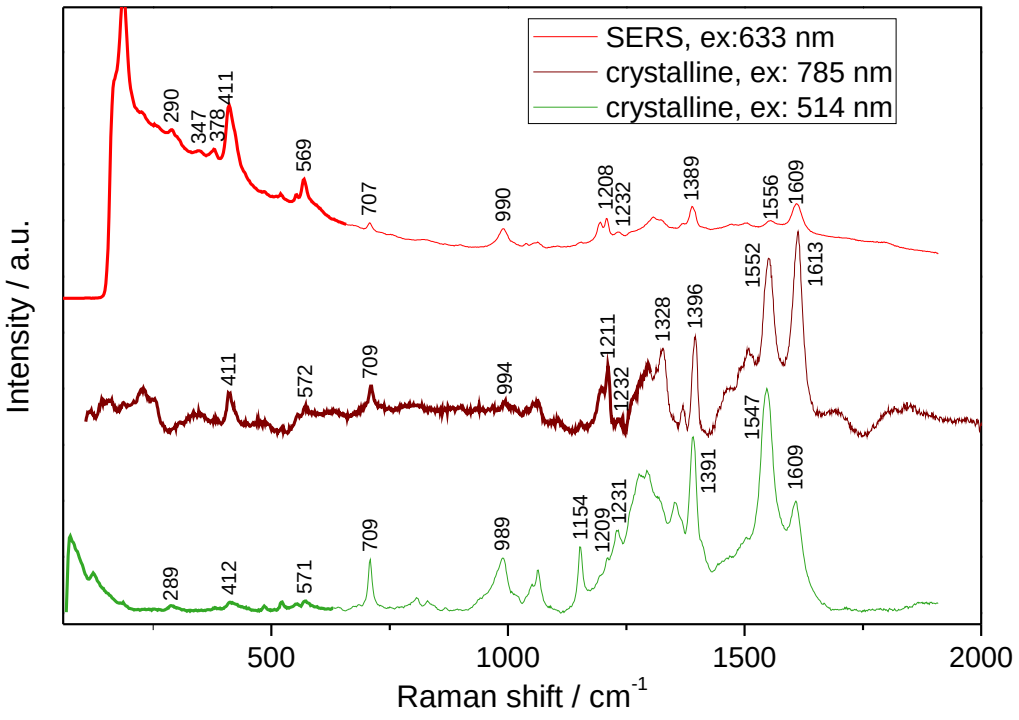

Figure 7.5: SERS spectrum of tri-*tert*-butylporphycene (SERS substrate: 25 µm×47 µm gold NRs, laser excitation: 632.8 nm, laser power: 50 µW, room temperature) and Raman spectra of a crystalline sample excited at 785 and 514 nm.

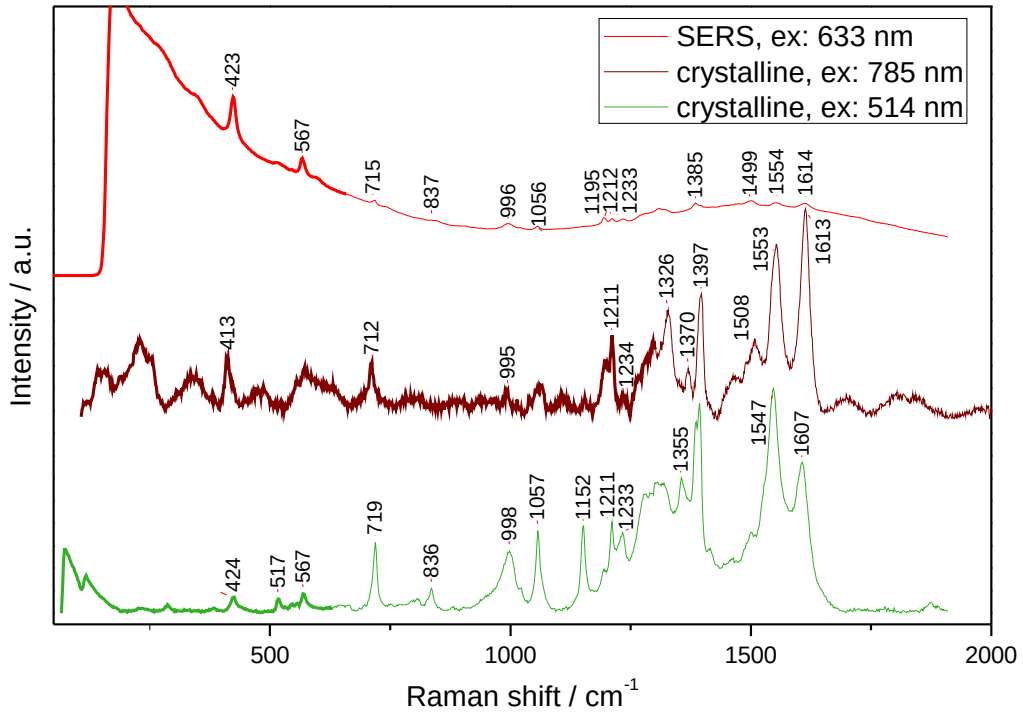

Figure 7.6: SERS spectrum of tetra-*tert*-butylporphycene (SERS substrate: 25 µm×47 µm gold NRs, laser excitation: 632.8 nm, laser power: 50 µW, room temperature) and Raman spectra of a crystalline sample excited at 785 and 514 nm.

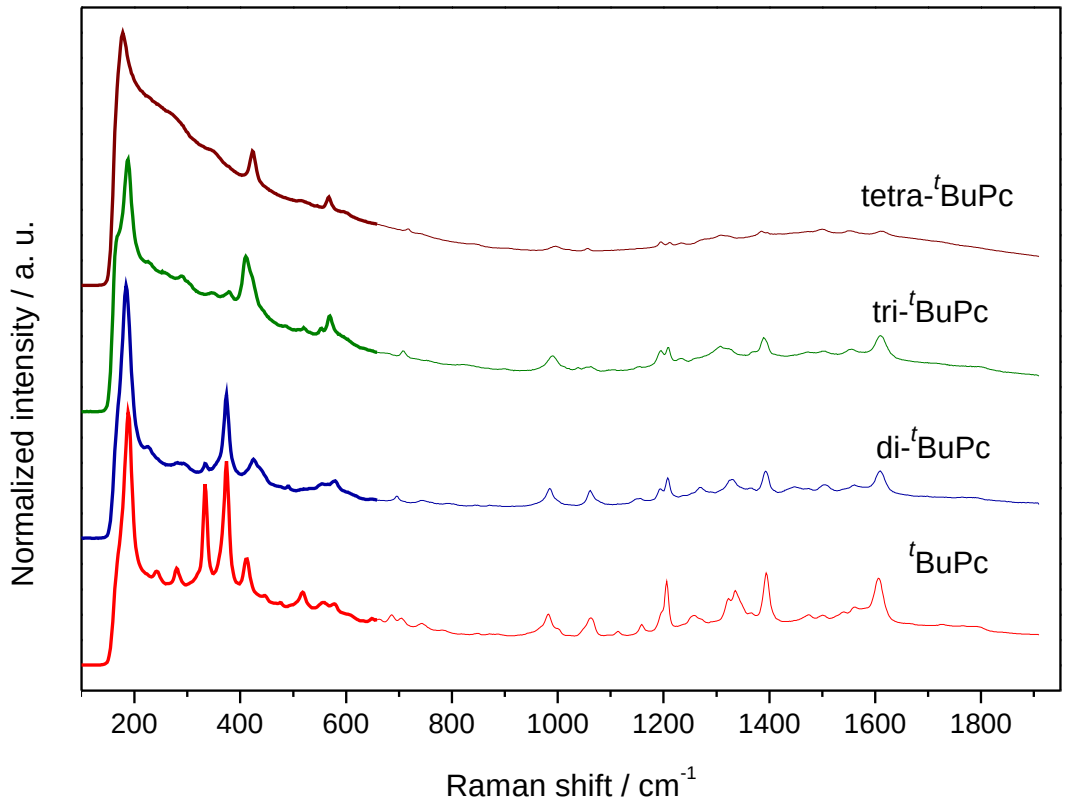

Figure 7.7: The SERS spectra of *tert*-butyl substituted porphycenes. SERS substrate: 25 µm×47 µm gold NRs, laser excitation: 632.8 nm, laser power: 50 µW, room temperature.

averaged over an area of 60x60 µm^2 obtained by drop-casting ethanol solution of 10^{-6} M concentration of the chromophore on a SERS substrate. The measured signal originates from both Raman scattering and luminescence. As it was mentioned earlier, under resonant conditions the competition between Raman scattering and luminescence determines detectability by the SERS technique. Therefore, it is worth to compare ratios between Raman signal intensities and luminescence background for different porphycenes. In order to calculate these ratios, the measured spectra were decomposed using spline functions with selected nodes (specific for each spectrum). Two examples of such decomposition are presented in Figure 7.8.

The calculated ratios for the studied compounds are gathered in Table 7.2. However, it should be emphasized that these ratios are specific for given conditions: SERS substrate and number of adsorbed molecules. Therefore, the meaningful comparison between selected compounds may be drawn only after measurements

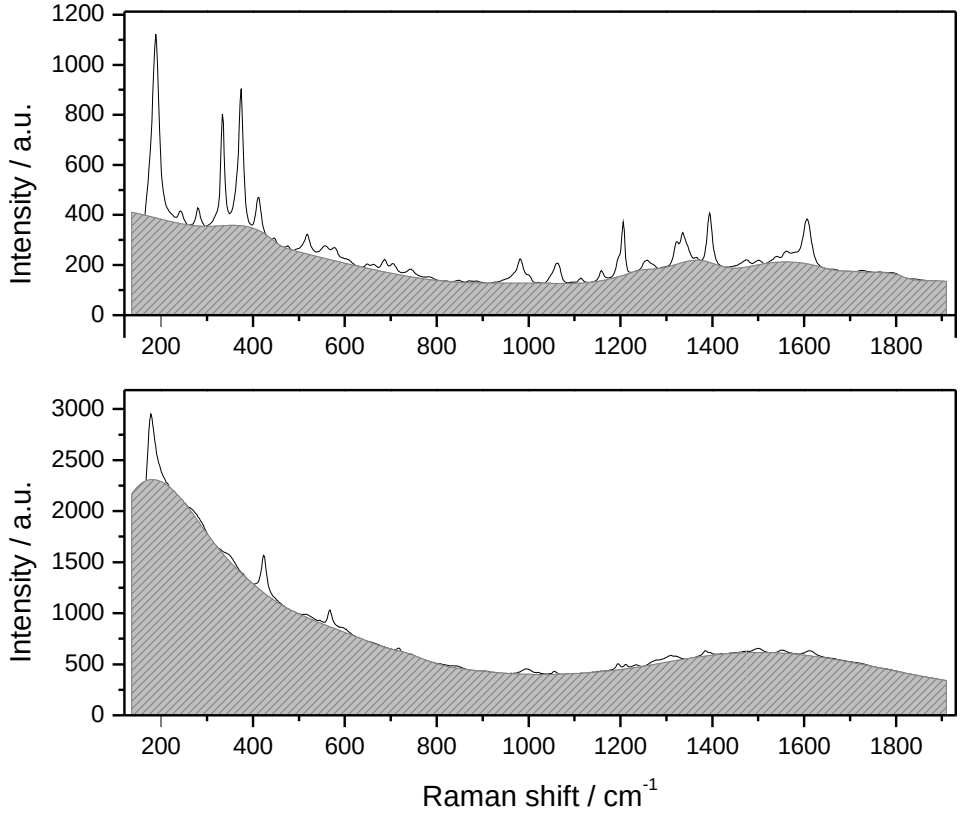

Figure 7.8: SERS spectra of mono- (top) and tetra-*tert*-butylporphycene (bottom) with marked luminescence background. SERS substrate: 25 µm×47 µm gold NRs, laser excitation: 632.8 nm, laser power: 50 µW, room temperature.

Table 7.2: Ratios of the integrated Raman scattering signal to the luminescence background in the SERS spectra of *tert*-butyl porphycenes (sample preparation and experimental conditions were the same for all compounds).

	Raman signal/luminescene
^{t}BuPc	0.177
di-^{t}BuPc	0.145
tri-^{t}BuPc	0.071
tetra-^{t}BuPc	0.029

of samples prepared by following the same procedure. We decided to use drop-casting, since it allowed us to control the number of molecules adsorbed on a surface. However, this method does not guarantee homogeneity across the whole sample. The number of molecules adsorbed near the edge of a drop deposited on a SERS substrate is probably higher than in the centre. Therefore, the area close to the central part was chosen for measurements. Presumably, immersion of SERS

substrates in solutions containing chromophores would provide better homogeneity, but then the number of the adsorbed molecules remains unknown. Moreover, most likely these numbers are different for each compound due to differences in surface affinities. Admittedly, our approach does not guarantee that the measured signal comes from virtually the same number of molecules. However, the trend of a decreasing ratio between Raman signal and fluorescence is clear: the more *tert*-butyl groups are attached, the higher is the fluorescence background. This is accompanied by lower Raman intensities.

Moreover, it is worth noting that such comparison (between selected species) would not be possible on every SERS substrate. Among many tested ones, vast majority did not allow us to observe any Raman features for tetra-*tert*-butyl porphycene at room temperature due to strong fluorescence. It was possible only on SERS substrates prepared from commercially available nanorods stabilized with CTAB. Then, on top of a high fluorescence background, Raman modes were still visible.

7.2 Single molecule character of mono-*tert*-butyl porphycene and di-*tert*-butyl porphycene

In the case of *tert*-butyl substituted porphycenes we could not apply the same procedure of deuteration as used for bare porphycene, since boiling these compounds in concentrated deuterated sulfuric acid at 180 °C would deprive them of *tert*-butyl groups. Therefore we did not apply the bi-analyte approach with isotopologues of the same species to proof the single molecule character of the obtained spectra. However, the registered time traces at sufficiently low concentration exhibited characteristic features for single molecules: fluctuations of Raman intensities and sudden disappearance of Raman peaks (step-like character). Figures 7.9 and 7.10 present single molecule SERS spectra registered from different hot spots for mono-*tert*-butylporphycene and di-*tert*-butylporphycene, respectively. In the majority of the recorded spectra, as in the case of bare porphycene, low frequency vibrations were more enhanced than vibrations in the high frequency region.

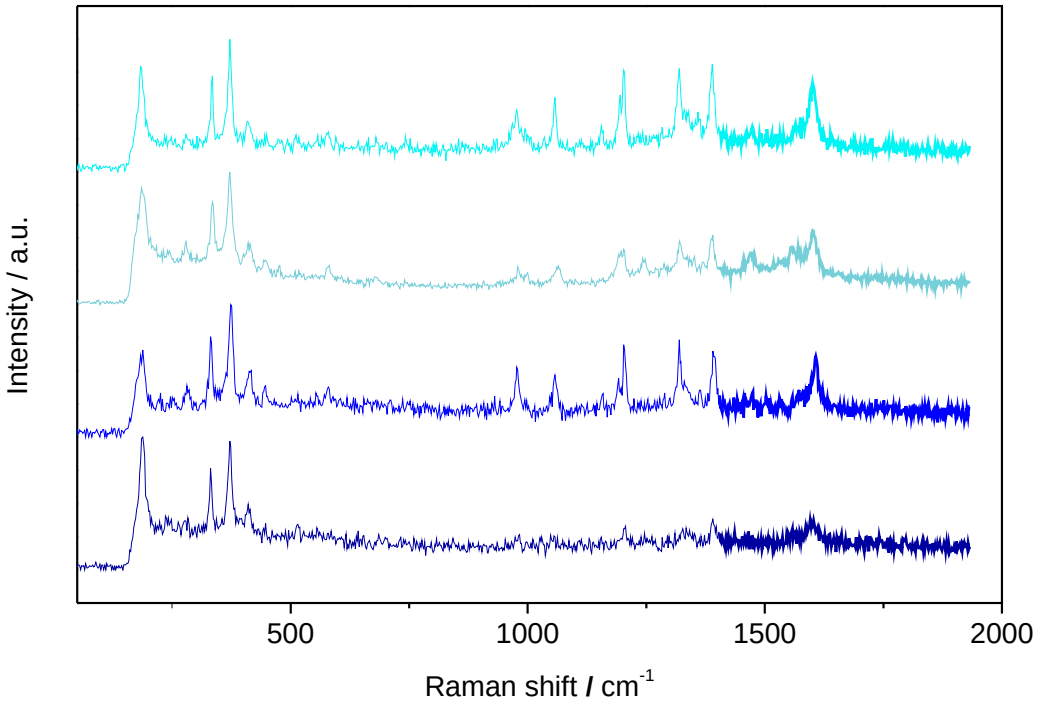

Figure 7.9: Single molecule SERS spectra of mono-*tert*-butylporphycene recorded from different hot spots. SERS substrate: Au nanoparticles obtained by electrodeposition at a three phase junction, laser excitation: 632.8 nm, laser power: 50 µW, room temperature.

Interestingly, we have observed two types of luminescence background behaviour. To illustrate this we present the results obtained for mono-*tert*-butyl porphycene adsorbed on electrochemically deposited nanoparticles at a three phase junction. The time traces shown in Figure 7.11 were measured on the same SERS substrate, but the drop-casted solutions had different concentrations of the chromophore: 10^{-7} and 10^{-8} M, respectively. In both cases Raman bands are visible on a fluorescence background, however the spectral shape of this luminescence is different for these two time traces. This may be caused by a distinct hot spot structure, which results in a shift of localized surface plasmon resonance. Moreover, this is also supported by significantly different intensity ratios of the selected Raman modes (e.g., low and high frequency ones) for these two cases. The sudden disappearance of the Raman signal in both cases confirms a single molecule character of the measured spectra. Interestingly, for a sample with a lower number of chromophore molecules, fluorescence background vanished at the same time as Raman bands. This indicates that most likely the observed fluorescence originates from

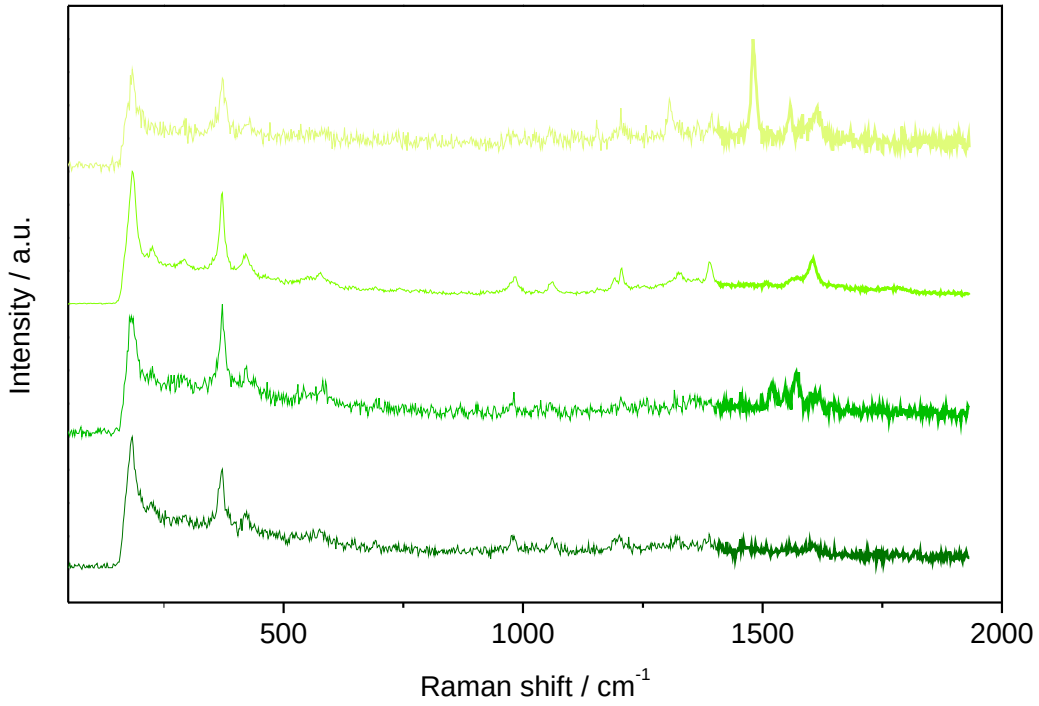

Figure 7.10: Single molecule SERS spectra of di-*tert*-butylporphycene recorded from different hot spots. SERS substrate: Au nanoparticles obtained by electrodeposition at a three phase junction, laser excitation: 632.8 nm, laser power: 50 µW, room temperature.

the same molecule as the Raman signal. The simultaneous observation of Raman signal and emission from the same single molecule is an important outcome. Even though a molecule was very close to the metal surface, as evidenced by strong enhancement of Raman scattering, the fluorescence was not fully quenched. So far, in most of the reported cases fluorescence background was attributed to the emission from a nanostructure, not from the molecule itself.[94]

In the case of time traces recorded for a sample with a higher number of chromophore molecules adsorbed, the fluorescence background did not vanish completely while the Raman signal bleached. Nevertheless, it is worth noting that at the same time when Raman peaks disappeared the fluorescence background noticeably decreased. The remaining luminescence most likely originates from molecules adsorbed on a SERS substrate, but not located in hot spots. Otherwise, the fluorescence should be much more efficiently quenched, while Raman scattering should be more enhanced. During the measurements of mono-*tert*-butyl porphycene and di-*tert*-butyl porphycene it turned out that observation of single molecules is more

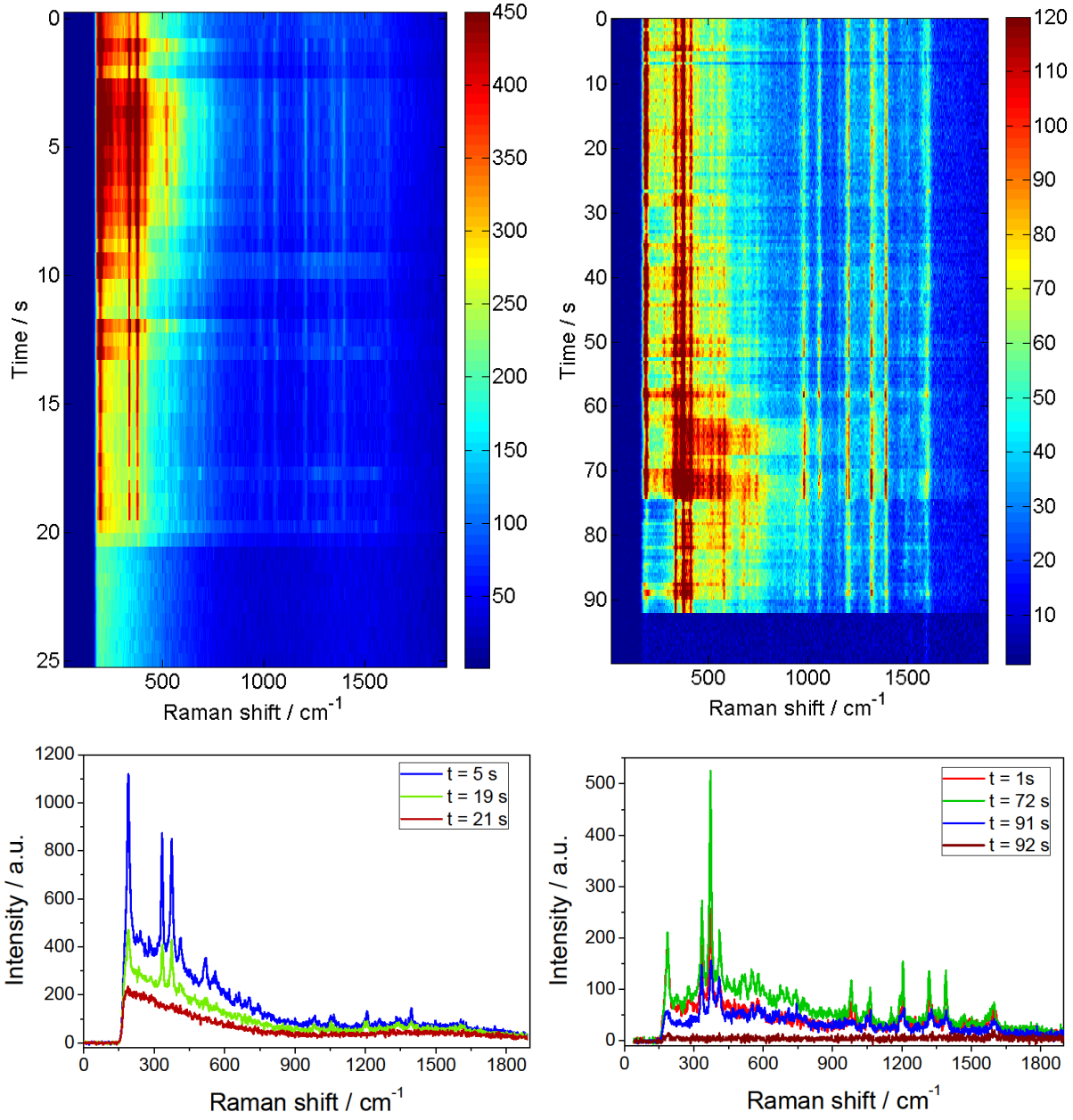

Figure 7.11: Time traces of mono-*tert*-butylporphycenes recorded for two different samples (prepared from ethanol solution of concentrations 10^{-7} M (left) and 10^{-8} M (right)). SERS substrate: Au nanoparticles obtained by electrodeposition at a three phase junction, laser excitation: 632.8 nm, laser power: 50 µW, room temperature.

challenging than for bare porphycene, therefore we decided to compare detectability between these species.

7.3 Histograms of occurrence of single molecule events

SERS substrates with multiple hot spots, essential to provide statistical reliability, allowed us to perform a semi-quantitative comparison of relative detectability on a single molecule level of differently substituted porphycenes. The simplest way is to perform the Raman mapping of a SERS substrate on which a drop of solution containing each of the studied species at the same concentration is dropcast. In this case dropcasting is preferred over immersing a SERS substrate in a solution due to possible differences in affinities to the used surface, which in turn may result in different numbers of molecules adsorbed on a SERS substrate. Owing to high spectral specificity of Raman spectroscopy, those measured SERS spectra which reveal Raman features (typically less than a few percent, other contain only noise) allow for assignment of the measured spectra to one of the studied compounds. On this basis, histograms of the number of the observed single molecule events of each species can be produced. The comparison between these numbers gives us relative detectability. If the detectability of each of the studied compounds were the same, we should observe approximately 1:1:1 ratio (in the case of mixture containing three species). Deviations from such distribution may originate from different 'hot spot affinities', resonance contribution, charge transfer contribution, diffusion coefficients, etc.

7.3.1 Comparison of detectability among *tert*-butyl substituted porphycenes

Figure 7.12 presents the results of the above described approach for ethanol solution containing three species: porphycene-d_{12}, mono-*tert*-butyl porphycene (blue)

and di-*tert*-butyl porphycene, each of 10^{-8} M concentration. We used porphycene-d_{12} instead of porphycene-d_0 because the substituted compounds may contain bare porphycene as a contamination.

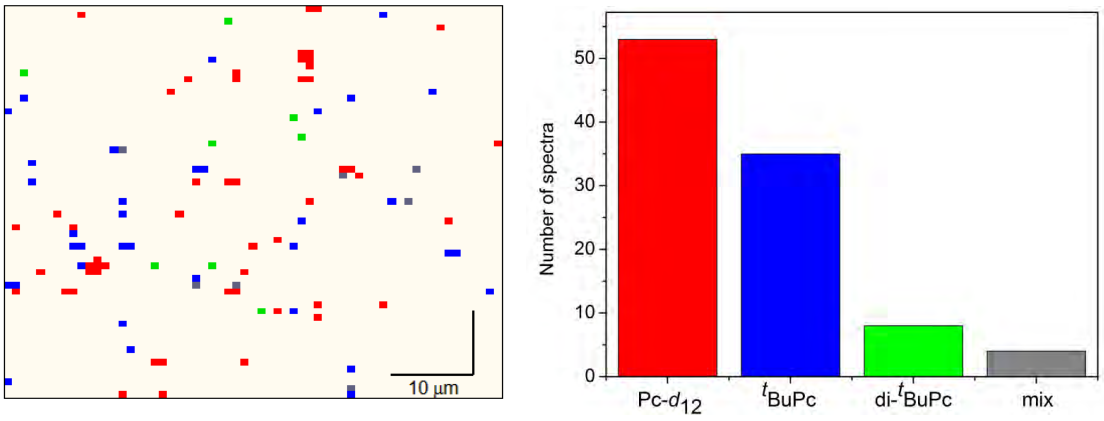

Figure 7.12: The distribution of the observed SERS spectra of differently substituted porphycenes from 1:1:1 mixture of ethanol solution (c=10^{-8} M) of porphycene-d_{12} (red), mono-*tert*-butylporphycene (blue) and di-*tert*-butylporphycene. Right, histogram of the observed spectra. SERS substrate: Au nanoparticles obtained by electrodeposition at a three phase junction, laser excitation: 632.8 nm, laser power: 50 µW, room temperature.

The obtained histogram of single molecule events clearly shows that the presence of *tert*-butyl groups strongly decreases the number of detected single molecules. There is a clear trend: the more *tert*-butyl groups, the lower the number of detected single molecules. This phenomenon is most likely caused by steric hindrance. Apparently, bulky substituents, such as *tert*-butyl groups tend to hinder the access to hot spots. Moreover, this conclusion is supported by the intensity ratios of the Raman to fluorescence signals within the family of *tert*-butyl derivatives presented in Table 7.2. When a molecule moves towards a hot spot, the enhancement of Raman scattering is accompanied by quenching of fluorescence, which is visible as lower luminescence background. Another possible reason for decrease in detectability on a single molecule level by the SERS technique upon introduction of *tert*-butyl moieties is related to charge-transfer (CT) effect. As described in Chapter 2 three distinct cases are recognized: (i) close proximity of metal surface induces changes in molecular polarizability, (ii) ground state CT or (iii) excited state CT. The probabilities of all of these processes depend on the distance between metal and a molecule. As *tert*-butyl groups increase the distance between chromophore and metal surface, they might affect the rate of these processes.

Nevertheless, the determination of the occurrence of charge transfer effect in porphycene requires further investigation which would include measurements with different laser line excitations and applied voltage. The comparison of detectability between *tert*-butyl derivatives demonstrates that in case of SERS technique interactions between molecules and metal surface, especially hot spots, are of crucial importance.

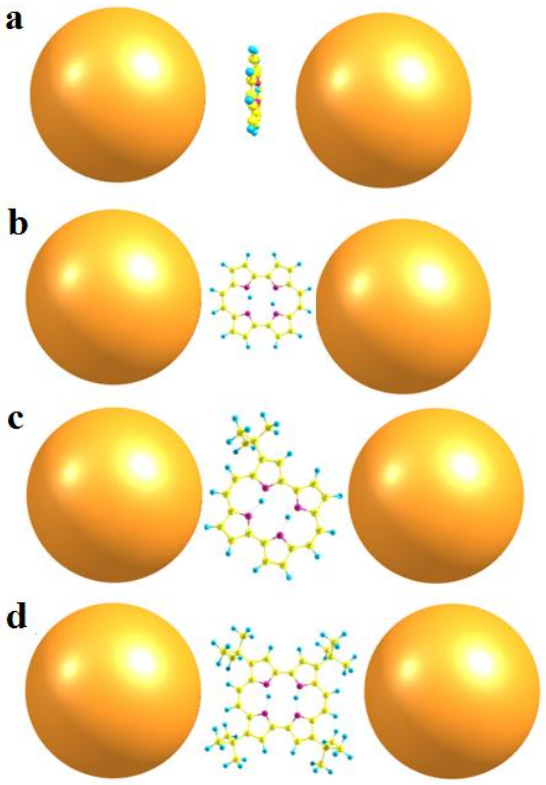

Figure 7.13: The model of molecules immobilized in a hot spot.

Finally, the observed effect of decreased number of detected single molecules is in line with the previously described studies on porphycene orientation in a hot spot. To remind, the single molecule spectra were observed for porphycene molecules oriented like in Figure 7.13a, i.e., parallel to the axis of a hot spot. To emphasise once again, we do not claim that porphycene prefers such orientation, but such orientation allowed us to obtain single molecule spectra. The signal from porphycene molecule located like in Figure 7.13a is just much weaker, therefore not detectable on a single molecule level. Analogously to the parent molecule, Figure 7.13c and d presents the possible orientation of mono-*tert*-butyl porphycene and

tetra-*tert*-butyl porphycene enabling their observation on a single molecule level. This scheme clearly shows that the bulky groups make very difficult for a molecule to reach a hot spot. Interestingly, porphycene substituted with *n*-propyl groups instead of *tert*-butyl substituents was also not detectable on a single molecule level at room temperature. The *n*-propyl group is not that bulky, but in the case of such orientation, it is a serious obstacle. At the same time, it was found that the substitution at the *meso* positions does not prevent from observation on a single molecules by the SERS technique. Although these findings should be supported by the systematic studies, most likely by the careful analysis of 1:1 mixtures of selected derivatives, it is clear that the position of substituent is of crucial importance for single molecule sensitivity.

To conclude, the observed phenomenon calls into question the direct application of the SERS technique in both qualitative and quantitative analysis. Certainly, such approach would require preliminary studies involving comparison between species selected for analysis and highly accurate calibration of the proposed method. Having the same concentration of broadly similar (chemically and spectroscopically) compounds, their detectability may be considerably different. The described experiment shows that it is worth to consider intramolecular factors which influence the sensitivity of SERS methods. Except electronic resonance, steric hindrance is an important factor, which may limit detection not only on a single molecule level.

7.4 Impact of temperature on SERS spectra

As it was shown in Chapter 4, lowering of temperature results in narrowing of Raman bands, which is accompanied by increase in their intensities. Therefore we decided to investigate the impact of change in temperature on the SERS spectra of tetra-*tert*-butyl porphycene, for which single-molecule SERS spectra are practically unattainable at room temperature. SERS spectra of this porphycene derivative measured at different temperatures and averaged over the same area are presented in Figure 7.14. Enormous increase of Raman bands intensities is observed. At the same time, the background in SERS spectra, originating mainly from

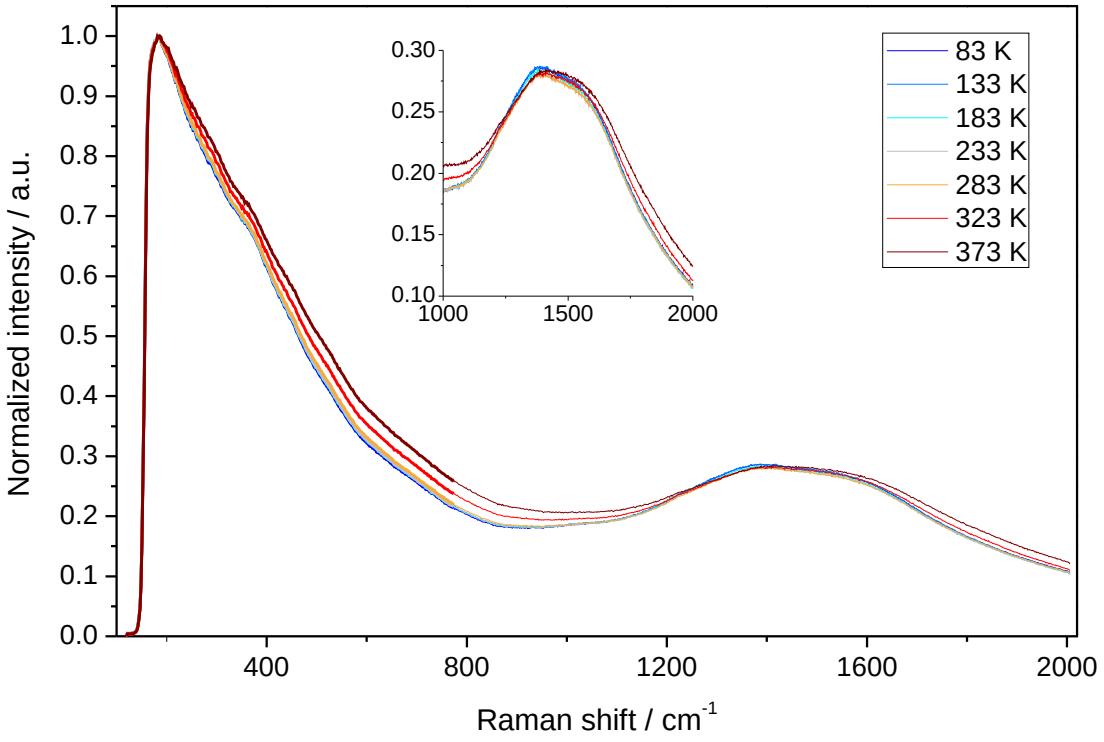

Figure 7.14: Averaged SERS spectra of tetra-*tert*-butyl porphycene adsorbed on gold nanorods (the concentration of the solution used for preparation was 10^{-7} M), measured at different temperatures. SERS substrate: 25 µm×47 µm gold NRs, laser excitation: 632.8 nm, laser power: 100 µW.

molecular fluorescence, does not change significantly. The obtained results demonstrate that for the relatively high concentration of tetra-*tert*-butyl porphycene (the concentration of the solution used for sample preparation was 10^{-7} M), the lowest background is observed for the room temperature. Upon decreasing the temperature it becomes slightly stronger, especially in the region above 1000 cm^{-1} (excitation with the 632.8 nm laser line). This region corresponds to the lower-energy range of fluorescence of the investigated species. Interestingly, the SERS spectra of tetra-*tert*-butyl porphycene obtained for one order of magnitude lower concentration, presented in Figure 7.15 revealed a different behaviour: the fluorescence background becomes lower while decreasing the temperature. However, it should be pointed out that the spectra shown in Figure 7.15 are not averaged over a larger area, but were recorded from different positions on a sample and were selected in such a way that the Raman bands are strong. Only a small number of Raman spectra revealed Raman features and averaging resulted in low quality spectra.

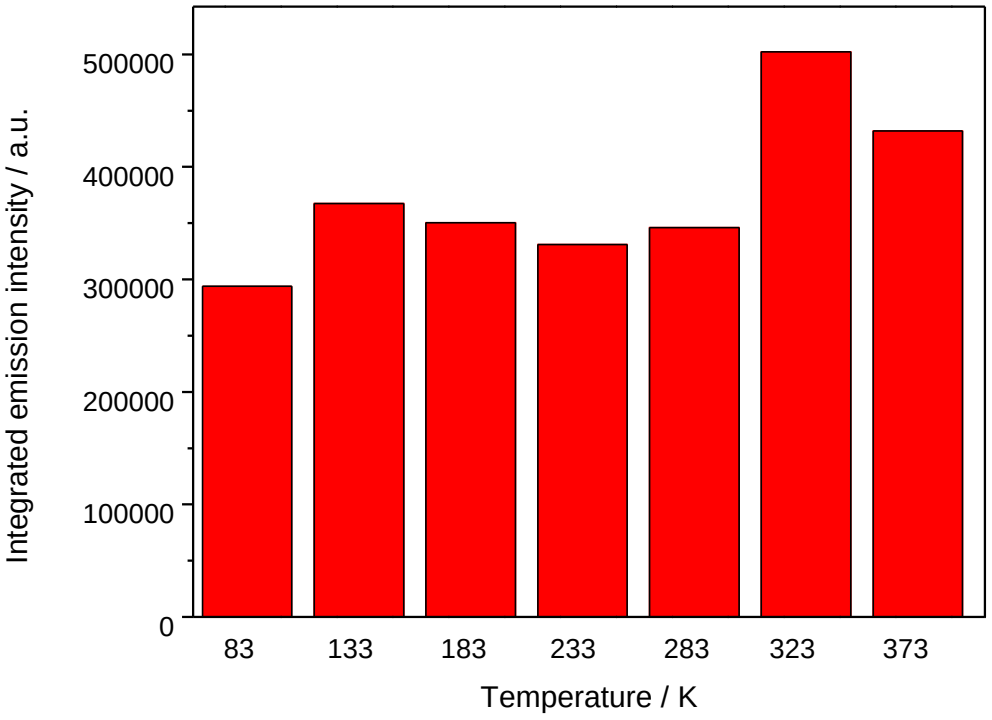

Figure 7.15: Selected SERS spectra of tetra-*tert*-butyl porphycene adsorbed on gold nanorods (the concentration of the solution used for preparation was 10^{-8} M), measured at different temperatures. SERS substrate: Au nanoparticles obtained by electrodeposition at a three phase junction, laser excitation: 632.8 nm, laser power: 50 μW.

In order to assess the contribution of hot spots presence to the observed changes in fluorescence background, the same experiment, but for molecules adsorbed on a gold film was performed. The roughness of this gold film prepared by vacuum evaporation was determined by AFM as a few nanometers. Figure 7.16 shows the normalized spectra (averaged over an area of 40×40 μm^2) obtained for different temperatures. Due to strong luminescence, no Raman features are observed, even at low temperatures. At higher temperatures luminescence is only slightly red shifted and its intensity does not depend on temperature, which is shown in Figure 7.17. We performed this experiment only for one concentration.

For a sample with plasmonic nanostructures the behaviour of fluorescence background depends on the molecular coverage. While for higher concentration the background is barely affected by the variation of temperature, for lower coverage the temperature has a strong impact on fluorescence background. This behaviour

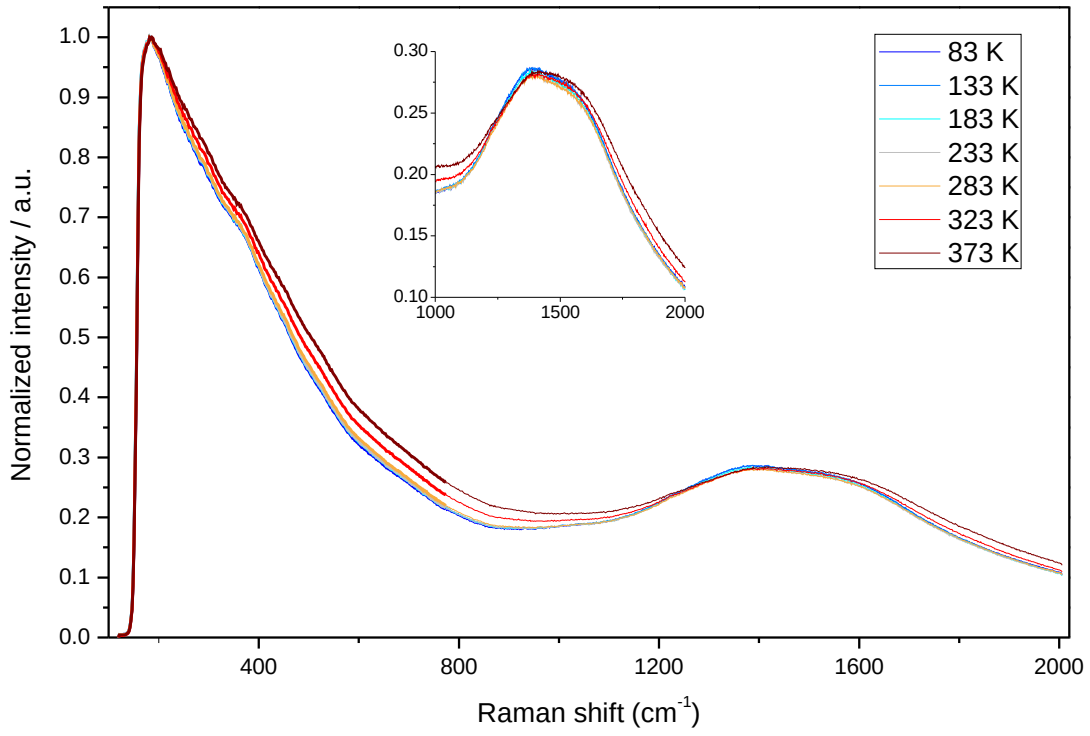

Figure 7.16: Averaged luminescence of tetra-*tert*-butyl porphycene adsorbed on a 50 nm thick gold film (vacuum evaporated on a cover slide) measured at different temperatures.

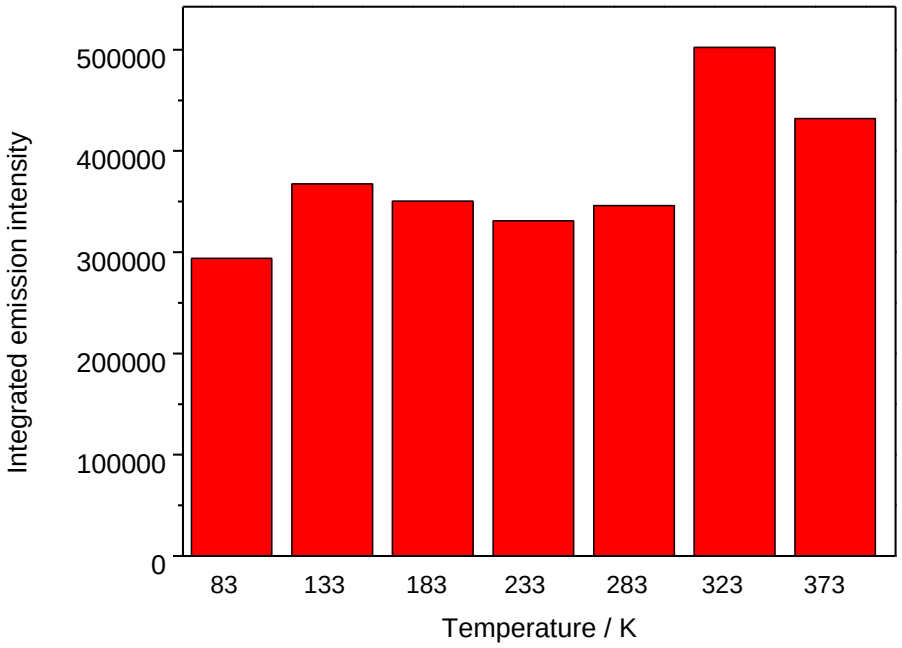

Figure 7.17: The averaged intensity of luminescence of tetra-*tert*-butylporphycene adsorbed on a 50 nm thick gold film (vacuum evaporated on a cover slide) measured at different temperatures.

can be justified when considering the number of molecules contributing to the observed spectra. At lower concentration, the recorded spectra originate only from one or a few molecules. For the simplicity, let us assume one molecule. Strong Raman signal indicates that the molecule is located in a region exhibiting large enhancement factor. Moreover, the fluorescence originates from the same molecule. As discussed earlier, the electromagnetic enhancement is extremely sensitive to the position in a hot spot and has the maximum value just in the middle between nanoparticles. One of the reason why Raman signal is stronger at lower temperature is due to lower thermal motions, i.e., a molecule spends on average more time in the region with the highest electromagnetic enhancement. It is accompanied by lower fluorescence background due to more efficient fluorescence quenching resulting from shorter distance to the metal surface. The situation is different for higher molecular concentration. Then a larger number of molecules contribute to the fluorescence background and the temperature barely affects its intensity, as only a very small number are placed in hot spots. Even if the fluorescence originating from a few molecules located in hot spots is quenched, the fluorescence coming from the others remains unchanged. The fluorescence quantum yield of these molecules can be even higher at low temperature, as there are less possible thermal deactivation channels. Nevertheless, the complete understanding of the observed phenomenon requires further studies.

7.5 Conclusions

The comparison between selected species revealed a peculiar behaviour and allowed us to assess an impact of the presence of *tert*-butyl groups in the molecular structure on SERS spectra. Given virtually the same absorption spectra of the investigated derivatives, the contribution to enhancement due to resonance may be considered of the same value. Therefore, the observed differences in detectability by the SERS technique may be attributed to the steric hindrance. The detectability of the SERS signal, which under resonant conditions is limited by the competition between Raman scattering and luminescence background originating from molecules adsorbed on nanoparticles acting as nonoantennas, is strongly influenced by *tert*-butyl groups. With the increasing number of these bulky groups the SERS

detectability dropped drastically. In the case of tetra-*tert*-butylporphycene Raman peaks were observed at room temperature exclusively on high-quality substrates, i.e., providing strong enhancement factor and efficient fluorescence quenching. We have managed to observe Raman features of this derivative only on gold nanorods and nanoparticles prepared at by electrodeposition at a three phase junction. On the other hand, the SERS spectra of bare porphycene are easily obtainable on a great variety of substrates. Difficulties in measurements of Raman features arise from the luminescence background, which is significantly higher for substituted porphycenes. This demonstrates that sensitivity of the SERS technique strongly depends on a molecule. What is more, it differs significantly even for chemically similar species. Hence, both qualitative and quantitative analysis is extremely challenging.

Interestingly, some molecules may be detected on a single molecule level only upon lowering the temperature. This is the case for tetra-*tert*-butyl porphycene. The studies shows that for low molecular coverage the molecular fluorescence considerably declines while cooling down a sample, contrary to the typical behaviour of molecules in solution, where the fluorescence quantum yield increases at low temperatures. This is accompanied by more intense Raman bands. The contrast between Raman signal and luminescence background increases, significantly improving the detectability of molecules by SERRS. It seems that at higher temperature the region of hot spot exhibiting the highest enhancement factor is just less frequently visited. Moreover, the geometry of a hot spot may slightly change upon lowering the temperature. The difference in the gap size between nanoparticles Δl related to the variation of temperature can be determined using the formula

$$\frac{\Delta l}{l} = \alpha_L \Delta T,$$

where α_L is the expansion coefficient, ΔT is temperature difference, l is initial length, and Δ_l is expansion. For gold α_L is equal to $14.2 \cdot 10^{-6}$m/mK. Hence, while decreasing the temperature by 100 K, a gold nanoparticle of 100 nm size will shrink by about 0.14 nm. This is not much, however, if we compare this value with the size of a typical hot spot, i.e., few nanometers, such change may slightly affect the SERS spectra.

Chapter 8

Proposed further studies/Future investigations

The aim of this chapter is to present single molecule studies by surface-enhanced Raman scattering as a prospective field of research. The obtained experimental results answered some questions, but at the same time raised new ones. Therefore we would like to suggest further experiments and indicate promising directions of research.

8.1 SERS excitation profile

Among four used excitation laser lines (325 nm, 514 nm, 633 nm, 785 nm), only 633 nm enabled observation of single molecules. Moreover, a 532 nm laser line was additionally checked and also did not allow for reaching a single molecule level. In Figure 8.1 these excitation energies are placed with respect to the electronic levels in porphycene. While exciting at 633 nm the intensity of Raman signal additionally benefits from the resonance effect. Despite the fact that the excitation by green lasers also should result in enhancement of Raman scattering due to resonance, single molecule sensitivity cannot be reached. As a matter of fact, the absorption coefficients at energies corresponding to green laser lines are significantly lower than at 633 nm. Nevertheless, given the intensities of the hottest observed hot

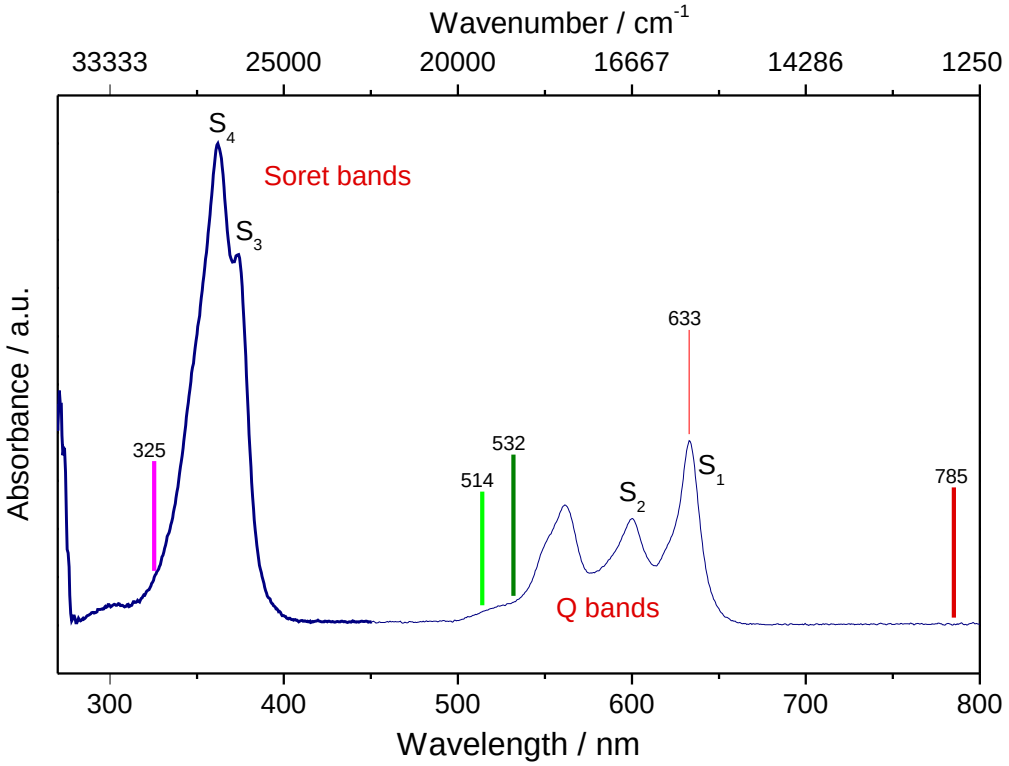

Figure 8.1: Electronic absorption of porphycene dissolved in ethanol.

spots, even 100-fold lower enhancement should still enable registration of single porphycene molecules.

To better understand where difficulties arise, knowledge of the surface-enhanced Raman excitation profiles (REPs) for different modes, i.e., their intensity dependence on the laser wavelength might be helpful. It is clearly recognized that the Raman excitation profiles are closely related to molecular electronic absorption.[153,154] Typically, the maxima of the REPs coincide with the absorption peaks. However, when molecules are located close to metal nanostructures, the surface-enhanced REPs are affected not only by the resonance Raman effect, but also by electromagnetic enhancement and additional surface effects. In order to extract the contribution originating from a SERS substrate, a comparison of profiles obtained from the studied species and a nonresonant molecule, such as benzenethiol should be made. This approach was successfully adopted by Dieringer et al. in studies on rhodamine 6G.[7] Providing no additional surface effects, the remaining part, which is affected by the resonance Raman effect should follow the REPs measured under normal conditions. Hence, any deviations are indicative of specific effects,

including the presence of chemical enhancement. Unfortunately, in some cases fluorescence seriously hampered the measurement of the Raman excitation profile, but theoretical predictions might be helpful.

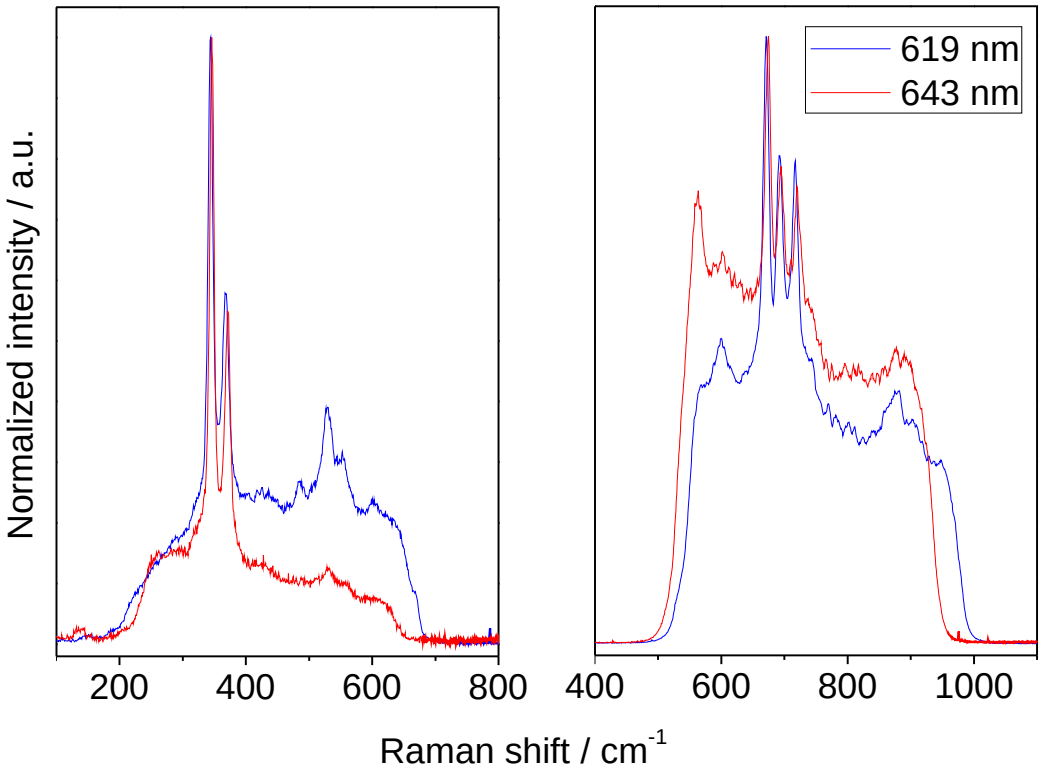

Figure 8.2: The SERS spectra obtained for porphycene excited at two different wavelengths. SERS substrate: 25 µm×47 µm gold NRs, laser power: 50 µW, room temperature.

Figure 8.2 presents two fragments of the SERS spectra of porphycene excited by two selected wavelengths provided by a dye laser. The spectra were measured with the help of tunable bandpass filter Semrock VersaChrom^{TM}. As the bandpass width is about 20 nm, the spectrum had to be measured part by part.

The relative intensities of the bands around 500 cm^{-1} and 343 cm^{-1} vary considerably while tuning the wavelength. Hence, SERS excitation profiles for these modes would surely show differences. The careful analysis would allow to rationalize the effect of any specific surface interactions.

8.2 Investigation of differences in surface diffusion of isotopologes and different chromophores

The observed unexpected imbalance in the numbers of detected Pc-d_0 and Pc-d_{12} molecules at concentrations by at least one order of magnitude lower than required to reach a single molecule limit could be attributed to differences in surface diffusion coefficients between isotopologues. This hypothesis, however, requires verification. Therefore, we propose to compare diffusion coefficients of different isotopologues on a metal surface by means of scanning tunnelling microscopy. Of course, such conditions differ from those during SERS experiment, where the molecules move not on an atomically flat surface, but on top of fractal-like nanostructures. Besides, most likely water or carbon dioxide molecules (maybe also some others) are adsorbed on SERS substrates. Typically, low-temperature ultra-high vacuum STM setups provide accurate control of temperature.

8.3 Improvement of time resolution

The minimum acquisition time in our experimental setup is equal to 300 ms and is caused by software limitation put on a CCD camera. The signal to noise ratio in the measured spectra would allow us to shorten this time by about one order of magnitude, still enabling the observation of Raman bands. Such improvement would be beneficial especially from the point of view of following the molecular dynamics. It would be probable to observe 'exotic' species or behaviours. For example, if a molecule would exists as a *cis* tautomeric form only for the time period of the order of miliseconds, this would be observed.

Moreover, achievement of better time resolution would help us to gather significantly larger collection of data required for the statistical analysis. Indeed, the low number of spectra registered before photobleaching makes it impossible to examine the correlations between Raman peaks intensities recorded from the same molecule. As the length of time traces is limited by photobleaching, only more frequent probing would provide larger number of spectra registered from a given hot spot.

Unfortunately, reachable accumulation times are far beyond the typical rotational diffusion times, which are of the order of picoseconds.

8.4 *Meso*-substituted derivatives

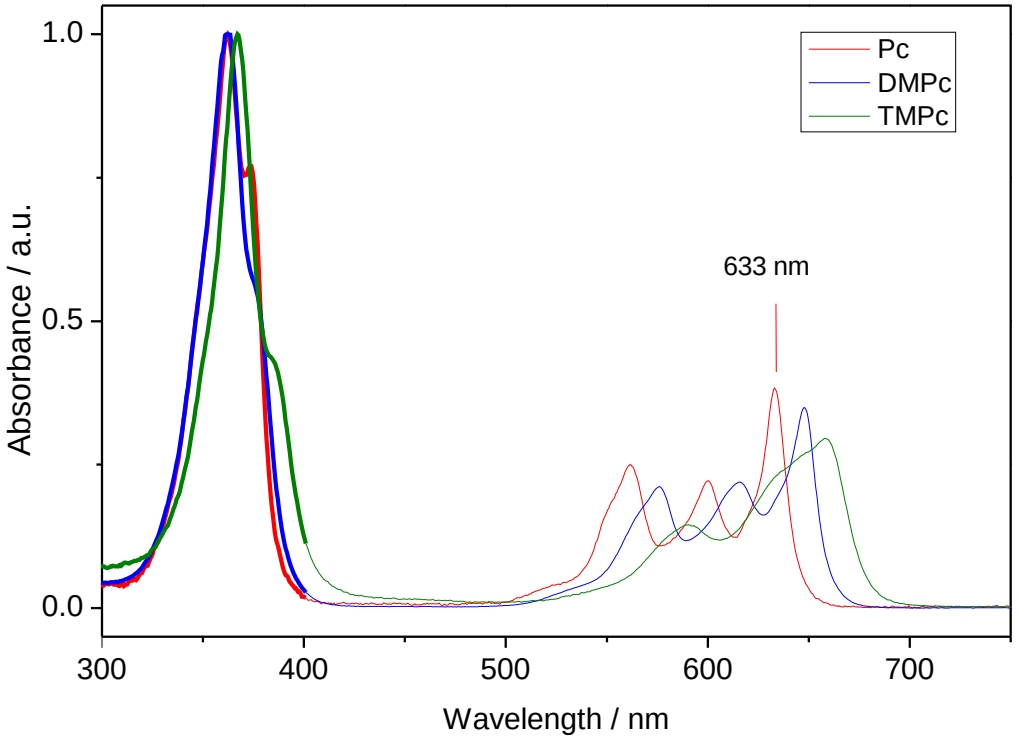

Figure 8.3: Electronic absorption of porphycene (Pc), 9,20-dimetylporphycene (DMPc) and 9,10,19,20-tetramethylporphycene (TMPc) in ethanol.

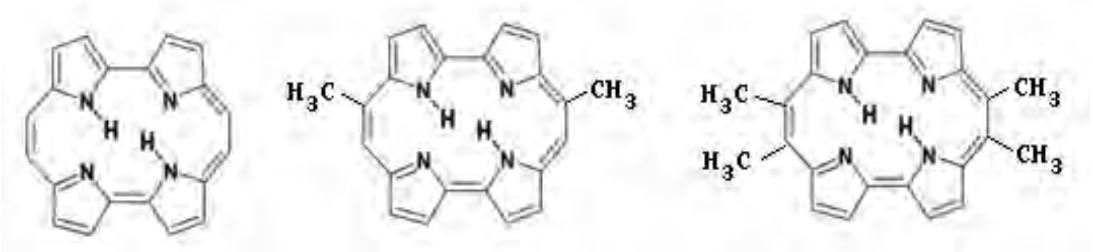

Figure 8.4: Structures of porphycene, 9,20-dimetylporphycene (DMPc) and 9,10,19,20-tetramethylporphycene (TMPc).

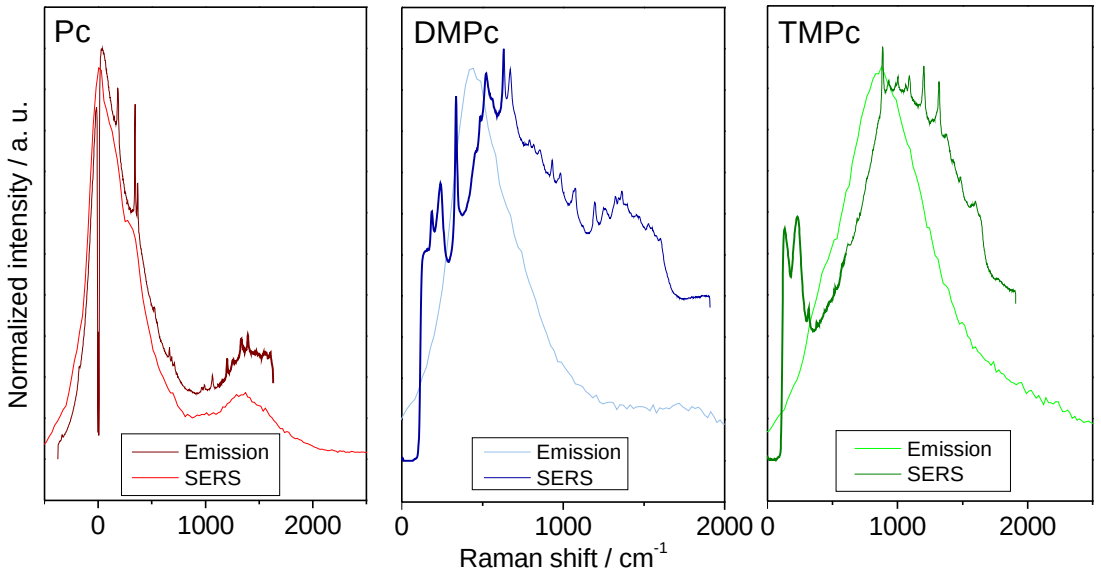

Figure 8.5: Emission and the SERS spectra of porphycene, dimethyl porphycene and tetramethyl porphycene. SERS substrate: Au nanoparticles obtained by electrodeposition at a three phase junction, laser excitation: 632.8 nm, laser power: 50 µW, room temperature.

Porphycenes substituted at the *meso* positions by methyl groups exhibit the red-shift of the 0-0 transition compared to bare porphycene. Naturally, this translates into the red-shift of their emission spectra. Figure 8.3 presents the absorption spectra of porphycene, 9,20-dimethylporphycene (DMPc) and 9,10,19,20-tetramethylporphycene (TMPc), of which the structures are depicted in Figure 8.4. The SERS spectra of Pc, DMPc and TMPc, presented in Figure 8.5, show that the highest enhancement is experienced by modes close to the emission maximum. This is clearly visible within this group of compounds, as the emission maximum shifts. Therefore, the detailed investigation and comparison of the SERS spectra of these species might shed some light on the impact of the fluorescence background on the relative intensities of the Raman bands. Although strong relationship between the relative intensities of the SERS peaks and the spectral shape and strength of the background was already reported, the background in the studied systems was attributed to the SERS substrate[155,94] or interactions between molecules and nanostructures.[8] Since the background in the SERS spectra of porphycenes is dominated by molecular fluorescence, the mechanism of modification of spectral intensities is different. The comparative studies of these species could contribute to a better understanding of the influence of emission on Raman bands intensities.

It is worth mentioning that the quantum yields of *meso*-alkylated derivatives, contrary to the parent porphycene, are highly viscosity-dependent due to the coupling of alkyl group rotation to inner hydrogen motion, which influences the non-radiative rate constant.[123] For instance, the quantum yield of TMPc in nonviscous *n*-hexane was estimated as $2.9 \cdot 10^{-4}$, while in more viscous DMSO as $1.5 \cdot 10^{-3}$. This viscosity dependence combined with detailed investigation of fluorescence background intensity may give us a better insight into the environment close to molecules and to the behaviour of molecules located in a hot spot. Such investigation, however, requires very tedious, and time-consuming studies.

8.5 Single molecule studies under reduced molecular mobility conditions

One of the characteristic features of single molecule SERS spectra is bleaching. A sudden disappearance of the signal may originate from photodegradation of a molecule or its escape from a hot spot. Differentiating between these situations is very difficult, often even impossible. In rare cases the registered time traces reveal fundamental changes in the SERS spectra, which suggests modification of the molecular structure. Much more often, however, Raman bands disappear completely. This does not necessarily mean that a molecule moved to a position with a significantly lower enhancement of the electromagnetic field. A molecule could have experienced such a structural modification that the product of the reaction is out of resonance, which, by the way, is very likely. As a consequence, the total enhancement becomes too low to observe any Raman bands.

It would be interesting to compare two situations: (i) when the molecules can move freely on a surface of a SERS substrate and (ii) when the mobility is somehow reduced. In the latter case a molecule would be tapped in a hot spot and the length of time traces should be mostly affected by photodecomposition. The analysis of such data could improve our understanding of the photobleaching and the role of laser forces, which might attract molecules to hot spots.

Limitation of molecular mobility might be imposed by applying a polymer film onto prepared samples. This approach, however, might face some experimental difficulties. For instance, the polymer may not penetrate the entire volume of hot spots. Nevertheless, we recommend it to undertake further research in this area.

Chapter 9

Summary

The studies presented in this thesis: (i) extend our knowledge regarding porphycene, (ii) contribute to the the better understanding of surface-enhanced Raman spectroscopy, especially phenomena on a single molecule level, (iii) demonstrate the power of single molecule studies, (iv) indicate the potential directions of further investigations.

The first part of the research, described in Chapter 5, was devoted to spectroscopic characteristics of porphycene by means of Raman and surface-enhanced Raman scattering. Reaching a single molecule sensitivity was proved by numerous observations: the result of bi-analyte approach performed for Pc-d_0 and Pc-d_{12}, intensity fluctuations, blinking, and one-step bleaching. It turned out that, owing to the possibility of measuring single molecules of porphycene some exotic species or behaviours, such as *trans-cis-trans* tautomerization reaction, were observed. In the bulk measurements, however, the presence of *cis* tautomer could not have been confirmed. The careful analysis of the enhancement factor was performed. The contributions to the observed total enhancement factor originating from both resonance Raman effect and electromagnetic effect were accessed. The resonance Raman effect provides enhancement of $\approx 10^3$, while the presence of nanoparticles results in enhancement up to $\approx 10^{11}$ (for the most intense single molecule spectra). Finally, the effect of lowering the temperature on spectral features and photostability was elucidated.

The next chapter also concerns porphycene, but is focused on the investigation of correlations between Raman modes. It demonstrates that this can be achieved in two ways: by the analysis of longer time traces or through studies of a collection of spectra from different hot spots. The analysis of time traces, specifically maps of the correlation coefficients, revealed that the molecular behaviour may change over time. For instance, the molecular rotation may start after a few seconds of even minutes. This finding indicates that a molecule immobilized in a hot spot does not move freely. Furthermore, the analysis of correlation coefficients for a large number of time traces recorded from different hot spots showed hight similarities in fluctuation patterns. This proves that the determined relationships are related to the chromophore itself, not to a hot spot structure, which changes from hot spot to hot spot.

The experimentally determined relationships were confronted with the theoretical predictions. For this purpose, resonance Raman spectra were calculated, followed by the analysis of Raman tensors. This allowed us to predict Raman spectra for different orientations of a single porphycene molecule in a hot spot. Moreover, the simulations of Raman spectra of a porphycene molecule rotating around C_2 axis confirmed the presence of fast *trans-trans* tautomerization. Furthermore, it was demonstrated that the presence of negative correlations in recorded time-traces is a signature of a molecular rotation in a hot spot. Finally, autocorrelation function showed longer dependencies in the case of time evolutions exhibiting negative correlations.

Chapter 7 discusses the influence of bulky *tert*-butyl groups on detectability by the SERS technique. The systematic studies showed that the increasing number of *tert*-butyl groups results in significantly higher fluorescence background in the SERS spectra, which may even completely cover Raman peaks. Moreover, it was demonstrated that the number of detected single molecules gradually decreases upon introduction of these bulky substituents. Despite that same concentration of the investigated species, the number of detected single molecules strongly depends on the number of *tert*-butyl groups. This finding has far-reaching consequences: the SERS technique cannot be directly applied to quantitative analysis. The usage of *tert*-butyl derivatives aimed at determination of the impact of steric hindrance.

As the studied species have virtually the same absorption spectra, similar contribution from resonance Raman can be assumed. Therefore, the observed differences in SERS spectra regarding detectability of single molecules and ratios between intensities of Raman peaks and fluorescence background may be attributed to steric hindrance. Finally, the temperature studies revealed that lowering the temperature makes it easier to observe single molecules. The higher intensity of the Raman peaks is accompanied with lower luminescence background. It it worth to note that tetra-*tert*-butyl porphycene was observed on a single molecule level exclusively at low temperature.

Finally, the last chapter proposes further directions of the single molecule studies using Raman spectroscopy, which might be a source of inspiration for future research.

To conclude, this thesis gathers a lot of experimental data regarding porphycene and its derivatives, and presents a great potential of single molecule studies. Although both data acquisition and analysis are time consuming, thanks to single molecule sensitivity we can observe and investigate phenomena undetectable on a bulk level.

Bibliography

[1] Harris, D.; Bertolucci, M. *Symmetry and Spectroscopy: An Introduction to Vibrational and Electronic Spectroscopy*; Dover Publications, 1989.

[2] Fleischmann, M.; Hendra, P. J.; McQuillan, A. J. *Chem. Phys. Lett.* **1974**, *26*, 163–166.

[3] Albrecht, M. G.; Creighton, J. A. *J. Am. Chem. Soc.* **1977**, *99*, 5215–5217.

[4] Jeanmaire, D. L.; Van Duyne, R. P. *J. Electroanal. Chem.* **1977**, *84*, 1–20.

[5] Nie, S.; Emory, S. R. *Science* **1997**, *275*, 1102–1106.

[6] Kneipp, K.; Wang, Y.; Kneipp, H.; Perelman, L. T.; Itzkan, I.; Dasari, R. R.; Feld, M. S. *Phys. Rev. Lett.* **1997**, *78*, 1667–1670.

[7] Dieringer, J. A.; Wustholz, K. L.; Masiello, D. J.; Camden, J. P.; Kleinman, S. L.; Schatz, G. C.; Van Duyne, R. P. *J. Am. Chem. Soc.* **2009**, *131*, 849–854.

[8] Weiss, A.; Haran, G. *J. Phys. Chem. B* **2001**, *105*, 12348–12354.

[9] Michaels, A. M.; Nirmal, M.; Brus, L. E. *J. Am. Chem. Soc.* **1999**, *121*, 9932–9939.

[10] Michaels, A. M.; Brus, L. *J. Phys. Chem. B* **2000**, *104*, 11965–11971.

[11] Cortés, E.; Etchegoin, P. G.; Le Ru, E. C.; Fainstein, A.; Vela, M. E.; Salvarezza, R. C. *J. Am. Chem. Soc.* **2010**, *132*, 10834–10837.

[12] Etchegoin, P. G.; Le Ru, E. C.; Fainstein, A. *Phys. Chem. Chem. Phys.* **2011**, *13*, 4500–4506.

[13] Camden, J. P.; Dieringer, J. A.; Wang, Y.; Masiello, D. J.; Marks, L. D.; Schatz, G. C.; Van Duyne, R. P. *J. Am. Chem. Soc.* **2008**, *130*, 12616–12617.

[14] Etchegoin, P. G.; Meyer, M.; Blackie, E.; Le Ru, E. C. *Anal. Chem.* **2007**, *79*, 8411–8415.

[15] Shegai, T. O.; Haran, G. *J. Phys. Chem* **2006**, *110*, 2459–2461.

[16] Le Ru, E. C.; Grand, J.; Sow, I.; Somerville, W. R. C.; Etchegoin, P. G.; Treguer-Delapierre, M.; Charron, G.; Félidj, N.; Lévi, G.; Aubard, J. *Nano Lett.* **2011**, *11*, 5013–5019.

[17] Kleinman, S. L.; Ringe, E.; Valley, N.; Wustholz, K. L.; Phillips, E.; Scheidt, K. A.; Schatz, G. C.; Van Duyne, R. P. *J. Am. Chem. Soc.* **2011**, *133*, 4115–4122.

[18] Sharaabi, Y.; Shegai, T.; Haran, G. *Chem. Phys.* **2005**, *318*, 44–49.

[19] dos Santos, D. P.; Temperini, M. L. A.; Brolo, A. G. *J. Am. Chem. Soc.* **2012**, *134*, 13492–13500.

[20] Artur, C.; Le Ru, E. C.; Etchegoin, P. G. *J. Phys. Chem. Lett.* **2011**, *2*, 3002–3005.

[21] Etchegoin, P. G.; Lacharmoise, P. D.; Le Ru, E. C. *Anal. Chem.* **2009**, *81*, 682–688.

[22] Etchegoin, P. G.; Meyer, M.; Le Ru, E. C. *Phys. Chem. Chem. Phys.* **2007**, *9*, 3006–3010.

[23] Dieringer, J. A.; Lettan, R. B.; Scheidt, K. A.; Van Duyne, R. P. *J. Am. Chem. Soc.* **2007**, *129*, 16249–16256.

[24] Bohn, J. E.; Le Ru, E. C.; Etchegoin, P. G. *J. Phys. Chem. C* **2010**, *114*, 7330–7335.

[25] Bizzarri, A. R.; Cannistraro, S. *Phys. Chem. Chem. Phys.* **2007**, *9*, 5315–5319.

[26] Darby, B. L.; Le Ru, E. C. *J. Am. Chem. Soc.* **2014**, *136*, 10965–10973.

[27] Le Ru, E. C.; Meyer, M.; Etchegoin, P. G. *J. Phys. Chem. B* **2006**, *110*, 1944–1948.

[28] Etchegoin, P. G.; Le Ru, E. C. *Phys. Chem. Chem. Phys.* **2008**, *10*, 6079–6089.

[29] Le Ru, E. C.; Blackie, E. J.; Meyer, M.; Etchegoin, P. G. *J. Phys. Chem. C* **2007**, *111*, 13794–13803.

[30] Le Ru, E. C.; Etchegoin, P. G.; Meyer, M. *J. Phys. Chem.* **2006**, *125*, 204701–204713.

[31] Stranahan, S. M.; Willets, K. A. *Nano Lett.* **2010**, *10*, 3777–3784.

[32] Gawinkowski, S.; Walewski, L.; Vdovin, A.; Slenczka, A.; Rols, S.; Johnson, M. R.; Lesyng, B.; Waluk, J. *Phys. Chem. Chem. Phys.* **2012**, *14*, 5489–5503.

[33] Long, D. A. *The Raman Effect: A Unified Treatment of the Theory of Raman Scattering by Molecules*; John Wiley & Sons, Ltd, 2002.

[34] Le Ru, E.; Etchegoin, P. *Principles of Surfance Enhanced Raman Spectroscopy and related plasmonic effets*; Elsevier, 2009.

[35] Valeur, B. *Molecular fuorescence: principles and applications*; Wiley-VCH Verlag GmbH, 2001.

[36] Mie, G. *Ann. Phys.* **1908**, *330*, 377–445.

[37] Smekal, A. *Naturwissenschaften* **1923**, *11*, 873–875.

[38] Raman, C. V.; Krishnan, K. S. *Nature* **1928**, *121*, 501–502.

[39] Maiman, T. H. *Nature* **1960**, *187*, 493–494.

[40] Schlücker, S. *Angew. Chem. Int. Ed.* **2014**, *53*, 4756–4795.

[41] Moskovits, M. *Rev. Mod. Phys.* **1985**, *57*, 783–826.

[42] Lombardi, J. R.; Birke, R. L.; Lu, T.; Xu, J. *J. Chem. Phys.* **1986**, *84*, 4174–4180.

[43] Billmann, J.; Otto, A. *Solid State Commun.* **1982**, *44*, 105–107.

[44] Furtak, T. E.; Macomber, S. H. *Chem. Phys. Lett.* **1983**, *95*, 328–332.

[45] Otto, A.; Mrozek, I.; Grabhorn, H.; Akemann, W. *J. Phys.: Condens. Matter* **1992**, *4*, 1143–1212.

[46] Ling, X.; Moura, L. G.; Pimenta, M. A.; Zhang, J. *J. Phys. Chem. C* **2012**, *116*, 25112–25118.

[47] Lippitsch, M. E. *Phys. Rev. B* **1984**, *29*, 3101–3110.

[48] Adrian, F. J. *J. Chem. Phys.* **1982**, *77*, 5302–5314.

[49] Hirschfeld, T. *Appl.Opt.* **1976**, *15*, 2965–2966.

[50] Moerner, W.; Kador, L. *Phys. Rev. Lett.* **1989**, *62*, 2535–2538.

[51] Orrit, M.; Bernard, J. *Phys. Rev. Lett.* **1990**, *65*, 2716–2719.

[52] Betzig, E.; Chichester, R. J. *Science* **1993**, *262*, 1422–1425.

[53] Macklin, J. J.; Trautman, J. K.; Harris, T. D.; Brus, L. E. *Science* **1996**, *272*, 255–258.

[54] Moerner, W. E.; Shechtman, Y.; Wang, Q. *Faraday Discuss.* **2015**, *184*, 9–36.

[55] Xu, H.; Aizpurua, J.; Käll, M.; Apell, P. *Phys. Rev. E* **2000**, *62*, 4318–4324.

[56] Etchegoin, P. G.; Le Ru, E. C.; Meyer, M. *J. Am. Chem. Soc.* **2009**, *131*, 2713–2716.

[57] Blackie, E.; Le Ru, E. C.; Meyer, M.; Timmer, M.; Burkett, B.; Northcote, P.; Etchegoin, P. G. *Phys. Chem. Chem. Phys.* **2008**, *10*, 4147–4153.

[58] Kneipp, K.; Kneipp, H.; Kartha, V. B.; Manoharan, R.; Deinum, G.; Itzkan, I.; Dasari, R. R.; Feld, M. S. *Phys. Rev. E* **1998**, *57*, 6281–6284.

[59] Maruyama, Y.; Ishikawa, M.; Futamata, M. *Chem. Lett.* **2001**, *8*, 834–835.

[60] Koo, T.-W.; Chan, S.; Sun, L.; Su, X.; Zhang, J.; Berlin, A. A. *Appl. Spectrosc.* **2004**, *58*, 1401–1407.

[61] Maruyama, Y.; Futamata, M. *J. Raman Spectrosc.* **2005**, *36*, 581–592.

[62] Futamata, M. *Faraday Discuss.* **2006**, *132*, 45–61.

[63] Blackie, E. J.; Le Ru, E. C.; Etchegoin, P. G. *J. Am. Chem. Soc.* **2009**, *131*, 14466–14472.

[64] Liu, H.; Zhang, L.; Lang, X.; Yamaguchi, Y.; Iwasaki, H.; Inouye, Y.; Xue, Q.; Chen, M. *Sci. Rep.* **2011**, *1*, 112–116.

[65] Etchegoin, P.; Liem, H.; Maher, R. C.; Cohen, L. F.; Brown, R. J. C.; Hartigan, H.; Milton, M. J. T.; Gallop, J. C. *Chem. Phys. Lett.* **2002**, *366*, 115–121.

[66] Lee, J.-H.; Nam, J.-M.; Jeon, K.-S.; Lim, D.-K.; Kim, H.; Kwon, S.; Lee, H.; Suh, Y. D. *ACS Nano* **2012**, *6*, 9574–9584.

[67] Luo, Z.; Loo, B. H.; Peng, A.; Ma, Y.; Fu, H.; Yao, J. *J. Raman Spectrosc.* **2011**, *42*, 319–323.

[68] Artur, C. G.; Miller, R.; Meyer, M.; Le Ru, E. C.; Etchegoin, P. G. *Phys. Chem. Chem. Phys.* **2012**, *14*, 3219–3225.

[69] Lippincott-Schwartz, J.; Altan-Bonnet, N.; Patterson, G. H. *Nat. Cell Biol.* **2003**, *Suppl*, S7–S14.

[70] Kasche, V.; Lindqvist, L. *J. Phys. Chem.* **1964**, *68*, 817–823.

[71] Song, L.; Hennink, E. J.; Young, I. T.; Tanke, H. J. *Biophys. J.* **1995**, *68*, 2588–2600.

[72] Soumpasis, D. M. *Biophys. J.* **1983**, *41*, 95–97.

[73] Widengren, J.; Rigler, R. *Bioimaging* **1996**, *4*, 149–157.

[74] Deschenes, L. A.; Vanden Bout, D. A. *Chem. Phys. Lett.* **2002**, *365*, 387–395.

[75] Wolkow, R. A.; Moskovits, M. *J. Phys. Chem* **1987**, *87*, 5858–5869.

[76] Bjerneld, E. J.; Svedberg, F.; Johansson, P.; Käll, M. *J. Phys. Chem. A* **2004**, *108*, 4187–4193.

[77] Galloway, C. M.; Artur, C.; Grand, J.; Le Ru, E. C. *J. Phys. Chem. C* **2014**, *118*, 28820–28830.

[78] Bjerneld, E. J.; Johansson, P.; Käll, M. *Single Mol.* **2000**, *1*, 239–248.

[79] Haran, G. *Isr. J. Chem.* **2004**, *44*, 385–390.

[80] Le Ru, E. C.; Etchegoin, P. G.; Grand, J.; Félidj, N.; Aubard, J.; Lévi, G. *J. Phys. Chem. C* **2007**, *111*, 16076–16079.

[81] Mahajan, S.; Cole, R. M.; Speed, J. D.; Pelfrey, S. H.; Russell, A. E.; Bartlett, P. N.; Barnett, S. M.; Baumberg, J. J. *J. Phys. Chem. C* **2010**, *114*, 7242–7250.

[82] Mooradian, A. *Phys. Rev. Lett.* **1969**, *22*, 185–187.

[83] Akemann, W.; Otto, A. *Philos. Mag. B* **1994**, *70*, 747–760.

[84] Moskovits, M. *J. Raman Spectrosc.* **2005**, *36*, 485–496.

[85] Jiang, J.; Bosnick, K.; Maillard, M.; Brus, L. *J. Phys. Chem. B* **2003**, *107*, 9964–9972.

[86] Akemann, W.; Otto, A. *Surf. Sci.* **1994**, *307-309*, 1071–1075.

[87] Akemann, W.; Otto, A.; Schober, H. R. *Phys. Rev. Lett.* **1997**, *79*, 5050–5053.

[88] Otto, A.; Timper, J.; Billmann, J.; Kovacs, G.; Pockrand, I. *Surf. Sci.* **1980**, *92*, L55–L57.

[89] Gass, A. N.; Kapusta, O. I.; Klimin, S. A.; Mal'shukov, A. G. *Solid State Commun.* **1989**, *71*, 749–753.

[90] Gersten, J. I.; Birke, R. L.; Lombardi, J. R. *Phys. Rev. Lett.* **1979**, *43*, 147–150.

[91] Beversluis, M. R.; Bouhelier, A.; Novotny, L. *Phys. Rev. B* **2003**, *68*, 115433.

[92] Heritage, J. P.; Bergman, J. G.; Pinczuk, A.; Worlock, J. M. *Chem. Phys. Lett.* **1979**, *67*, 229–232.

[93] Maruyama, Y.; Futamata, M. *Chem. Phys. Lett.* **2005**, *412*, 65–70.

[94] Lin, K.-Q.; Yi, J.; Zhong, J.-H.; Hu, S.; Liu, B.-J.; Liu, J.-Y.; Zong, C.; Lei, Z.-C.; Wang, X.; Aizpurua, J.; Esteban, R.; Ren, B. *Nature Commun.* **2017**, *8*, 14891–14899.

[95] Vogel, E.; Köcher, M.; Schmickler, H.; Lex, J. *Angew. Chem. Int. Ed. Engl.* **1986**, *25*, 257–259.

[96] Kadish, K. M.; Smith, K. M.; Guilard, R. *Handbook of Porphyrin Science: with Applications to Chemistry, Physics, Materials Science, Engineering, Biology and Medicine, Volume 6-10*; World Scientific, 2010; pp 359–436.

[97] Malsch, K.; Hohlneicher, G. *J. Phys. Chem. A* **1997**, *101*, 8409–8416.

[98] Starukhin, A.; Vogel, E.; Waluk, J. *J. Phys. Chem. A* **1998**, *102*, 9999–10006.

[99] Mengesha, E. T.; Sepioł, J.; Borowicz, P.; Waluk, J. *J. Chem. Phys.* **2013**, *138*, 174201–1—-174201–14.

[100] Mengesha, E. T.; Zehnacker-Rentien, A.; Sepioł, J.; Kijak, M.; Waluk, J. *J. Phys. Chem. B* **2015**, *119*, 2193–2203.

[101] Vdovin, A.; Waluk, J.; Dick, B.; Slenczka, A. *ChemPhysChem* **2009**, *10*, 761–765.

[102] Piwoński, H.; Stupperich, C.; Hartschuh, A.; Sepioł, J.; Meixner, A.; Waluk, J. *J. Am. Chem. Soc.* **2005**, *127*, 5302–5303.

[103] Piwoński, H.; Hartschuh, A.; Urbańska, N.; Pietraszkiewicz, M.; Sepioł, J.; Meixner, A. J.; Waluk, J. *J. Phys. Chem. C* **2009**, *113*, 11514–11519.

[104] Piwoński, H.; Sokołowski, A.; Kijak, M.; Nonell, S.; Waluk, J. *J. Phys. Chem. Lett.* **2013**, *4*, 3967–3971.

[105] Kumagai, T.; Hanke, F.; Gawinkowski, S.; Sharp, J.; Kotsis, K.; Waluk, J.; Persson, M.; Grill, L. *Nat. Chem.* **2014**, *6*, 41–46.

[106] Kumagai, T.; Hanke, F.; Gawinkowski, S.; Sharp, J.; Kotsis, K.; Waluk, J.; Persson, M.; Grill, L. *Phys. Rev. Lett.* **2013**, *111*, 246101–1–246101–5.

[107] Ladenthin, J. N.; Grill, L.; Gawinkowski, S.; Liu, S.; Waluk, J.; Kumagai, T. *ACS Nano* **2015**, *9*, 7287–7295.

[108] Wu, Y.-D.; Chan, K. W. K.; Yip, C.-P.; Vogel, E.; Plattner, D. A.; Houk, K. N. *J. Org. Chem.* **1997**, *62*, 9240–9250.

[109] Kozlowski, P. M.; Zgierski, M. Z.; Baker, J. *J. Chem. Phys.* **1998**, *109*, 5905–5913.

[110] Waluk, J.; Vogel, E. *J. Phys. Chem* **1994**, *98*, 4530–4535.

[111] Gil, M.; Waluk, J. *J. Am. Chem. Soc.* **2007**, *129*, 1335–1341.

[112] Fita, P.; Urbańska, N.; Radzewicz, C.; Waluk, J. *Chem. Eur. J.* **2009**, *15*, 4851–4856.

[113] Waluk, J.; Müller, M.; Swiderek, P.; Köcher, M.; Vogel, E.; Hohlneicher, G.; Michl, J. *J. Am. Chem. Soc.* **1991**, *113*, 5511–5527.

[114] Nogala, W.; Kannan, P.; Gawinkowski, S.; Jönsson-Niedziolka, M.; Kominiak, M.; Waluk, J.; Opałło, M. *Nanoscale* **2015**, *7*, 10767–10774.

[115] Gawinkowski, S.; Pszona, M.; Gorski, A.; Niedziółka-Jönsson, J.; Kamińska, I.; Nogala, W.; Waluk, J. *Nanoscale* **2016**, *8*, 3337–3349.

[116] Urbańska, N.; Pietraszkiewicz, M.; Waluk, J. *J. Porphyrins Phthalocyanines* **2007**, *11*, 596–600.

[117] Czerski, I.; Listkowski, A.; Nawrocki, J.; Urbańska, N.; Piwoński, H.; Sokołowski, A.; Pietraszkiewicz, O.; Pietraszkiewicz, M.; Waluk, J. *J. Porphyrins Phthalocyanines* **2012**, *16*, 589–602.

[118] Vogel, E.; Köcher, M.; Lex, J.; Ermer, O. *Isr. J. Chem.* **1989**, *29*, 257–266.

[119] Leopold, N.; Lendl, B. *J. Phys. Chem. B* **2003**, *107*, 5723–5727.

[120] Dendisová-Vyškovská, M.; Prokopec, V.; Člupek, M.; Matějka, P. *J. Raman Spectrosc.* **2012**, *43*, 181–186.

[121] Creighton, J. A.; Alvarez, M. S.; Weitz, D. a.; Garoff, S.; Kim, M. W. *J. Phys. Chem* **1983**, *87*, 4793–4799.

[122] Kamińska, I.; Jönsson-Niedziółka, M.; Kamińska, A.; Pisarek, M.; Hołyst, R.; Opałło, M.; Niedziółka-Jönsson, J. *J. Phys. Chem. C* **2012**, *116*, 22476–22485.

[123] Gil, M.; Dobkowski, J.; Wiosna-Sałyga, G.; Urbańska, N.; Fita, P.; Radzewicz, C.; Pietraszkiewicz, M.; Borowicz, P.; Marks, D.; Glasbeek, M.; Waluk, J. *J. Am. Chem. Soc.* **2010**, *132*, 13472–13485.

[124] Becke, A. D. *J. Chem. Phys.* **1993**, *98*, 5648–5652.

[125] Lee, C.; Yang, W.; Parr, R. G. *Phys. Rev. B* **1988**, *37*, 785–789.

[126] Vosko, S. H.; Wilk, L.; Nusair, M. *Can. J. Phys.* **1980**, *58*, 1200–1211.

[127] Frisch, M. J. et al. *Gaussian 09, Revision B.01*, 2010.

[128] Baerends, E. J. et al. *ADF2017, SCM, Theoretical Chemistry, Vrije Universiteit, Amsterdam, The Netherlands, https://www.scm.com*.

[129] Becke, A. D. *Phys. Rev. A* **1988**, *38*, 3098–3100.

[130] Perdew, J. P. *Phys. Rev. B* **1986**, *33*, 8822–8824.

[131] Polavarapu, P. L. *J. Phys. Chem* **1990**, *94*, 8106–8112.

[132] Kneipp, K.; Moskovits, M.; Kneipp, H. *Surface-Enhanced Raman Scattering: Physics and Applications*; Springer, 2006.

[133] Ren, B.; Lin, X.-F.; Yang, Z.-L.; Liu, G.-K.; Aroca, R. F.; Mao, B.-W.; Tian, Z.-Q. *J. Am. Chem. Soc.* **2003**, *125*, 9598–9599.

[134] Lin, X.-F.; Ren, B.; Yang, Z.-L.; Liu, G.-K.; Tian, Z.-Q. *J. Raman Spectrosc.* **2005**, *36*, 606–612.

[135] Stipe, B. C.; Rezaei, M. A.; Ho, W. *Phys. Rev. Lett.* **1999**, *82*, 1724–1727.

[136] Eichberger, M.; Marschall, M.; Reichert, J.; Weber-Bargioni, A.; Auwärter, W.; Wang, R. L. C.; Kreuzer, H. J.; Pennec, Y.; Schiffrin, A.; Barth, J. V. *Nano Lett.* **2008**, *8*, 4608–4613.

[137] Buchner, F.; Zillner, E.; Röckert, M.; Glässel, S.; Steinrück, H.-P.; Marbach, H. *Chem. Eur. J.* **2011**, *17*, 10226–10229.

[138] Buchner, F.; Xiao, J.; Zillner, E.; Chen, M.; Röcket, M.; Ditze, S.; Stark, M.; Steinrück, H.-P.; Gottfried, J. M.; Marbach, H. *J. Phys. Chem. C* **2011**, *115*, 24172–24177.

[139] Marbach, H.; Steinrück, H.-P. *Chem. Comm.* **2014**, *50*, 9034–9048.

[140] Kneipp, K.; Wang, Y.; Kneipp, H.; Itzkan, I.; Dasari, R. R.; Feld, M. S. *Phys. Rev. Lett.* **1996**, *76*, 2444–2447.

[141] Le Ru, E. C.; Schroeter, L. C.; Etchegoin, P. G. *Anal. Chem.* **2012**, *84*, 5074–5079.

[142] Auguié, B.; Reigue, A.; Le Ru, E. C.; Etchegoin, P. G. *Anal. Chem.* **2012**, *84*, 7938–7945.

[143] Reigue, A.; Auguié, B.; Etchegoin, P. G.; Le Ru, E. C. *J. Raman Spectrosc.* **2013**, *44*, 573–581.

[144] Suzaki, Y.; Tachibana, A. *Appl. Opt.* **1975**, *14*, 2809–2810.

[145] Boyle, L. L. *Int. J. Quantum Chem.* **1969**, *3*, 231–243.

[146] Kęcki, Z. *Podstawy spektroskopii molekularnej*; Wydawnictwo Naukowe PWN, 1972.

[147] Takahashi, M.; Goto, M.; Ito, M. *Chem. Phys. Lett.* **1985**, *121*, 458–463.

[148] Goulet, P. J. G.; Pieczonka, N. P. W.; Aroca, R. F. *Anal. Chem.* **2003**, *75*, 1918–1923.

[149] Sepioł, J.; Stepanenko, Y.; Vdovin, A.; Mordziński, A.; Vogel, E.; Waluk, J. *Chem. Phys. Lett.* **1998**, *296*, 549–556.

[150] Ciąćka, P.; Fita, P.; Listkowski, A.; Radzewicz, C.; Waluk, J. *J. Phys. Chem. Lett.* **2016**, *7*, 283–288.

[151] Langer, U.; Hoelger, C.; Wehrle, B.; Latanowicz, L.; Vogel, E.; Limbach, H.-H. *J. Phys. Org. Chem.* **2000**, *13*, 23–34.

[152] Aragón, S. R.; Pecora, R. *Biopolymers* **1975**, *14*, 119–138.

[153] Myers, A. B. *J. Raman Spectrosc.* **1997**, *28*, 389–401.

[154] Hildebrandt, P.; Stockburger, M. *J. Phys. Chem.* **1984**, *88*, 5935–5944.

[155] Itoh, T.; Yoshida, K.; Biju, V.; Kikkawa, Y.; Ishikawa, M.; Ozaki, Y. *Phys. Rev. B* **2007**, *76*, 085405–1–085405–5.

Publications

1. Near-Field Spectral Response of Optically Excited Scanning Tunneling Microscope Junctions Probed by Single-Molecule Action Spectroscopy
   Böckmann, H.; Müller, M.; Hammud, A.; Willinger, M. G.; Pszona, M.; Waluk, J.; Wolf, M.; Kumagai, T. *J. Phys. Chem. Lett.* 2019, 10, 2068-2074.

2. Unusual effects in single molecule tautomerization: hemiporphycene
   Kim, V.; Piątkowski, Ł.; Pszona, M.; Jäger, R.; Ostapko, J.; Sepioł, J.; Meixner, A. J.; Waluk, J. *Phys. Chem. Chem. Phys* 2018, 20, 26591-26596

3. Plasmon-Mediated Surface Engineering of Silver Nanowires for Surface-Enhanced Raman Scattering
   Lu, G.; Yuan, H.; Su, L.; Kenens, B.; Fujita, Y.; Chamtouri, M.; Pszona, M.; Fron, E.; Waluk, J.; Hofkens, J.; Uji-i, H. *J. Phys. Chem. Lett.* 2017, 8, 2774-2779.

4. Spectroscopic and microscopic studies of tautomerization in porphycenes: condensed phase, supersonic jets, and single molecule studies
   Fita, P.; Grill, L.; Listkowski, A.; Piwoński, H.; Gawinkowski, S.; Pszona, M.; Sepioł, J.; Mengesha, E. T.; Kumagai, T.; Waluk, J. *Phys. Chem. Chem. Phys.* 2017, 19, 4921-4937.

5. Single molecule Raman spectra of porphycene isotopologues
   Gawinkowski, S.; Pszona, M.; Gorski, A.; Niedziółka-Jönsson, J.; Kamińska, I.; Nogala, W.; Waluk, J. *Nanoscale*, 2016, 8, 3337-3349.

6. An electropolymerized molecularly imprinted polymer for selective carnosine sensing with impedimetric capacity
   Wojnarowicz, A.; Sharma, P. S.; Sosnowska, M.; Lisowski, W.; Huynh, T. P.; Pszona, M.; Borowicz, P.; D'Souza, F.; Kutner, W., *J. Mater. Chem. B*, 2016, 4, 1156-1165.

7. Substituent and solvent effects on the excited state deactivation channels in anils and boranils
   Dobkowski, J.; Wnuk, P.; Buczyńska, J.; Pszona, M.; Orzanowska, G.; Frath,

D.; Ulrich, G.; Massue, J.; Mosquera-Vaszquez, S.; Vauthey, E.; Radzewicz, C.; Ziessel, R.; Waluk.; J. *Chem. Eur. J.*, 2015, 21, 1312-1327.

8. Synthesis, spectroscopy, and photophysics of porphyrins attached to gold nanoparticles via one or two linkers
Ostapko, J.; Buczyńska, J.; Pszona, M.; Kowalska, P.; Waluk, J. *J. Porphyrins Phthalocyanines*, 2014, 18, 686-697.

9. Tautomerization in 2,7,12,17-tetraphenylporphycene and 9-amino-2,7,12,17- tetraphenylporphycene: Influence of asymmetry on the direction of the transition moment
Fita, P.; Pszona, M.; Orzanowska, G.; Sánchez-García, D.; Nonell, S.; Vauthey, E., Waluk, J. *Chem. Eur. J.*, 2012, 18, 13160-13167.

Conferences

1. M.Pszona, S. Gawinkowski, A. Gorski, J. Waluk *Surface-Enhanced Raman Spectroscopy – down to a single molecule level*; Advanced Infrared and Raman Spectroscopy, 16-18.11.2012, Łochów, Poland; poster

2. S. Gawinskowski, M. Pszona, A. Gorski, J. Waluk *From a macro ensemble down to a single-molecule level SERRS of porphycene*; Dweek School on Nanoplasmonics, 9-14.12.2012, Rehovot, Israel; poster

3. M.Pszona *Statistics of single molecule SERRS spectra of porphycene*; Seminar on Vibrational Biospectroscopy and Imaging, 19.06.2013, Kraków, Poland; oral presentation

4. M. Pszona, S. Gawinskowski,I. Kamińska, J. Waluk *The influence of tert-butyl substituents on single-molecule SERRS spectra of porphycene* 26th International Conference on Photochemistry (ICP 2013), 21-26.07.2013, Leuven, Belgium; poster

5. M. Pszona, S. Gawinskowski,I. Kamińska, J. Waluk *The influence of different substituents on single-molecule SERRS spectra of porphycene* Frontiers in Photochemistry, 25-28.08.2013, Les Diablerets, Switzerland; poster

6. M. Pszona, S. Gawinkowski, I. Kamińska, J. Niedziółka-Jönsson, M. Opałło, J. Waluk *The relationships between surface-enhanced Raman scattering and fluorescence in porphycene and its derivatives* 13th Conference on Methods and Applications of Fluorescence, 8-11.09.2013 Genua, Italy; poster

7. M. Pszona, S. Gawinkowski, I. Kamińska, J. Niedziółka-Jönsson, R. Ambroziak, M. Opałło, J. Waluk, *Behaviour of single molecules of porphycene at different substrates* Surface-Enhanced Spectroscopies 2014, 7-10.08.2014 Chemnitz, Germany; poster

8. M. Pszona, S. Gawinkowski, I. Kamińska, J. Niedziółka-Jönsson, M. Opałło, J. Waluk, *Studies of single molecules of porphycene at different temperatures by SERRS* XXIV. International Conference on Raman Spectroscopy, 10-15.08.2014, Jena, Germany; poster

9. M. Pszona, S. Gawinkowski, I. Kamińska, J. Niedziółka-Jönsson, M. Opałło, J. Waluk, *Detectability of some porphycenes on a single molecule level by SERS* Single Molecule Spectroscopy and Ultra Sensitive Analysis in the Life Sciences, 2-5.09.2014, Berlin, Gemany; poster

10. M. Pszona, S. Gawinkowski, I. Kamińska, J. Niedziółka-Jönsson, J. Waluk, *Single molecule SERS of porphycene* Summer School 2015, Methods in Molecular Energy Research: Theory and Spectroscopy, 30.08 - 4.09.2015, Gelsenkirchen, Germany; poster

11. M. Pszona, S. Gawinkowski, I. Kamińska, J. Niedziółka-Jönsson, J. Waluk *Competition between single molecule Surface-Enhanced Raman Scattering and fluorescence in porphycene and its derivatives* 13th Conference on Methods and Applications of Fluorescence, 13-16.09.2013 Würzburg, Germany; poster

12. M. Pszona, S. Gawinkowski, I. Kamińska, J. Niedziółka-Jönsson, J. Waluk *Behavior of single molecules of porphycene in hot spots studied by Surface-Enhanced Raman Spectroscopy* Central European Conference on Photochemistry CECP, 14-18. 02.2016, Bad Hofgastein, Austria; poster; best poster presentation prize

13. M. Pszona *Surface-Enhanced Raman Spectroscopy: down to a single molecule level*, Polish Photoscience Seminar, 25-26.11.2016 Warszawa, Polska; oral presentation